IN VIVO EVALUATION OF THE EFFICACY AND SAFETY OF RAPID SHORT-PULSE SEQUENCES FOR ULTRASOUND-MEDIATED DELIVERY OF AGENTS TO THE BRAIN

SOPHIE MORSE

A thesis submitted for the degree of Doctor of Philosophy

DEPARTMENT OF BIOENGINEERING

IMPERIAL COLLEGE LONDON

JULY 2020

To my Family and

my Snookums

ABSTRACT

The blood-brain barrier is essential to the maintenance of homeostasis in the brain, but it also prevents 98% of small molecule drugs and imaging agents from entering the brain. Focused ultrasound in combination with microbubbles is a method that can increase the permeability of the blood-brain barrier in a non-invasive, localised and transient manner, allowing drugs and imaging agents into the brain. In conventional ultrasound methods, a sequence of long pulses is applied to the brain, which can cause undesired effects, such as uneven drug distributions and a barrier altered for several hours, exposing the brain to unwanted bloodborne substances. In this thesis, we have investigated whether the efficacy and safety of drug delivery can be improved *in vivo* by emitting ultrasound in a Rapid Short-Pulse (RaSP) sequence.

We first investigated the differences in performance and safety between emitting a RaSP sequence and a long pulse sequence to deliver a dextran model drug. We found that a more uniform drug distribution was achieved using RaSP, with a delivered dose comparable to that of long pulses. The barrier permeability was altered for less than 10 minutes, minimising the amount of endogenous proteins entering the brain, while no tissue damage was observed. We then investigated whether RaSP could deliver large 100 nm liposomes into the brain. We showed that RaSP can achieve this with an improved safety profile, although higher pressures were needed compared to long pulses. Finally, we evaluated whether a dual-modal MRI-optical probe could be delivered into the brain, using long pulses, to image neurons. We confirmed uptake within neurons and detected both fluorescence and MRI signals *ex vivo*. This work demonstrates that ultrasound sequences can be designed to improve the efficacy and safety of drug delivery for the diagnosis and treatment of brain diseases.

CONTENTS

DECLARATION 10

ACKNOWLEDGMENTS 11

PUBLICATIONS 12

LIST OF FIGURES 15

LIST OF TABLES 22

ABBREVIATIONS 24

1 Introduction 27

1.1 Brain diseases 27

1.2 The blood-brain barrier 27

1.2.1 The main components 27

1.2.2 The junction proteins in the blood-brain barrier 30

1.2.3 Transport across the blood-brain barrier 32

1.3 Overcoming the blood-brain barrier 33

1.4 Drug delivery across the blood-brain barrier using focused ultrasound 38

1.4.1 Focused ultrasound 38

1.4.2 Microbubbles 41

1.4.3 Applications of focused ultrasound and microbubble-mediated delivery across the blood-brain barrier 45

1.4.4 Mechanisms of increased blood-brain barrier permeability with focused ultrasound 46

1.4.5 Monitoring microbubbles emissions 47

1.4.6 Clinical trials with focused ultrasound and microbubbles 49

1.4.7 Long pulse ultrasound sequences 52

1.5 Redesigning ultrasound sequencing 56

1.6 Thesis aims 59

1.7 References 60

2 Efficacy and safety of rapid short-pulse sequences for drug delivery 82

2.1 Background 82

2.1.1 Evaluating the efficacy of RaSP 90
2.1.2 Evaluating the safety of RaSP 91
2.1.3 Evaluating the hypothesis behind the design of the rapid short-pulse sequence 92
2.2 Aims and objectives 93
2.3 Materials and methods 94
2.3.1 Pulse sequence parameters 94
2.3.2 Ultrasound setup 97
2.3.3 Targeting 100
2.3.4 Animals 103
2.3.5 Dextran and microbubbles 105
2.3.6 Experimental workflow 106
2.3.7 Histological staining 107
2.3.8 Microscopy and analysis 114
2.3.9 Acoustic signal analysis 116
2.3.10 Statistical analysis 117
2.4 Results 118
2.4.1 Pressure Threshold 118
2.4.2 Delivery and distribution 120
2.4.3 Cellular uptake 127
2.4.4 Time window for molecular delivery 139
2.4.5 Extravasation of endogenous proteins into the brain 142
2.4.6 Safety profile 149
2.4.7 Dextran excretion from the brain 152
2.4.8 Predictability 154
2.4.9 Energy and lifetime of microbubble activity 156
2.4.10 Frequency content of microbubble emissions 161
2.5 Discussion 163
2.5.1 Delivery 164
2.5.2 Cellular uptake 166
2.5.3 Time window for delivery 171
2.5.4 Extravasation of endogenous proteins 173
2.5.5 Safety profile 174
2.5.6 Dextran excretion 175
2.5.7 Acoustic emissions analysis and predictability 176

2.5.8 Clinical relevance 179
2.5.9 Limitations and future work 180
2.6 Conclusions 185
2.7 References 186

3 Delivery of liposomes to the brain with rapid short-pulse sequences 203

3.1 Background 203
3.1.1 Liposomes 203
3.1.2 Liposome delivery with focused ultrasound 205
3.2 Aims and objectives 206
3.3 Materials and methods 207
3.3.1 Ultrasound setup 208
3.3.2 Animals 209
3.3.3 Liposomes and microbubbles 211
3.3.4 Experimental workflow 212
3.3.5 Histological staining 213
3.3.6 Microscopy 213
3.3.7 Analysis 214
3.3.8 Statistical analysis 215
3.4 Results 216
3.4.1 Detected dose 216
3.4.2 Delivery distribution 219
3.4.3 Subcellular localisation 221
3.4.4 Cellular uptake 222
3.4.5 Safety profile 226
3.5 Discussion 228
3.5.1 Delivery 228
3.5.2 Distribution 230
3.5.3 Cellular uptake 231
3.5.4 Safety profile 235
3.5.5 Limitations and future work 236
3.6 Conclusion 239
3.7 References 240

4 Neuron labelling with an optical-MRI dual-modal imaging agent delivered to the brain via focused ultrasound 249

4.1 Background 249

4.1.1 MRI and Gd-based MRI contrast agents 249

4.1.2 Enhancing cellular uptake of Gd(III)-based contrast agents 254

4.1.3 Brain extravasation of Gd(III)-based contrast agents 256

4.2 Aims and objectives 256

4.3 Materials and methods 257

4.3.1 Animals 257

4.3.2 Ultrasound setup and experimental conditions 258

4.3.3 Microbubble and probe delivery 260

4.3.4 Histological staining 261

4.3.5 Microscopy and analysis 262

4.3.6 Binding of Gd(rhodamine-pip-DO3A) to endogenous albumin 263

4.3.7 *Ex vivo* MRI 263

4.3.8 Statistical analysis 265

4.4 Results 265

4.4.1 Delivery of Gd(rhodamine-pip-DO3A) to the brain 265

4.4.2 Cellular uptake of Gd(rhodamine-pip-DO3A) in the brain 268

4.4.3 Distribution of Gd(rhodamine-pip-DO3A) compared to Texas Red dextran in the brain 272

4.4.4 Detection of Gd(rhodamine-pip-DO3A) with MRI 277

4.4.5 Gd(rhodamine-pip-DO3A) binding to albumin 280

4.4.6 Safety of ultrasound delivery parameters 280

4.5 Discussion 282

4.5.1 Delivery and cellular uptake 283

4.5.2 Delivery comparison with 3 kDa dextran 285

4.5.3 MRI detection 286

4.5.4 Binding to albumin 287

4.5.5 Safety profile 288

4.5.6 Limitations and future work 288

4.6 Conclusion 289

4.7 References 290

5 Conclusions 297

6 Appendix 300

Chapter 2 300

6.1 Temperature increase calculation 300

Chapter 3 319

6.2 Experimental – Liposome Synthesis 319

6.2.1 Reagents and equipment 319

6.2.2 Synthesis 319

6.2.3 Serum stability of fluorescent liposomes 320

Chapter 4 325

6.4 Experimental – Gd(rhodamine-pip-DO3A) synthesis 325

6.4.1 Reagents and equipment 325

6.4.2 Synthesis 325

References 330

Permission documents for republication of copyrighted work 330

DECLARATION

Declaration of Originality

I confirm that all the work reported in this thesis is my own, unless stated otherwise. Contributions from collaborators have been clearly indicated and all source material has been appropriately referenced and acknowledged.

Declaration of Copyright

The copyright of this thesis rests with the author. Unless otherwise indicated, its contents are licensed under a Creative Commons Attribution-Non Commercial-No Derivatives 4.0 International Licence (CC BY-NC-ND). Under this licence, you may copy and redistribute the material in any medium or format on the condition that you credit the author, do not use it for commercial purposes and do not distribute modified versions of the work. When reusing or sharing this work, ensure you make the licence terms clear to others by naming the licence and linking to the licence text. Please seek permission from the copyright holder for uses of this work that are not included in this licence or permitted under UK Copyright Law.

ACKNOWLEDGMENTS

First, I would like to thank my supervisors, Dr James Choi and Prof Nicholas Long, for their scientific guidance throughout my PhD. I am extremely grateful for all the support and career advice they have provided me. They have given me much appreciated constructive criticism and have encouraged and enabled me to attend many conferences, which have been essential in my journey to improve as a researcher.

Second, I would like to thank all the members of the NSB laboratory that I have had the pleasure of working with. Many have become close friends of mine and have made this journey truly enjoyable. A special thank you to Tiffany Chan who has been an amazing experimental lab partner, someone I could always talk to and an invaluable critic of my work. To Antonios Pouliopoulos who not only built the *in vivo* setup before I arrived and trained me in little time, but also answered my daily questions, which have turned into many fruitful discussions over the last four years. A big thank you to Cameron Smith, Ahmed El Ghamrawy, Syed Mohd Nooh Syed Omar, Matthew Copping, Julien Lin, Krit Sujarittam, Zheng Jiang, Betul Ilbilgi Yildiz, James Bezer, Dani Chattenton, Harry Davies, Christoforos Charalambous and Aishwarya Mishra. I have learnt so much from all your expertise and I thank you for grilling me at group meetings, for providing moral support, reminding me not to work too hard, bringing me food during lockdown and all your other kind gestures. A big thank you to Dr Helena Watts, who I wish I had met many years ago, as her biological advice and positive energy are contagious and make me excited for the future of my work. I would also like to thank members of the Long Group, particularly Bethany Harriss, who made me realise synthetic chemistry was not my thing, and Tamara Boltersdorf who has been such a joy to work with and who I hope to collaborate again with in the future. A big thank you to all the students that I have co-supervised and who have helped me with my work: Auxtine Micalet, Neil wright, Thao Ngo, David Jung and Grainne Geoghegan.

Third, I would like to thank all those I have been lucky enough to collaborate with: Dr Nicoleta Baxan for all your hard work and sweet messages, I hope to work with you again; Dr Rafael T.M. de Rosales for such an enjoyable collaboration, which allowed me to explore the wonders of liposomes; Dr Magdalena Sastre and Prof Steve Gentleman, my discussions with whom have guided me through the difficulties of staining and the biology of the brain; Dr Nelofer Syed and Dr Richard Perryman who have given me a glimpse into the exciting world of cancer research; Stephen Rothery and Dr David Gaboriau at the FILM microscopy facility, for helping me with all microscope issues with a smile on their face; Dr Claire Higgins for allowing me to use her cryostat on which I have spent many days; and Prof Mengxing Tang, for his academic support, scientific advice, for being so welcoming in his group meetings and without whom lots of my work would not have been possible.

Finally, I would like to thank all my friends and family, your support has been invaluable. To Giuseppe Cinque, my italian and latin teacher, who many years ago taught me how to give talks in front of large audiences and who I miss very much. Francesca Mazzone, Elena Galdacci, Lucia Aliffi, Gloria di Leonardo, Ellis Hudson, Peter Gawne and Francesco Ciaramitaro, thank you for listening to my PhD adventures. To all my proof-readers, Tiffany Chan, Javier Cudeiro Blanco, Kate Morse, Paul Morse, William Lim Kee Chang, Aishwarya Mishra, Krit Sujarittam, I am extremely grateful to you all. To Kate Morse, who has helped me add creativity to my writing and encouraged me to come out of my PhD bubble to see the real world. To Georgia Morse, who has made me smile and see the bright side of things along the way. To my mum, who has calmed me down in difficult moments, lovingly nudged me to complete this thesis and whose artwork makes that bubble I live in so much more beautiful. To my dad, whose humour, advice and rabbit updates have made me laugh, miss home and inspired me to pursue my passions. Finally, an infinite thank you to Javier Cudeiro Blanco, with whom I manage to both agree and disagree with great conviction in our research discussions, who believes in me, stands by me, and with whom I hope to share many more adventures.

PUBLICATIONS

The following journal papers and conference presentations were based on the current doctoral dissertation:

Journal papers

Morse S V, Pouliopoulos A N, Chan T G, Copping M J, Lin J, Long N J and Choi J J, 2019, Rapid short-pulse ultrasound delivers drugs uniformly across the murine blood-brain barrier with negligible disruption, *Radiology*, 291(2), 459-466. (**Chapter 2**)

Morse S V, Boltersdorf T, Harriss B, Chan T G, Baxan N, Jung H S, Pouliopoulos A N, Choi J J and Long N J, 2020, Neuron labelling with rhodamine-conjugated Gd-based MRI contrast agents delivered to the brain via focused ultrasound, *Theranostics*, 10(6), 2659-2674. (**Chapter 4**)

Conference papers

Morse S V, Chan T G, Pouliopoulos A N, Long N J, Choi J J, Noninvasive and localised drug delivery across the blood-brain barrier using focused ultrasound and microbubbles. *Cancer Research UK – AACR, London, UK, October 2019*.

Morse S V, Chan T G, Pouliopoulos A N, Long N J, Choi J J, Getting drugs to the brain with ultrasound and microbubbles. *STEM for Britain, Parliament, London, UK, March 2019* (1st prize Engineering Gold Medal and the Westminster Medal overall winner).

Morse S V, Davies H J, Copping M J, Chan T G, Tang M, Long N J, Choi J J, Single-cycle ultrasound drug delivery and passive acoustic mapping in the brain in vivo. *The 24th European Symposium on Ultrasound Contrast Imaging, Rotterdam, Netherlands, January 2019* (Won therapy monitoring presentation competition).

Morse S V, Chan T G, Copping M J, Pouliopoulos, Long N J, Choi J J, Minutes-long blood-brain barrier opening with Rapid Short-Pulse (RaSP) ultrasound and

microbubbles *in vivo*. *The 8th Annual UK & Ireland Early Career BBB Symposium, Oxford, UK, November 2018*.

Morse S V, Chan T G, Copping M J, Pouliopoulos, Long N J, Choi J J, Improved performance and safety of drug delivery to the brain *in vivo* with Rapid Short-Pulse (RaSP) sequences. *IEEE International Ultrasonics Symposium (iUS IEEE), Kobe, Japan, October 2018*.

Morse S V, Chan T G, Copping M J, Pouliopoulos, Long N J, Choi J J, On the safety of brain drug delivery using Rapid Short-Pulse (RaSP) sequences. *The 23rd European Symposium on Ultrasound Contrast Imaging, Rotterdam, Netherlands, January 2018* (Finalist in poster presentation competition).

Morse S V, Pouliopoulos, Chan T G, Lin J, Copping M J, Long N J, Choi J J, Improved drug distribution to the brain *in vivo* using Rapid Short-Pulse (RaSP) sequences. *Therapy Ultrasound Group (THUGs), London, UK, December 2017*.

Morse S V, Pouliopoulos, Chan T G, Lin J, Copping M J, Long N J, Choi J J, Rapid Short-Pulse (RaSP) sequences improve the distribution of drug delivery to the brain *in vivo*. *IEEE International Ultrasonics Symposium (iUS IEEE), Washington DC, USA, September 2017*.

Morse S V, Pouliopoulos, Chan T G, Lin J, Copping M J, Long N J, Choi J J, Drug delivery to the brain using Rapid Short-Pulse (RaSP) ultrasound sequences and microbubbles *in vivo*. *Imperial College Dementia Network Centre Summer Symposium, London, UK, July 2017* (Won 1st prize poster competition).

Morse S V, Pouliopoulos, Chan T G, Lin J, Long N J, Choi J J, Rapid Short-Pulse (RaSP) sequences – a new therapeutic ultrasound exposure paradigm to enhance drug delivery to the brain *in vivo*. *International Society for Therapeutic Ultrasound, Nanjing, China, May 2017* (Finalist in oral presentation competition).

LIST OF FIGURES

Figure 1.1	The structural components of the blood-brain barrier.	28
Figure 1.2	Components of the junction proteins in the blood-brain barrier.	31
Figure 1.3	Transport pathways across the blood-brain barrier.	33
Figure 1.4	Longitudinal sound wave.	39
Figure 1.5	Ultrasound wave parameters.	40
Figure 1.6	Mechanical phenomena caused by microbubbles.	44
Figure 1.7	Long pulse ultrasound sequence.	52
Figure 1.8	Rapid short-pulse ultrasound sequence.	57
Figure 2.1	Comparison between a rapid short-pulse (RaSP) and long pulse sequence.	84
Figure 2.2	Morphology of resting and activated microglia.	85
Figure 2.3	Morphology of resting and activated astrocytes.	87
Figure 2.4	Excretion pathway of agents delivered to the brain with focused ultrasound.	90
Figure 2.5	Structure of rapid short-pulse (RaSP) and long pulse sequences.	96
Figure 2.6	Ultrasound experimental setup.	98
Figure 2.7	Sutures of the mouse skull and example raster scan.	101
Figure 2.8	Ultrasound targeting.	102
Figure 2.9	Experimental workflow for *in vivo* experiments.	107
Figure 2.10	Direct and indirect immunofluorescence methods and staining workflow.	110
Figure 2.11	H&E staining workflow.	114
Figure 2.12	Acoustic pressure threshold for dextran delivery to the brain with long pulses	119

Figure 2.13	Quantification of the detected dextran dose in brains treated with three different pressures.	120
Figure 2.14	Distribution of dextran delivered with rapid short-pulse (RaSP) and long pulse sequences.	122
Figure 2.15	Detected dose and distribution of dextran delivered with rapid short-pulse (RaSP) and long pulse sequences at 0.35 MPa.	123
Figure 2.16	Dextran distribution throughout the parenchyma and in cells in RaSP-treated brains.	125
Figure 2.17	Dextran distribution throughout the parenchyma and in cells in long-pulse-treated brains.	126
Figure 2.18	Brain slices stained for neurons, microglia and astrocytes.	127
Figure 2.19	Uptake of dextran within neurons in RaSP and long-pulse-treated brains at 0 h.	129
Figure 2.20	Number of neurons with dextran uptake in brains treated with RaSP or long pulses observed at 0 h, 2 h, 24 h and 48 h after ultrasound treatment.	130
Figure 2.21	Neuronal uptake in RaSP and long-pulse-treated brains at 0 h, 2 h, 24 h and 48 h after ultrasound treatment.	131
Figure 2.22	Dextran uptake within microglia in RaSP and long-pulse-treated brains at 0 h.	133
Figure 2.23	Number of microglia with dextran uptake in brains treated with RaSP or long pulses observed at 0 h, 2 h, 24 h and 48 h after ultrasound treatment.	134
Figure 2.24	Dextran uptake within microglia in RaSP and long-pulse-treated brains at 0 h, 2 h, 24 h and 48 h after ultrasound treatment.	135
Figure 2.25	Dextran uptake within astrocytes in RaSP and long-pulse-treated brains at 0 h.	137
Figure 2.26	Number of astrocytes with dextran uptake in brains treated with RaSP or long pulses observed at 0 h, 2 h, 24 h and 48 h after ultrasound treatment.	138
Figure 2.27	Dextran uptake within astrocytes in RaSP and long-pulse-treated brains at 0 h, 2 h, 24 h and 48 h after ultrasound treatment.	138

Figure 2.28	Dextran delivery at 0, 10 and 20 min after ultrasound treatment with RaSP and long pulse sequences.	140
Figure 2.29	BBB closing timeline with RaSP and long pulse sequences.	141
Figure 2.30	Albumin extravasation into the brain 0, 10 and 20 min after ultrasound exposure with RaSP and long pulse sequences.	143
Figure 2.31	Albumin extravasation with RaSP and long pulse sequences.	144
Figure 2.32	Immunoglobulin extravasation into the brain 0, 10 and 20 min after ultrasound exposure with RaSP and long pulse sequences.	145
Figure 2.33	Immunoglobulin extravasation with RaSP and long pulse sequences.	146
Figure 2.34	Distribution of albumin and dextran in RaSP and long-pulse-treated brains at 0 min.	147
Figure 2.35	Distribution of immunoglobulin and dextran in RaSP and long-pulse-treated brains at 0 min.	148
Figure 2.36	H&E staining on RaSP-treated brains to assess tissue damage.	150
Figure 2.37	H&E staining on long-pulse-treated brains to assess tissue damage.	151
Figure 2.38	Number of sites with red blood cell extravasations, microvacuolations and dark neurons in RaSP and long pulse brains.	152
Figure 2.39	Dextran excretion from RaSP-treated brains between 0 and 48 h.	153
Figure 2.40	Dextran excretion from long-pulse-treated brains between 0 and 48 h.	154
Figure 2.41	Predicting the detected dextran dose based on the energy of the acoustic emissions.	155
Figure 2.42	Energy from acoustic emissions during RaSP and long pulse sequence treatment.	157
Figure 2.43	Lifetime of acoustic emissions from microbubbles.	158
Figure 2.44	Average energy of each pulse within a burst during a RaSP treatment.	159

Figure 2.45	Energy of each pulse across the ultrasound treatment emitting a RaSP sequence.	160
Figure 2.46	Spectral content of the acoustic emissions produced by RaSP and long pulse sequences.	162
Figure 3.1	Schematic representation of different liposome delivery systems.	204
Figure 3.2	Ultrasound experimental setup.	209
Figure 3.3	DiD-PEGylated liposome structure.	211
Figure 3.4	Liposomal delivery with rapid short-pulse (RaSP) and long pulse sequences at 0.4 and 0.6 MPa, and at 0 and 2 h after ultrasound treatment.	217
Figure 3.5	Detected dose of liposomes delivered with rapid short-pulse (RaSP) and long pulse sequences at 0.4 and 0.6 MPa, and at 0 h or 2 h after the ultrasound treatment.	218
Figure 3.6	Distribution of liposomes delivered with rapid short-pulse (RaSP) and long pulse sequences at 0.4 and 0.6 MPa, and at 0 h or 2 h after the ultrasound treatment.	219
Figure 3.7	Number of areas with liposome delivery above 100 μm^2.	220
Figure 3.8	Subcellular localisation of liposomes.	221
Figure 3.9	Uptake of liposomes within neurons in RaSP and long-pulse-treated brains.	223
Figure 3.10	Number of neurons with liposome uptake in brains treated with RaSP or long pulses at 0.4 or 0.6 MPa, and at 0 h or 2 h after the ultrasound treatment.	224
Figure 3.11	Uptake of liposomes within microglia in RaSP and long-pulse-treated brains.	224
Figure 3.12	Number of microglia with liposome uptake in brains treated with RaSP or long pulses at 0.4 or 0.6 MPa, and at 0 h or 2 h after the ultrasound treatment. .	225
Figure 3.13	Uptake of liposomes within astrocytes in RaSP and long-pulse-treated brains.	225
Figure 3.14	H&E staining on RaSP-treated brains at 0.6 MPa to assess tissue damage.	226

Figure 3.15	H&E staining on long-pulse-treated brains at 0.6 MPa to assess tissue damage.	227
Figure 3.16	Average number of sites with red blood cell extravasations, microvacuolations and dark neurons in RaSP and long pulse brains at 0.6 MPa.	228
Figure 4.1	Hydrogen atom behavior in a magnetic field and magnetisation changes over time.	251
Figure 4.2	Structure of the gadolinium(III) complex Gd(DOTA).	252
Figure 4.3	Longitudinal and transverse relaxation times.	254
Figure 4.4	Rhodamine B interconverting between a non-fluorescent and a fluorescent form.	255
Figure 4.5	Ultrasound experimental setup.	259
Figure 4.6	3D reconstruction of the mouse brain from the MRI images and sagittal, axial and coronal brain slices.	264
Figure 4.7	Successful delivery of Gd(rhodamine-pip-DO3A) to the left hemisphere of all seven mouse brains.	267
Figure 4.8	Delivery of Gd(rhodamine-pip-DO3A) to the left hemisphere of the mouse brain.	267
Figure 4.9	Neuronal staining of brain slices with Gd(rhodamine-pip-DO3A) delivery.	268
Figure 4.10	Microglia staining of brain slices with Gd(rhodamine-pip-DO3A) delivery.	269
Figure 4.11	Astrocyte staining of brain slices with Gd(rhodamine-pip-DO3A) delivery.	271
Figure 4.12	Number of neurons, microglia and astrocytes overlapping with Gd(rhodamine-pip-DO3A).	272
Figure 4.13	Distribution of Gd(rhodamine-pip-DO3A) within the brain.	273
Figure 4.14	Subcellular localisation of Gd(rhodamine-pip-DO3A) within neuronal-like cells.	274
Figure 4.15	Distribution of dextran within the brain.	275
Figure 4.16	Neuronal, microglial and astrocyte staining of brain slices with dextran delivery.	276

Figure 4.17	Quantified distribution of Gd(rhodamine-pip-DO3A) and dextran within the brain.	276
Figure 4.18	*Ex vivo* MRI images of Gd(rhodamine-pip-DO3A) delivery to the left hemisphere.	278
Figure 4.19	Increase in fluorescence and MRI signal in the left hemisphere.	279
Figure 4.20	Fluorescence detection of Gd(rhodamine-pip-DO3A) in brain scanned with MRI.	279
Figure 4.21	Binding of Gd(rhodamine-pip-DO3A) to albumin.	280
Figure 4.22	H&E staining to assess damage.	281
Figure 6.1	Experimental setup.	301
Figure 6.2	Beam profiles.	301
Figure 6.3	Graphical user interface (GUI).	302
Figure 6.4	Exact dimensions for the stainless-steel cross.	302
Figure 6.5	Pulse-echo mode connections.	303
Figure 6.6	Example raster scans with different methods tested.	303
Figure 6.7	Example raster scans with the final grid chosen.	304
Figure 6.8	Anatomical orientations for the mouse brain.	312
Figure 6.9	Code to perform the NOD and COV quantification.	312
Figure 6.10	Examples of artefacts in fluorescence images.	315
Figure 6.11	Dextran within glial cells and capillaries when delivered with a RaSP sequence.	316
Figure 6.12	Dextran distribution and neuronal uptake when delivered with a long pulse sequence.	316
Figure 6.13	Dextran delivery to glial cells and vessels when delivered with a long pulse sequence.	317
Figure 6.14	H&E and dextran images in RaSP-treated brains.	318
Figure 6.15	H&E and dextran images in long-pulse-treated brains	318

Figure 6.16	Spectral content of acoustic emissions from bursts of RaSP and long pulses.	319
Figure 6.17	Stability of liposomes in serum.	322
Figure 6.18	Synthesis of Gd(rhodamine-pip-DO3A)	330

LIST OF TABLES

Table 1.1	Methods to deliver drugs across the blood-brain barrier.	36
Table 1.2	Clinical trials using focused ultrasound and microbubbles in the brain.	51
Table 1.3	Studies using short ultrasound pulses.	59
Table 2.1	Ultrasound exposure parameters.	97
Table 2.2	Targeting issues.	102
Table 2.3	Summary of mice used in each experiment.	103
Table 2.4	Primary and secondary antibodies used to stain for albumin, immunoglobulin, neurons, microglia and astrocytes.	112
Table 2.5	Optimisation of staining protocols performed.	113
Table 2.6	Excitation and emission filters for the fluorophores.	115
Table 2.7	Sum and maximum energies from the acoustic emissions for all RaSP and long-pulse-treated brains.	161
Table 3.1	Summary of mice used in each study.	210
Table 3.2	Primary and secondary antibodies used to stain for neurons, microglia and astrocytes.	213
Table 3.3	Excitation and emissions filters for the fluorophores.	214
Table 4.1	Summary of mice used in each experiment.	258
Table 4.2	Primary and secondary antibodies used to stain for neurons, microglia and astrocytes.	262
Table 6.1	Protocol for cryosectioning.	304
Table 6.2	Protocol for albumin staining.	306
Table 6.3	Protocol for immunoglobulin staining.	307
Table 6.4	Protocol for neuron staining.	308

Table 6.5	Protocol for microglia staining.	309
Table 6.6	Protocol for astrocyte staining.	310
Table 6.7	Protocol for H&E staining.	311
Table 6.8	Protocol for paraffin-embedding.	311
Table 6.9	Studies showing delivery of liposomes into the brain using focused ultrasound and microbubbles.	323

ABBREVIATIONS

A	**ANOVA**	A one-way analysis of variance
B	**BBB**	Blood-brain barrier
	BL	Burst length
	BODIPY	Boron dipyrromethene
	BRF	Burst repetition frequency
	BSA	Bovine serum albumin
	B_0	Magnetic field of the magnetic resonance imaging scanner
C	**COV**	Coefficient of variation
	CPP	Cell penetrating peptide
	CSF	Cerebrospinal fluid
	Cy5/Cy7	Cyanine 5/Cyanine 7
D	**DAB**	3,3′-diaminobenzidine
	DAMPs	Damage associated molecular proteins
	DAPI	4′,6-diamodino-2phenylindole
	DiD	1,1′-dioctadecyl-3,3,3′,3′-tetramethylindodicarbocyanine, 4-chlorobenzensulfonate salt
	DOTA	tetraazacyclododecane-1,4,7,10-tetraacetic acid
F	**f**	Frequency
	F_C	Centre frequency
	FFT	Fast Fourier transform
	FITC	Fluorescein isothiocyanate
	FWHM	Full width at half maximum
G	**Gd**	Gadolinium
	GFAP	Glial fibrillary acidic protein
	GFP	Green fluorescent protein
	GUI	Graphical user interface

H	**H&E**	Haematoxylin and eosin
	Hz	Hertz
I	**I**	Intensity
	Iba1	Ionised calcium binding adaptor molecule 1
	IV	Intravenous
	ICV	Intracerebroventricular
M	**MI**	Mechanical index
	MIP	Maximum intensity projections
	MR	Magnetic resonance
	MRI	Magnetic resonance imaging
	ms	Millisecond
	M_{xy}	Transverse magnetisation
	M_z	Longitudinal magnetisation
N	**N_B**	Number of bursts
	NeuN	Neuronal nuclei antigen
	NOD	Normalised optical density
O	**OCT**	Optical cutting temperature
P	**P**	Pressure
	Pa	Pascal
	PAM	Passive acoustic mapping
	PBS	Phosphate buffered saline
	PC	Personal computer
	PCD	Passive cavitation detector
	PDX	Dibutyl phthalate polystyrene xylene
	PEG	Polyethyleneglycol-lipids
	PL	Pulse length
	P_{neg}	Peak-negative pressure
	P_{pos}	Peak-positive pressure
	PRF	Pulse repetition frequency

	PVDF	Polyvinylidene difluoride
R	**RaSP**	Rapid Short-Pulse
	RBC	Red blood cell
	RF	Radio frequency
	ROI	Region of interest
T	**T_1**	Longitudinal relaxation time
	T_2	Transverse relaxation time
	T_E	Echo time
	T_R	Repetition time
Z	**Z**	Acoustic impedance

1 | Introduction

1.1 Brain diseases

One third of the worldwide disease burden is caused by brain diseases, which increases every year due to an ageing population [1]–[3]. Different categories of brain diseases exist, including tumours such as glioblastoma, neurodegenerative conditions like Alzheimer's disease and Parkinson's disease, and autoimmune conditions such as multiple sclerosis. Many of these diseases still lack a cure and more research is needed to find effective treatment methods [3].

Although some treatments have been developed for brain diseases, most drugs are ineffective in patients. This is probably due to insufficient concentrations of the drugs reaching the diseased regions of the brain [4]. Intravenously administered drugs enter the brain from the blood vessels but first they need to cross the blood-brain barrier (BBB). Most drugs are unable to cross the BBB and the few that do are actively excreted from the brain via efflux transporters, preventing therapeutically effective drug doses from being reached [4]. There is therefore a need to circumvent the BBB to achieve therapeutically relevant drug doses in order to effectively treat brain diseases.

1.2 The blood-brain barrier

1.2.1 The main components

The blood-brain barrier is a natural, semi-permeable, physical transport and metabolic barrier that separates the cerebral vasculature from the parenchyma of the brain. This barrier is in place to maintain homeostasis within the brain, which is critical for neuronal function. It does so by tightly regulating the movement of both exogeneous and endogenous substances in and out of the brain [5]. In this way, the BBB protects the brain from pathogens, toxins, inflammation, injury and disease.

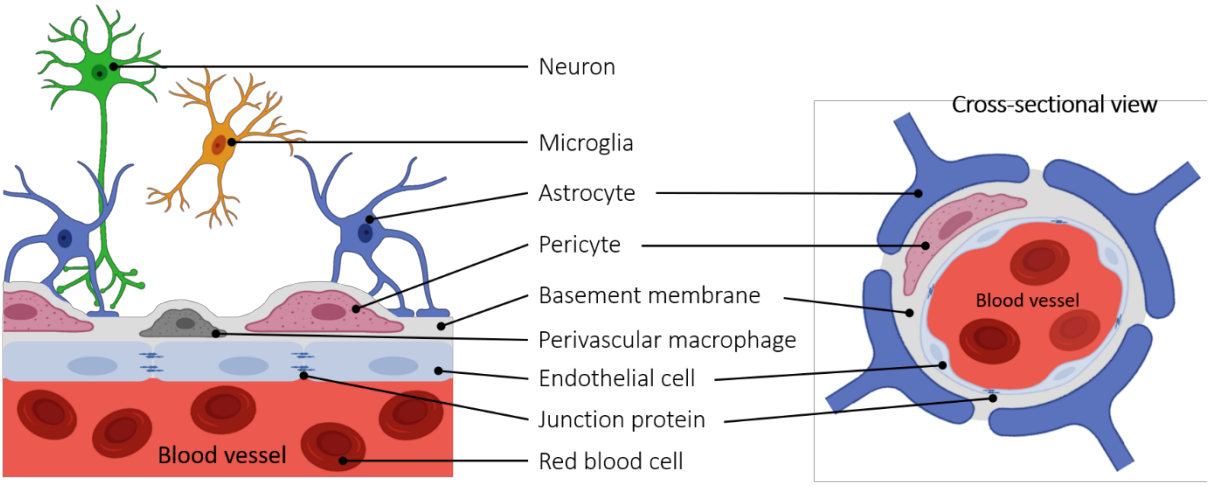

Figure 1.1. The structural components of the blood-brain barrier. Endothelial cells are connected by tight junction proteins and surrounded by a basement membrane and astrocyte endfeet. Perivascular macrophages and pericytes are embedded in the basement membrane, while microglia and neurons are found in the extracellular matrix of the brain. This diagram is based on a figure from T. Chan's thesis [6].

The main components of the BBB are the brain endothelial cells, basement membrane, pericytes, astrocyte endfeet and perivascular macrophages (Figure 1.1) [7]. Endothelial cells form the walls of blood vessels within the brain, which are unique compared to the rest of the body as they are continuous and non-fenestrated. The endothelial cells of cerebral vessels are sealed with tight junction and adherens junction proteins. Due to these junctions, brain capillaries are 50-100 times less permeable than peripheral capillaries [8]. The walls of the larger arteries and veins in the brain are made up of several layers of endothelial cells, while the smallest capillaries only have a monolayer of very thin endothelial cells with less than 0.25 μm separating the inside of the vessel from the parenchymal surface [9], [10]. Compared to the endothelial cells in the rest of the body, those in the brain have a lower rate of transcytosis [10], which contributes towards the tight regulation of transport across the BBB. Two different types of transporters are expressed on the surface of these brain endothelial cells: efflux transporters and nutrient transporters. The former transport lipophilic molecules into the blood, to avoid the neurotoxic adverse effects that would otherwise accumulate in the brain. The latter transport nutrients into the brain and remove waste products [11],

[12]. Brain endothelial cells also have more mitochondria than cells in the rest of the body, which may be to maintain the ion gradients between the blood and the extracellular fluid in the brain [13]. These cells also express extremely low levels of leukocyte adhesion molecules to limit the number of immune cells entering the brain [14].

The vessels in the brain are surrounded by two extracellular matrices known as basement membranes: the inner vascular and outer parenchymal [15], [16]. The inner vascular membrane is secreted by endothelial cells and pericytes, while the outer parenchymal is secreted by astrocytes. These membranes serve as an additional barrier for molecules and cells, before reaching the neurons within the brain [17]. The pores within the network of the extracellular matrix are approximately 60 nm in diameter [18].

Pericytes are cells that are embedded in the vascular basement membrane and line the endothelial cells of brain vessels [19]. They extend cellular processes along the surface of the endothelial cells and can span the length of several endothelial cell bodies, covering 80% of the capillary surface [18]. The ratio of endothelial cells to pericytes is between 1:1 and 3:1 – the highest in the body [20]. Pericytes regulate immune cell infiltration and blood flow in response to neuronal activity by controlling the diameter of capillaries [21]. They are also involved in wound healing and deposit the extracellular matrix that forms the basement membrane [22].

Astrocytes are another major component of the BBB. These glial cells extend specialised processes towards the cerebral microvasculature, known as astrocyte endfeet, and also extend processes towards neurons, creating a link between the blood vessels and the neuronal circuitry [8]. Astrocytes regulate blood flow depending on neuronal activity by controlling the vascular smooth muscle cells around arterioles and the pericytes around capillaries [17], [23]. They are the most abundant cells in the brain, outnumbering neurons by over fivefold, and are involved in a number of critical

processes such as clearing toxins, maintaining and repairing the BBB, and regulating water and ion diffusion [24], [25].

Finally, immune cells, such as perivascular macrophages and microglial cells, are also part of the BBB. Perivascular macrophages are resident tissue macrophages located between the endothelial basement membrane and the vessels. They are found infrequently and are involved in phagocytosing and degrading unwanted substances, as well as producing inflammatory signals [26], [27]. Microglia, on the other hand, are the resident immune cells within the brain parenchyma and are capable of removing debris, destroying invading micro-organisms and promoting tissue repair by secreting growth factors [28], [29]. These cells respond rapidly not only to structural changes in the brain, but also to small changes in the microenvironment [30]. Microglia have been shown to rapidly migrate to sites of damage [31].

1.2.2 The junction proteins in the blood-brain barrier

The endothelial cells of blood vessels in the brain are held together by tight and adherens junctions, restricting paracellular transport of substances between the blood and the brain (Figure 1.2). Tight junctions are composed of transmembrane adhesion proteins that connect the cytoskeleton of the cell where they are located to transmembrane proteins of adjacent cells [32], [33]. Claudins, occludins and junctional adhesion molecules are the main transmembrane proteins. Claudins (20-30 kDa) are the main sealing components and are crucial in tight junction formation. Different types of claudins can be found in brain endothelial cells (claudin-3, -5 and -12). Claudin-5 is the predominant tight junction protein and its suppression leads to the disruption of BBB integrity, which allows larger molecules to cross the BBB [34], [35]. Occludins (~ 60 kDa) are transmembrane proteins that have two extracellular loops: one interacts with the actin cytoskeleton and the other regulates adhesion properties between cells. Its function is thought to be regulatory rather than for adhesion alone [36], [37]. Lastly, junctional adhesion molecules (30-40 kDa) are part of the

immunoglobulin family and are thought to be involved in the formation of tight junctions and in regulating leukocyte adhesion [38]–[40].

Adherens junctions are positioned next to tight junctions and have a similar organisation. They contain transmembrane proteins that are connected to the intracellular cytoskeleton and are involved in regulating signalling processes in and out of the cells, stabilising adhesion between cells and regulating the cytoskeleton [33], [41].

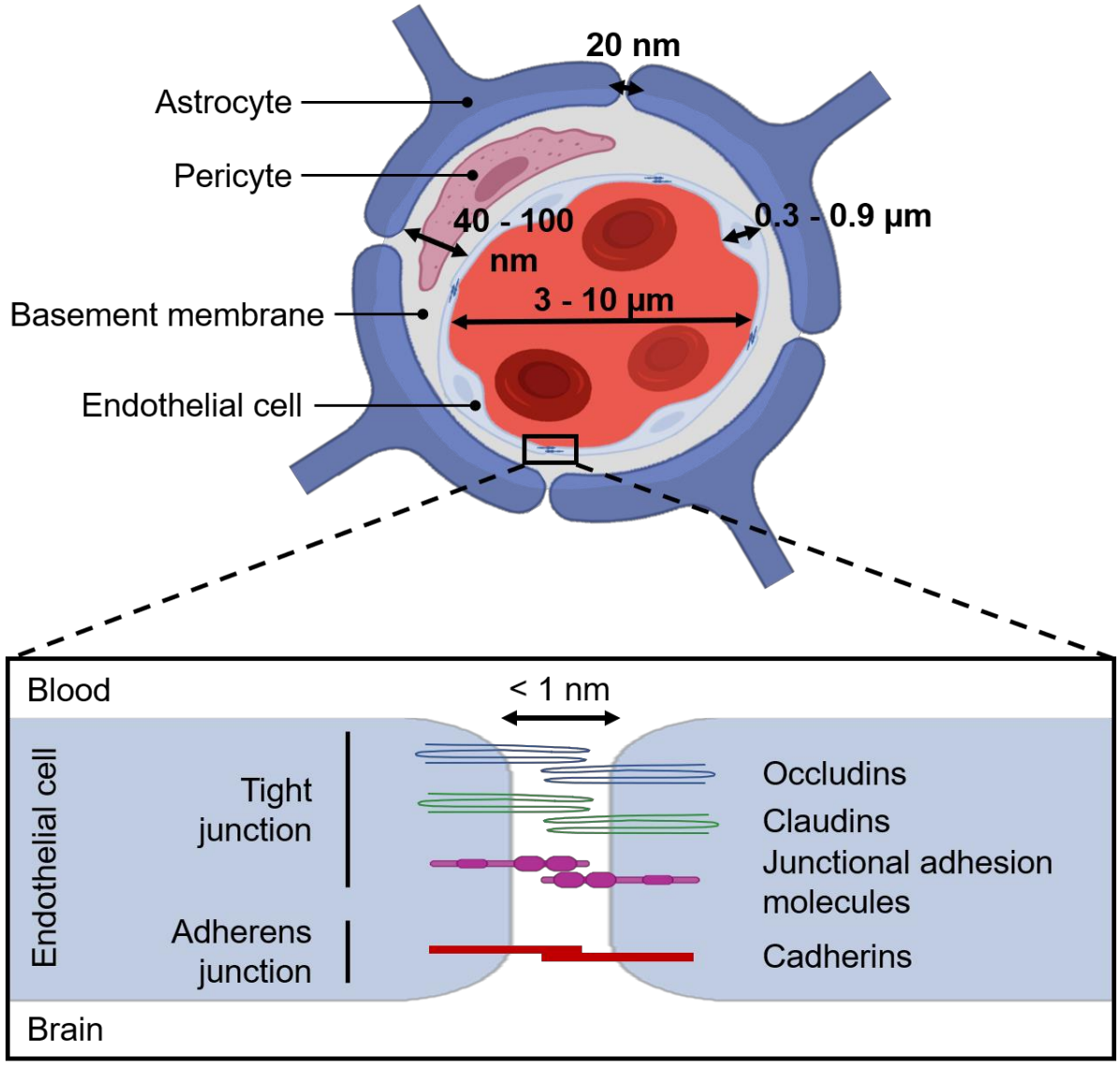

Figure 1.2. Components of the junction proteins in the blood-brain barrier. In the BBB, there are two main junctional complexes that restrict paracellular transport: tight junctions and adherens junctions. Tight junction transmembrane proteins include occludins, claudins and

junctional adhesion molecules. Adherens junctions contain transmembrane proteins such as cadherins. This diagram is based on a figure from T. Chan's thesis [6].

1.2.3 Transport across the blood-brain barrier

The BBB is the biggest limiting factor in allowing drugs into the brain, as all large molecule drugs and more than 98% of small molecule drugs do not cross this barrier [42]–[47]. Large molecule drugs include antibodies, proteins, peptides, RNA-based drugs and gene therapies [44]. Small molecule drug therapies that can cross the BBB, on the other hand, currently only treat some brain diseases including epilepsy, chronic pain, schizophrenia and depression [48]. The BBB is therefore a major obstacle in the development of treatments for neurodegenerative diseases, cerebrovascular diseases and brain cancer.

The two main pathways for molecules to cross the BBB are the paracellular route, between endothelial cells, and the transcellular route, across the two layers of the cell membrane and the cytoplasm (Figure 1.3). The junction proteins between the endothelial cells of the brain (< 1 nm diameter) eliminate most paracellular transport across the BBB, except for small ions and molecules [10], [18], [44], [49]. Transcellular transport is possible for small and sufficiently lipophilic molecules (oxygen, carbon dioxide and ethanol) by passive diffusion, while specialised transporters allow active transport of glucose, peptides and proteins across the BBB [50]–[52]. For a molecule to cross the BBB, it must have a molecular mass under 400-500 Da and high lipid solubility [44]. Molecules that can naturally cross the barrier also tend to form fewer than 8-10 hydrogen bonds with water [44].

Even though molecules can cross the BBB, efflux pumps regulate the return of unwanted molecules back to the vascular system. Transporters include multidrug resistance proteins, such as P-glycoprotein found at the BBB. These transporters are present on both the luminal and abluminal side of the cell membrane [53] and can prevent drugs from accumulating within the brain [54]–[56]. They are the reason drug

doses that reach the brain are often insufficient, even if the drugs being used have been modified to be able to cross the BBB [11].

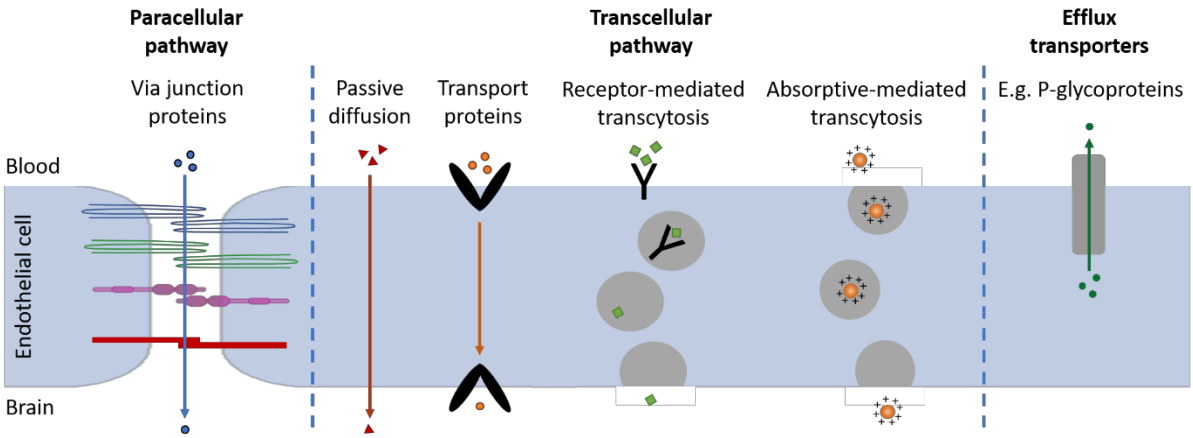

Figure 1.3. Transport pathways across the blood-brain barrier. Molecules cross the BBB using paracellular, transcellular or efflux transporter pathways. The paracellular route involves bypassing junction proteins. Transcellular routes include passive diffusion for small ions and sufficiently lipophilic molecules (e.g. oxygen, carbon dioxide and ethanol), while active transport routes are necessary to allow glucose, peptides and proteins across. Transmembrane proteins transport glucose and amino acids, receptor-mediated transcytosis transports molecules such as insulin and immunoglobulins, and absorptive-mediated transcytosis transports albumin. Another active transport pathway is made up of efflux transporters, such as P-glycoproteins, which transport drugs back into the bloodstream. This diagram is based on a figure from T. Chan's thesis [6].

1.3 Overcoming the blood-brain barrier

Many approaches have been explored to allows drugs to cross the BBB (Table 1.1), such as lowering the drug's molecular weight and polarity, and changing the drug's lipophilicity and propensity for hydrogen bonding. However, such modifications are often complicated. If they are successful, drugs may still not reach therapeutically relevant concentrations in the brain and may increase off-target uptake (e.g. in the liver) that can lead to morbidity [57]–[60]. Modifying drugs can also reduce their specificity and effectiveness. Given the limited success of these approaches, alternative strategies have been explored that do not involve chemical modifications.

Methods that involve injecting drugs directly into the ventricles or into the brain parenchyma have been tested. Intracerebroventricular injections involve penetrating the skull to inject drugs directly into the lateral ventricle of the brain, which is filled with cerebrospinal fluid (CSF) [61]. This technique reduces the systemic toxicity from administered agents compared to their intravenous injection, but it is invasive and there is a risk of infection and increased intracranial pressure. In addition, drugs can only diffuse slowly into the parenchyma, often exiting the ventricles faster than they can diffuse in [62]. Drugs can also be injected directly into the parenchyma via injection or implants. Intraparenchymal administration allows drugs to be delivered locally, but here again the technique is invasive and drugs have difficulty penetrating far from the delivery site solely via passive diffusion [63], [64]. Alternatively, the brain can be surgically exposed in order to place a small catheter into the parenchymal space, a method called convection-enhanced delivery. Drugs are released from the catheter with a pressure gradient, allowing them to move via diffusion and fluid convection [65]–[67]. Although drugs distribute better using this technique, the procedure is again invasive, and the risks of infection, high pressures and tissue injury are still present.

Techniques that involve drugs reaching the CSF to then enter the brain have also been explored. Drugs can be injected into the subarachnoid space of the spinal cord via a lumbar puncture [68]. This method is less invasive than those described above, but there are risks of infection and harmful immune responses [68], [69]. Intratympanic administration, through the inner ear, also via the CSF, has been shown to lead to higher drug concentrations in the brain compared to intravenous injections; however, again there are doubts regarding the efficacy of delivering drugs via the CSF [70], [71].

Intranasal delivery has emerged as a non-invasive route for drugs to bypass the BBB, reaching the central nervous system via the olfactory pathway [72], [73]. The risks of side-effects from systemic exposure are reduced and it is a comfortable administration route for patients. Compared to intravenous and oral routes of administration, this method achieves better drug concentrations, with rapid drug absorption. However,

distribution patterns vary depending on the drug, often with rapid clearance from the CSF and limited drug penetration in some regions. Frequent use has also led to damaged nasal mucosa [74], [75].

With a different approach, the properties of the BBB itself can be modified to increase its permeability. This is done by intravenously injecting hyperosmotic solutions [76]. Solutions such as mannitol create osmotic pressure in the capillaries leading to the shrinkage of endothelial cells to equilibrate the ion imbalance [77]. The junctions are therefore widened, increasing the permeability of the BBB. This method has been shown to increase the delivery of hydrophilic drugs by up to 20-fold, restoring the barrier's permeability within 8 h [78], [79]. However, this technique is not local and can therefore lead to off-target side effects, including seizures [80], [81].

The BBB can also be modified by developing auxiliary agents that inhibit efflux pumps, a method that still needs to be explored clinically. As it is not local, it can have off-target effects and allow substances other than the drug to also enter the brain [82]. This method is thought to have potential for the treatment of acute diseases, such as brain tumours [83].

Lastly, drugs can be delivered by temporarily opening the BBB with external stimuli such as microwave irradiation and electromagnetic fields. Although both techniques have been investigated to temporarily open the BBB, there are related safety concerns as the microwave method involves elevated temperatures inside of the brain [84], [85] and electromagnetic fields potentially have carcinogenic effects [86], [87].

Table 1.1. Methods to deliver drugs across the blood-brain barrier. Different methods to overcome this barrier with respective details of the technique are listed together with their advantages and disadvantages. IV = intravenous, CSF = cerebrospinal fluid.

Method	Details	Non-invasive	Localised	Comments
Direct injection	Intraparenchymal	X	√	Poor drug penetration beyond injection site
	Intracerebroventricular (ICV)	X	X	Reduced systemic toxicity, risk of infection, increased intracranial pressure, slow diffusion into parenchyma
	Convection-enhanced delivery (catheter in parenchyma)	X	√	Drugs released with pressure gradient, better drug distribution, risk of infection and tissue injury
Spinal cord injection	Subarachnoid space of spinal cord	X	X	Less invasive than direct injection methods, risk of infection, immune response, uncertain of delivery efficiency
Intratympanic delivery	Via inner ear	√	X	High drug delivery compared to systemic injection, uncertain delivery efficiency via CSF
Intranasal delivery	Via olfactory pathway	√	X	Reduced side effects, easy administration, better concentrations than IV or oral routes; poor drug penetration beyond injection site, varied distribution patterns and cases of damaged nasal mucosa
Osmotic disruption	Systemic injection of hyperosmotic solutions that shrink endothelial cells of the BBB	√	X	Increased delivery of hydrophilic drugs up to 20-fold, temporary opening of barrier; side effects include seizures

Method	Details	Non-invasive	Localised	Comments
Inhibit efflux pumps	-	-	X	Potentially suitable to treat acute diseases; off-target effects, substances other than drug also enter the brain
External stimuli	Microwave irradiation	√	-	Elevated temperatures can cause tissue damage
	Electromagnetic fields	√	-	Potential carcinogenic effects
Modifications to delivered agents	Lowering molecular weight, polarity, propensity for hydrogen bonding, changing lipophilicity	√	X	Easy administration; often poor efficiency, not trivial: need to consider clearance, immune response, off-target effects etc
Focused ultrasound and microbubbles	Systemically injected microbubbles oscillate within blood vessels due to the ultrasound, enhancing the BBB permeability	√	√	Transient; possible side effects depending on ultrasound parameters, bloodborne proteins also enter the brain

1.4 Drug delivery across the blood-brain barrier using focused ultrasound

All the methods described above are either invasive, non-localised or fail to achieve therapeutically relevant drug concentrations within the targeted regions of the brain. Focused ultrasound combined with microbubbles has developed in the last twenty years as a non-invasive, localised and transient way to increase the permeability of the BBB [88]. With this technique, ultrasound is focused onto the targeted region of the brain. Microbubbles are then injected intravenously into the bloodstream and, only in the region where the ultrasound is focused, these microbubbles oscillate, mechanically stimulating an increase in BBB permeability.

1.4.1 Focused ultrasound

Ultrasound is a pressure wave with frequencies above the audible range for humans (> 20 kHz). Ultrasound waves are generated by probes called ultrasonic transducers, which transform electrical energy into mechanical energy using piezoelectric materials. Applying an electric current to a piezoelectric crystal, makes it expand and contract, which generates sound waves. When sound waves travel through a material, energy propagates from particle to particle, making them move back and forth around their resting position without a net displacement (Figure 1.4). It is therefore the energy of the wave, and not the matter, that propagates through the material. When the particles are closer together, the pressure is high, and this is known as a region of compression. When the particles are further apart, the pressure is low, known as a region of rarefaction. Ultrasound is classified as a longitudinal wave, as the particles move in the direction of wave propagation.

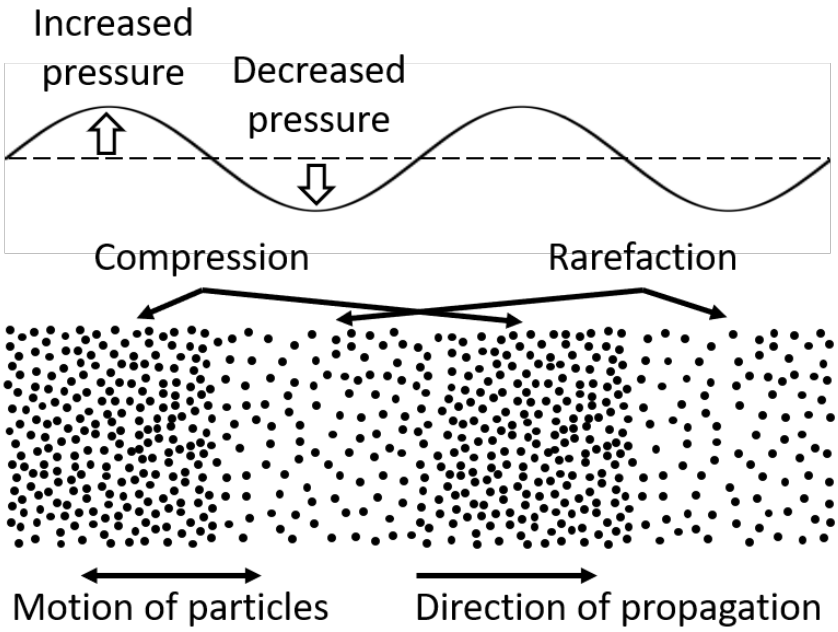

Figure 1.4. Longitudinal sound wave. Ultrasound is a longitudinal wave where particles move in the direction of wave propagation. When the ultrasound pressure increases, the particles are compressed, whereas when the pressure decreases, the particles are further apart. As the energy of the wave propagates through the material, the particles move back and forth creating these areas of compression and rarefaction.

Ultrasound waves are characterised by several parameters, including frequency, wavelength, phase, pulse length, pressure, intensity and mechanical index (Figure 1.5). The frequency (f) of a sound wave is defined by the number of oscillations (cycles) completed per second and is measured in hertz (Hz = 1 cycle/second). Frequency is inversely proportional to the wavelength (λ), which is defined as the distance travelled by sound in a single cycle ($f = c/\lambda$; c is the speed of sound). The speed of sound through a medium depends on the material's density and stiffness; the speed increases if the stiffness is increased or if the density is increased. In soft tissue, the average speed of sound is 1540 m/s. Ultrasound waves also have a phase, which indicates the stage the wave is at within the cycle. These waves are emitted in pulses that have a pulse length (PL), which can be found by multiplying the total number of cycles by their wavelength. An ultrasound pulse has a centre frequency (f_c) and an ultrasound pressure (P), which is the amplitude of the wave, measured in pascal (Pa). The peak-rarefactional pressure is the amplitude of the peak-negative (P_{neg}) part of the acoustic pressure wave and the

peak-compressional is the amplitude of the peak-positive (P_{pos}) part. By squaring the pressure and dividing it by twice the acoustic impedance (Z), one can find the ultrasound intensity, which is the concentration of energy in a sound beam ($I = P^2/2Z$; watts/cm^2). The acoustic impedance is an inherent property of the medium and depends on the density and speed of sound of the material ($Z = \rho c$, ρ is density and c speed of sound). Lastly, the mechanical index (MI) quantifies the likelihood that ultrasound will produce non-thermal bioeffects [89]. Traditionally, it is calculated by dividing the peak negative pressure by the square root of the centre frequency of the ultrasound wave ($MI = P_{neg}/\sqrt{f_c}$). A more recent modification to this formula incorporates the effect of pulse length, where longer pulse lengths increase the potential for mechanically produced bioeffects ($MI = \frac{P_{neg}}{P_{t,n}\sqrt{f_c}}$ where $P_{t,n} = A + BL_p^{-m}$, with L_p being the pulse length, $A = 0.536$, $B = 0.475$ and $m = 1.099$ in blood) [90].

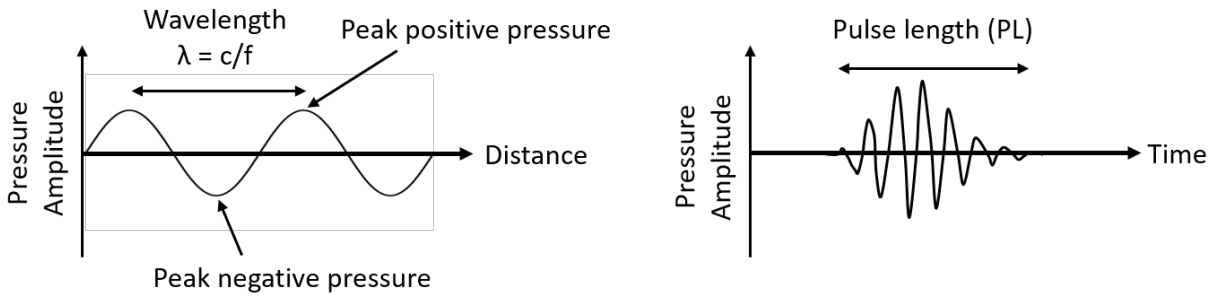

Figure 1.5. Ultrasound wave parameters. (Left) The ultrasound pressure is the amplitude of the wave, with maximum peak positive and peak negative pressure values. The wavelength (λ) represents the distance that the wave travels in a single cycle and is inversely proportional to the frequency (f). **(Right)** An ultrasound pulse has a centre frequency (f_c) and a pulse length (PL).

When ultrasound waves travel through the body, their amplitude decreases with distance as they lose energy. This process is known as attenuation and is due to reflection, refraction, diffraction, absorption and scattering within the body. Reflection and refraction occur at interfaces between tissues, while absorption and scattering occur within tissue. Most attenuation is due to absorption, when energy is converted into heat. Scattering occurs when the wave encounters structures smaller than its

wavelength, which scatter waves in all directions. Refraction occurs when waves pass through interfaces with different properties, which leads to a change in the speed of the wave and therefore a deflection in the direction of the wave's propagation. Diffraction involves a change in the direction of the waves as they pass through apertures or around objects. Significant diffraction occurs when the aperture or object has similar dimensions to the wavelength of the incident wave. Lastly, reflections occur at the interface between tissues with different impedances. Some of the wave will propagate further into the body and some of it will reflect back to the ultrasound probe. These reflected waves, known as echoes, are picked up by ultrasound receivers and used to create ultrasound images. By calculating the time needed for the echoes to reach the receivers, the distance at which the interface is located can be calculated. The intensity of the image will be higher or lower depending on the strength of these returning echoes.

Traditionally, ultrasound has been used in the clinic as an imaging tool, but it is also suitable for non-invasive therapeutic purposes. Ultrasound can be focused onto specific regions deep inside the body, without affecting the tissue between the transducer that generates the ultrasound waves and its focus. Ultrasound can also be focused through an intact scalp and skull onto small regions, in the order of millimetres, deep within the brain. Currently, focused ultrasound is used to thermally ablate tumours and to break up kidney stones (lithotripsy); however, for these purposes, ultrasound is emitted at high intensities [91], [92]. At low intensities, focused ultrasound can enhance the permeability of blood vessels when used in combination with microbubbles, allowing drugs to cross barriers, such as the blood-brain barrier.

1.4.2 Microbubbles

Microbubbles are structures composed of a gas core surrounded by a lipid or protein shell. Their diameters typically range between 0.5 and 10 μm, a similar size to red blood cells, which allows them to flow through blood vessels in the body. This includes capillaries, whose average diameter is 4 μm in mice and 7 μm in humans [93]–[98]. For

therapeutic purposes, the ability of microbubbles to flow within capillaries is important, as nutrients and drugs can reach the brain via a capillary network that is over 600 km in total length [99]. The average distance between these capillaries is 40 μm, which places each neuron within 10-20 μm from the nearest capillary [100], [101]. For drugs to be delivered efficiently within targeted brain regions, microbubbles need to enhance the permeability of vessels at the capillary level, where transport is most efficient, due to these vessels being the closest to the brain cells.

Microbubbles are commercially available and clinically approved as contrast agents for ultrasound imaging [102], [103]. The gas core acts as an ultrasound scatterer for imaging, which provides signals that are orders of magnitude higher than those coming from tissue [104], [105]. The compressibility of the gas also provides a mechanism to enhance drug delivery as a result of the microbubble's volumetric oscillations. The shell, on the other hand, is needed to stabilise the gas bubble, which would otherwise be unstable due to surface tension effects [93], [106]. Commonly used microbubbles, such as Definity® and SonoVue™ [102], [103], have phospholipid shells with poly(ethylene glycol) (PEG) brushes attached, which prevent coalescence and increase the *in vivo* half-life of these bubbles [107].

Microbubbles are highly responsive to changes in pressure. Under the influence of an ultrasound pressure wave, microbubbles expand and contract during the rarefactional and compressional phases of the pressure wave [108], a behaviour known as acoustic cavitation [108], [109]. Multiple forces influence the behaviour of the bubble: hydrostatic pressure, surface tension, gas pressure inside the bubble, inertia of the surrounding liquid, and damping forces due to acoustic radiation and the liquid's viscosity. The radial oscillation of microbubbles, however, is mainly determined by the ultrasound pressure, the inertia of the surrounding liquid and the internal gas pressure [110].

When a microbubble is exposed to low acoustic pressures, the ultrasound pressure is the dominant driving force and the microbubbles oscillate stably about a mean radius,

undergoing what is described as stable or non-inertial cavitation [109]. As the pressure increases, the amplitude of the microbubble's radial oscillations increases until the inertia of the surrounding fluid becomes the dominant driving force [111]. Above this pressure threshold, the microbubbles undergo inertial cavitation [112]. This regime of oscillation is characterised by a relatively slow expansion to large radii, followed by a more rapid contraction driven by the inertia of the surrounding liquid. The rapid compression of the gas core may lead to the production of shock waves and high temperatures [109], [113]. If the inertial cavitation is persistent over several acoustic cycles, then it can be considered stable inertial cavitation. If the inertial cavitation is temporary, due to bubble destruction or compositional and morphological changes to the bubbles, then the inertial cavitation activity can be considered transient [114]. The threshold for inertial cavitation is dependent on many factors, including the resting diameter of the microbubble, its gas content, the medium's properties and the centre frequency of the ultrasound emitted.

Depending on the ultrasound parameters, microbubbles can cause mechanical, thermal and chemical phenomena, some of which can be used for therapeutic purposes [93], [115]. Several mechanical phenomena can be generated by microbubbles (Figure 1.6). First, microbubbles oscillate radially. This motion can exert significant forces on nearby cell membranes and blood vessel walls by distending them during the bubbles' expansion, or pulling them during their contraction [116]. Second, microbubbles can move from one location to another (translational motion), due to the pressure generated by the ultrasound wave. This pressure is known as the primary radiation force [117]. Due to this force, microbubbles can reach velocities that allow them to push against or penetrate tissues, or improve the local release of drugs [118]–[124]. Third, microbubbles can cause surrounding fluid to move. This fluid movement is known as microstreaming and can be caused by both radial and surface oscillations of the microbubbles. Microstreaming follows specific patterns and can exert constant or oscillating fluid shear forces on neighbouring surfaces [125]. The presence of any nearby surface will also enhance non-spherical oscillations, reinforcing the streaming

even further [126], [127]. Fourth, microbubbles can collapse asymmetrically when they are near surfaces. This process can create liquid jets that rush towards the surface at high speed, known as microjetting. Although biological effects induced by these jets have been hard to predict, microjetting is thought to produce pronounced effects on surrounding vessels, particularly within small capillaries [70], [128]. Fifth, bubbles can generate sharp changes in pressure within a narrow time frame, producing what is known as a shockwave. This process can occur when bubbles collapse due to the inertia of the surrounding fluid, allowing the bubble wall to reach supersonic velocities. Lastly, oscillating bubbles generate their own sound waves. These waves can interact with those of other bubbles, causing attraction or repulsion between them, due to forces that are known as secondary radiation forces [129]. These forces lead to the translational movement of bubbles and determine whether they agglomerate or disperse [130]–[132].

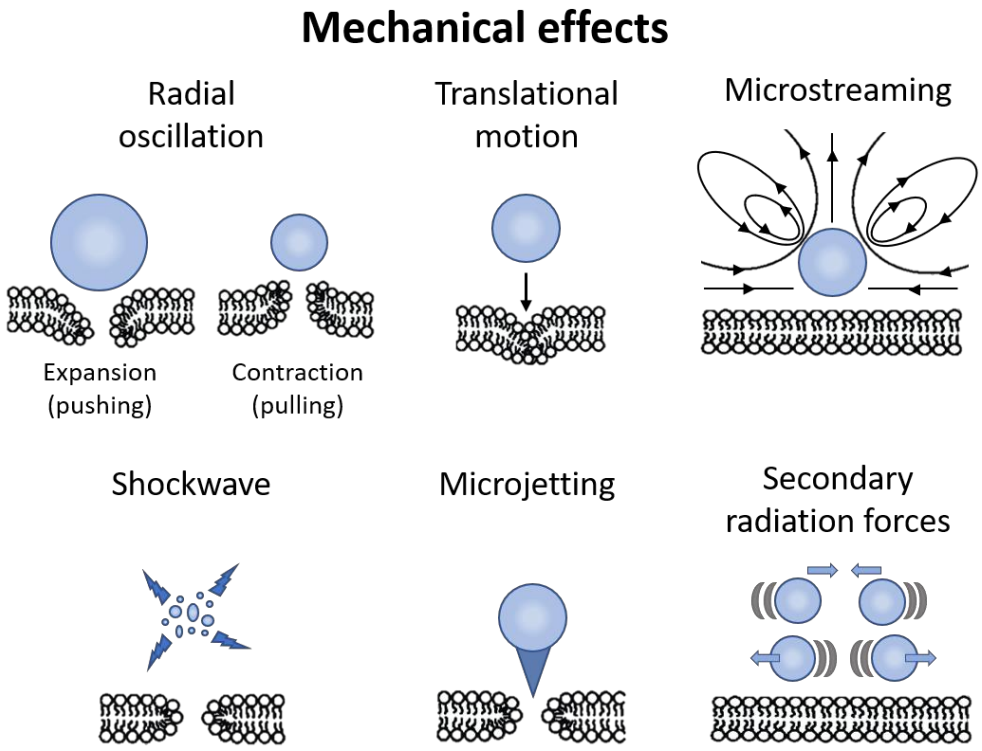

Figure 1.6. Mechanical phenomena caused by microbubbles. Microbubbles oscillate radially, which can push and pull tissue (radial oscillation); they can be pushed against surfaces in the direction of the ultrasound propagation (translational motion); they can make surrounding fluid move, which can cause pressure on nearby surfaces (microstreaming); they

can reach supersonic velocities (shockwave); microbubbles can collapse asymmetrically near surfaces, with jets rushing towards nearby tissue (microjetting); lastly, microbubbles generate their own sound waves that interact with those of other bubbles, leading to their attraction or repulsion (secondary radiation forces).

In addition to mechanical phenomena, microbubbles can also create thermal and chemical effects. Temperature rises in the tissue surrounding microbubbles have been shown to be relatively small; however, those that occur inside the bubbles during an inertial collapse can reach several thousand Kelvins [133]. During this collapse, the gas pressure also increases. The extreme temperature and pressure can produce reactive chemical species, such as reactive oxygen species, as well as the release of large amounts of energy in the form of electromagnetic radiation, a phenomenon called sonoluminescence. Both these thermal and chemical effects can impact biological processes and drug activity [134]–[136]. Reactive oxygen species, for example, have been correlated with an increase in permeability both in and between endothelial cells [137], [138].

1.4.3 Applications of focused ultrasound and microbubble-mediated delivery across the blood-brain barrier

To safely increase the permeability of the BBB, ultrasound is applied at low intensities and microbubbles are used to mechanically stimulate the microvasculature from the inside. Ultrasound-mediated BBB permeability enhancement with microbubbles was first demonstrated in rabbits in 2001 [88]. Since then, many preclinical studies have been published, and clinical trials are ongoing in patients with brain tumours and Alzheimer's disease [139]–[141]. Therapeutic agents of different sizes have been delivered with this technology, including chemotherapeutic drugs (~ 500 Da) [142]–[144], neurotrophins (~ 20 kDa) [145], antibodies (~ 150 kDa) [146]–[148] and gene vectors (~ 4 MDa) [149], [150]. Many imaging agents have also been delivered, including fluorescent dextrans (3-2,000 kDa) [151]–[155], magnetic resonance (MR) contrast agents (< 1 kDa, 1-65 nm diameter) [156]–[159], nanoparticles (5-200 nm

diameter) [6], [160]–[162] and liposomes (50-200 nm) [144], [163]–[165]. These drugs and imaging agents have either been co-administered with the microbubbles, or loaded inside or on the microbubbles themselves [166], [167]. Many of the abovementioned agents have been delivered to improve the treatment and diagnosis of brain diseases *in vivo*, such as brain tumours [142], [168]–[174], Alzheimer's disease [146], [175]–[178], Parkinson's disease [174], [179] and Huntington's disease [180].

1.4.4 Mechanisms of increased blood-brain barrier permeability with focused ultrasound

The exact mechanism by which focused ultrasound and microbubbles increase the permeability of the BBB remains unknown. However, studies have identified several potential mechanisms of passage across this barrier, which include both transcellular and paracellular routes [181]–[185]. Transport via transcellular pathways has been observed via caveolae and cytoplasmic vacuoles [181], [183], [185]. Caveolae are invaginations in the cell membrane, which pinch off and form vesicles in the cytoplasm. They are involved in internalising macromolecules, toxins and viral pathogens [186]. Observations suggest that ultrasound and microbubbles trigger mechanisms that lead to the formation of these vesicles and their transcellular trafficking, which have been found at both luminal and abluminal fronts of endothelial cells [183]. Alongside caveolae, labelled molecules delivered via focused ultrasound have also been observed in vacuoles, which are membrane-bound fluid-filled organelles in the cytoplasm.

In terms of paracellular transport, agents have been shown to cross channels in between cells where tight junctions are present [182], [183], [185]. The distribution of these junction proteins in cerebral microvessels has been studied at different time points after ultrasound treatment [182]. A reduction in number and the reorganisation of these proteins was observed. However, this BBB disruption was found to be reversible and lasted for approximately four hours after the ultrasound treatment.

Several potential interactions between microbubbles and the surrounding vasculature could lead to the above-mentioned bioeffects. Ultrasound causes microbubbles to

expand and contract, and the expansion of large bubbles can fill the entire lumen of capillaries, mechanically stretching the vessel walls. This could be a mechanism by which tight junction proteins are opened and reorganised. These changes in pressure within capillaries can affect the BBB [187] and may lead to biochemical reactions such as proinflammatory signals, that trigger the increase in permeability observed [188]. Microbubble oscillations have been shown to vasoconstrict arterioles [184], reducing blood flow and inducing transient ischemia, which is known to increase transcytosis [189]. Vasoconstriction could therefore be one potential cause for increased transcytosis.

The stimulation of vessel walls that leads to the increase in permeability could also be due to microbubbles being pushed against vessel walls, under the influence of the force of the ultrasound wave (translational motion) or the movement of the surrounding fluid as the microbubbles oscillate. Microbubbles can also collapse during sonication, causing localised shock waves and fluid jets, which could exert forces on the vessel walls. The increase in BBB permeability has also been shown to be dependent on microbubble size. If the microbubbles are similar to the capillary diameter, then the detection of what is thought to be inertial cavitation is not necessary, but with smaller bubbles it is [190]. Interestingly, increased permeability in vessels also often occurs at bifurcations in vessels, possibly due to microbubbles being more likely to build up or be trapped in these areas [184].

However, more work is needed to elucidate whether all these mechanisms occur together, to determine which mechanisms are most relevant and whether changing the ultrasound parameters can enhance one mechanism over another. The interaction of ultrasound with microbubbles within the microvasculature and their relationship with this complex biological barrier still needs to be studied in more depth.

1.4.5 Monitoring microbubble emissions

During focused ultrasound treatments, microbubbles emit sound. These emissions can be used to determine whether microbubbles are present in the targeted bloodstream,

and to interpret what type of microbubble activity is occurring. Certain types of microbubble activity have been associated with adverse bioeffects. Therefore, these emissions can help monitor ultrasound treatments to improve their efficacy and safety. Although many studies have analysed and interpreted these acoustic signals, drawing correlations with certain bioeffects, it is important to note that these signals are still being studied and previous conclusions may be inaccurate.

During ultrasound exposure, microbubbles can undergo different modes of cavitation, which have been characterised in previous work by analysing the acoustic emissions from the microbubbles. Frequency domain analysis of these signals has shown features such as integer multiples (harmonics) and submultiples (subharmonics) of the centre frequency, as well as odd multiples of half the centre frequency (ultraharmonics) and broadband acoustic emissions. In previous work, subharmonic and ultraharmonic emissions have been associated with high magnitude non-inertial and low magnitude inertial cavitation [108], while broadband emissions have been linked to microbubbles during inertial cavitation, undergoing an unstable expansion followed by a rapid and violent collapse [114]. These features, however, are not produced by the microbubbles alone, but are instead what ultrasound receivers, mostly single-element sensors, detect once the microbubble emissions have interacted with the entire system around them, which includes surrounding tissues and the detecting system itself.

Previous work has linked acoustic features thought to be due to inertial cavitation with cell damage within vessels [191], [192], red blood cell extravasation and tissue damage [193]. However, the same features that are thought to be due to non-inertial or low magnitude inertial cavitation have also been linked to safer delivery of agents to the brain [151], [194], [195]. Based on the frequency content of microbubble signals captured from single-element sensors, there is uncertainty as to whether inertial cavitation is necessary to increase the permeability of the BBB [185], [196]. The detection of higher order harmonic signals (second to fifth) has been correlated with BBB permeability enhancement [151], [194], [195]. The identification of subharmonics

and ultraharmonics has also been associated with the lack of adverse events. The presence of these subharmonics and ultraharmonics has been found to correlate better with BBB permeability increase compared to the detection of broadband emissions [197]–[199]. In fact, ultrasound treatments have been conducted emitting long pulses (>1 ms in pulse length) at 50% of the pressure at which subharmonic activity was detected, with no gross tissue damage observed [198], [200]. Current clinical trials are utilising this type of real-time acoustic feedback monitoring system in combination with tools such as magnetic resonance imaging (MRI) guidance, to establish where agents are being delivered and whether haemorrhage is occurring.

1.4.6 Clinical trials with ultrasound and microbubbles

Given the promising results in preclinical models of disease, several clinical trials have taken place to demonstrate the efficacy and safety of this technology within the brain (Table 1.2). The first published clinical trial reported the use of ultrasound and microbubbles to increase BBB permeability in patients with brain tumours (glioblastoma multiforme) [139]. However, this was performed by invasively fixing an implantable unfocused transducer, SonoCloud, within the bone of the skull [139], [201], [202]. Due to the size limitations of this device, the use of a focused transducer in this case would have made the focal region smaller than desired. Patients had monthly treatments before receiving carboplatin, a systemically administered chemotherapeutic drug. Results showed that the BBB could be disrupted with pressures of up to 1.1 MPa with hypointense regions on MRI images, indicating areas of bleeding. The results of this trial showed signs of enhanced BBB permeability at equidistant locations, an indication of standing waves within the brain, which would lead to drug delivery in untargeted regions. More recently, increased survival was shown in a larger cohort of glioblastoma patients if a clear BBB permeability disruption was observed, with signs of transient edema but no carboplatin-related neurotoxicity [203]. A clinical trial with this implantable device is also currently ongoing in Alzheimer's disease patients (NCT03119961).

Other trials using non-invasive approaches have taken place using hemispherical ultrasound arrays in combination with MRI guidance (ExAblate system, Insightec Inc.). This system involves fixing the patient's head within a stereotactic frame, which is then placed on the MRI table, before the hemispherical array around the patient's head is put inside the MRI scanner. Alzheimer's disease patients have received ultrasound treatments with this technology and a reversible increase in the BBB permeability has been shown, with no contrast detected after 24 h, indicating BBB closure [140]. Using the same system, glioblastoma patients have also been treated with focused ultrasound followed by systemic administration of temozolomide or doxorubicin [141]. Small sites of red blood cell extravasation, however, were detected via MRI [204]. More clinical trials are ongoing using this ExAblate system in patients with Alzheimer's (NCT02986932, NCT03671889, NCT03739905), glioblastoma (NCT03322813, NCT03551249, NCT03616860, NCT03712293), Parkinson's disease (NCT03608553), breast cancer metastasis in the brain (NCT03714243) and amyotrophic lateral sclerosis (NCT03321487).

An alternative technique using a single-element transducer system (NaviFUS) is being used in ongoing clinical trials on Alzheimer's (NCT04118764), glioblastoma (NCT03626896) and drug-resistant epilepsy patients (NCT03860298). This approach has the advantage of not requiring MRI guidance but is instead assisted by neuronavigation and real-time cavitation monitoring [205]–[207]. Neuronavigation, also called frameless stereotaxy, relies on imaging techniques to establish the location of the transducer relative to the targeted region of interest. In this way, there is no need to fix the patient's skull to a rigid frame [208], which in the ExAblate system causes patients discomfort and pain.

Table 1.2. Clinical trials using ultrasound and microbubbles in the brain. Three main ultrasound systems have been used in clinical trials that have either already taken place or are ongoing: an unfocused single-element implantable transducer device (SonoCloud); an MR-guided hemispherical array system (ExAblate); and a neuronavigation-assisted single element transducer system (NaviFUS). Published work with associated clinical trial identifiers is listed, with the targeted diseases and any positive and negative outcomes described from these studies.

System	Clinical Study	Identifier	Disease	Positive Outcomes	Negative Outcomes
SonoCloud implantable device	*Carpentier et al. 2016*	NCT02253212	Glioblastoma multiforme	No tumour progression in targeted region	Standing wave effects Invasive
	Idbaih et al. 2018	NCT02253212	Glioblastoma multiforme	Tumour reduction in some patients	Transient edema Invasive
	-	NCT03744026	Glioblastoma multiforme	Aimed to enlarge treatment volume	Invasive
	-	NCT03119961	Alzheimer's disease	-	Invasive
MR-guided ExAblate system	*Lipsman et al. 2018*	NCT02986932	Alzheimer's disease	Reversible opening No contrast after 24 h	Small sites of red blood cell extravasation
	Rezai et al. 2020	NCT03671889	Alzheimer's disease	Recovery after 24 h Reliable repeated opening	-
	-	NCT03739905	Alzheimer's disease	-	-
	Mainprize et al. 2019	NCT02343991	Glioblastoma multiforme	Demonstrates feasibility No adverse clinical or radiological effects	-
	-	NCT03322813 NCT03616860 NCT03551249 NCT03712293	Glioblastoma multiforme	-	-
	-	NCT03714243	Breast cancer brain metastasis	-	-
	Abrahao et al. 2019	NCT03321487	Amyotrophic lateral sclerosis	Feasibility, no adverse effects observed	-
	-	NCT03608553	Parkinson's disease dementia	-	-
NaviFUS Neuronavigation system	-	NCT04118764	Alzheimer's disease	To assess safety and feasibility	-
	-	NCT03626896	Glioblastoma multiforme	-	-
	-	NCT03860298	Drug resistant epilepsy	-	-

1.4.7 Long pulse ultrasound sequences

In preclinical and clinical studies, focused ultrasound is most commonly emitted in sequences of millisecond-long pulses to enhance the permeability of the BBB in combination with microbubbles [139], [196], [209]. This sequence is formed of long pulses emitted in a slow (Hz) sequence and is designed to drive the microbubbles to mechanically stimulate the blood vessel walls when the ultrasound pulse is turned on, and to replenish the area with new microbubbles once the pulse is turned off (Figure 1.7) [153], [158], [182], [210], [211]. A relatively long interval between pulses is necessary to replenish the targeted microvasculature due to the long pulses destroying, dissolving or modifying a portion of the microbubbles [108], [114], [212], which could reduce their ability to enhance the BBB permeability efficiently and safely [213].

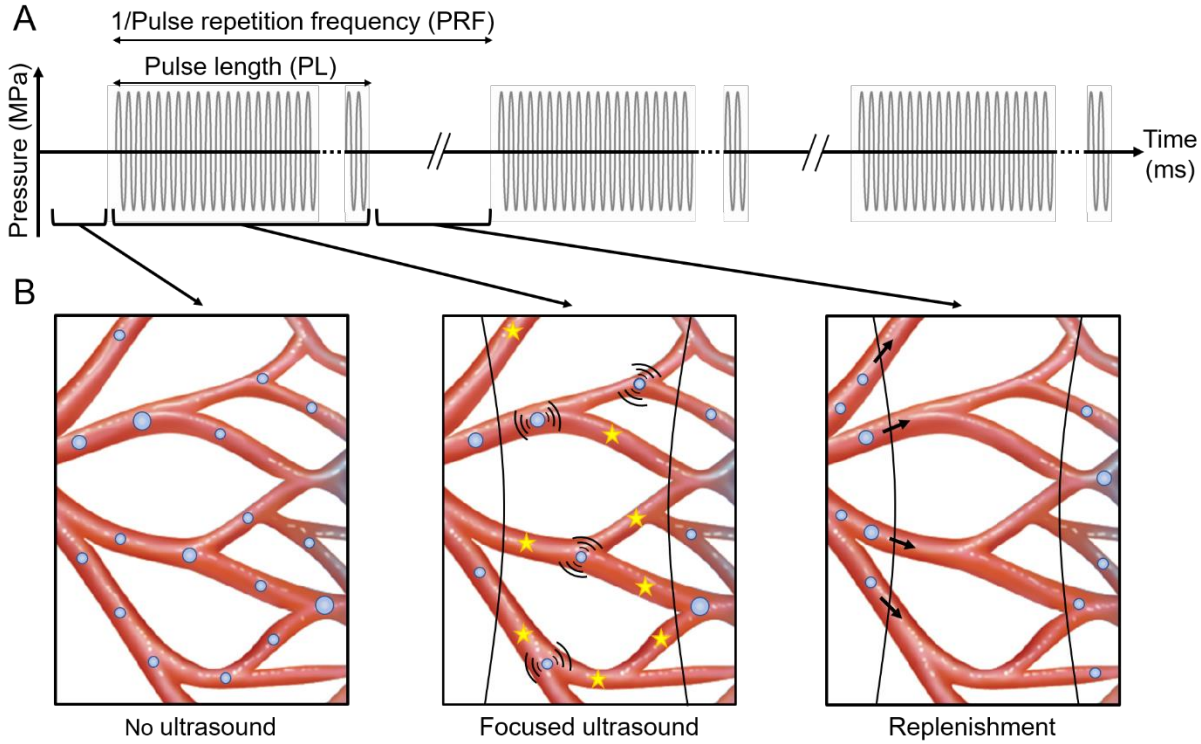

Figure 1.7. Long pulse ultrasound sequence. Ultrasound is conventionally emitted in millisecond-long pulses separated by long off-time periods to allow the microbubbles that have been destroyed or dissolved (represented by yellow stars) during the ultrasound pulse to be replenished.

In both preclinical and clinical studies, however, several limitations have been observed using these long pulse sequences. First, the drug distribution is not uniform within the ultrasound beam [151], [153], [158], [210], [214]. This results in high concentrations of agents being delivered to some regions and little or none to others, with some areas being overtreated and others undertreated. This uneven treatment is unwanted when delivering an imaging agent for diagnosis or a drug to treat a diseased tissue region of the brain.

Second, unwanted biological responses can occur as a result of long pulse sequences, including haemorrhage, the extravasation of red blood cells or blood-derived proteins, neuronal damage and neuroinflammation [148], [211], [215]. Evidence of haemorrhage and the extravasation of red blood cells has been found in numerous preclinical studies, depending on the ultrasound parameters used [154], [193], [194], [211], [216]–[219]. Recently, a clinical study has also shown the presence of potential microhaemorrhages following treatment with long ultrasound pulses, observed in the form of hypointense areas on T2 MRI scans [140]. Extravasated bloodborne substances, other than red blood cells, have also been found [220]. For example, albumin, the most common protein in the blood, has been observed in the brain 24 h after ultrasound treatment [221]. This protein is normally not present within the brain and is thought to be neurotoxic [222], [223]. Therefore, ideally, we want little or none of these proteins in the brain. Inflammation has also been observed when using long pulse sequences [164], [220], [223]–[230]. These safety concerns have been a topic of debate, as responses are dependent on the experimental parameters used, and include not only the ultrasound parameters emitted, but also the type and number of microbubbles injected [220]. In addition, an acute and mild inflammatory response can, in some scenarios, be thought of as a positive bioeffect; for instance the clearance of amyloid-beta from the brain can be mediated by microglial activation [231].

Third, it takes between 4 and 48 h for the permeability of the BBB to return to normal depending on the ultrasound parameters used [182], [185], [232], [233]. This duration

allows other molecules to enter the brain from the bloodstream, including potentially neurotoxic agents such as albumin, which can trigger neuroinflammation [221]–[223]. Ideally, we want to reduce the duration of enhanced permeability of the BBB and, thereby, the number of bloodborne substances entering the brain. We need the enhanced permeability to last long enough to allow the necessary concentrations of delivered agents to reach the brain, while avoiding prolonged exposure of the brain to unwanted molecules.

If only a single focused ultrasound treatment is performed, these effects may not represent a prohibitive risk; however, frequent focused ultrasound and microbubble treatments may be needed, depending on the disease that is being treated. Therefore, all the above adverse effects should be avoided if possible. To do so, different parameters have been investigated and feedback systems have been developed. A recent study has also shown that by injecting dexamethasone following ultrasound, the production of inflammatory markers can be prevented, mitigating the risks from inflammation-induced tissue damage [230]. Dexamethasone could be used if a solution that avoids the damage caused by inflammation cannot be found. Regarding monitoring systems, although studies have proposed that tissue damage can be avoided by using acoustic feedback systems, so far, temporary tissue damage has still been observed in experiments where the emitted pressure was established based on microbubble emissions [170], [198], [200], [220], [225], [226], [234]–[236].

To find the best trade-off between efficacy and safety, many different ultrasound parameters have been investigated. The long pulse ultrasound sequence is the most commonly used and involves a burst length of 10 ms and a repetition frequency of 1 Hz, with rarefactional pressure amplitudes varying, depending on the ultrasound centre frequency used. Higher ultrasound centre frequencies (1-1.7 MHz) are more suitable for smaller animal models, such as mice and rats, while in rabbits, monkeys and humans, lower frequencies (< 1 MHz) are necessary to focus the ultrasound through a thicker skull and reach deeper regions of the brain [185]. High ultrasound

pressures have delivered higher drug doses, but the potential for tissue damage also increases [185], [237]. The pressure threshold to enhance the BBB permeability will be lower if a lower ultrasound frequency is emitted [196]. Delivery using pressures around this threshold have so far yielded the most promising results in terms of efficacy and safety [211]. A range of different pulses lengths have been tested and have shown that above 0.2 ms, more consistent delivery results can be achieved [210]. Pulse lengths above 10 ms show a plateau effect, with higher pulse lengths producing no significant difference in drug delivery [88], [210], [238]. Generally, pulse lengths of 10-20 ms are emitted; however, the molecules are delivered heterogeneously, with high accumulation around large blood vessels [152]. Lower pulse lengths lead to lower drug doses being delivered, but also result in more homogeneous drug distributions. In order to observe delivery, the pulse repetition frequency (PRF) also needs to be balanced; PRFs below 1 Hz are inefficient, as the microbubbles are not being stimulated as often as they could be, while PRFs > 5 Hz show no significant difference in the delivery achieved [210]. This could be due to reperfusion being interrupted too early. Higher PRFs have also shown more heterogenous distributions, and are associated with a higher probability of adverse effects occurring [210], [211]. Finally, the overall number of pulses emitted is chosen based on the circulation time of microbubbles within the body, which is approximately 5 minutes [239].

Although delivered drug doses can be adjusted when using long pulse sequences, the spatial and temporal distribution of the agent delivery is poorly controlled. This is thought to be due to the microbubble activity being inhomogeneously distributed within the vasculature and having poor control over the type of cavitation activity that occurs. The observed tissue damage could be due to high magnitude inertial cavitation and other microbubble activity such as clustering, coalescence and microjetting, which we have little control over during long pulse sequences. So far, long pulse sequences have not been able to achieve the desired efficacy and safety when delivering drugs to the brain using focused ultrasound and microbubbles.

1.5 Redesigning ultrasound sequencing

To deliver molecules efficiently and safely across the BBB with focused ultrasound, our group has designed a new rapid short-pulse sequence. This sequence is designed to allow the microbubbles to gently stimulate the blood vessel walls homogeneously throughout the microvasculature, enhancing the uniformity of increased BBB permeability, and therefore, drug delivery. To achieve this, we designed a low-energy sequence of short pulses emitted at a high repetition frequency, with each group of rapidly fired short pulses being termed a burst (Figure 1.8). The low energy, with low peak rarefactional pressures and short pulse lengths, is necessary to reduce the likelihood of microbubble destruction, and thus prolong the lifetime of the microbubbles, allowing them to act at more than one location along the vasculature. This would in turn reduce the likelihood of adverse events occurring, both in terms of overtreated regions and tissue damage [153], [191], [240]. The high repetition frequency between these short pulses was chosen to increase the likelihood of delivery, compensating for the shorter pulse length and lower pressure. Our hypothesis is that by emitting these short pulses at a high rate, the microbubbles would be allowed enough time to enhance the BBB permeability, but not enough to overstress any given site within the capillary, stimulating the vasculature more gently over time. In the time periods when the ultrasound is turned off, due to the lack of radiation forces generated by the ultrasound wave, we hypothesise that the microbubbles can flow freely in the vasculature with the blood flow, allowing their activity to distribute along the vessel (Figure 1.8). These pulses were grouped into bursts to allow the replenishment of the targeted area with new microbubbles in between bursts, as done with the long pulse sequences.

This Rapid Short-Pulse (RaSP) sequence design was based on previous *in vitro* and *in vivo* work [153], [241], [242]. In previous *in vitro* studies, microbubbles have been observed to move more when short pulses were emitted compared to long pulses [106], [243], supporting our hypothesis that microbubbles are able to move between

rapidly fired short-pulses. In addition, long pulses have been shown to increase the number and size of microbubble clusters forming *in vitro* [244], which could explain the vascular effects and safety concerns. We speculate that the uneven distribution observed with long pulses is caused by cavitation activity being higher in some regions compared to others, which has previously been demonstrated with passive acoustic mapping data [242], [245]. Such biased activity, particularly if in the inertial cavitation regime, would lead to microbubble destruction, which has been shown to result in damaged sites with extravasated erythrocytes and spot-like accumulation of delivered agents [214].

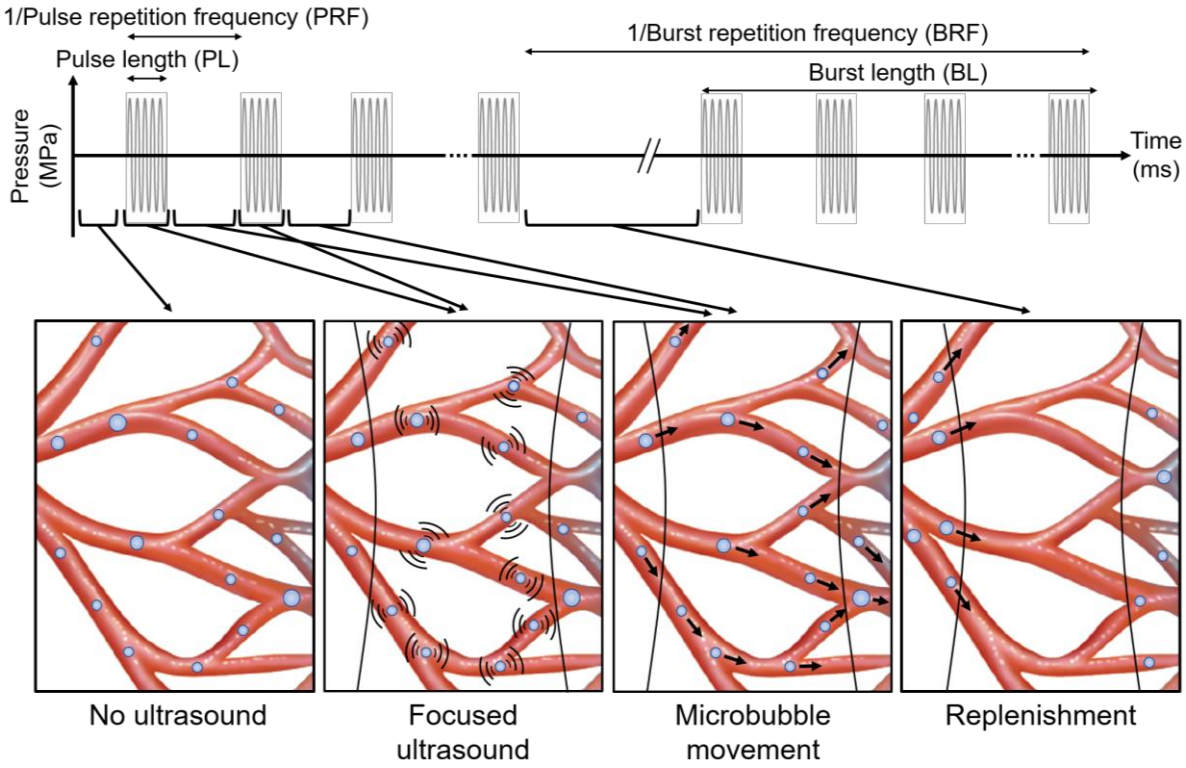

Figure 1.8. Rapid short-pulse ultrasound sequence. Ultrasound is emitted in groups (bursts) of short pulses fired at a rapid repetition frequency (PRF). During the short pulse, the microbubbles oscillate, enhancing the BBB permeability at those locations. When the pulse is turned off, the microbubbles move with the blood flow until the next pulse is turned on, at which point the microbubbles will be at a new location where they can enhance the permeability again. By emitting short pulses, the lifetime of the microbubbles is prolonged, and by having short off-time periods, the bubbles can move between pulses, spatially

distributing the permeability enhancement. The bursts are separated by long off-time periods to allow the microbubbles to replenish the ultrasound targeted area.

The use of short pulses has also previously been shown to improve the distribution of agent delivery *in vivo*, but has either not been able to achieve high enough doses within the brain or has required high ultrasound pressures to achieve such doses (Table 1.3) [210], [233], [246]–[248]. Closely spaced short pulses have also been shown to distribute drug delivery more uniformly [153]. Further investigation into the efficacy and safety of such pulses was needed, and no direct comparison with long pulse sequences was shown.

Based on these previous studies, we have designed a sequence hypothesised to improve the efficacy and safety of drug delivery to the brain *in vivo*. With this sequence we aim to achieve a more uniform delivery of molecules to the targeted brain region at a high enough dose. In terms of safety, we aim to deliver molecules across the BBB with minimal disruption to the homeostasis of the BBB, reducing adverse effects, such as the extravasation of bloodborne proteins and red blood cells, tissue damage and prolonged periods of enhanced permeability.

Table 1.3. Studies using short ultrasound pulses. List of studies showing delivery using short pulses of focused ultrasound and microbubbles in the brain *in vivo*. Key parameters such as pulse length, peak rarefactional pressure, centre frequency and pulse repetition frequency (PRF) are highlighted, as well as whether the pulses were grouped into bursts.

Paper	Pulse Length	Pressure	Centre Frequency	PRF	Bursts
Hynynen et al 2003, UMB	10 µs	6.3 MPa	1.5 MHz	1 kHz	No
Bing et al 2009, UMB	2 µs	2.7 MPa	5.7 MHz	10 Hz	No
Choi et al 2011, JCBF	33 µs	0.46 MPa	1.5 MHz	10 Hz	No
Choi et al 2011, PNAS	2.3 µs	0.51 MPa	1.5 MHz	100 kHz	Yes
O'Reilly et al 2011, UMB	3 µs	0.54 MPa	1.18 MHz	1 Hz	Yes

1.6 Thesis aims

The aim of this doctoral thesis was to investigate the capabilities of rapid short-pulse sequences in delivering agents to the brain *in vivo*. The first objective was to evaluate whether RaSP could improve the efficacy and safety of delivery *in vivo*. Efficacy was assessed by looking at the observed amount of model drug delivered and its distribution in comparison with conventionally used long ultrasound pulses. Safety was assessed by investigating the duration of enhanced BBB permeability, the extravasation of endogenous proteins, tissue damage and whether immune cells were involved. Acoustic emissions were used to monitor the ultrasound treatment, to determine whether the delivered dose could be predicted and to assess whether the observed improvements were linked to the hypotheses behind our sequence design.

The second objective was to evaluate whether RaSP could improve the delivery of much larger molecules, specifically liposomes approximately 100 nm in diameter. In

parallel, we sought to investigate whether a dual-modal MRI-optical probe could be used to label neurons, once delivered through the BBB with focused ultrasound and microbubbles. Overall, the research here presented aimed to explore whether a RaSP sequence could significantly improve the way drugs and imaging agents are delivered to the brain, creating a non-invasive, localised and transient therapeutic technology that can be used for more efficient and safer delivery of agents to patients with brain diseases.

1.7 References

[1] Geneva, "Global Health estimates 2016: Disease burden by cause, age, sex, by country, and by region, 2000-2016," 2018.

[2] A. Raggi and M. Leonardi, "Burden of brain disorders in Europe in 2017 and comparison with other non-communicable disease groups," *Journal of Neurology, Neurosurgery and Psychiatry*, vol. 91, no. 1. pp. 104–105, 2020.

[3] M. Di Luca *et al.*, "Towards earlier diagnosis and treatment of disorders of the brain," *Bulletin of the World Health Organization*, vol. 96, no. 5. 2018.

[4] W. Löscher and H. Potschka, "Drug resistance in brain diseases and the role of drug efflux transporters," *Nature Reviews Neuroscience*, vol. 6, no. 8. pp. 591–602, 2005.

[5] J. P. Patel and B. N. Frey, "Disruption in the blood-brain barrier: The missing link between brain and body inflammation in bipolar disorder?," *Neural Plasticity*, vol. 2015. 2015.

[6] T. Chan, "Synthesis, in vitro and in vivo evaluation of nanoparticles and metal complexes for the treatment of brain diseases," 2020.

[7] Y. Persidsky, S. H. Ramirez, J. Haorah, and G. D. Kanmogne, "Blood-brain barrier: Structural components and function under physiologic and pathologic conditions," in *Journal of Neuroimmune Pharmacology*, 2006, vol. 1, no. 3, pp. 223–236.

[8] N. J. Abbott, L. Rönnbäck, and E. Hansson, "Astrocyte-endothelial interactions at the blood-brain barrier," *Nature Reviews Neuroscience*, vol. 7, no. 1. pp. 41–53, 2006.

[9] W. C. Aird, "Phenotypic heterogeneity of the endothelium: I. Structure, function, and mechanisms," *Circulation Research*, vol. 100, no. 2. pp. 158–173, 2007.

[10] B. L. Coomber and P. A. Stewart, "Morphometric analysis of CNS microvascular endothelium," *Microvasc. Res.*, vol. 30, no. 1, pp. 99–115, 1985.

[11] W. Löscher and H. Potschka, "Blood-brain barrier active efflux transporters: ATP-binding cassette gene family," *NeuroRx*, vol. 2, no. 1, pp. 86–98, 2005.

[12] R. K. Mittapalli, V. K. Manda, C. E. Adkins, W. J. Geldenhuys, and P. R. Lockman, "Exploiting nutrient transporters at the blood-brain barrier to improve brain distribution of small molecules," *Therapeutic Delivery*, vol. 1, no. 6. pp. 775–784, 2010.

[13] W. H. Oldendorf, M. E. Cornford, and W. J. Brown, "The large apparent work capability of the blood-brain barrier: A study of the mitochondrial content of capillary endothelial cells in brain and other tissues of the rat," *Ann. Neurol.*, vol. 1, no. 5, pp. 409–417, 1977.

[14] D. D. Henninger *et al.*, "Cytokine-induced VCAM-1 and ICAM-1 expression in different organs of the mouse," *J. Immunol.*, vol. 158, no. 4, pp. 1825–32, 1997.

[15] G. J. Del Zoppo and R. Milner, "Integrin-matrix interactions in the cerebral microvasculature," *Arteriosclerosis, Thrombosis, and Vascular Biology*, vol. 26, no. 9. pp. 1966–1975, 2006.

[16] L. Sorokin, "The impact of the extracellular matrix on inflammation," *Nature Reviews Immunology*, vol. 10, no. 10. pp. 712–723, 2010.

[17] R. Daneman and A. Prat, "The blood–brain barrier," *Cold Spring Harb. Perspect. Biol.*, vol. 7, no. 1, 2015.

[18] C. D. Arvanitis, G. B. Ferraro, and R. K. Jain, "The blood–brain barrier and blood–tumour barrier in brain tumours and metastases," *Nature Reviews Cancer*, vol. 20, no. 1. pp. 26–41, 2020.

[19] D. E. Sims, "The pericyte-A review," *Tissue and Cell*, vol. 18, no. 2. pp. 153–174, 1986.

[20] D. Shepro and N. M. L. Morel, "Pericyte physiology," *FASEB J.*, vol. 7, no. 11, pp. 1031–1038, 1993.

[21] C. N. Hall *et al.*, "Capillary pericytes regulate cerebral blood flow in health and disease," *Nature*, vol. 508, no. 1, pp. 55–60, 2014.

[22] A. Armulik, G. Genové, and C. Betsholtz, "Pericytes: Developmental, Physiological, and Pathological Perspectives, Problems, and Promises," *Developmental Cell*, vol. 21, no. 2. pp. 193–215, 2011.

[23] G. R. J. Gordon, C. Howarth, and B. A. Macvicar, "Bidirectional control of arteriole diameter by astrocytes," in *Experimental Physiology*, 2011, vol. 96, no. 4, pp. 393–399.

[24] Y. Chen and R. A. Swanson, "Astrocytes and brain injury," *Journal of Cerebral Blood Flow and Metabolism*, vol. 23, no. 2. pp. 137–149, 2003.

[25] H. Kubotera, H. Ikeshima-Kataoka, Y. Hatashita, A. L. Allegra Mascaro, F. S. Pavone, and T. Inoue, "Astrocytic endfeet re-cover blood vessels after removal by laser ablation," *Sci. Rep.*, vol. 9, no. 1, 2019.

[26] F. Mercier, J. T. Kitasako, and G. I. Hatton, "Anatomy of the brain neurogenic zones revisited: Fractones and the fibroblast/macrophage network," *J. Comp. Neurol.*, vol. 451, no. 2, pp. 170–188, 2002.

[27] B. O. Fabriek, "Perivascular Macrophages in Neuroinflammation, the role of the Scavenger Receptor CD163," 2006.

[28] W. J. Streit, J. R. Conde, S. E. Fendrick, B. E. Flanary, and C. L. Mariani, "Role of microglia in the central nervous system's immune response," *Neurological Research*, vol. 27, no. 7. pp. 685–691, 2005.

[29] G. W. Kreutzberg, "Microglia: A sensor for pathological events in the CNS," *Trends in Neurosciences*, vol. 19, no. 8. pp. 312–318, 1996.

[30] A. Nimmerjahn, F. Kirchhoff, and F. Helmchen, "Resting microglial cells are highly dynamic surveillants of brain parenchyma in vivo," *Neuroforum*, vol. 11, no. 3, pp. 95–96, 2005.

[31] N. Levtova *et al.*, "Comparative morphology and phagocytic capacity of primary human adult microglia with time-lapse imaging," *J. Neuroimmunol.*, vol. 310, pp. 143–149, 2017.

[32] S. M. Stamatovic, A. M. Johnson, R. F. Keep, and A. V. Andjelkovic, "Junctional proteins of the blood-brain barrier: New insights into function and dysfunction," *Tissue Barriers*, vol. 4, no. 1. 2016.

[33] G. Bazzoni and E. Dejana, "Endothelial cell-to-cell junctions: Molecular organization and role in vascular homeostasis," *Physiological Reviews*, vol. 84, no. 3. pp. 869–901, 2004.

[34] C. Greene *et al.*, "Dose-dependent expression of claudin-5 is a modifying factor in schizophrenia," *Mol. Psychiatry*, vol. 23, no. 11, pp. 2156–2166, 2018.

[35] T. Nitta *et al.*, "Size-selective loosening of the blood-brain barrier in claudin-5-deficient mice," *J. Cell Biol.*, vol. 161, no. 3, pp. 653–660, 2003.

[36] M. M. Buschmann *et al.*, "Occludin OCEL-domain interactions are required for maintenance and regulation of the tight junction barrier to macromolecular flux," *Mol. Biol. Cell*, vol. 24, no. 19, pp. 3056–3068, 2013.

[37] C. Bellmann *et al.*, "Highly conserved cysteines are involved in the oligomerization of occludin-Redox dependency of the second extracellular loop," *Antioxidants Redox*

Signal., vol. 20, no. 6, pp. 855–867, 2014.

[38] E. P. Wojcikiewicz *et al.*, "LFA-1 binding destabilizes the JAM-A homophilic interaction during leukocyte transmigration," *Biophys. J.*, vol. 96, no. 1, pp. 285–293, 2009.

[39] N. Sladojevic *et al.*, "Inhibition of junctional adhesion molecule-A/LFA interaction attenuates leukocyte trafficking and inflammation in brain ischemia/reperfusion injury," *Neurobiol. Dis.*, vol. 67, pp. 57–70, 2014.

[40] M. Itoh, H. Sasaki, M. Furuse, H. Ozaki, T. Kita, and S. Tsukita, "Junctional adhesion molecule (JAM) binds to PAR-3: A possible mechanism for the recruitment of PAR-3 to tight junctions," *J. Cell Biol.*, vol. 154, no. 3, pp. 491–497, 2001.

[41] M. Giannotta, M. Trani, and E. Dejana, "VE-cadherin and endothelial adherens junctions: Active guardians of vascular integrity," *Developmental Cell*, vol. 26, no. 5. pp. 441–454, 2013.

[42] S. Ohtsuki and T. Terasaki, "Contribution of carrier-mediated transport systems to the blood-brain barrier as a supporting and protecting interface for the brain; importance for CNS drug discovery and development," *Pharmaceutical Research*, vol. 24, no. 9. pp. 1745–1758, 2007.

[43] B. T. Hawkins and T. P. Davis, "The blood-brain barrier/neurovascular unit in health and disease," *Pharmacological Reviews*, vol. 57, no. 2. pp. 173–185, 2005.

[44] W. M. Pardridge, "Blood-brain barrier drug targeting: the future of brain drug development," *Molecular interventions*, vol. 3, no. 2. 2003.

[45] W. M. Pardridge, "Re-engineering biopharmaceuticals for delivery to brain with molecular Trojan horses," *Bioconjugate Chemistry*, vol. 19, no. 7. pp. 1327–1338, 2008.

[46] W. M. Pardridge, "Biopharmaceutical drug targeting to the brain," *Journal of Drug Targeting*, vol. 18, no. 3. pp. 157–167, 2010.

[47] W. M. Pardridge, "Molecular Trojan horses for blood-brain barrier drug delivery," *Current Opinion in Pharmacology*, vol. 6, no. 5. pp. 494–500, 2006.

[48] A. D. Wong, M. Ye, A. F. Levy, J. D. Rothstein, D. E. Bergles, and P. C. Searson, "The blood-brain barrier: An engineering perspective," *Frontiers in Neuroengineering*, no. JUL. 2013.

[49] N. J. Abbott, "Astrocyte-endothelial interactions and blood-brain barrier permeability," *Journal of Anatomy*, vol. 200, no. 6. pp. 629–638, 2002.

[50] K. M. Giacomini *et al.*, "Membrane transporters in drug development," *Nature Reviews Drug Discovery*, vol. 9, no. 3. pp. 215–236, 2010.

[51] N. J. Abbott, A. A. K. Patabendige, D. E. M. Dolman, S. R. Yusof, and D. J. Begley, "Structure and function of the blood-brain barrier," *Neurobiology of Disease*, vol. 37, no. 1. pp. 13–25, 2010.

[52] M. Ueno, "Mechanisms of the Penetration of Blood-Borne Substances into the Brain," *Curr. Neuropharmacol.*, vol. 7, no. 2, pp. 142–149, 2009.

[53] B. V. Zlokovic, "The Blood-Brain Barrier in Health and Chronic Neurodegenerative Disorders," *Neuron*, vol. 57, no. 2. pp. 178–201, 2008.

[54] E. C. M. De Lange, "Potential role of ABC transporters as a detoxification system at the blood-CSF barrier," *Advanced Drug Delivery Reviews*, vol. 56, no. 12. pp. 1793–1809, 2004.

[55] G. Lee, S. Dallas, M. Hong, and R. Bendayan, "Drug transporters in the central nervous system: Brain barriers and brain parenchyma considerations," *Pharmacological Reviews*, vol. 53, no. 4. pp. 569–596, 2001.

[56] A. H. Schinkel, "P-Glycoprotein, a gatekeeper in the blood-brain barrier," *Advanced Drug Delivery Reviews*, vol. 36, no. 2–3. pp. 179–194, 1999.

[57] C. A. Lipinski, F. Lombardo, B. W. Dominy, and P. J. Feeney, "Experimental and computational approaches to estimate solubility and permeability in drug discovery and development settings," *Advanced Drug Delivery Reviews*, vol. 64, no. SUPPL. pp. 4–17, 2012.

[58] V. A. Levin, "Relationship of Octanol/Water Partition Coefficient and Molecular Weight to Rat Brain Capillary Permeability," *J. Med. Chem.*, vol. 23, no. 6, pp. 682–684, 1980.

[59] E. G. Chikhale, K. Y. Ng, P. S. Burton, and R. T. Borchardt, "Hydrogen Bonding Potential as a Determinant of the in Vitro and in Situ Blood–Brain Barrier Permeability of Peptides," *Pharm. Res. An Off. J. Am. Assoc. Pharm. Sci.*, vol. 11, no. 3, pp. 412–419, 1994.

[60] M. F. Salvatore *et al.*, "Point source concentration of GDNF may explain failure of phase II clinical trial," *Exp. Neurol.*, vol. 202, no. 2, pp. 497–505, 2006.

[61] M. F. Bennewitz and W. M. Saltzman, "Nanotechnology for Delivery of Drugs to the Brain for Epilepsy," *Neurotherapeutics*, vol. 6, no. 2, pp. 323–336, 2009.

[62] R. G. Blasberg, C. Patlak, and J. D. Fenstermacher, "Intrathecal chemotherapy: brain tissue profiles after ventriculo cisternal perfusion," *J. Pharmacol. Exp. Ther.*, vol. 195, no. 1, pp. 73–83, 1975.

[63] R. K. Jain, "Delivery of novel therapeutic agents in tumors: Physiological barriers and

strategies," *J. Natl. Cancer Inst.*, vol. 81, no. 8, pp. 570–576, 1989.

[64] E. J. Mufson *et al.*, "Intrastriatal and intraventricular infusion of brain-derived neurotrophic factor in the cynomologous monkey: Distribution, retrograde transport and co-localization with substantia nigra dopamine-containing neurons," *Neuroscience*, vol. 71, no. 1, pp. 179–191, 1996.

[65] S. Kunwar *et al.*, "Phase III randomized trial of CED of IL13-PE38QQR vs Gliadel wafers for recurrent glioblastoma," *Neuro. Oncol.*, vol. 12, no. 8, pp. 871–881, 2010.

[66] J. H. Sampson *et al.*, "Intracerebral infusion of an EGFR-targeted toxin in recurrent malignant brain tumors," *Neuro. Oncol.*, vol. 10, no. 3, pp. 320–329, 2008.

[67] J. Zhou *et al.*, "Highly penetrative, drug-loaded nanocarriers improve treatment of glioblastoma," *Proc. Natl. Acad. Sci. U. S. A.*, vol. 110, no. 29, pp. 11751–11756, 2013.

[68] X. Yi, D. S. Manickam, A. Brynskikh, and A. V. Kabanov, "Agile delivery of protein therapeutics to CNS," *Journal of Controlled Release*, vol. 190. pp. 637–663, 2014.

[69] M. I. Papisov, V. V. Belov, and K. S. Gannon, "Physiology of the intrathecal bolus: The leptomeningeal route for macromolecule and particle delivery to CNS," *Mol. Pharm.*, vol. 10, no. 5, pp. 1522–1532, 2013.

[70] G. Chen, X. Zhang, F. Yang, and L. Mu, "Disposition of Nanoparticle-Based Delivery System via Inner Ear Administration," *Curr. Drug Metab.*, vol. 11, no. 10, pp. 886–897, 2011.

[71] X. Zhang *et al.*, "Novel multiple agents loaded PLGA nanoparticles for brain delivery via inner ear administration: In vitro and in vivo evaluation," *Eur. J. Pharm. Sci.*, vol. 48, no. 4–5, pp. 595–603, 2013.

[72] R. G. Thorne, G. J. Pronk, V. Padmanabhan, and W. H. Frey, "Delivery of insulin-like growth factor-I to the rat brain and spinal cord along olfactory and trigeminal pathways following intranasal administration," *Neuroscience*, vol. 127, no. 2, pp. 481–496, 2004.

[73] R. G. Thorne, C. R. Emory, T. A. Ala, and W. H. Frey, "Quantitative analysis of the olfactory pathway for drug delivery to the brain," *Brain Res.*, vol. 692, no. 1–2, pp. 278–282, 1995.

[74] T. Musumeci, A. Bonaccorso, and G. Puglisi, "Epilepsy disease and nose-to-brain delivery of polymeric nanoparticles: An overview," *Pharmaceutics*, vol. 11, no. 3. 2019.

[75] H. Wu, K. Hu, and X. Jiang, "From nose to brain: Understanding transport capacity and transport rate of drugs," *Expert Opinion on Drug Delivery*, vol. 5, no. 10. pp. 1159–1168, 2008.

[76] S. I. Rapoport, M. Hori, and I. Klatzo, "Testing of a hypothesis for osmotic opening of the blood-brain barrier.," *Am. J. Physiol.*, vol. 223, no. 2, pp. 323–331, 1972.

[77] S. I. Rapoport, "Osmotic opening of the blood-brain barrier: Principles, mechanism, and therapeutic applications," *Cellular and Molecular Neurobiology*, vol. 20, no. 2. pp. 217–230, 2000.

[78] T. Siegal *et al.*, "In vivo assessment of the window of barrier opening after osmotic blood- brain barrier disruption in humans," *J. Neurosurg.*, vol. 92, no. 4, pp. 599–605, 2000.

[79] S. I. Rapoport, K. Ohno, W. R. Fredericks, and K. D. Pettigrew, "Regional cerebrovascular permeability to [14C]sucrose after osmotic opening of the blood-brain barrier," *Brain Res.*, vol. 150, no. 3, pp. 653–657, 1978.

[80] N. D. Doolittle *et al.*, "Safety and efficacy of a multicenter study using intraarterial chemotherapy in conjunction with osmotic opening of the blood-brain barrier for the treatment of patients with malignant brain tumors," *Cancer*, vol. 88, no. 3, pp. 637–647, 2000.

[81] N. Marchi *et al.*, "Seizure-promoting effect of blood-brain barrier disruption," *Epilepsia*, vol. 48, no. 4, pp. 732–742, 2007.

[82] M. Werle, "Natural and synthetic polymers as inhibitors of drug efflux pumps," *Pharmaceutical Research*, vol. 25, no. 3. pp. 500–511, 2008.

[83] D. J. Begley, "ABC transporters and the blood-brain barrier," *Curr Pharm Des*, vol. 10, no. 12, pp. 1295–312, 2004.

[84] J. H. Merritt, A. F. Chamness, and S. J. Allen, "Studies on blood-brain barrier permeability after microwave-radiation," *Radiat. Environ. Biophys.*, vol. 15, no. 4, pp. 367–377, 1978.

[85] E. Moriyama, M. Salcman, and R. D. Broadwell, "Blood-brain barrier alteration after microwave-induced hyperthermia is purely a thermal effect: I. Temperature and power measurements," *Surg. Neurol.*, vol. 35, no. 3, pp. 177–182, 1991.

[86] J. H. Kim, J. K. Lee, H. G. Kim, K. B. Kim, and H. R. Kim, "Possible effects of radiofrequency electromagnetic field exposure on central nerve system," *Biomolecules and Therapeutics*, vol. 27, no. 3. pp. 265–275, 2019.

[87] L. G. Salford, A. Brun, K. Sturesson, J. L. Eberhardt, and B. R. R. Persson, "Permeability of the blood-brain barrier induced by 915 MHz electromagnetic radiation, continuous wave and modulated at 8, 16, 50, and 200 Hz," *Microsc. Res. Tech.*, vol. 27, no. 6, pp. 535–

542, 1994.

[88] K. Hynynen, N. McDannold, N. Vykhodtseva, and F. A. Jolesz, "Noninvasive MR imaging-guided focal opening of the blood-brain barrier in rabbits," *Radiology*, vol. 220, no. 3, pp. 640–646, 2001.

[89] T. Şen, O. Tüfekçioğlu, and Y. Koza, "Mechanical index," *Anadolu Kardiyol. Derg.*, vol. 15, no. 4, pp. 334–336, 2015.

[90] C. C. Church, "Frequency, pulse length, and the mechanical index," *Acoust. Res. Lett. Online*, 2005.

[91] S. Yoshizawa, T. Ikeda, A. Ito, R. Ota, S. Takagi, and Y. Matsumoto, "High intensity focused ultrasound lithotripsy with cavitating microbubbles," *Med. Biol. Eng. Comput.*, vol. 47, no. 8, pp. 851–860, 2009.

[92] G. ter Haar and C. Coussios, "High intensity focused ultrasound: Physical principles and devices," *Int. J. Hyperth.*, vol. 23, no. 2, pp. 89–104, 2007.

[93] S. R. Sirsi and M. A. Borden, "Microbubble compositions, properties and biomedical applications," *Bubble Science, Engineering and Technology*, vol. 1, no. 1–2. pp. 3–17, 2009.

[94] J. R. Lindner, J. Song, A. R. Jayaweera, J. Sklenar, and S. Kaul, "Microvascular rheology of definity microbubbles after intra-arterial and intravenous administration," *J. Am. Soc. Echocardiogr.*, vol. 15, no. 5, pp. 396–403, 2002.

[95] M. Diez-Silva, M. Dao, J. Han, C.-T. Lim, and S. Suresh, "Shape and Biomechanical Characteristics of Human Red Blood Cells in Health and Disease," *MRS Bull.*, vol. 35, no. 5, pp. 382–388, 2010.

[96] J. Karbowski, "Scaling of brain metabolism and blood flow in relation to capillary and neural scaling," *PLoS One*, vol. 6, no. 10, 2011.

[97] J. Steinman, M. M. Koletar, B. Stefanovic, and J. G. Sled, "3D morphological analysis of the mouse cerebral vasculature: Comparison of in vivo and ex vivo methods," *PLoS One*, vol. 12, no. 10, 2017.

[98] P. S. Tsai *et al.*, "Correlations of neuronal and microvascular densities in murine cortex revealed by direct counting and colocalization of nuclei and vessels," *J. Neurosci.*, vol. 29, no. 46, pp. 14553–14570, 2009.

[99] B. V. Zlokovic, "Neurovascular mechanisms of Alzheimer's neurodegeneration," *Trends in Neurosciences*, vol. 28, no. 4. pp. 202–208, 2005.

[100] H. Duvernoy, S. Delon, and J. L. Vannson, "The vascularization of the human cerebellar cortex," *Brain Res. Bull.*, vol. 11, no. 4, pp. 419–480, 1983.

[101] C. Nicholson, "Diffusion and related transport mechanisms in brain tissue," *Reports Prog. Phys.*, vol. 64, no. 7, pp. 815–884, 2001.

[102] M. Schneider, "Characteristics of SonoVue™," *Echocardiography*, vol. 16, no. s1, pp. 743–746, 1999.

[103] C. P. Nolsøe and T. Lorentzen, "International guidelines for contrast-enhanced Ultrasonography: Ultrasound imaging in the new millennium," *Ultrasonography*, vol. 35, no. 2. pp. 89–103, 2016.

[104] N. de Jong, M. Emmer, A. van Wamel, and M. Versluis, "Ultrasonic characterization of ultrasound contrast agents," *Med. Biol. Eng. Comput.*, vol. 47, no. 8, pp. 861–873, 2009.

[105] M. Ressner *et al.*, "Backscattered ultrasound from contrast microbubbles: Effects of tissue and bubble interaction," in *Annual International Conference of the IEEE Engineering in Medicine and Biology - Proceedings*, 2004, vol. 26 II, pp. 849–852.

[106] P. S. Epstein and M. S. Plesset, "On the stability of gas bubbles in liquid-gas solutions," *J. Chem. Phys.*, vol. 18, no. 11, pp. 1505–1509, 1950.

[107] K. W. Ferrara, M. A. Borden, and H. Zhang, "Lipid-shelled vehicles: Engineering for ultrasound molecular imaging and drug delivery," *Acc. Chem. Res.*, vol. 42, no. 7, pp. 881–892, 2009.

[108] R. E. Apfel, "Sonic effervescence: A tutorial on acoustic cavitation," *J. Acoust. Soc. Am.*, vol. 101, no. 3, pp. 1227–1237, 1997.

[109] T. G. Leighton and R. E. Apfel, "The Acoustic Bubble," *J. Acoust. Soc. Am.*, vol. 96, no. 4, pp. 2616–2616, 1994.

[110] H. G. Flynn, "Cavitation dynamics. i. a mathematical formulation," *J. Acoust. Soc. Am.*, vol. 57, no. 6, pp. 1379–1396, 1975.

[111] A. Prosperetti, "Physics of acoustic cavitation in liquids: H. G. Flynn's review 35 years later," *J. Acoust. Soc. Am.*, vol. 103, no. 5, pp. 2970–2970, 1998.

[112] C. C. Church and E. L. Carstensen, "'Stable' inertial cavitation," *Ultrasound Med. Biol.*, vol. 27, no. 10, pp. 1435–1437, 2001.

[113] R. E. Apfel, "Acoustic cavitation: A possible consequence of biomedical uses of ultrasound," *Br. J. Cancer*, vol. 45, no. Suppl. 5, pp. 140–146, 1982.

[114] J. E. Chomas, P. Dayton, D. May, and K. Ferrara, "Threshold of fragmentation for

ultrasonic contrast agents," *J. Biomed. Opt.*, vol. 6, no. 2, p. 141, 2001.

[115] K. Kooiman *et al.*, "Ultrasound-Responsive Cavitation Nuclei for Therapy and Drug Delivery," *Ultrasound Med. Biol.*, vol. 46, no. 6, pp. 1296–1325, 2020.

[116] C. C. Church and D. L. Miller, "A Two-Criterion Model for Microvascular Bio-Effects Induced In Vivo by Contrast Microbubbles Exposed to Medical Ultrasound," *Ultrasound Med. Biol.*, vol. 42, no. 6, pp. 1385–1398, 2016.

[117] P. A. Dayton, J. S. Allen, and K. W. Ferrara, "The magnitude of radiation force on ultrasound contrast agents," *J. Acoust. Soc. Am.*, vol. 112, no. 5, pp. 2183–2192, 2002.

[118] P. Dayton, A. Klibanov, G. Brandenburger, and K. Ferrara, "Acoustic radiation force in vivo: A mechanism to assist targeting of microbubbles," *Ultrasound Med. Biol.*, vol. 25, no. 8, pp. 1195–1201, 1999.

[119] C. F. Caskey, S. Qin, P. A. Dayton, and K. W. Ferrara, "Microbubble tunneling in gel phantoms," *J. Acoust. Soc. Am.*, vol. 125, no. 5, p. EL183, 2009.

[120] K. B. Bader, M. J. Gruber, and C. K. Holland, "Shaken and Stirred: Mechanisms of Ultrasound-Enhanced Thrombolysis," *Ultrasound Med. Biol.*, vol. 41, no. 1, pp. 187–196, 2015.

[121] C. N. Acconcia, B. Y. C. Leung, and D. E. Goertz, "The microscale evolution of the erosion front of blood clots exposed to ultrasound stimulated microbubbles," *J. Acoust. Soc. Am.*, vol. 139, no. 5, pp. EL135–EL141, 2016.

[122] A. van Wamel *et al.*, "Vibrating microbubbles poking individual cells: Drug transfer into cells via sonoporation," *J. Control. Release*, vol. 112, no. 2, pp. 149–155, 2006.

[123] N. Kudo, "High-Speed In Situ Observation System for Sonoporation of Cells With Size- and Position-Controlled Microbubbles," *IEEE Trans. Ultrason. Ferroelectr. Freq. Control*, vol. 64, no. 1, pp. 273–280, 2017.

[124] H. Chen, A. A. Brayman, W. Kreider, M. R. Bailey, and T. J. Matula, "Observations of translation and jetting of ultrasound-activated microbubbles in mesenteric microvessels," *Ultrasound Med. Biol.*, vol. 37, no. 12, pp. 2139–2148, 2011.

[125] J. Kolb and W. L. Nyborg, "Small-Scale Acoustic Streaming in Liquids," *J. Acoust. Soc. Am.*, vol. 28, no. 6, pp. 1237–1242, 1956.

[126] P. Marmottant and S. Hilgenfeldt, "Controlled vesicle deformation and lysis by single oscillating bubbles," *Nature*, vol. 423, no. 6936, pp. 153–156, 2003.

[127] W. L. Nyborg, "Acoustic Streaming near a Boundary," *J. Acoust. Soc. Am.*, vol. 30, no. 4,

pp. 329–339, 1958.

[128] N. Kudo and Y. Kinoshita, "Effects of cell culture scaffold stiffness on cell membrane damage induced by sonoporation," *J. Med. Ultrason.*, vol. 41, no. 4, pp. 411–420, 2014.

[129] L. A. Crum, "Bjerknes forces on bubbles in a stationary sound field," *J. Acoust. Soc. Am.*, vol. 57, no. 6, pp. 1363–1370, 1975.

[130] A. A. Doinikov and S. T. Zavtrak, "On the mutual interaction of two gas bubbles in a sound field," *Phys. Fluids*, vol. 7, no. 8, pp. 1923–1930, 1995.

[131] N. A. Pelekasis, A. Gaki, A. Doinikov, and J. A. Tsamopoulos, "Secondary Bjerknes forces between two bubbles and the phenomenon of acoustic streamers," *J. Fluid Mech.*, no. 500, pp. 313–347, 2004.

[132] E. A. Zabolotskaya, "Interaction of Gas Bubbles in a Sound Field.," *Sov. physics. Acoust.*, vol. 30, no. 5, pp. 365–368, 1984.

[133] E. B. Flint and K. S. Suslick, "The temperature of cavitation," *Science (80-.).*, vol. 253, no. 5026, pp. 1397–1399, 1991.

[134] C. C. Winterbourn, "Reconciling the chemistry and biology of reactive oxygen species," *Nature Chemical Biology*, vol. 4, no. 5. pp. 278–286, 2008.

[135] I. Rosenthal, J. Z. Sostaric, and P. Riesz, "Sonodynamic therapya review of the synergistic effects of drugs and ultrasound," *Ultrasonics Sonochemistry*, vol. 11, no. 6. pp. 349–363, 2004.

[136] E. Beguin, S. Shrivastava, N. V. Dezhkunov, A. P. Mchale, J. F. Callan, and E. Stride, "Direct Evidence of Multibubble Sonoluminescence Using Therapeutic Ultrasound and Microbubbles," *ACS Appl. Mater. Interfaces*, vol. 11, no. 22, pp. 19913–19919, 2019.

[137] L. J. M. Juffermans *et al.*, "Ultrasound and Microbubble-Induced Intra- and Intercellular Bioeffects in Primary Endothelial Cells," *Ultrasound Med. Biol.*, vol. 35, no. 11, pp. 1917–1927, 2009.

[138] K. Kooiman, A. F. W. Van Der Steen, and N. De Jong, "Role of intracellular calcium and reactive oxygen species in microbubble-mediated alterations of endothelial layer permeability," *IEEE Trans. Ultrason. Ferroelectr. Freq. Control*, vol. 60, no. 9, pp. 1811–1815, 2013.

[139] A. Carpentier *et al.*, "Clinical trial of blood-brain barrier disruption by pulsed ultrasound," *Sci. Transl. Med.*, vol. 8, no. 343, p. 343re2, 2016.

[140] N. Lipsman *et al.*, "Blood–brain barrier opening in Alzheimer's disease using MR-guided

focused ultrasound," *Nat. Commun.*, vol. 9, no. 1, 2018.

[141] T. Mainprize *et al.*, "Blood-Brain Barrier Opening in Primary Brain Tumors with Non-invasive MR-Guided Focused Ultrasound: A Clinical Safety and Feasibility Study," *Sci. Rep.*, vol. 9, no. 1, 2019.

[142] L. H. Treat, N. McDannold, Y. Zhang, N. Vykhodtseva, and K. Hynynen, "Improved Anti-Tumor Effect of Liposomal Doxorubicin After Targeted Blood-Brain Barrier Disruption by MRI-Guided Focused Ultrasound in Rat Glioma," *Ultrasound Med. Biol.*, vol. 38, no. 10, pp. 1716–1725, 2012.

[143] L. H. Treat, N. McDannold, N. Vykhodtseva, Y. Zhang, K. Tam, and K. Hynynen, "Targeted delivery of doxorubicin to the rat brain at therapeutic levels using MRI-guided focused ultrasound," *Int. J. Cancer*, vol. 121, no. 4, pp. 901–907, 2007.

[144] M. Aryal, N. Vykhodtseva, Y. Z. Zhang, and N. McDannold, "Multiple sessions of liposomal doxorubicin delivery via focused ultrasound mediated blood-brain barrier disruption: A safety study," *J. Control. Release*, vol. 204, pp. 60–69, 2015.

[145] B. Baseri *et al.*, "Activation of signaling pathways following localized delivery of systemically administered neurotrophic factors across the bloodbrain barrier using focused ultrasound and microbubbles," *Phys. Med. Biol.*, vol. 57, no. 7, 2012.

[146] J. F. Jordão *et al.*, "Amyloid-β plaque reduction, endogenous antibody delivery and glial activation by brain-targeted, transcranial focused ultrasound," *Exp. Neurol.*, vol. 248, pp. 16–29, 2013.

[147] M. Kinoshita, N. McDannold, F. A. Jolesz, and K. Hynynen, "Targeted delivery of antibodies through the blood-brain barrier by MRI-guided focused ultrasound," *Biochem. Biophys. Res. Commun.*, vol. 340, no. 4, pp. 1085–1090, 2006.

[148] M. Kinoshita, N. McDannold, F. A. Jolesz, and K. Hynynen, "Noninvasive localized delivery of Herceptin to the mouse brain by MRI-guided focused ultrasound-induced blood-brain barrier disruption," *Proc. Natl. Acad. Sci. U. S. A.*, vol. 103, no. 31, pp. 11719–11723, 2006.

[149] Q. Huang *et al.*, "Targeted gene delivery to the mouse brain by MRI-guided focused ultrasound-induced blood-brain barrier disruption," *Exp. Neurol.*, vol. 233, no. 1, pp. 350–356, 2012.

[150] E. Thévenot *et al.*, "Targeted delivery of self-complementary adeno-associated virus serotype 9 to the brain, using magnetic resonance imaging-guided focused ultrasound,"

Hum. Gene Ther., vol. 23, no. 11, pp. 1144–1155, 2012.

[151] T. Nhan, A. Burgess, E. E. Cho, B. Stefanovic, L. Lilge, and K. Hynynen, "Drug delivery to the brain by focused ultrasound induced blood-brain barrier disruption: Quantitative evaluation of enhanced permeability of cerebral vasculature using two-photon microscopy," *J. Control. Release*, vol. 172, no. 1, pp. 274–280, 2013.

[152] J. J. Choi, S. Wang, Y. S. Tung, B. Morrison, and E. E. Konofagou, "Molecules of Various Pharmacologically-Relevant Sizes Can Cross the Ultrasound-Induced Blood-Brain Barrier Opening in vivo," *Ultrasound Med. Biol.*, vol. 36, no. 1, pp. 58–67, 2010.

[153] J. J. Choi, K. Selert, F. Vlachos, A. Wong, and E. E. Konofagou, "Noninvasive and localized neuronal delivery using short ultrasonic pulses and microbubbles," *Proc. Natl. Acad. Sci. U. S. A.*, vol. 108, no. 40, pp. 16539–16544, 2011.

[154] H. Chen and E. E. Konofagou, "The size of blood-brain barrier opening induced by focused ultrasound is dictated by the acoustic pressure," *J. Cereb. Blood Flow Metab.*, vol. 34, no. 7, pp. 1197–1204, 2014.

[155] S. V. Morse *et al.*, "Rapid short-pulse ultrasound delivers drugs uniformly across the murine blood-brain barrier with negligible disruption," *Radiology*, vol. 291, no. 2, pp. 459–466, 2019.

[156] B. Marty *et al.*, "Dynamic study of blood-brain barrier closure after its disruption using ultrasound: A quantitative analysis," *J. Cereb. Blood Flow Metab.*, vol. 32, no. 10, pp. 1948–1958, 2012.

[157] Y. S. Tung, F. Vlachos, J. J. Choi, T. Deffieux, K. Selert, and E. E. Konofagou, "In vivo transcranial cavitation threshold detection during ultrasound-induced blood-brain barrier opening in mice," *Phys. Med. Biol.*, vol. 55, no. 20, pp. 6141–6155, 2010.

[158] J. J. Choi, M. Pernot, T. R. Brown, S. A. Small, and E. E. Konofagou, "Spatio-temporal analysis of molecular delivery through the blood-brain barrier using focused ultrasound," *Phys. Med. Biol.*, vol. 52, no. 18, pp. 5509–5530, 2007.

[159] J. J. Choi, M. Pernot, S. A. Small, and E. E. Konofagou, "Noninvasive, transcranial and localized opening of the blood-brain barrier using focused ultrasound in mice," *Ultrasound Med. Biol.*, vol. 33, no. 1, pp. 95–104, 2007.

[160] R. J. Diaz *et al.*, "Focused ultrasound delivery of Raman nanoparticles across the blood-brain barrier: Potential for targeting experimental brain tumors," *Nanomedicine Nanotechnology, Biol. Med.*, vol. 10, no. 5, pp. e1075–e1087, 2014.

[161] H. L. Liu *et al.*, "Magnetic resonance monitoring of focused ultrasound/magnetic nanoparticle targeting delivery of therapeutic agents to the brain," *Proc. Natl. Acad. Sci. U. S. A.*, vol. 107, no. 34, pp. 15205–15210, 2010.

[162] E. Nance *et al.*, "Non-invasive delivery of stealth, brain-penetrating nanoparticles across the blood-brain barrier using MRI-guided focused ultrasound," *J. Control. Release*, vol. 189, pp. 123–132, 2014.

[163] M. Aryal, I. Papademetriou, Y. Z. Zhang, C. Power, N. McDannold, and T. Porter, "MRI Monitoring and Quantification of Ultrasound-Mediated Delivery of Liposomes Dually Labeled with Gadolinium and Fluorophore through the Blood-Brain Barrier," *Ultrasound Med. Biol.*, vol. 45, no. 7, pp. 1733–1742, 2019.

[164] Z. Kovacs, P. Luciani, P. Roth, J.-C. Leroux, E. Martin, and B. Werner, "Blood-brain barrier opening-based local delivery of 80 nm-sized liposomes in mice using pulsed focused ultrasound," *J. Ther. Ultrasound*, vol. 3, no. S1, 2015.

[165] Y. Shen *et al.*, "Delivery of liposomes with different sizes to mice brain after sonication by focused ultrasound in the presence of microbubbles," *Ultrasound Med. Biol.*, vol. 42, no. 7, pp. 1499–1511, 2016.

[166] K. Kooiman, H. J. Vos, M. Versluis, and N. De Jong, "Acoustic behavior of microbubbles and implications for drug delivery," *Advanced Drug Delivery Reviews*, vol. 72. pp. 28–48, 2014.

[167] I. Lentacker, S. C. De Smedt, and N. N. Sanders, "Drug loaded microbubble design for ultrasound triggered delivery," *Soft Matter*, vol. 5, no. 11, pp. 2161–2170, 2009.

[168] M. Aryal, N. Vykhodtseva, Y. Z. Zhang, J. Park, and N. McDannold, "Multiple treatments with liposomal doxorubicin and ultrasound-induced disruption of blood-tumor and blood-brain barriers improve outcomes in a rat glioma model," *J. Control. Release*, vol. 169, no. 1–2, pp. 103–111, 2013.

[169] A. Dréan *et al.*, "Temporary blood–brain barrier disruption by low intensity pulsed ultrasound increases carboplatin delivery and efficacy in preclinical models of glioblastoma," *J. Neurooncol.*, vol. 144, no. 1, pp. 33–41, 2019.

[170] T. Sun *et al.*, "Closed-loop control of targeted ultrasound drug delivery across the blood–brain/tumor barriers in a rat glioma model," *Proc. Natl. Acad. Sci. U. S. A.*, vol. 114, no. 48, pp. E10281–E10290, 2017.

[171] H. L. Liu *et al.*, "Focused ultrasound enhances central nervous system delivery of

Bevacizumab for malignant glioma treatment," *Radiology*, vol. 281, no. 1, pp. 99–108, 2016.

[172] A. Papachristodoulou *et al.*, "Chemotherapy sensitization of glioblastoma by focused ultrasound-mediated delivery of therapeutic liposomes," *J. Control. Release*, vol. 295, pp. 130–139, 2019.

[173] K. C. Wei *et al.*, "Focused Ultrasound-Induced Blood-Brain Barrier Opening to Enhance Temozolomide Delivery for Glioblastoma Treatment: A Preclinical Study," *PLoS One*, vol. 8, no. 3, 2013.

[174] C. H. Fan *et al.*, "Noninvasive, Targeted, and Non-Viral Ultrasound-Mediated GDNF-Plasmid Delivery for Treatment of Parkinson's Disease," *Sci. Rep.*, vol. 6, 2016.

[175] P. H. Hsu *et al.*, "Focused Ultrasound-Induced Blood-Brain Barrier Opening Enhances GSK-3 Inhibitor Delivery for Amyloid-Beta Plaque Reduction," *Sci. Rep.*, vol. 8, no. 1, 2018.

[176] S. B. Raymond, L. H. Treat, J. D. Dewey, N. J. McDannold, K. Hynynen, and B. J. Bacskai, "Ultrasound enhanced delivery of molecular imaging and therapeutic agents in Alzheimer's disease mouse models," *PLoS One*, vol. 3, no. 5, 2008.

[177] J. F. Jordão *et al.*, "Antibodies targeted to the brain with image-guided focused ultrasound reduces amyloid-β plaque load in the TgCRND8 mouse model of Alzheimer's disease," *PLoS One*, vol. 5, no. 5, 2010.

[178] T. Alecou, M. Giannakou, and C. Damianou, "Amyloid β plaque reduction with antibodies crossing the blood-brain barrier, which was opened in 3 sessions of focused ultrasound in a rabbit model," *J. Ultrasound Med.*, vol. 36, no. 11, pp. 2257–2270, 2017.

[179] B. P. Mead *et al.*, "Novel Focused Ultrasound Gene Therapy Approach Noninvasively Restores Dopaminergic Neuron Function in a Rat Parkinson's Disease Model," *Nano Lett.*, vol. 17, no. 6, pp. 3533–3542, 2017.

[180] C. Y. Lin *et al.*, "Focused ultrasound-induced blood brain-barrier opening enhanced vascular permeability for GDNF delivery in Huntington's disease mouse model," *Brain Stimul.*, vol. 12, no. 5, pp. 1143–1150, 2019.

[181] N. Sheikov, N. McDannold, F. Jolesz, Y. Z. Zhang, K. Tam, and K. Hynynen, "Brain arterioles show more active vesicular transport of blood-borne tracer molecules than capillaries and venules after focused ultrasound-evoked opening of the blood-brain barrier," *Ultrasound Med. Biol.*, vol. 32, no. 9, pp. 1399–1409, 2006.

[182] N. Sheikov, N. McDannold, S. Sharma, and K. Hynynen, "Effect of Focused Ultrasound Applied With an Ultrasound Contrast Agent on the Tight Junctional Integrity of the Brain Microvascular Endothelium," *Ultrasound Med. Biol.*, vol. 34, no. 7, pp. 1093–1104, 2008.

[183] N. Sheikov, N. McDannold, N. Vykhodtseva, F. Jolesz, and K. Hynynen, "Cellular mechanisms of the blood-brain barrier opening induced by ultrasound in presence of microbubbles," *Ultrasound Med. Biol.*, vol. 30, no. 7, pp. 979–989, 2004.

[184] S. B. Raymond, J. Skoch, K. Hynynen, and B. J. Bacskai, "Multiphoton imaging of ultrasound/Optison mediated cerebrovascular effects in vivo," *J. Cereb. Blood Flow Metab.*, vol. 27, no. 2, pp. 393–403, 2007.

[185] K. Hynynen, N. McDannold, N. A. Sheikov, F. A. Jolesz, and N. Vykhodtseva, "Local and reversible blood-brain barrier disruption by noninvasive focused ultrasound at frequencies suitable for trans-skull sonications," *Neuroimage*, vol. 24, no. 1, pp. 12–20, 2005.

[186] L. Pelkmans and A. Helenius, "Endocytosis via caveolae," *Traffic*, vol. 3, no. 5. pp. 311–320, 2002.

[187] L. Kongstad and P. O. Grände, "Arterial hypertension increases intracranial pressure in cat after opening of the blood-brain barrier," *J. Trauma*, vol. 51, no. 3, pp. 490–496, 2001.

[188] K. J. Gurney, E. Y. Estrada, and G. A. Rosenberg, "Blood-brain barrier disruption by stromelysin-1 facilitates neutrophil infiltration in neuroinflammation," *Neurobiol. Dis.*, vol. 23, no. 1, pp. 87–96, 2006.

[189] M. J. Cipolla, R. Crete, L. Vitullo, and R. D. Rix, "Transcellular transport as a mechanism of blood-brain barrier disruption during stroke," *Front. Biosci.*, vol. 9, pp. 777–785, 2004.

[190] Y.-S. Tung, F. Vlachos, J. A. Feshitan, M. A. Borden, and E. E. Konofagou, "The mechanism of interaction between focused ultrasound and microbubbles in blood-brain barrier opening in mice," *J. Acoust. Soc. Am.*, vol. 130, no. 5, pp. 3059–3067, 2011.

[191] J. H. Hwang, J. Tu, A. A. Brayman, T. J. Matula, and L. A. Crum, "Correlation between inertial cavitation dose and endothelial cell damage in vivo," *Ultrasound Med. Biol.*, vol. 32, no. 10, pp. 1611–1619, 2006.

[192] J. Tu, T. J. Matula, A. A. Brayman, and L. A. Crum, "Inertial cavitation dose produced in ex vivo rabbit ear arteries with Optison® by 1-MHz pulsed ultrasound," *Ultrasound Med. Biol.*, vol. 32, no. 2, pp. 281–288, 2006.

[193] H. L. Liu *et al.*, "Hemorrhage Detection During Focused-Ultrasound Induced Blood-

Brain-Barrier Opening by Using Susceptibility-Weighted Magnetic Resonance Imaging," *Ultrasound Med. Biol.*, vol. 34, no. 4, pp. 598–606, 2008.

[194] N. McDannold, C. D. Arvanitis, N. Vykhodtseva, and M. S. Livingstone, "Temporary disruption of the blood-brain barrier by use of ultrasound and microbubbles: Safety and efficacy evaluation in rhesus macaques," *Cancer Res.*, vol. 72, no. 14, pp. 3652–3663, 2012.

[195] J. Deng *et al.*, "The role of caveolin-1 in blood-brain barrier disruption induced by focused ultrasound combined with microbubbles," *J. Mol. Neurosci.*, vol. 46, no. 3, pp. 677–687, 2012.

[196] N. McDannold, N. Vykhodtseva, and K. Hynynen, "Targeted disruption of the blood-brain barrier with focused ultrasound: Association with cavitation activity," *Phys. Med. Biol.*, vol. 51, no. 4, pp. 793–807, 2006.

[197] M. A. Oreilly and K. Hynynen, "A PVDF receiver for ultrasound monitoring of transcranial focused ultrasound therapy," *IEEE Trans. Biomed. Eng.*, vol. 57, no. 9, pp. 2286–2294, 2010.

[198] M. A. O'Reilly and K. Hynynen, "Blood-brain barrier: Real-time feedback-controlled focused ultrasound disruption by using an acoustic emissions-based controller," *Radiology*, vol. 263, no. 1, pp. 96–106, 2012.

[199] C. D. Arvanitis, M. S. Livingstone, N. Vykhodtseva, and N. McDannold, "Controlled Ultrasound-Induced Blood-Brain Barrier Disruption Using Passive Acoustic Emissions Monitoring," *PLoS One*, vol. 7, no. 9, 2012.

[200] R. M. Jones, L. Deng, K. Leung, D. McMahon, M. A. O'Reilly, and K. Hynynen, "Three-dimensional transcranial microbubble imaging for guiding volumetric ultrasound-mediated blood-brain barrier opening," *Theranostics*, vol. 8, no. 11, pp. 2909–2926, 2018.

[201] L. Goldwirt *et al.*, "Enhanced brain distribution of carboplatin in a primate model after blood-brain barrier disruption using an implantable ultrasound device," *Cancer Chemother. Pharmacol.*, vol. 77, no. 1, pp. 211–216, 2016.

[202] C. Horodyckid *et al.*, "Safe long-term repeated disruption of the blood-brain barrier using an implantable ultrasound device: A multiparametric study in a primate model," *J. Neurosurg.*, vol. 126, no. 4, pp. 1351–1361, 2017.

[203] A. Idbaih *et al.*, "Safety and feasibility of repeated and transient blood-brain barrier

disruption by pulsed ultrasound in patients with recurrent glioblastoma," *Clin. Cancer Res.*, vol. 25, no. 13, pp. 3793–3801, 2019.

[204] N. Lipsman *et al.*, "Scdt-51. Initial Experience of Blood-Brain Barrier Opening for Chemotherapeutic-Drug Delivery To Brain Tumours By Mr-Guided Focused Ultrasound," *Neuro. Oncol.*, vol. 19, no. suppl_6, pp. vi275–vi275, 2017.

[205] A. N. Pouliopoulos, S. Y. Wu, M. T. Burgess, M. E. Karakatsani, H. A. S. Kamimura, and E. E. Konofagou, "A Clinical System for Non-invasive Blood–Brain Barrier Opening Using a Neuronavigation-Guided Single-Element Focused Ultrasound Transducer," *Ultrasound Med. Biol.*, vol. 46, no. 1, pp. 73–89, 2020.

[206] K. C. Wei *et al.*, "Neuronavigation-guided focused ultrasound-induced blood-brain barrier opening: A preliminary study in swine," *Am. J. Neuroradiol.*, vol. 34, no. 1, pp. 115–120, 2013.

[207] S. Y. Wu *et al.*, "Efficient blood-brain barrier opening in primates with neuronavigation-guided ultrasound and real-time acoustic mapping," *Sci. Rep.*, vol. 8, no. 1, 2018.

[208] P. W. A. Willems, J. W. B. Van Der Sprenkel, C. A. F. Tulleken, M. A. Viergever, and M. J. B. Taphoorn, "Neuronavigation and surgery of intracerebral tumours," *Journal of Neurology*, vol. 253, no. 9. pp. 1123–1136, 2006.

[209] M. E. Downs *et al.*, "Long-term safety of repeated blood-brain barrier opening via focused ultrasound with microbubbles in non-human primates performing a cognitive task," *PLoS One*, vol. 10, no. 5, 2015.

[210] J. J. Choi, K. Selert, Z. Gao, G. Samiotaki, B. Baseri, and E. E. Konofagou, "Noninvasive and localized blood-brain barrier disruption using focused ultrasound can be achieved at short pulse lengths and low pulse repetition frequencies," *J. Cereb. Blood Flow Metab.*, vol. 31, no. 2, pp. 725–737, 2011.

[211] B. Baseri, J. J. Choi, Y. S. Tung, and E. E. Konofagou, "Multi-modality safety assessment of blood-brain barrier opening using focused ultrasound and definity microbubbles: A short-term study," *Ultrasound Med. Biol.*, vol. 36, no. 9, pp. 1445–1459, 2010.

[212] M. A. Borden, D. E. Kruse, C. F. Caskey, S. Zhao, P. A. Dayton, and K. W. Ferrara, "Influence of lipid shell physicochemical properties on ultrasound-induced microbubble destruction," *IEEE Trans. Ultrason. Ferroelectr. Freq. Control*, vol. 52, no. 11, pp. 1992–2002, 2005.

[213] S. Samuel, M. A. Cooper, J. L. Bull, J. B. Fowlkes, and D. L. Miller, "An ex vivo Study of the

Correlation Between Acoustic Emission and Microvascular Damage," *Ultrasound Med. Biol.*, vol. 35, no. 9, pp. 1574–1586, 2009.

[214] S. M. Stieger *et al.*, "Enhancement of vascular permeability with low-frequency contrast-enhanced ultrasound in the chorioallantoic membrane model," *Radiology*, vol. 243, no. 1, pp. 112–121, 2007.

[215] J. Shin *et al.*, "Focused ultrasound-mediated noninvasive blood-brain barrier modulation: Preclinical examination of efficacy and safety in various sonication parameters," *Neurosurg. Focus*, vol. 44, no. 2, 2018.

[216] H. C. Tsai, C. H. Tsai, W. S. Chen, C. Inserra, K. C. Wei, and H. L. Liu, "Safety evaluation of frequent application of microbubble-enhanced focused ultrasound blood-brain-barrier opening," *Sci. Rep.*, vol. 8, no. 1, 2018.

[217] H. L. Liu *et al.*, "Magnetic resonance imaging enhanced by superparamagnetic iron oxide particles: Usefulness for distinguishing between focused ultrasound-induced blood-brain barrier disruption and brain hemorrhage," *J. Magn. Reson. Imaging*, vol. 29, no. 1, pp. 31–38, 2009.

[218] C. H. Fan, H. L. Liu, C. Y. Huang, Y. J. Ma, T. C. Yen, and C. K. Yeh, "Detection of Intracerebral Hemorrhage and Transient Blood-Supply Shortage in Focused-Ultrasound-Induced Blood-Brain Barrier Disruption by Ultrasound Imaging," *Ultrasound Med. Biol.*, vol. 38, no. 8, pp. 1372–1382, 2012.

[219] J. C. Weng, S. K. Wu, W. L. Lin, and W. Y. I. Tseng, "Detecting blood-brain barrier disruption within minimal hemorrhage following transcranial focused ultrasound: A correlation study with contrast-enhanced MRI," *Magn. Reson. Med.*, vol. 65, no. 3, pp. 802–811, 2011.

[220] D. McMahon and K. Hynynen, "Acute inflammatory response following increased blood-brain barrier permeability induced by focused ultrasound is dependent on microbubble dose," *Theranostics*, vol. 7, no. 16, pp. 3989–4000, 2017.

[221] A. Alonso, E. Reinz, M. Fatar, M. G. Hennerici, and S. Meairs, "Clearance of albumin following ultrasound-induced blood-brain barrier opening is mediated by glial but not neuronal cells," *Brain Res.*, vol. 1411, pp. 9–16, 2011.

[222] D. Shlosberg, M. Benifla, D. Kaufer, and A. Friedman, "Blood-brain barrier breakdown as a therapeutic target in traumatic brain injury," *Nature Reviews Neurology*, vol. 6, no. 7. pp. 393–403, 2010.

[223] Z. I. Kovacsa *et al.*, "Disrupting the blood-brain barrier by focused ultrasound induces sterile inflammation," *Proc. Natl. Acad. Sci. U. S. A.*, vol. 114, no. 1, pp. E75–E84, 2017.

[224] J. Silburt, N. Lipsman, and I. Aubert, "Disrupting the blood–brain barrier with focused ultrasound: Perspectives on inflammation and regeneration," *Proceedings of the National Academy of Sciences of the United States of America*, vol. 114, no. 33. pp. E6735–E6736, 2017.

[225] D. McMahon, E. Mah, and K. Hynynen, "Angiogenic response of rat hippocampal vasculature to focused ultrasound-mediated increases in blood-brain barrier permeability," *Sci. Rep.*, vol. 8, no. 1, 2018.

[226] D. Mcmahon, R. Bendayan, and K. Hynynen, "Acute effects of focused ultrasound-induced increases in blood-brain barrier permeability on rat microvascular transcriptome," *Sci. Rep.*, vol. 7, 2017.

[227] Z. I. Kovacs, S. R. Burks, and J. A. Frank, "Reply to Silburt et al.: Concerning sterile inflammation following focused ultrasound and microbubbles in the brain," *Proceedings of the National Academy of Sciences of the United States of America*, vol. 114, no. 33. pp. E6737–E6738, 2017.

[228] C. F. Calvo, E. Amigou, M. Tencé, T. Yoshimura, and J. Glowinski, "Albumin stimulates monocyte chemotactic protein-1 expression in rat embryonic mixed brain cells," *J. Neurosci. Res.*, vol. 80, no. 5, pp. 707–714, 2005.

[229] Z. I. Kovacs *et al.*, "MRI and histological evaluation of pulsed focused ultrasound and microbubbles treatment effects in the brain," *Theranostics*, vol. 8, no. 17, pp. 4837–4855, 2018.

[230] D. McMahon, W. Oakden, and K. Hynynen, "Investigating the effects of dexamethasone on blood-brain barrier permeability and inflammatory response following focused ultrasound and microbubble exposure," *Theranostics*, vol. 10, no. 4, pp. 1604–1618, 2020.

[231] L. Biosolutions, "Albumin (ALB)," *Lee Biosolutions products*, 2020. https://www.leebio.com/product/1273/albumin-alb-mouse-serum-101-50 (accessed Feb. 26, 2020).

[232] G. Samiotaki and E. E. Konofagou, "Dependence of the reversibility of focused-ultrasound-induced blood-brain barrier opening on pressure and pulse length in vivo," *IEEE Trans. Ultrason. Ferroelectr. Freq. Control*, vol. 60, no. 11, pp. 2257–2265, 2013.

[233] B. Zhao *et al.*, "Blood-brain barrier disruption induced by diagnostic ultrasound combined with microbubbles in mice," *Oncotarget*, vol. 9, no. 4, pp. 4897–4914, 2018.

[234] S. J. Mooney, K. Shah, S. Yeung, A. Burgess, I. Aubert, and K. Hynynen, "Focused ultrasound-induced neurogenesis requires an increase in blood-brain barrier permeability," *PLoS One*, vol. 11, no. 7, 2016.

[235] S. J. Mooney, J. N. Nobrega, A. J. Levitt, and K. Hynynen, "Antidepressant effects of focused ultrasound induced blood-brain-barrier opening," *Behav. Brain Res.*, vol. 342, pp. 57–61, 2018.

[236] A. Burgess *et al.*, "Alzheimer disease in a mouse model: Mr imaging-guided focused ultrasound targeted to the hippocampus opens the blood-brain barrier and improves pathologic abnormalities and behavior," *Radiology*, vol. 273, no. 3, pp. 736–745, 2014.

[237] N. McDannold, N. Vykhodtseva, S. Raymond, F. A. Jolesz, and K. Hynynen, "MRI-guided targeted blood-brain barrier disruption with focused ultrasound: Histological findings in rabbits," *Ultrasound Med. Biol.*, vol. 31, no. 11, pp. 1527–1537, 2005.

[238] N. McDannold, N. Vykhodtseva, and K. Hynynen, "Effects of Acoustic Parameters and Ultrasound Contrast Agent Dose on Focused-Ultrasound Induced Blood-Brain Barrier Disruption," *Ultrasound Med. Biol.*, vol. 34, no. 6, pp. 930–937, 2008.

[239] S. Sirsi, J. Feshitan, J. Kwan, S. Homma, and M. Borden, "Effect of microbubble size on fundamental mode high frequency ultrasound imaging in mice," *Ultrasound Med. Biol.*, vol. 36, no. 6, pp. 935–948, 2010.

[240] J. Song, J. C. Chappell, M. Qi, E. J. VanGieson, S. Kaul, and R. J. Price, "Influence of injection site, microvascular pressure and ultrasound variables on microbubble-mediated delivery of microspheres to muscle," *J. Am. Coll. Cardiol.*, vol. 39, no. 4, pp. 726–731, 2002.

[241] A. N. Pouliopoulos, S. Bonaccorsi, and J. J. Choi, "Exploiting flow to control the in vitro spatiotemporal distribution of microbubble-seeded acoustic cavitation activity in ultrasound therapy," *Phys. Med. Biol.*, vol. 59, no. 22, pp. 6941–6957, 2014.

[242] A. N. Pouliopoulos, C. Li, M. Tinguely, V. Garbin, M.-X. Tang, and J. J. Choi, "Rapid short-pulse sequences enhance the spatiotemporal uniformity of acoustically driven microbubble activity during flow conditions," *J. Acoust. Soc. Am.*, vol. 140, no. 4, pp. 2469–2480, 2016.

[243] A. N. Pouliopoulos, "Controlling microbubble dynamics in ultrasound therapy," 2017.

[244] C. Lazarus, A. N. Pouliopoulos, M. Tinguely, V. Garbin, and J. J. Choi, "Clustering dynamics of microbubbles exposed to low-pressure 1-MHz ultrasound," *J. Acoust. Soc. Am.*, vol. 142, no. 5, pp. 3135–3146, 2017.

[245] J. J. Choi, R. C. Carlisle, C. Coviello, L. Seymour, and C. C. Coussios, "Non-invasive and real-time passive acoustic mapping of ultrasound-mediated drug delivery," *Phys. Med. Biol.*, vol. 59, no. 17, pp. 4861–4877, 2014.

[246] M. A. O'Reilly, A. C. Waspe, M. Ganguly, and K. Hynynen, "Focused-Ultrasound Disruption of the Blood-Brain Barrier Using Closely-Timed Short Pulses: Influence of Sonication Parameters and Injection Rate," *Ultrasound Med. Biol.*, vol. 37, no. 4, pp. 587–594, 2011.

[247] K. F. Bing, G. P. Howles, Y. Qi, M. L. Palmeri, and K. R. Nightingale, "Blood-Brain Barrier (BBB) Disruption Using a Diagnostic Ultrasound Scanner and Definity® in Mice," *Ultrasound Med. Biol.*, vol. 35, no. 8, pp. 1298–1308, 2009.

[248] K. Hynynen, N. McDannold, H. Martin, F. A. Jolesz, and N. Vykhodtseva, "The threshold for brain damage in rabbits induced by bursts of ultrasound in the presence of an ultrasound contrast agent (Optison®)," *Ultrasound Med. Biol.*, vol. 29, no. 3, pp. 473–481, 2003.

2 | Efficacy and safety of rapid short-pulse sequences for drug delivery

2.1 Background

To improve how molecules are delivered across the blood-brain barrier (BBB) using focused ultrasound and microbubbles, a new rapid short-pulse (RaSP) sequence has been developed. The need to redesign ultrasound sequences has been driven by the undesired effects observed in both preclinical and human studies when emitting conventionally used millisecond-long pulse sequences. These unwanted side effects include an uneven distribution of the delivered agents, prolonged periods of enhanced BBB permeability, the extravasation of red blood cells into the brain as well as other bloodborne substances, such as potentially neurotoxic endogenous proteins.

In long pulse sequences, pulse lengths above 10 ms are normally emitted at a repetition frequency above 1 Hz (Figure 2.1) [1]–[6]. The off-time in between these long pulses is designed to allow the targeted vasculature to be replenished with microbubbles, many of which dissolve or are destroyed during the long pulses. However, this sequence has been associated with tissue damage and other side effects, which are thought to arise due to the production of high magnitudes of inertial cavitation and other bubble activities, such as clustering, coalescence, rectified diffusion and microjetting [7]–[13].

The RaSP sequence, however, is designed to improve both the efficacy and safety of drug delivery with focused ultrasound by stimulating microbubble activity that is less likely to cause disruption to the homeostasis of the brain (Figure 2.1) [13], [14]. It is therefore meant to promote stable cavitation and discourage unnecessarily high magnitudes of inertial cavitation. The aim is to gently stimulate the microbubbles using low pressures and short pulse lengths to reduce bubble destruction, thereby prolonging the lifetime of

the microbubbles so they can act at multiple locations along the vasculature. The pulse-sequence parameters are selected to provide a time interval for the microbubbles to move with the blood flow in between the pulses, reducing the stress exerted at any given capillary site. By allowing each microbubble to gently stimulate the vasculature multiple times as it moves with the blood flow, the increase in BBB permeability is hypothesised to be more widely distributed and the agent delivery to be more homogeneous. Each group of rapidly fired short pulses is termed a burst. Long off-time periods between these bursts are designed to allow the ultrasound focal region to be replenished with new microbubbles.

This RaSP sequence has been designed and tested in previous *in vitro* work [13], [14]. When short pulses were emitted, microbubbles were shown to move more than with long pulses, which supports our hypothesis that microbubbles move in between rapidly fired short pulses. This work also showed that shorter pulse lengths maintained a more uniform distribution of microbubble activity for longer durations with more consistent energy throughout the sonication. These parameters, that showed the most uniform cavitation distribution and the longest lifetime of microbubble activity in these *in vitro* studies, have not yet been tested *in vivo*.

Previous *in vivo* work has shown improved uniformity of delivery by emitting ultrasound in short pulses. However, only low drug doses were achieved and high ultrasound pressures were required [2], [15]–[19]. Moreover, no previous *in vivo* work has made direct comparisons between RaSP and long pulse sequences. There is therefore a need for a thorough assessment of the differences in efficacy and safety between these two sequences. In terms of safety, the brain's immune response following focused ultrasound and microbubble treatment has recently been a topic of debate, due to the beneficial or detrimental consequences that it can have [6], [20]–[26].

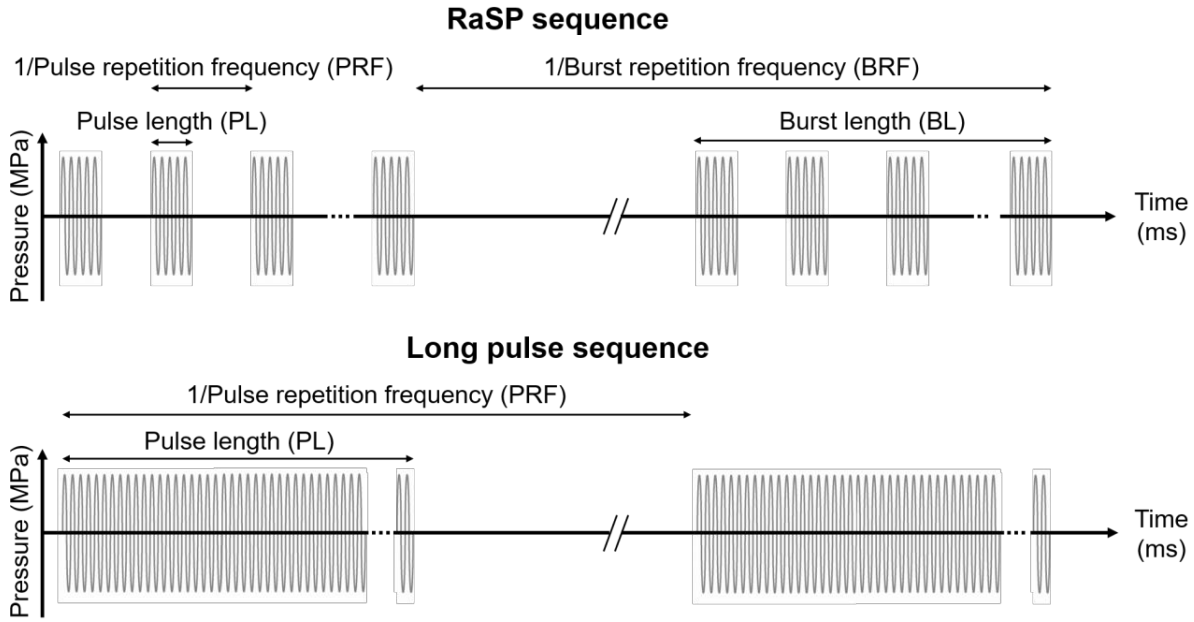

Figure 2.1. Comparison between a rapid short-pulse (RaSP) and long pulse sequence. The RaSP sequence is composed of short, low-energy pulses emitted at a rapid rate and in a slow burst (groups of pulses) sequence. The long pulse sequence is composed of long high-energy pulses emitted at a slow rate.

The brain has always been considered an immune privileged organ, where inflammation only occurs when there is a direct infection or disruption in the BBB, leading to the infiltration of peripheral immune cells into the brain. However, neuroinflammation also occurs in several brain diseases, such as Alzheimer's disease, Parkinson's disease, Huntington's disease and amyotrophic lateral sclerosis. Any pro-inflammatory signals within the brain will divert immune-competent cells from their "housekeeping" functions to instead deal with the abnormal situation. Inflammation in the brain is characterised by the activation of glial cells, including microglia and astrocytes, along with inflammatory mediators within the brain parenchyma and changes in the transcription of genes [27]–[29]. Both microglia and astrocytes, when activated or reactive, undergo changes in their morphology and in their gene and protein expression levels to deal with any abnormal disruption in the brain's homeostasis.

Microglia are the brains' resident immune cells and make up 5-10% of brain cells [30]. Although they are distributed throughout the brain, their density varies depending on the brain region [31]. When no inflammatory stimulus is present, microglia are in a resting surveillance state. They have a ramified phenotype with numerous processes, and are constantly moving and surveying their surrounding area, dynamically reorganising to ensure the maintenance of homeostasis [32]. These processes facilitate the interaction of microglia with neighbouring blood vessels, neurons and astrocytes, all of which are important interactions for neuronal plasticity and cerebral tissue maintenance [33]–[35]. Microglial processes are constantly used to scan for dysfunctional synapses or unwanted debris, which they can then discard via phagocytosis [34], [36]. The physiological functions of microglia are important for maintaining homeostasis within the brain, neuronal integrity and network functioning. Following neurodegeneration, microglial loss or functional deviation can occur, which contributes to disease progression.

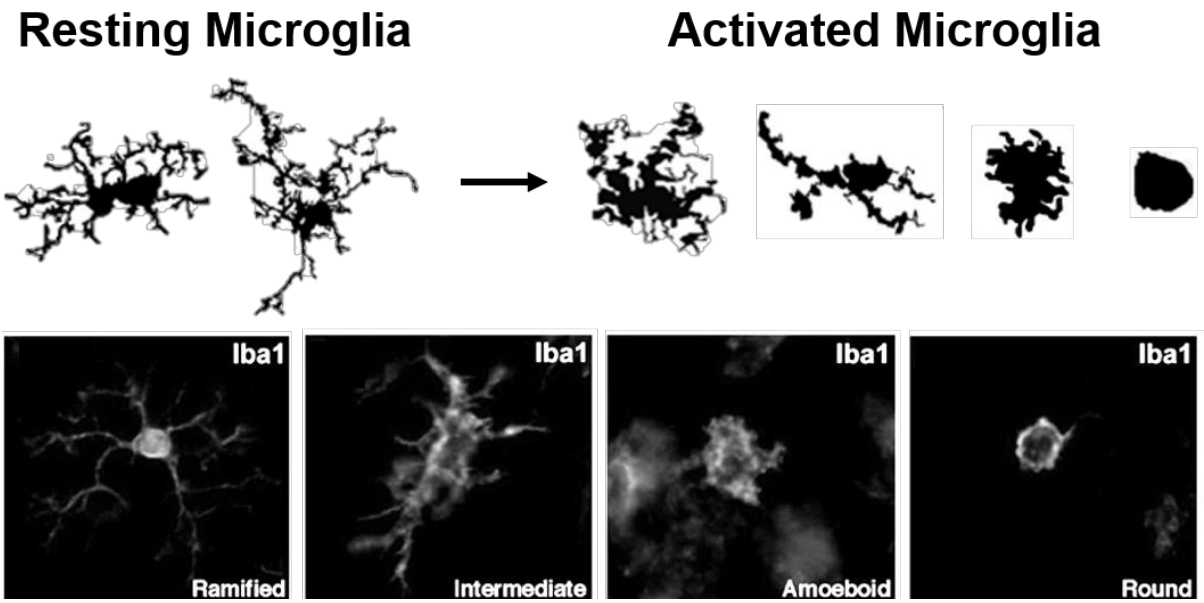

Figure 2.2. Morphology of resting and activated microglia. (Top) Individual microglia are shown in their ramified resting state, in which they survey the surrounding environment. Microglia can rapidly transition into an activated state, where they adopt a more rounded amoeboid-like form, retracting their processes. (Bottom) Fluorescence images of Iba1 (ionised calcium binding

adaptor molecule 1) staining show microglia transitioning from their ramified resting state to a more amoeboid and rounder shape when they are activated. These images were taken from Karperien et al, *Front. Cell. Neurosci.*, 2013, 7:3 and Ekdahl, *Front. Pharmacol.*, 2012, 3, 41 [37], [38].

After an inflammatory stimulus is detected from cytokines or damage-associated molecular patterns (DAMPs), microglia transition from a resting surveillance state to an activated state [39], [40]. An activated state is characterised by microglial processes retracting, resulting in the microglial cell body being rounded and in an ameboid-like shape, with little or no processes (Figure 2.2). Activated microglia are mobile, have a phagocytic role and can promote the release of reactive oxygen species and nitric oxide [41]–[43]. However, if activation is sustained, the continued production of inflammatory mediators can result in chronic inflammation, leading to tissue damage [44], [45]. The sustained exposure of neurons to pro-inflammatory mediators can cause the suppression of axonal transport, leading to neuronal dysfunction and cell death [46], [47].

Other cells in the brain, such as astrocytes, neurons and endothelial cells, can also express innate immune receptors or be activated by them. Many of these cells express receptors for cytokines and inflammatory mediators. Astrocytes are the most common type of glial cell in the brain and have a star-like shape with many processes (Figure 2.3). They have processes that interact with neuronal synapses and those that reach the basement membrane surrounding endothelial cells and pericytes in the brain vasculature are called astrocyte end-feet. Astrocytes have numerous roles within the brain, including maintaining and controlling a healthy brain environment by regulating synapse formation, blood flow and the release of transmitters, and by regulating pH, water and ion homeostasis [48]–[53].

Depending on their location and morphology, astrocytes can be differentiated into protoplasmic and fibrous astrocytes. Protoplasmic astrocytes are found in grey matter and are characterised by many fine branched processes, while fibrous astrocytes are found

in white matter and have long fibre-like processes [50]. Following insult to the brain, astrocytes undergo reactive astrogliosis, where their morphology changes and gene expression is altered (Figure 2.3) [54]–[56]. During this process, astrocytes become hypertrophic and express enhanced levels of glial fibrillary acidic protein (GFAP), an intermediate filament protein found in astrocytes [57]. Astrogliosis can be both protective and harmful. In the protective mode, reactive astrocytes phagocytose debris within the brain [50], which leads to neuroprotection, reconstruction of the BBB and remodelling of brain circuits [58], [59]. Detrimental astrocytes have instead been shown to lead to neuronal loss [54]. Identifying whether microglia and astrocytes undergo changes following focused ultrasound with RaSP and long pulse treatments is therefore of interest.

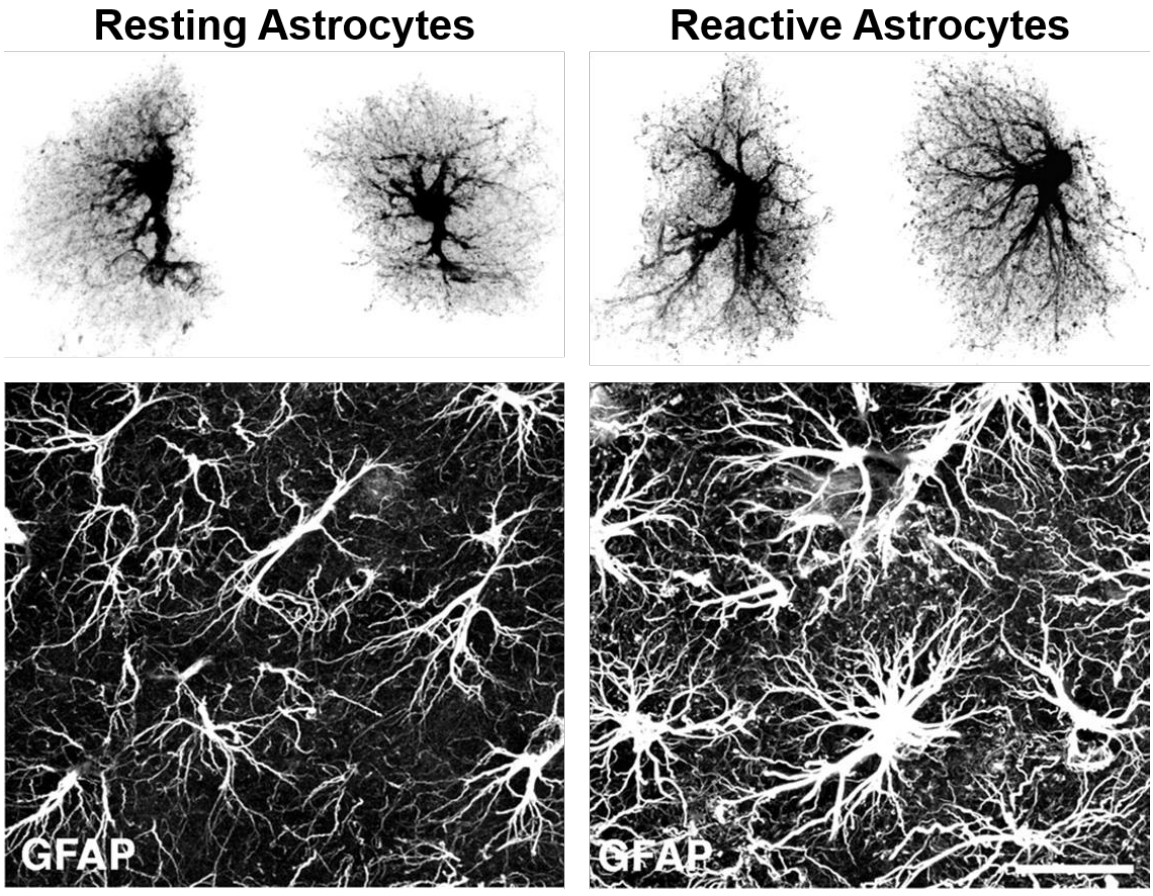

Figure 2.3. Morphology of resting and reactive astrocytes. Resting astrocytes have a star-like shape with many processes; however, when they are reactive, they become hypertrophic and

express increased levels of GFAP (glial fibrillary acidic protein), as shown in the stained sections at the bottom. GFAP is found in reactive astrocytes, but not in all resting astrocytes, and only in the main stem branches, which is why the finer branching processes are not visible. These images were taken from Wilhelmsson et al., *PNAS*, 2006, 103(46):17513-8 (Copyright (2006) National Academy of Sciences, U.S.A.) [55].

Another aspect of safety, following focused ultrasound treatment, is the duration of enhanced BBB permeability. With long pulse sequences, the BBB has been shown to take between 4-48 h to return to normal conditions, depending on the ultrasound parameters chosen and the method used to assess recovery [4], [15], [60], [61]. A prolonged increase in the permeability of the BBB poses important safety questions such as whether the side effects caused by bloodborne substances extravasating into the brain outweigh the benefits of the drug delivery process itself.

Endogenous proteins represent a subset of bloodborne substances that could extravasate into the brain when the BBB permeability is increased. Albumin and immunoglobulin are the most abundant proteins circulating in the bloodstream (accounting for ~ 90% of the total protein pool) and are often used to assess whether the BBB is leaky [62]. Albumin is a 67-kDa protein and immunoglobulin is approximately 150 kDa [63], [64]. Both proteins are not normally found in the brain [65]. In some studies, neurons uptaking albumin have been associated with DNA fragmentation and cell death [66]. Its presence in the brain parenchyma can activate microglia and astrocytes, while inducing the production of chemokines, cytokines and cell adhesion molecules, characteristic of a sterile inflammatory response to injury [67]–[70]. The extravasation of albumin into the brain following focused ultrasound treatment has previously been reported and has been linked to the activation of microglia [25], [71]–[73]. Clearance of albumin after ultrasound has been shown to be mediated by glial cells, with cells that phagocytosed albumin staining positive for Iba1 and being identified as active microglia [71]. In these *in vivo* experiments, astrocytes were also found to phagocytose albumin. Immunoglobulins, much larger

endogenous proteins, have also been found capable of inducing phagocytotic activity in microglia if extravasated into the brain [46]. When investigating the safety of ultrasound sequences, it is therefore of interest to establish whether these proteins are extravasating into the brain and possibly leading to phagocytotic activity in glial cells.

In terms of safety, it is important to assess whether focused ultrasound treatments result in any tissue damage. Haematoxylin and eosin staining (H&E) is normally performed for this purpose, where the brain tissue is assessed for any changes in cell morphology, sites of red blood cell extravasation, neuronal death or microvacuolations. This technique has been used to assess tissue damage in many previous studies following ultrasound treatment, where any observed damage was found to depend on the ultrasound parameters used [8], [11], [12], [74]–[79].

Once a drug or imaging agent has been delivered to the brain, it is important to know how long the agent will stay there, particularly if its properties change due to prolonged exposure inside of the body or if, being present for long period of time, they are toxic to the brain. The excretion pathway of the delivered agent is of particular interest, as the brain does not have a lymphatic system but instead clears proteins and compounds out of the brain via movement of cerebrospinal fluid (CSF) through the parenchyma (Figure 2.4). The CSF enters the parenchyma along the perivascular spaces surrounding the arteries in the brain and is then cleared along perivenous drainage pathways [80], [81]. Evidence of this excretion pathway following ultrasound treatment has recently been shown in humans with Gd-based magnetic resonance contrast agents [80].

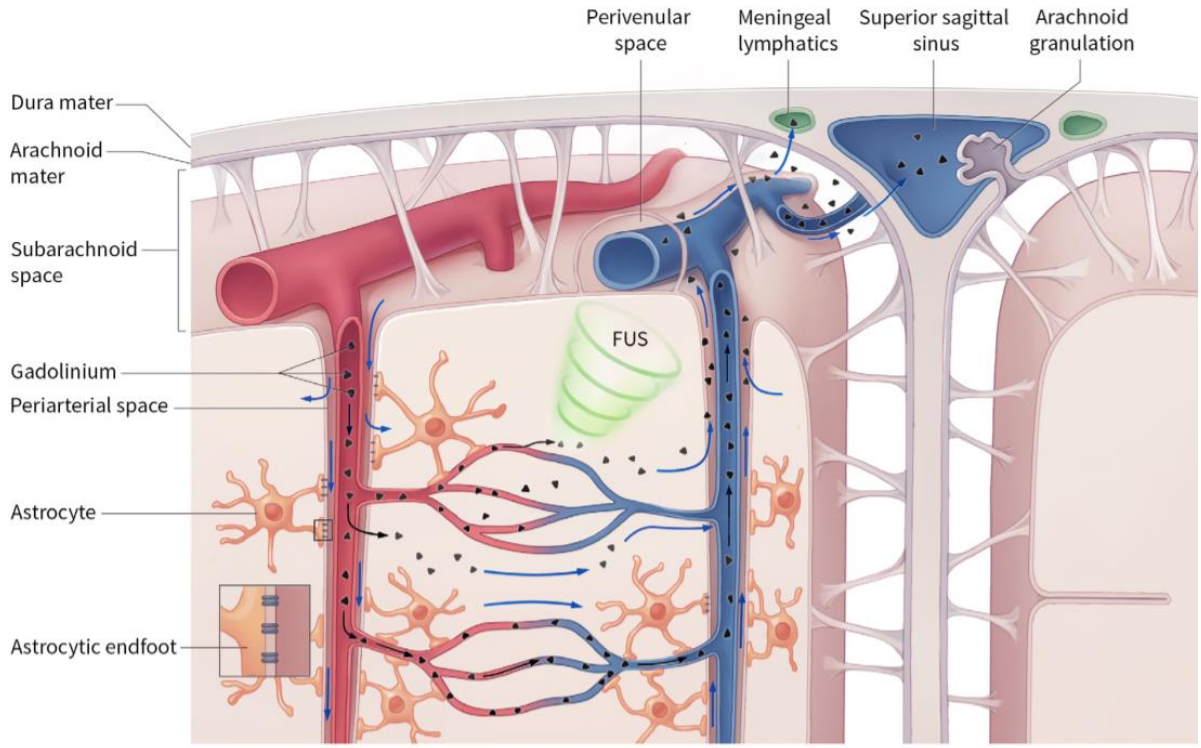

Figure 2.4. Excretion pathway of agents delivered to the brain via focused ultrasound. The enhanced permeability of the blood-brain barrier, induced by focused ultrasound treatment with systemically administered microbubbles, leads to agents entering the brain parenchyma and then being excreted from the brain due to the bulk flow of cerebrospinal fluid (CSF). CSF moves from the perivascular space into the perivenular space (blue arrows). Agents transported by the CSF are then cleared via meningeal lymphatics, subarachnoid CSF and dural sinuses. Image from Meng et al., *Ann. Neurol.*, 2019, 86(6): 975-80 [80].

2.1.1 Evaluating the efficacy of RaSP

In this chapter, two main factors were assessed to evaluate the efficacy of the RaSP sequence *in vivo*: the observed dose and the distribution of the model drug delivered. Since previous work emitting short ultrasound pulses has only been able to deliver low drug doses and has required high ultrasound pressures to be emitted [2], [15], [16], [18], [19], we wanted to see whether, by emitting ultrasound in rapid short pulses, the amount of drug delivered into the brain was significantly lower than with long pulses. Previous *in*

vivo work emitting short pulses has also shown improved uniformity of delivery [17]. We therefore analysed the distribution of the delivered model drug, to prove that we could distribute the drug delivery more uniformly by designing a RaSP sequence that better distributed microbubble activity spatially and temporally.

Once delivered into the brain with focused ultrasound, our model drug - fluorescently-tagged 3-kDa dextran - has been reported to accumulate within neurons [17]. When looking into the distribution of dextran in the brain, we were interested in knowing whether the dextran reached and was taken up by more neurons in RaSP-treated brains than in long-pulse-treated brains, which could be useful depending on the target of the delivered agent. We were also specifically interested in whether dextran was uptaken by glial cells (microglia and astrocytes), as these results could be connected to some of the safety aspects evaluated.

2.1.2 Evaluating the safety of RaSP

To evaluate the safety of the RaSP sequence, we investigated a number of things: whether glial cells were involved in removing our model drug from the brain, the duration of the BBB permeability enhancement, the amount of endogenous proteins extravasating into the brain and any tissue damage.

The brain's immune response following focused ultrasound treatment has been a recent topic of debate, due to its beneficial and detrimental consequences [6], [20]–[26]. We therefore analysed whether microglia and astrocytes were involved in the phagocytosis of our model drug and whether they displayed any obvious signs of activation or reactivity.

The duration of enhanced permeability of the BBB was also investigated, in addition to the amount of endogenous proteins extravasating into the brain during this period of increased BBB permeability. The extravasation of immunoglobulins, as well as albumin,

was investigated, as their size is much larger than our 3 kDa model drug and could therefore indicate whether drugs the size of antibodies would be able to cross the BBB. Ideally, we want the amount of albumin and immunoglobulin entering the brain to be minimised, and, if present, for their clearance to be rapid to prevent any associated neuronal cell death.

To assess whether the focused ultrasound treatments resulted in any tissue damage, haematoxylin and eosin staining (H&E) was performed. Brain tissue was assessed for any changes in cell morphology, sites of red blood cell extravasation, neuronal death or microvacuolations. Here, we were interested in seeing whether by using such short low pressure closely spaced pulses, tissue damage could be avoided. The excretion pathway of dextran, together with how quickly it was removed from the brain, were also investigated.

Lastly, when delivering agents to the brain with this technology, to provide an efficient and safe delivery method, monitoring systems need to be in place to help predict where the agents are being delivered and if any adverse effects have occurred. Here, the microbubble's acoustic emissions were acquired and processed in order to see whether the extent of drug delivery observed could be predicted based on the magnitude of such acoustic emissions.

2.1.3 Evaluating the hypothesis behind the design of the rapid short-pulse sequence

The final part of this chapter is dedicated to evaluating whether our hypothesis behind the design of the RaSP sequence is linked to the improved efficacy and safety results observed *in vivo*. To do so, a passive cavitation detector (PCD) was used to record the acoustic emissions from the oscillating microbubbles during the ultrasound exposure, which can be used for real-time monitoring [82]–[86]. This is a passive technique as bubble activity can be monitored without interfering with the emitted therapeutic pulses.

Firstly, we evaluated whether the acoustic emissions from the microbubbles had a prolonged lifetime as hypothesised. The distribution of these emissions was evaluated across the entire sonication and within single bursts of the RaSP sequence. The magnitude of these acoustic emissions has been shown in previous *in vitro* work to decrease more rapidly during long pulse sequence exposure compared with exposure to RaSP, which displayed more prolonged cavitation activity [13], [14]. This rapid decrease with long pulses has also been observed *in vivo* [87], [88]. We aimed to evaluate whether prolonged bubble activity could be maintained *in vivo* under sonication with the RaSP sequence.

Secondly, we evaluated whether potential bubble activity associated with tissue damage could be avoided using the RaSP sequence. The type of microbubble activity during long and RaSP sonications in the brain were differentiated by analysing the frequency content of the bubble emissions. Studies have linked the occurrence of broadband emissions, believed to have resulted from inertial cavitation, to tissue damage [5], [7]–[9], [12]. On the other hand, the detection of subharmonics and ultraharmonics has been linked to a safer and more predictable BBB permeability enhancement [79], [89]–[94]. Here, we investigated whether different emissions were observed when sonicating with the two sequences.

2.2 Aims and objectives

The overall aim of the work presented in this chapter was to investigate the efficacy and safety of drug delivery *in vivo* when emitting focused ultrasound in a rapid short-pulse sequence. In terms of efficacy, the ultrasound pressure required to deliver our model drug into the brain with our ultrasound setup was first identified by emitting a conventional long pulse sequence. The uniformity of the drug distribution was then investigated by emitting a RaSP sequence, while comparing the amount of delivered drug with that achieved with long pulses. We then assessed where the model drug was delivered within

the brain and in which cells. Whether glial cells were phagocytosing the model drug and being activated was also investigated. In terms of safety, we first determined the duration of the blood-brain barrier permeability enhancement. We then investigated the amount of albumin and immunoglobulin proteins extravasating into the brain with both sequences. Thirdly, we assessed whether any tissue damage was present within the brain, and determined how long the model drug remained within the brain and how it was then excreted. After that, we established whether the extent of drug delivery could be predicted from the microbubble's acoustic emissions. Lastly, we established whether the lifetime of microbubble emissions increased with a RaSP emission and whether unnecessary broadband emissions from inertial cavitation were avoided.

2.3 Materials and methods

This section describes the experiments carried out to evaluate efficacy and safety aspects when emitting ultrasound in a RaSP sequence. A model drug was delivered into the mouse brain by emitting ultrasound in a RaSP or long pulse sequence. Brain tissue was collected to determine the detected amount and distribution of the model drug, and the tissue's state. Immunohistological staining and image processing was performed on these samples to determine whether glial cells were involved in removing the drug from the brain, whether endogenous proteins were entering the brain and if any tissue damage could be observed. Analysis on the acoustic emissions received from the microbubbles was carried out to verify *in vivo* some of the hypotheses on which the design of the RaSP sequence was based.

2.3.1 Pulse sequence parameters

Focused ultrasound was emitted in either a rapid short-pulse ultrasound sequence or a conventionally used long pulse sequence (Figure 2.5; Table 2.1). In the rapid short-pulse sequence, short 5 cycle pulses were emitted at a rapid pulse repetition frequency of 1.25

kHz. Thirteen of these short pulses were grouped into bursts with a total duration of 10 ms. These bursts were emitted at a slow burst repetition frequency of 0.5 Hz. In the long pulse sequence, long pulses of 10,000 cycles were emitted at a slow pulse repetition frequency of 0.5 Hz. The duty cycle, known as the ratio of the ultrasound on-time to the total time, was calculated to be 0.0000025% for the RaSP sequence and 0.005% for the long pulse sequence. Depending on the experiment, all pulses described above were emitted at peak-negative pressures of 0.18, 0.35 or 0.53 $MPa_{pk\text{-}neg}$. For both sequences, 125 pulses or bursts were emitted (all parameters are summarised in Table 2.1).

The parameters of the long pulse sequence were selected based on what is conventionally used in the literature [1]–[6]. The rapid short-pulse sequence parameters were chosen based on previous *in vitro* work by Dr Pouliopoulos (former PhD student, NSB Lab) [95]. A pulse length of 5 cycles and pulse repetition frequency of 1.25 kHz were selected as they were found *in vitro,* to maintain a more uniform spatial and temporal cavitation distribution for longer durations, with a more consistent total energy throughout the duration of the treatment [13], [14]. The acoustic pressure, burst length and burst repetition frequency were kept the same as the long pulse sequence so that we could directly compare how emitting many short pulses, instead of a long pulse, would influence the observed drug delivery. For both sequences, 125 bursts were emitted, extending over a duration of 4.2 minutes. This duration was chosen to cover the lifetime of the microbubbles *in vivo*, as 80% of circulating SonoVue microbubbles are cleared from the vasculature within 2-4 min [96], [97]. The overall energy of the RaSP sequence was 150 times lower than that emitted from the long pulse sequence.

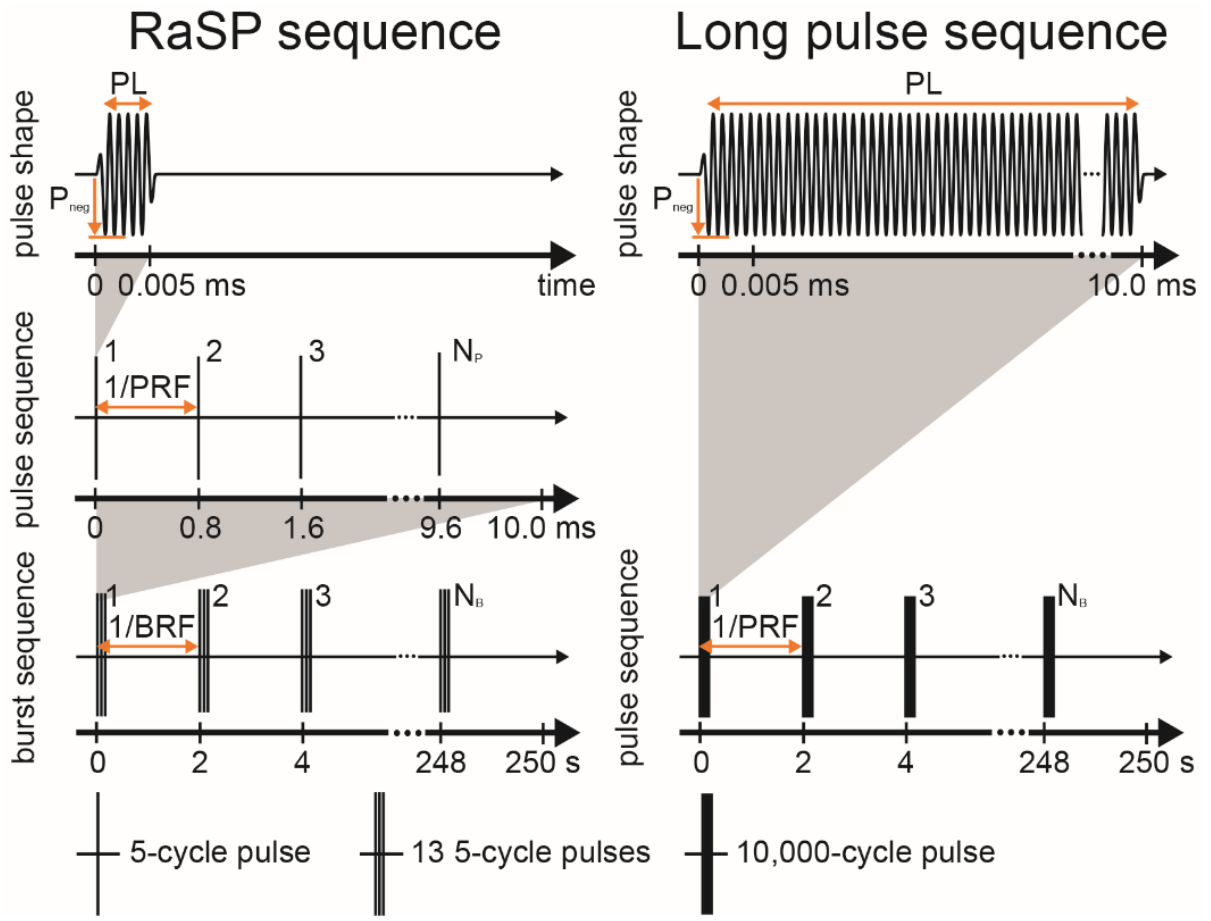

Figure 2.5. Structure of rapid short-pulse (RaSP) and long pulse sequences. The RaSP sequence involved emitting thirteen short (5 cycle) pulses in a rapid succession (1.25 kHz), which were then grouped into bursts (10 ms) emitted at a slow rate (0.5 Hz). The long pulse sequence involved emitting long (10,000 cycle) pulses at a slow rate (0.5 Hz). The ultrasound was turned off between bursts of short pulses and long pulses to allow microbubbles to replenish the targeted ultrasound area. With RaSP, 150 times less energy was emitted overall compared to the long pulse sequence. Image taken from Morse et al, *Radiology*, 2019, 291:459-466.

Table 2.1. Ultrasound exposure parameters. The ultrasound parameters used for RaSP and long pulse sequences are shown here, both those related to the pulse shape and to the sequence of emitted pulses/bursts. The mechanical index (MI) shown was calculated for the 0.35 MPa pressure.

Sequence type		Symbol	Parameter	Value/Units
Long pulse sequence	Pulse shape	f_C	Centre frequency	1 MHz
		PL	Pulse length	10,000 cycles
		$P_{pk\text{-}neg}$	Peak-negative pressure	0.18, 0.35, 0.53 MPa
	Pulse sequence	PRF	Pulse repetition frequency	0.5 Hz
		N_B	Number of pulses	125
Rapid Short-Pulse (RaSP) sequence	Pulse shape	f_C	Centre frequency	1 MHz
		PL	Pulse length	5 cycles
		$P_{pk\text{-}neg}$	Peak-negative pressure	0.35 MPa
	Pulse sequence	PRF	Pulse repetition frequency	1.25 kHz
		BL	Burst length	10 ms
		BRF	Burst repetition frequency	0.5 Hz
		N_B	Number of bursts	125
Both		MI	Mechanical Index	0.35

2.3.2 Ultrasound setup

All *in vivo* ultrasound experiments were performed using a benchtop system (Figure 2.6; Appendix Figure 6.1). Therapeutic ultrasound pulses were emitted from a single element spherical-segment focused ultrasound transducer (centre frequency: 1 MHz; active diameter: 90 mm; focal depth: 60.5 mm; part number: H-198; Sonic Concepts, Bothell, WA, USA). The acoustic field generated by this transducer was calibrated using a 0.2 mm polyvinylidene difluoride (PVDF) needle hydrophone (Precision Acoustics, Dorchester, England) in a degassed water tank. Calibration results showed that the ultrasound beam had an elevational diameter of 1 mm, lateral diameter of 2 mm and an axial length of 20 mm, defined by the full-width at half maximum (FWHM) of the peak-rarefactional pressure (Appendix Figure 6.2). The acoustic pressures reported in this thesis are derated

using an 11% attenuation (11.2 ± 3.2 %), which was measured experimentally by placing the top layer of a mouse skull (n = 4) between the transducer and the focal point, where a hydrophone was placed. The attenuation value was calculated as the percent decrease in the peak-rarefactional pressure at the focal point before and after the skull was placed between the transducer and the hydrophone.

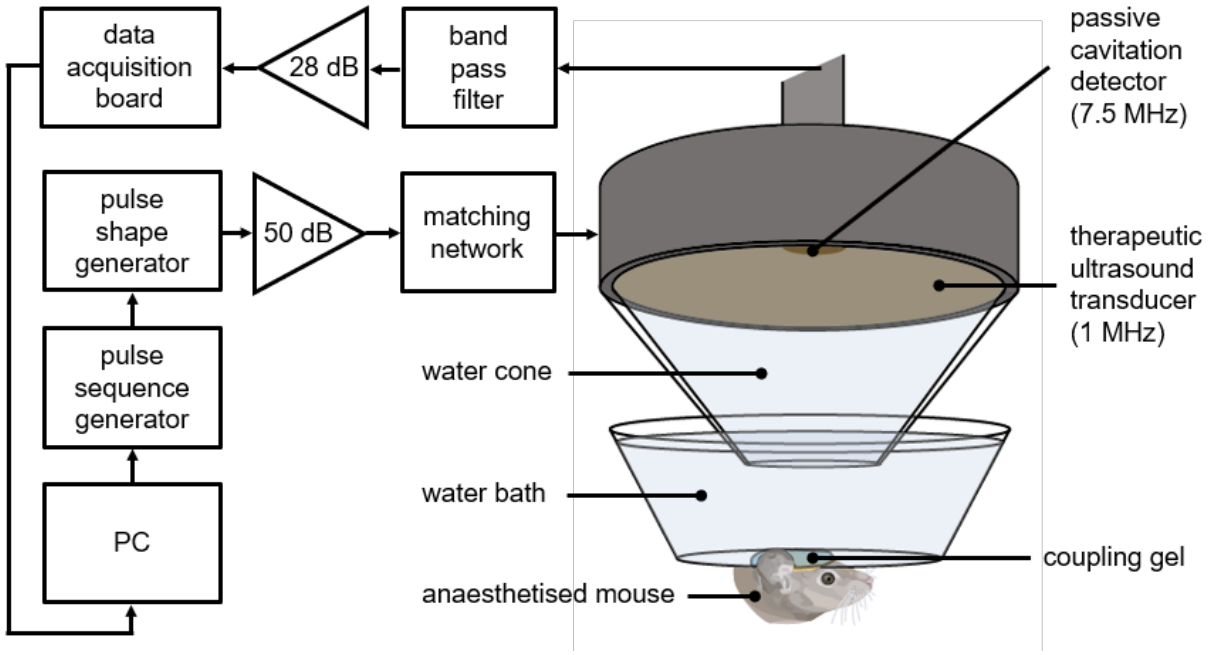

Figure 2.6. Ultrasound experimental setup. The left hippocampus of mice was exposed to 1 MHz focused ultrasound emitted in a rapid short-pulse (RaSP) or long pulse sequence, while the right hippocampus was used as a control. Ultrasound was applied through an intact scalp and skull with the pulse sequences being generated by function generators, passed through a 50-dB power amplifier and a matching network before being emitted by the therapeutic transducer. Acoustic emissions from the microbubbles were captured by a 7.5 MHz passive cavitation detector, passed through a band pass filter and a 28-dB pre-amplifier, before being captured by the data acquisition board. PC = personal computer. Image taken from Morse et al, *Radiology*, 2019, 291:459-466.

The transducer was driven by one or two function generators (33500B Series; Agilent Technologies, Santa Clara, CA, USA), through a 50-dB power amplifier (2100L Electronics

and Innovation, Rochester, NY) and an impedance matching box (Sonic Concepts, WA, USA). For the rapid short-pulse sequence, two function generators were used in order to define the pulse shape and the pulse sequence. Only one function generator was needed for the long pulse sequence. The case surrounding the transducer was mounted onto a programmable three-dimensional positioning system (Velmex, Bloomfield, NY, USA) allowing the transducer to be moved to the target location with as low as 5 μm step sizes in all three dimensions. The entire system was controlled on Matlab using a graphical user interface (GUI) written by Dr Pouliopoulos and modified by M. Copping (PhD students, NSB Lab, see Appendix Figure 6.3).

To monitor the microbubble activity during the ultrasound treatment, a 7.5 MHz spherically-focused passive cavitation detector (PCD; part number: U8423539; diameter: 12.7 mm, focal length: 76.2 mm; Olympus Industrial, Essex, UK) was positioned inside of a 3D-printed case and placed through the rectangular central opening of the therapeutic transducer with the foci overlapping. The acoustic emissions were captured by the PCD and filtered by a 3-30 MHz band-pass filter (part number: ZABP-16+; Mini Circuits, Brooklyn, NY, USA), thus removing the large contribution of the fundamental frequency and avoiding saturation of the signal. The filtered signal was amplified by a 28-dB pre-amplifier (Stanford Research Systems, Sunnyvale, CA, USA), which was then recorded by an 8-bit oscilloscope (PicoScope 3205A; Pico Technology, Cambridge, UK) at a 250 MS/s sampling rate. Time domain traces were displayed in real-time and were also saved for off-line processing.

To allow the ultrasound to propagate into the mouse's head, the transducer casing had a cone attached, which was filled with distilled water and covered with an acoustically transparent parafilm membrane. After placing the mouse head in a stereotaxic frame (45° ear bars; World Precision Instruments, Hertfordshire, UK), a second water bath, covered by transparent parafilm filled with degassed water, was coupled to the shaved mouse's

head with ultrasound coupling gel. This coupling allowed the acoustic impedances to be matched, enabling the ultrasound to propagate without significant attenuation or distortion into the mouse brain. The ultrasound gel was centrifuged to reduce the likelihood of air bubbles forming. Finally, the cone attached to the transducer was lowered into the second water bath to target the region of interest.

2.3.3 Targeting

The left hippocampus of the mouse brain was targeted in all *in vivo* ultrasound experiments. The hippocampus is a region of the brain that has a fundamental role in some forms of learning and memory and has been implicated in many disorders ranging from Alzheimer's to depression and schizophrenia [98], [99]. This region was chosen as our target due to the low attenuation of the parietal bone, its distinctive and readily identifiable structure and its potential use as a therapeutic target. This choice also allowed us to use the opposite right hippocampus as a non-sonicated control.

A previously reported protocol was used to target the hippocampus [1], which involved removing the fur from the mouse's head, placing the ultrasound gel and the water bath on top and then aligning a metal cross (Appendix Figure 6.4) with the lambdoidal and sagittal sutures of the mouse's skull (Figure 2.7 A). These sutures are normally visible through the intact skin of the head and are located at defined distances from the hippocampus. Using the three-dimensional positioning system, the transducer was placed roughly above the grid and a 10 mm x 10 mm raster scan was performed using a pulser-receiver (Figure 2.7 B; 0.5 mm resolution; DPR300; Insidix, Seyssins, France) and the therapeutic transducer in pulse-echo mode (Appendix Figure 6.5). The trigger delay and length of acquisition were adjusted to see the reflections from the metal grid, based on its expected position. Based on the amplitude of the reflections recorded by the PicoScope, the metal grid was identified by integrating the squared time-domain signals within specified time intervals for each position in the raster scan. Adjusting the limits of

the integration window (start and end time points) allowed us to delineate the metal grid (Figure 2.7 B). By using the centre of the cross in the raster scan as a reference point, the transducer was moved 3 mm lateral of the sagittal suture and 0.5 mm anterior of the lambdoid suture onto the left hippocampus. The depth of the focus was adjusted using pulse-echo to be approximately 3 mm beneath the top of the skull, which is where the centre of the hippocampus is approximately located.

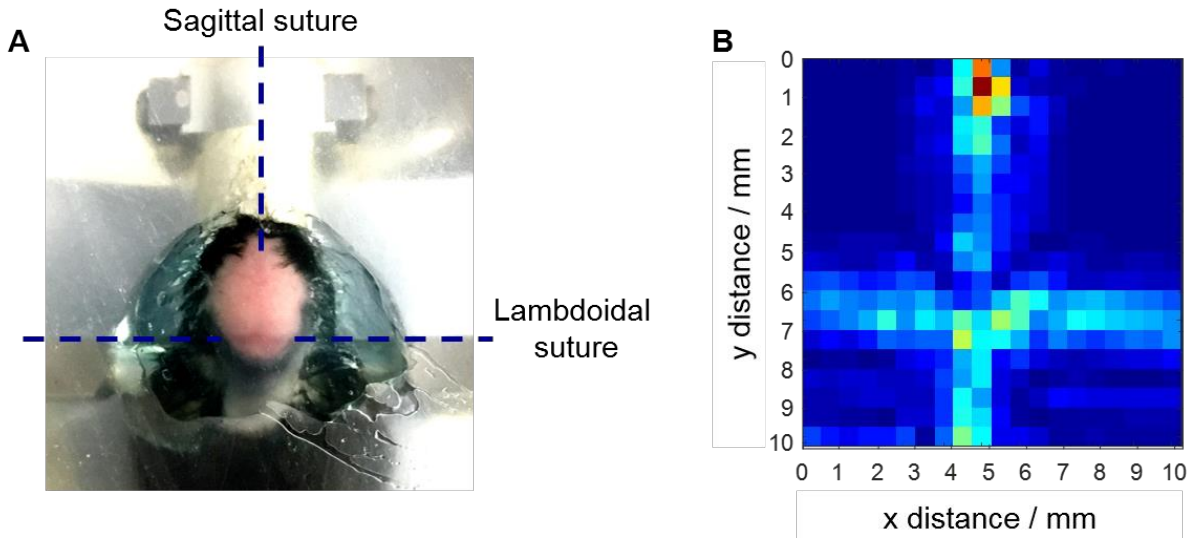

Figure 2.7. Sutures of the mouse skull and example raster scan. (A) View of the mouse from above with lambdoid and sagittal sutures visible through the intact scalp. These sutures were used to target the left hippocampus by placing a metal cross in alignment with them. **(B)** Example of a raster scan of the metal grid, generated using the therapeutic transducer in pulse-echo mode. High intensity regions (yellow and red) correspond to stronger echoes due to the ultrasound bouncing off the metal grid.

To achieve the above protocol, however, many modifications were made as initial attempts were unsuccessful at targeting the desired hippocampus region consistently. The two main issues were the sutures not being visible through the scalp and the metal cross not being clearly visible on the raster scan. These issues were solved by testing different methods, which are summarised in the table below with the respective solutions found (Table 2.2 and Appendix Figures 6.6-6.7).

Table 2.2 Targeting issues. The main problems encountered, the methods attempted to solve such issues and the final solution are listed. More information can be found in the Appendix Figures 6.6-6.7.

Problem		Things tried	Solution
Sutures not visible:	through black skin	Different ages of mice	Ordering older mice
	through pink skin	Different lights to highlight sutures	Making sure skin is tight
Cross not visible:	rod not flat	Designed different types of crosses	Flat rod design
	water bath not flat	Aligned it flat	Aligned for each mouse
	side lobes creating non existent rods	Adjusting position of transducer, 3rd harmonic pulse-echo, cross in diagonal position	Adjusting position of transducer
	grid not reflecting enough	Designed crosses of different materials	Stainless steel flat cross

Lastly, the original targeting protocol involved moving 2.5 mm lateral of the sagittal suture and 2 mm anterior of the lambdoid suture [1]. However, due to the different setup and cross, these values were changed to 3 mm left and 0.5 mm distal from the centre of the cross visible on the raster scan, which allowed reliable targeting of the left hippocampus (Figure 2.8).

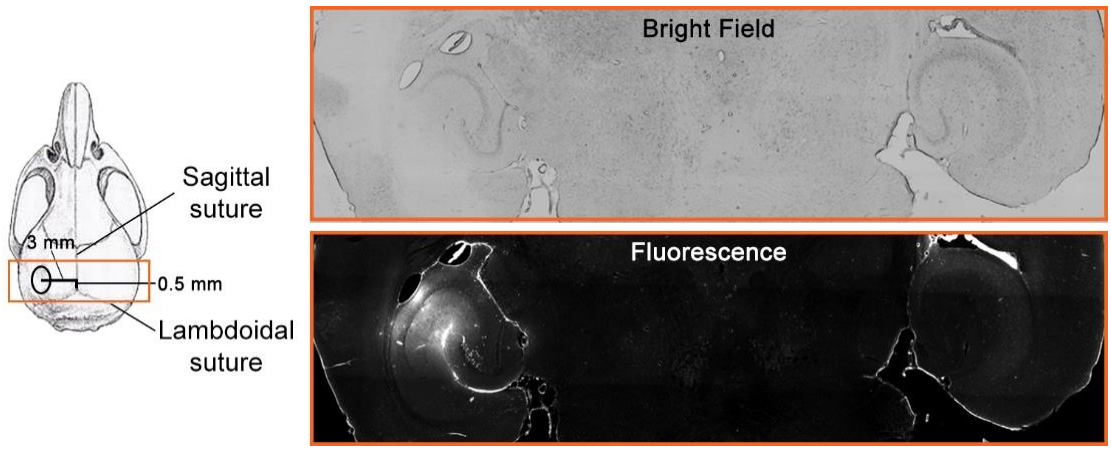

Figure 2.8. Ultrasound targeting. The left targeted hippocampus is highlighted in reference to the skull sutures (black circle): 0.5 mm anterior to the lambdoid suture and 3 mm lateral to the sagittal suture. Bright field and fluorescence images of the left targeted and right control hippocampi region (orange rectangle) show where the ultrasound was targeted. High intensity regions correspond to areas of drug delivery. The edges of the brain slices and ventricles also

appear bright as the drug flows within the cerebrospinal fluid in the subarachnoid space and ventricles. Image taken from Morse et al, *Radiology*, 2019, 291:459-466.

2.3.4 Animals

All animal experiments were performed in approval with the UK Home Office and Imperial College London's animal facility committee. Fifty-five female C57bl/6 wild-type mice (8-12 weeks old, 20.7 g ± 1.2; Envigo, Huntingdon, UK) were used in this study. A range of different experiments were performed with these mice and are summarised in Table 2.3. All animals were kept in standard conditions and followed a normal diet.

Table 2.3 Summary of mice used in each experiment. The name of each experiment group is shown with the number of mice used, explaining the breakdown of what these mice were used for with the specific sequence type. When the same mice were used for multiple investigations, a note was made in the explanation section.

Study	Number of mice	Explanation	Pulse sequence type
Pressure threshold	9	3x at 0.18 MPa 3x at 0.35 MPa 3x at 0.53 MPa	ms-long
RaSP vs ms-long	10	5x with ms-long pulse sequence (3x used in pressure threshold)	ms- long
		5x with RaSP sequence	RaSP
BBB closing	22	10x with 0 min wait (used in RaSP vs ms-long)	RaSP and ms-long
		6x with 10 min wait	RaSP and ms-long
		6x with 20 min wait	RaSP and ms-long
Brains with recovery	18	6x with 2 h wait	RaSP and ms-long
		6x with 24 h wait	RaSP and ms-long
		6x with 48 h wait	RaSP and ms-long
Tissue damage assessment	6	3x with ms-long	ms-long
		3x with RaSP	RaSP
Control	3	3x Control brains	None
Total:	**55**		

Nine mice were used to investigate the pressure needed to deliver our model drug into the brain with long pulses. For this pressure threshold experiment, three different pressures were tested: 0.18, 0.35 and 0.53 MPa (n = 3 for each pressure).

Ten mice were then used to compare the efficacy and safety of the RaSP sequence with that of the long pulse sequence at 0.35 MPa (n = 5 for each sequence type; three of the long sequence treated mice were ones used in the pressure threshold experiment at 0.35 MPa).

To investigate safety, the duration of increased BBB permeability was investigated using 22 mice: ten mice at 0 min (n = 5 for each sequence type), six at 10 min and six at 20 min (n = 3 for each sequence type). The extent of albumin and immunoglobulin extravasation was also evaluated in these mice.

Additional experiments with different recovery times were performed to explore the glial cell response and excretion of the model drug from the brain over time (n = 6 with 2 h wait, n = 6 with 24 h wait and n = 6 with 48 h wait; half with RaSP and the other half with the long pulse sequence).

To assess damage, six mice were treated at 0.35 MPa to perform haematoxylin and eosin (H&E) staining on the brain slices (n = 3 with RaSP and n = 3 with long pulse sequence).

Two controls were used in this study: mice unexposed to ultrasound (n = 3) and in all mice, the right hippocampus, which was unexposed to ultrasound. By using all animals as their own control, variabilities caused by physiological differences amongst animals were reduced. All sample sizes were chosen based on power analysis [100]; we established that when comparing two or more groups (e.g., dose and distribution quantifications), a sample size of n = 5 was required for 80% power (for alpha 0.05).

2.3.5 Dextran and microbubbles

A lysine-fixable Texas Red 3 kDa dextran (hydrodynamic diameter ~ 2-3 nm [3], [101]; Life Technologies, Paisley, UK) was chosen as our model drug due to its size, its biological and chemical inertness, and its prevalence in focused ultrasound-mediated BBB opening studies [3], [11], [17], [102], [103]. Molecules of this molecular weight tend to be impermeable to the BBB, being above the 400-600 Da threshold [104], and are thus not expected to be present in non-sonicated regions of the brain. The Texas Red fluorophore attached allows its location to be detected *ex vivo* with fluorescence microscopy. A dextran concentration of 100 µg/g of body mass was used for all experiments except for the 2, 24 and 48 h waiting brains, where a concentration of 30 µg/g of body mass was used to save resources. These dextran concentrations are in a similar range to those used in the literature: 50-100 µg/g of body mass [11], [17], [105], [106]. The dextran (0.6 mg or 2 mg) was diluted in 100 µL of phosphate-buffered saline and injected intravenously.

SonoVue (Bracco, Milan, Italy) microbubbles were injected before the dextran (concentration: 5 µl/g of body mass, volume: 100 µL, mean diameter: 2.5 µm [107], vial concentration: $3x10^8$/mL). As a reference, the clinically recommended dose of SonoVue for ultrasound imaging applications is 0.030 µl/g [108]. The concentration used here was chosen, despite it being higher than the clinical dose, as we are investigating the use of these microbubbles for therapeutic, rather than diagnostic applications. A 30-gauge home-made catheter was used for the tail vein injection and the microbubbles were injected over the course of 30 seconds. Microbubbles were injected ten seconds into the sonication to allow the first five pulses/bursts (one every two seconds) to be used as control pulses/bursts. A fresh vial of microbubbles was activated on each day of experiments and used within six hours from activation, following the manufacturer's instructions.

2.3.6 Experimental workflow

The experimental workflow followed is shown in Figure 2.9. Mice were first anesthetised in an induction chamber for five minutes with 4% vaporised isoflurane (Zoetis, London, UK) mixed with oxygen (1 L/min) by using an anaesthesia vaporiser (Harvard Apparatus, Cambridge, UK). They were then transferred to a nose cone, so that the fur could be removed from the head using an electric razor and depilatory cream. This allowed the skull sutures to be visualised through the skin and avoided air bubbles getting trapped in between the fur when applying the ultrasound gel to the head. The skin was kept intact. The mice were then transferred to the stereotaxic frame, the head was fixed with ear bars, and the isoflurane was kept between 1 and 2%, continuously monitoring the breathing rate and vital signs throughout the experiment. Ultrasound gel was applied on top of the head to allow ultrasound to propagate and the water bath was lowered onto the gel, making sure it laid flat. The metal cross was then positioned in alignment with the skull sutures as described in the targeting section (2.3.3). The transducer was moved to target the left hippocampus using the raster scan as a reference, keeping the right hippocampus as a control. At this point, the ultrasound beam was in position to target the hippocampus of interest within the brain.

Once the catheter was inserted into the tail vein, twenty ultrasound pulses were applied without injecting microbubbles. The dextran was then injected intravenously, and the brain was sonicated with 125 pulses or bursts, depending on the sequence type (Table 2.1). Five control pulses were emitted before the injection of the SonoVue microbubbles. We kept the dextran and microbubble injections separate because we found that co-injection lowered the microbubble signal received by the PCD.

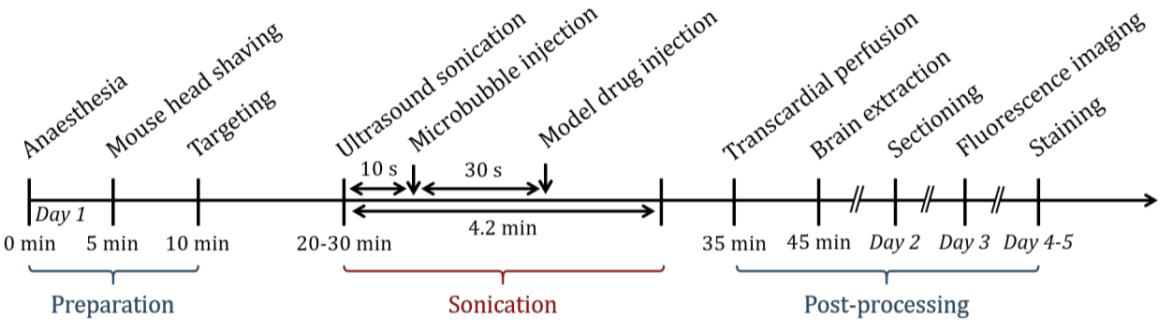

Figure 2.9. Experimental workflow for *in vivo* experiments. Mice were first anaesthetised, the head was shaved, the left hippocampus was targeted with the transducer and then the catheter was placed in the tail vein. The ultrasound sonication started and then the microbubbles were injected, followed by the model drug. Mice were then transcardially perfused and the brain was extracted. Brains were then sectioned, imaged with fluorescence microscopy and stained.

Following the sonication, an overdose of pentobarbital was administered intraperitoneally (0.1 mL) and the mice were transcardially perfused with 20 mL ice cold phosphate-buffered saline with added heparin (20 units/mL; Sigma Aldrich, St Louis, MO, USA) to clear the vessels of blood. Ice-cold 10% formalin solution (Sigma Aldrich) was then circulated in the vasculature to fix the tissue. The perfusion rate was controlled by using a peristaltic pump at approximately 5 mL/min. The brain was carefully extracted and placed in 10 mL of 10% formalin overnight and then in 15% sucrose for 6 h and 30% sucrose overnight to cryoprotect the tissue before cryosectioning. Sucrose is a dehydrant, which helps preserve cellular morphology by preventing ice crystals from forming during the freezing process. Brains used for H&E staining were instead kept in formalin until prepared for paraffin-embedding to section using a microtome.

2.3.7 Histological staining

All brains were cryosectioned, except for those stained with H&E; these were paraffin embedded, a procedure which preserves tissue morphology better and was therefore used to assess tissue damage. However, paraffin embedding is a process that quenches

fluorescence signals during embedding and masks antigens (to which antibodies bind) due to protein cross-linking following prolonged exposure in a fixative [109]. Therefore, it is not suitable for fluorescence microscopy detection or for immunohistochemical staining.

For cryosectioning (protocol in Appendix Table 6.1), brains were embedded in optimal cutting temperature (OCT; Agar Scientific, Stansted, UK) which when frozen, has the same density as frozen tissue. The sample was snap-frozen by placing it in a bath of isopentane and dry ice for five minutes and was then sectioned into 30 µm horizontal slices using a cryostat (CryoStar NX70; Thermo Fisher, Waltham, MA, USA) set at -12 to - 14 °C. Initially, 1.5 mm was trimmed from the bottom of the OCT embedded brain and then sixty 30 µm slices were cut to cover the entire hippocampus. Brain slices were collected on positively charged slides (Superfrost^{TM} Ultra Plus Adhesion Slides, Thermo Fisher) and stored in the dark at 4 °C until they were imaged.

Immunostaining was performed to detect albumin, immunoglobulin, neurons, microglia and astrocytes (3-4 slices of each brain for each stain). Immunohistochemical staining methods can be either direct or indirect (Figure 2.10 A). The direct method involves a single antibody which binds to the antigen of interest and is labelled with a fluorophore. This method is quick, but it lacks sensitivity, resulting in a lower fluorescence signal. The indirect method, however, involves two antibodies: an unlabelled primary antibody that binds to the antigen and a labelled secondary antibody, raised against the primary antibody, that is used for detection. This technique achieves higher signal intensities as more than one secondary antibody can bind to the primary [110]. An indirect method was used for all protocols, except when staining for immunoglobulin, as samples with endogenous immunoglobulin can result in high background signal when using indirect methods.

The general steps of indirect immunostaining protocols are antigen retrieval (if necessary), permeabilisation, blocking, primary antibody labelling, washing, secondary antibody labelling, washing and then imaging (Figure 2.10 B). Antigen retrieval takes place after the tissue has been fixed and cut, and involves heating the tissue to unmask epitopes, which are regions of the antigen that bind to antibodies [110]. This unmasking is sometimes necessary, as the process of fixation involves the formation of addition products between the formalin (fixative) and reactive amino groups in the tissue. This allows cross-links to form, which can make it difficult for antibodies to reach the antigens.

The second or first step, depending on the protocol, involves permeabilising the tissue. This step allows antibodies to pass through cellular membranes to reach the antigens. Triton X-100 was used for this as it is a detergent that permeabilises all lipid bilayers by solubilising the cell membranes, including the nuclear membrane where some antigens are present. Depending on the location of the target antigen, this step can be omitted; however, in all stains used in this study, a permeabilisation step was needed as all targets were intracellular. This step was also performed when staining for extravasated albumin and immunoglobulin to detect these proteins not only in the extracellular matrix, but also when taken up by cells.

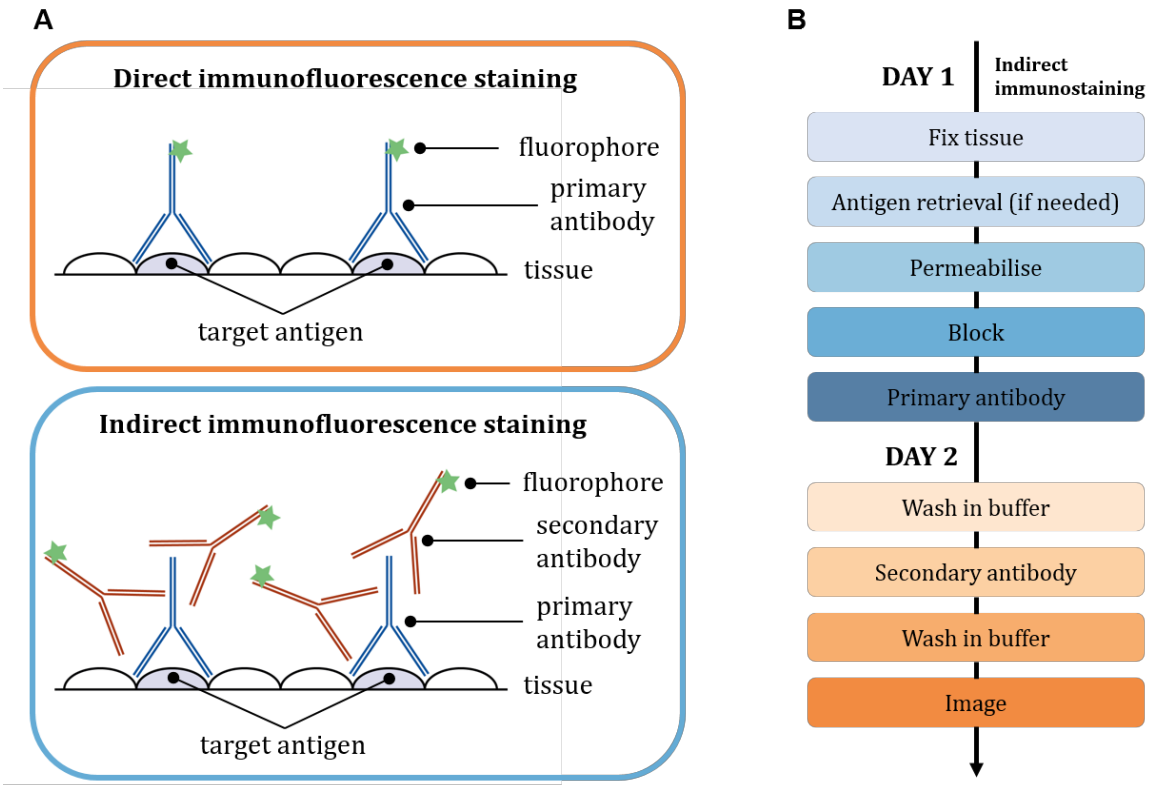

Figure 2.10. Direct and indirect immunofluorescence methods and staining workflow. (A) Direct and indirect immunofluorescence staining schematic shows the method of staining with just one labelled antibody (direct), and the use of a primary unlabelled antibody and a labelled secondary antibody that binds to the primary antibody (indirect). **(B)** The staining workflow shows the general steps followed when performing the indirect staining method. This figure was adapted from T. Chan's thesis (PhD student, NSB Lab) [111].

For each target, antibodies were carefully chosen based on the literature. To stain neurons, NeuN (neuronal nuclei antigen) was targeted, an RNA-binding protein that regulates splicing events and is localised in both the nucleus and cytoplasm. NeuN staining is highly neuron-specific and works well on formalin-fixed tissue and on neurons throughout the nervous system of adult mice [112], [113]. To stain microglia, Iba1 (ionised calcium binding adaptor molecule 1) was targeted, an actin-binding protein that plays a role in phagocytosis and is localised in the cytoskeleton within the cytoplasm. Iba1 is specifically

expressed in microglia and macrophages, and is upregulated when these cells are activated [114]. Lastly, to stain astrocytes, GFAP (glial fibrillary acidic protein) was targeted, an intermediate filament protein localised in the cytoplasm of astrocytes. GFAP is uniquely found in astrocytes and plays a critical role in astrocyte activation [115], [116]. GFAP expression is regarded as a reliable marker for most, if not all, reactive astrocytes; however, not all non-reactive astrocytes express detectable levels of GFAP [50]. To detect all these described antigens, which are localised in the cytoplasm and nucleus of cells, a permeabilisation step was necessary.

Following permeabilisation, a blocking step is performed, which is needed to achieve high signal-to-noise ratio, as it prevents non-specific binding of antibodies to the tissue. Intermolecular forces can promote non-specific binding between antibodies and other molecules in the tissue. To prevent such interactions, serum was used, as it contains antibodies that bind to non-specific sites. The serum was matched to the species of the secondary antibody to prevent unspecific binding of the secondary antibody directly with the tissue. Bovine serum albumin (BSA) was also added to the blocking solution to further block non-specific antibody binding. When in excess, these serum antibodies should out-compete the primary antibody for non-specific binding sites, improving the signal-to-noise ratio. Subsequently, primary and secondary antibody staining steps are performed, separated by washes in buffered solution to prevent any change in pH. The final antibodies and dilutions used for each protocol are shown in Table 2.4.

Table 2.4. Primary and secondary antibodies used to stain for albumin, immunoglobulin, neurons, microglia and astrocytes.

Stain	Primary Antibody	Secondary Antibody
Albumin	Anti-mouse serum albumin antibody (ab19196) - 1:100	Donkey anti-rabbit IgG H&L (Alexa Fluor® 488) (ab150073) - 1:200
Immunoglobulin	-	Donkey anti-mouse IgG H&L (Alexa Fluor® 488) (ab150105) - 1:200
Neurons	Recombinant anti-NeuN antibody [EPR12763] (ab177487) - 1:500	Goat anti-rabbit IgG H&L (Alexa Fluor® 488) (ab150077) - 1:500
Microglia	Anti-Iba1 antibody (ab5076) - 1:500	Donkey anti-goat IgG H&L (Alexa Fluor® 488) (ab150129) - 1:500
Astrocytes	GFAP monoclonal antibody (2.2B10) (13-0300) - 1:100	Mouse anti-rat IgG2a (FITC) (11-4817-82) - 1:500

These final protocols, however, were attained by optimising the procedures for each target (Table 2.5). Neuron and astrocyte protocols were optimised with H.S. Jung (MRes student, NSB Lab). A high background signal was one of the predominant issues in the optimisation procedure, due to unspecific antibody binding and improper tissue preparation or incubation parameters. The main steps that required optimisation were the antigen retrieval, permeabilisation and antibody labelling steps (all final protocols are in Appendix Tables 6.2-6.6).

To reduce autofluorescence in all protocols, brain slices were finally stained with a Sudan black dye, which quenches fluorescence. Before applying a coverslip, a mounting medium with DAPI (4',6-diamidino-2-phenylindole) was applied, designed to preserve fluorescence when imaging (anti-fade properties), whilst also allowing cell nuclei to be detected.

Table 2.5. Optimisation of staining protocols performed. The parameters that were varied to optimise each protocol are shown, with the final parameters chosen highlighted in bold.

Step	Albumin	Immunoglobulin	Neurons	Microglia	Astrocytes
Antigen Retrieval	**without**	**without**	**with /** without	**without**	**with /** without
Permeabilisation	**with /** without	**with**	**with**	**with /** without	**with**
	30 min	**30 min**	**30 min**	**30 min**	30 min **60 min**
	0.25% Tx	**0.25% Tx**	**0.1% Tx** 0.2% Tx 0.3% Tx 0.4% Tx 0.5% Tx	**0.25% Tx /** 0.4% Tx	0.1% Tx 0.2% Tx **0.3% Tx** 0.4% Tx 0.5% Tx
Blocking	**with**	**with**	**with**	**with /** without	**with**
Primary Antibody	**ab19196 /** ALB11-FITC	-	**EPR12763**	ab209064 / **ab5076**	ab7260 / **2.2B10**
	(1:100)	-	(1:50) (1:100) (1:200) **(1:500)** (1:1000)	**(1:500)**	(1:50) **(1:100)** (1:200) (1:500) (1:1000)
Secondary Antibody	**ab150073**	**ab150105**	**ab150077**	ab150077 / **ab150129**	ab150077 / **11-4817-82**
	(1:200)	**(1:200)** (1:500)	(1:100) (1:200) **(1:500)**	**(1:500)** (1:1000)	(1:100) (1:200) **(1:500)**

Brains that were stained with H&E (Figure 2.11; full protocol in Appendix Table 6.7) were first sent to the IQPath laboratory at University College London to be paraffin-embedded (protocol in Appendix Table 6.8) and sectioned into 6 µm thick slices. These brains had 1.5 mm trimmed and discarded from the dorsal side of the brain (Appendix Figure 6.8) and eleven levels with six sections each were then cut, with 80 µm of tissue discarded between levels. The first slide of each level (covering the entire focal volume) was stained with H&E. These slides were cleared in Histo-Clear II (Agar Scientific, Stansted, UK) for 5 min and then 10 min. The slides were then hydrated in water and submerged for 5 min in Harris Haematoxylin (Thermo Fisher). Tap water was used to rinse the slides, which were then dipped (3 times) in 1% acid alcohol (1% hydrochloric acid in 70% ethanol) and rinsed. They were then stained in eosin (Sigma Aldrich) for 50 s, rinsed and then dehydrated in

90% and 100% ethanol (30 s each). Lastly, they were placed in Histo-Clear II, wiped and mounted with PDX (dibutylphthalate polystyrene xylene), coverslipped and imaged using a widefield microscope (Zeiss Axio Observed Inverted Widefield).

Brain sections stained for H&E were analysed for histological damage. To know which regions of the brain slices needed to be examined for tissue damage, unstained sections adjacent to the H&E slices were first checked under a fluorescence microscope to identify where the dextran had been delivered. Dextran delivery was observed in all nine sections of each of the eleven levels. Three histological measures were evaluated in each H&E-stained section: the number of sites with more than five red blood cells extravasated, the number of microvacuolations and the number of dark neurons. The different values were plotted for RaSP and long-pulse-treated brains. Histological evaluations of the targeted and control hippocampi were performed without knowledge of which side was targeted with ultrasound.

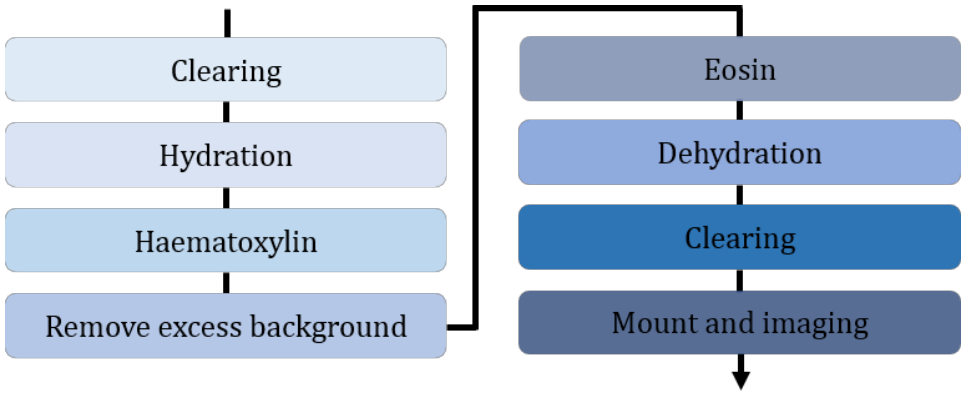

Figure 2.11. H&E staining workflow. General workflow for H&E staining, omitting washing steps. Full protocol can be found in Appendix Table 6.7.

2.3.8 Microscopy and analysis

Images were acquired using either a widefield microscope (10x; Zeiss Axio Observer, Oberkochen, Germany) or a confocal microscope (20x; Zeiss LSM-510 inverted, Oberkochen, Germany). Images were taken using both brightfield and fluorescent

channels. The three main fluorophores that were used are DAPI, to stain for nuclei; Alexa 488 or FITC (fluorescein isothiocyanate), to stain for albumin, immunoglobulin, neurons, microglia or astrocytes; and Texas Red, which is the fluorophore attached to our model drug. Excitation and emission filters used for each fluorophore are shown in Table 2.6. All imaging parameters, such as laser power and exposure time, were kept constant to allow quantitative measurements.

Table 2.6. Excitation and emission filters for the fluorophores. Excitation and emission filters are given as centre wavelength and the bandwidth.

Fluorophore	Excitation (nm)	Emission (nm)
DAPI	390/40	450/40
Alexa 488, FITC	470/40	525/50
Texas Red	562/40	624/40

To give an indication of the amount of model drug delivered, as well as the extent of albumin and immunoglobulin extravasation into the brain, the normalised optical density (NOD) was calculated from the acquired images [17]. To perform these measurements, regions of interest (ROIs) around the left and right hippocampus were selected using Matlab R2018b (Mathworks, Natick, MA, USA). If present, artefacts, such as folds and air bubbles, were removed from these regions. To calculate the NOD, pixels with intensities above twice the standard deviation added to the mean of the control pixel intensities were summed in both ROIs (Appendix Figure 6.9). The sum in the targeted ROI was subtracted by that of the control ROI to obtain the NOD. Delivery was considered successful if the NOD was at least two standard deviations above the mean of the control region. The NOD was used as a normalised measurement of the detected dose of the model drug in the pressure threshold experiment to compare RaSP with long pulse treatments, assess the duration of increased BBB permeability, identify the extent of

albumin and immunoglobulin extravasation, and predict drug delivery from the acoustic emissions. These measurements were made on five slices for each quantified brain.

The distribution of the model drug was instead quantified with the coefficient of variation (COV; Appendix Figure 6.9). Regions of interest (ROIs) around the left hippocampus were selected using Matlab and the COV was quantified as the ratio of the standard deviation over the mean fluorescence pixel intensity in these targeted regions. This measurement was used to quantify the distribution of the model drug when comparing RaSP with long pulse treatments and was performed on five sections for each brain.

2.3.9 Acoustic signal analysis

The acoustic signals emitted from the microbubbles during ultrasound treatments provided information regarding the cavitation activity produced in the brain. These acoustic emissions were captured with a focused passive cavitation detector (PCD; centre frequency: 7.5 MHz; Figure 2.5), whose signal was fed through a bandpass filter and pre-amplifier, before being recorded by an oscilloscope. The signal was then processed in Matlab using both temporal and spectral methods.

The uncalibrated acoustic energy of the microbubble emissions is related to the number and strength of the cavitation activities produced in the brain. To obtain the uncalibrated energy of the emissions, the time-domain voltage signal recorded by the PCD was squared, integrated over time and corrected for electronic noise using Matlab [14]. To correct for this noise, each energy value in the 10 ms pulse/burst length was subtracted by the mean noise energy, which was computed in a signal region where no acoustic cavitation was detected. In addition to this correction, the mean energy of the five initial control pulses (taken before the microbubbles were injected) was also subtracted from each energy point. This energy difference was plotted over time.

The energy variations across the duration of the ultrasound treatment were used to compare the duration of the acoustic emissions. This was quantified by determining the t80 constant, defined as the time required for the energy emissions to reach 80% of the cumulative energy [14].

The maximum energy values and the sum of all energy values across the sonication were recorded and compared between RaSP and long-pulse-treated brains. The energy sum values were used to see whether the extent of drug delivery (NOD) could be correlated with the energy of the acoustic emissions. How the energy changed over time was not only determined across the duration of the sonication, but also within a RaSP burst. We investigated how the energy of each short pulse varied within a burst, where the average energy ± standard deviation was plotted for each of the 13 pulses within a RaSP burst. In addition, the energy changes of each of the 13 pulses were plotted across the duration of the ultrasound treatment to see which pulse contributed to the highest energy, and whether this energy was sustained throughout the sonication.

To determine the mode of cavitation activity, we analysed the spectral content of the acoustic emissions using the FFT (fast Fourier transform) and plotted it across the duration of the sonication to observe how the frequency content of the signal changed over time. We were particularly interested in any pulses that resulted in broadband emissions, which are associated with inertial cavitation and are probably accompanied by microbubble destruction. Other features of interest were any harmonic and ultraharmonic emissions, which are a sign of safer acoustic cavitation taking place and the type of microbubble activity that we wanted to encourage when designing the RaSP sequence.

2.3.10 Statistical analysis

A one-way analysis of variance (ANOVA) test was conducted to assess whether there was a significant difference between the three groups in the pressure threshold experiment.

Post hoc Bonferroni analysis was performed to estimate any significant differences in a pairwise manner.

A two-sided Student *t* test determined whether there was a significant difference ($P < 0.05$) between rapid short-pulse and long-pulse-treated brains in terms of the NOD (for dextran delivery, albumin and immunoglobulin), COV, number of neurons, microglia and astrocytes with dextran uptake, and t_{80} values at the different time points evaluated. A Wilcoxon rank-sum test was performed to test whether differences in the number of tissue damaged sites (red blood cell extravasation, microvacuolations and dark neurons) were significant. The relationship between drug dose and acoustic emissions was assessed with a least-squares linear regression and by calculating the correlation coefficient. All analysis was performed using Matlab R2018b.

2.4 Results

2.4.1 Pressure Threshold

We first conducted an experiment to identify the pressure required to deliver our model drug (Texas Red 3 kDa dextran) to the brain. A long pulse sequence was emitted (pulse length = 10,000 cycles, pulse repetition frequency = 0.5 Hz) at three different pressures: 0.18, 0.35 and 0.53 $MPa_{pk\text{-}neg}$ (Table 2.1). At the lowest pressure, 0.18 MPa, no drug was detected in the targeted brain region. However, at 0.35 and 0.53 MPa, delivery was observed (Figure 2.12 A-C). These observations were confirmed by quantifying the normalised optical density (NOD; Figure 2.13), a measure of the detected dextran dose in the targeted region, compared with the control region. Delivery was considered successful if the NOD was positive, which corresponds to it being above the mean pixel intensity in the control region, plus twice its standard deviation. A significant difference between the NOD of all three experimental groups was found using a one-way ANOVA test followed by post hoc Bonferroni analysis ($P < 0.0001$). In the control right hippocampus, no drug

delivery was observed in any of the brains (Figure 2.12 D-F). These results demonstrate that 3 kDa dextran does not cross the BBB by itself, but that it can enter the brain locally if focused ultrasound is applied to a targeted area. At 0.35 and 0.53 MPa, dextran was delivered not only within the main focal region located on the hippocampus, but also within the more anterior lower-pressure side lobe (Figure 2.12 B-C).

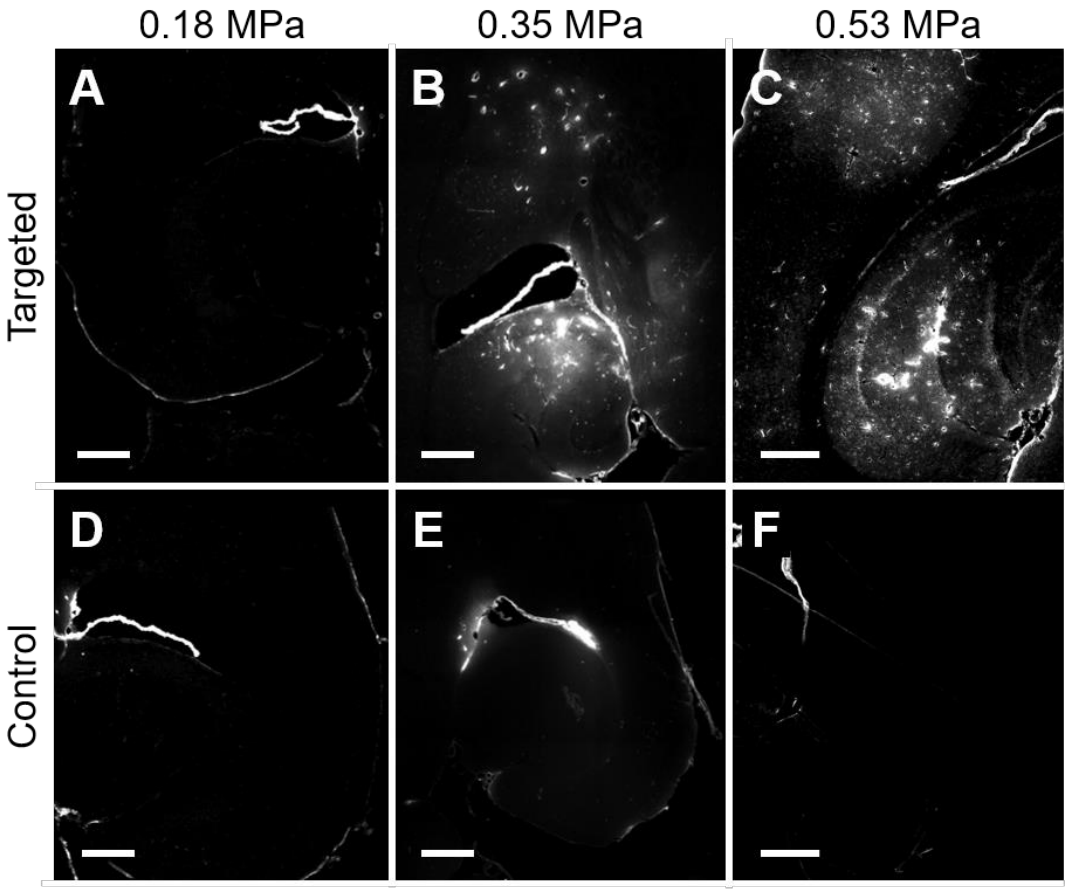

Figure 2.12. Acoustic pressure threshold for dextran delivery to the brain with long pulses. (A-F) Example fluorescence images (10x) show the targeted (A-C) and control regions (D-F) for the three derated peak-negative pressures tested (0.18, 0.35 and 0.53 MPa). A long pulse sequence was emitted (10,000 cycles at 0.5 Hz repetition frequency) onto the targeted region, where bright spots indicate the presence of the model drug (Texas Red 3 kDa dextran). Drug delivery was observed at 0.35 and 0.53 MPa, but not at 0.18 MPa in all targeted hippocampi. Some regions, such as the outline of ventricles, appear bright in the control regions and in the 0.18 MPa treated

brains due to the presence of artefacts (e.g. tissue folding), and because dextran flows in the cerebrospinal fluid (CSF) along the subarachnoid space at the edges of the brain (Appendix Figure 6.10). The scale bars indicate 500 µm.

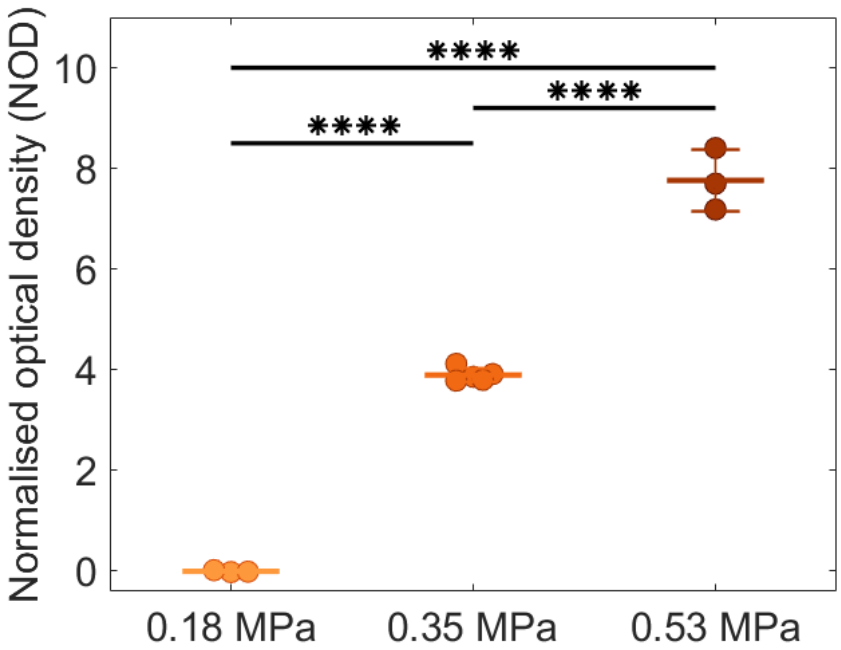

Figure 2.13. Quantification of the detected dextran dose in brains treated with three different pressures. Normalised optical density (NOD) measurements from the fluorescence images (performed on five slices per brain) show that signal was detected in the targeted left hippocampus at 0.35 and 0.53 MPa. At 0.18 MPa, no signal above that of the opposite right control hippocampus was detected. The NOD was calculated by summing the pixels with intensities higher than the mean of the control plus twice its standard deviation in both the targeted and control regions. The sum of the control region was then subtracted from the targeted region to obtain the NOD. Only when the NOD was at least two standard deviations above the mean of the control (NOD > 0) was the delivery considered successful. The NODs of the three pressure groups were found to be significantly different from each other ($P < 0.0001$).

2.4.2 Delivery and distribution

To investigate whether a more efficient and safer BBB permeability enhancement could be achieved by treating brains with a RaSP ultrasound sequence compared to the

conventionally used long pulse sequence, the left hippocampus of mice was sonicated with either a RaSP or long pulse sequence (n = 5 for each sequence type). Given the results from the pressure threshold experiment (Figure 2.13), all brains were treated with the lowest pressure at which delivery was observed (0.35 MPa). Qualitatively, the fluorescence images of the treated brain regions showed that our model drug was distributed more homogeneously with RaSP (Figure 2.14 A, C) than with the long pulse sequence (Figure 2.14 B, D). With the latter, a more spot-like pattern was observed, with high intensity regions detected in the same areas as regions with low or no detectable intensity. Although bright spots were also observed in RaSP-treated brains, these areas corresponded to cells taking up the drug, rather than accumulating around blood vessels. No delivery was observed in any of the control right hippocampus regions. Within the targeted and control regions of all brains, high intensity areas were observed at the edges of brain slices where the tissue folds, as well as within the ventricles, which appear bright when filled with cerebrospinal fluid (CSF) that regulates the extracellular environment of neurons, removing dextran from the brain.

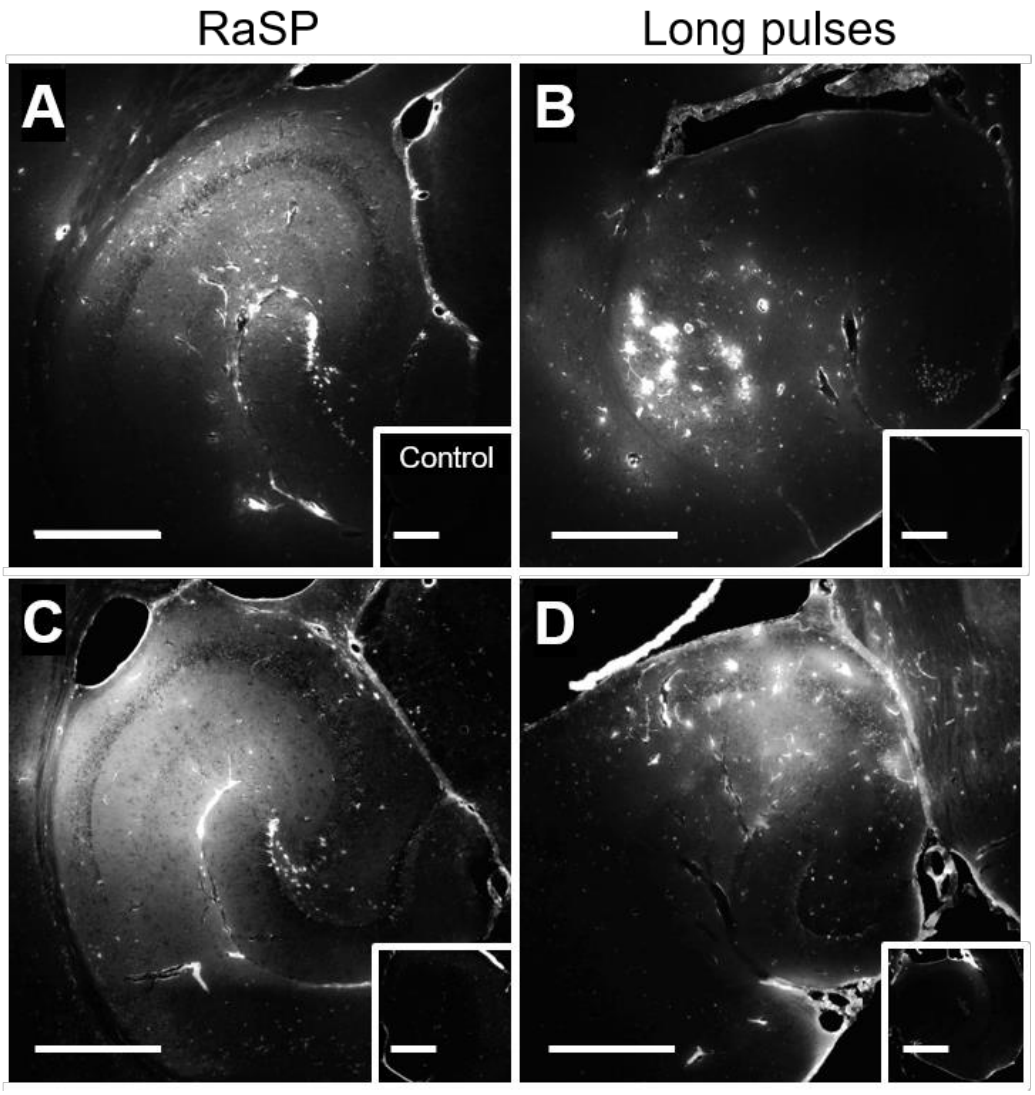

Figure 2.14. Distribution of dextran delivered with rapid short-pulse (RaSP) and long pulse sequences. Two examples of dextran delivery in the left hippocampus of different brains treated with **(A, C)** a RaSP sequence or **(B, D)** a long pulse ultrasound sequence. Right hippocampus control regions are shown in white boxes in the bottom right corner of each image. A more uniform dextran distribution was observed in RaSP-treated brains, whilst a more spot-like distribution was observed in the long-pulse-treated brains. In RaSP brains, the bright round spots correspond to cells uptaking the model drug. The scale bars indicate 500 μm. Image modified from Morse et al, *Radiology*, 2019, 291:459-466.

To find out the amount of model drug detected with the RaSP treatment compared to that delivered with the long pulses, we calculated the NOD. The calculated NOD showed that delivery was achieved in all sections in the evaluated mice. This positive NOD was confined to the targeted tissue region and was not observed in untargeted areas. Although 150 times less energy was deposited into the tissue by using the RaSP sequence, the quantification showed no significant difference between the NODs of RaSP and long-pulse-treated brains ($p > 0.05$, Figure 2.15 A).

The model drug distribution was quantified with the coefficient of variation, calculated as the ratio of the standard deviation to the mean fluorescence intensity in the targeted region. The observed difference in distribution was confirmed quantitatively with the COV being lower (less variation) for RaSP-treated mice ($p < 0.001$, Figure 2.15 B).

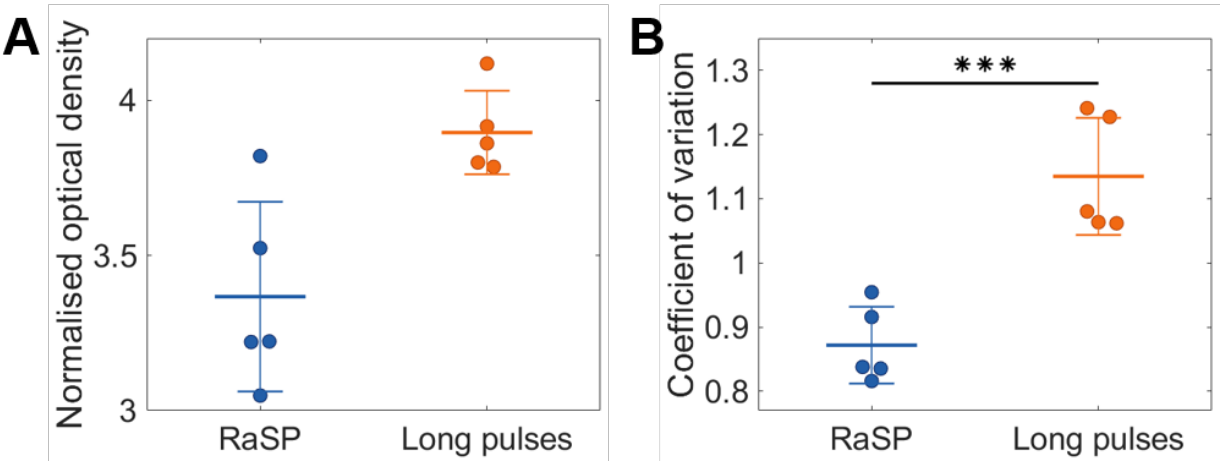

Figure 2.15. Detected dose and distribution of dextran delivered with rapid short-pulse (RaSP) and long pulse sequences at 0.35 MPa. (A) The detected dose was quantified with the normalised optical density (NOD) (performed on five slices per brain), with no significant difference found between brains treated with the RaSP (blue) and those treated with the long pulse sequence (orange; $P > 0.05$). **(B)** The distribution quantified with the coefficient of variation was found to be statistically significant between the two pulse sequences used ($P < 0.001$). Image modified from Morse et al, *Radiology*, 2019, 291:459-466.

The drug distribution produced by the two pulse sequences was closely inspected with confocal images of the treated regions. With RaSP, dextran was delivered to the parenchyma in a uniform distribution (Figure 2.16 B-C), while in the long-pulse-treated brains, a high accumulation around blood vessels was observed (Figure 2.17 B). Within this spread of dextran, cellular uptake was observed within neuronal-like cells (Figure 2.16 D-E and Figure 2.17 D) and glial-like cells (Figure 2.16 F and Figure 2.17 F) with both pulse sequence types. However, neuronal uptake was higher in RaSP-treated brains and was observed most frequently in the granule cells of the dentate gyrus, which is part of the hippocampal formation (Figure 2.16 D). Dextran uptake in glial-like cells was more common in long-pulse-treated brains (Figure 2.17 E-F). Dark circular-like regions within the dextran-distributed areas correspond to cells with no dextran uptake or cells not in the imaging plane. Additional examples of brain slices with these features can be found in Appendix Figures 6.11-6.13.

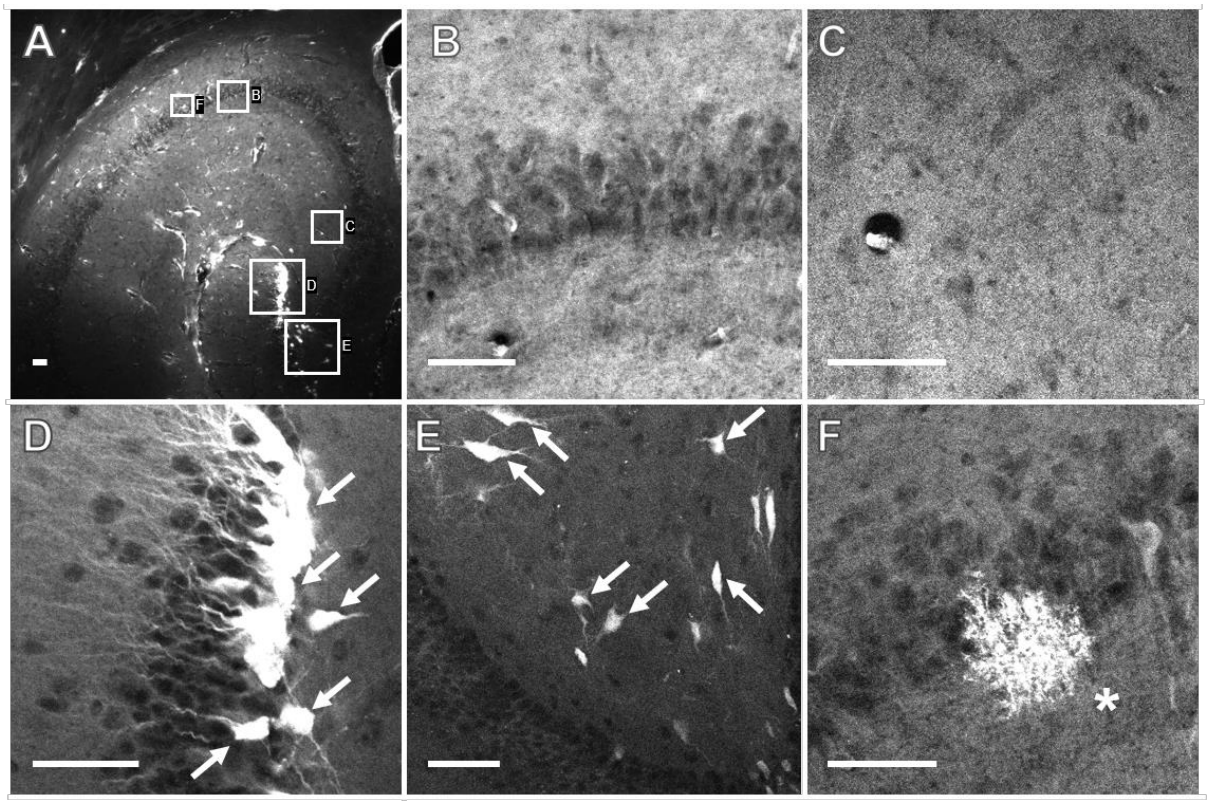

Figure 2.16. Dextran distribution throughout the parenchyma and in cells in RaSP-treated brains. (A) An example fluorescence image (10x) of dextran delivery in a brain treated with RaSP shows several characteristics in the distribution and cellular uptake of this probe, which can be explored in more detail in confocal microscopy images (20x). Such images reveal **(B-C)** a homogeneous dextran distribution within the brain parenchyma, **(D-E)** high dextran uptake in neurons (white arrows), such as **(D)** in the granule cells of the dentate gyrus, and in rare circumstances, **(F)** in glial cells (asterisk). Dark circular regions within these uniform spreads of dextran correspond to cells without dextran uptake or cells not in the imaging plane. The scale bars indicate 50 μm. Image modified from Morse et al, *Radiology*, 2019, 291:459-466.

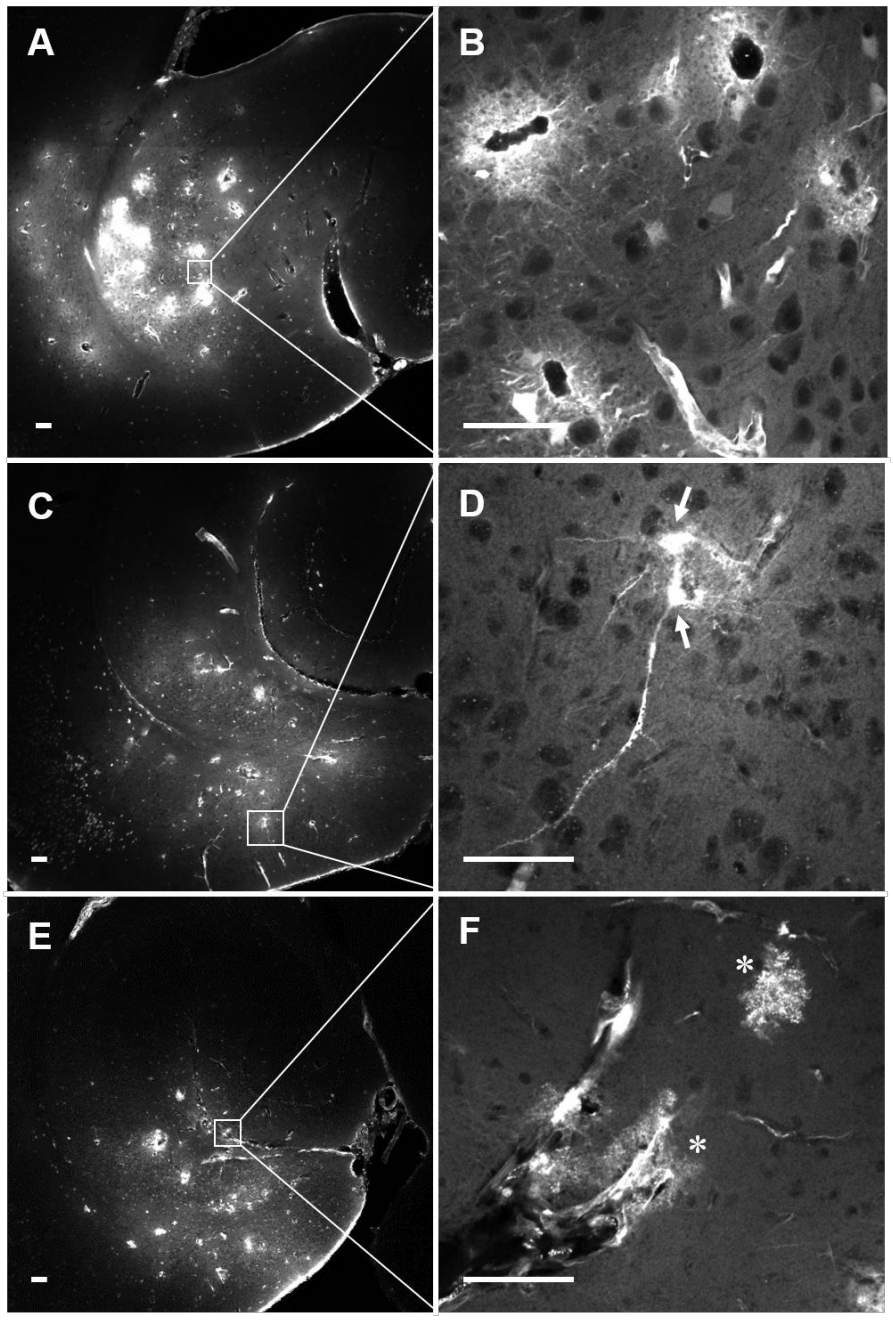

Figure 2.17. Dextran distribution throughout the parenchyma and in cells in long-pulse-treated brains. (A, C, E) Three example fluorescence images (10x) of dextran delivery show its characteristic distribution when delivered to the brain emitting long pulse sequences. **(B, D, F)** Confocal images (20x) reveal **(B)** high concentrations of dextran around blood vessels, which contribute to its heterogeneous delivery pattern, **(D)** neuronal uptake (white arrows) and **(F)** glial cell uptake. Less neuronal uptake and more glial cell uptake is observed compared to the RaSP-

treated brains. Dark circular regions within the images correspond to cells without dextran uptake or cells not within the imaging plane. The scale bars indicate 50 μm. Image modified from Morse et al, *Radiology*, 2019, 291:459-466.

2.4.3 Cellular uptake

To confirm which cells were uptaking our model drug, brain slices from all treated brains were stained for neurons, microglia and astrocytes (Figure 2.18).

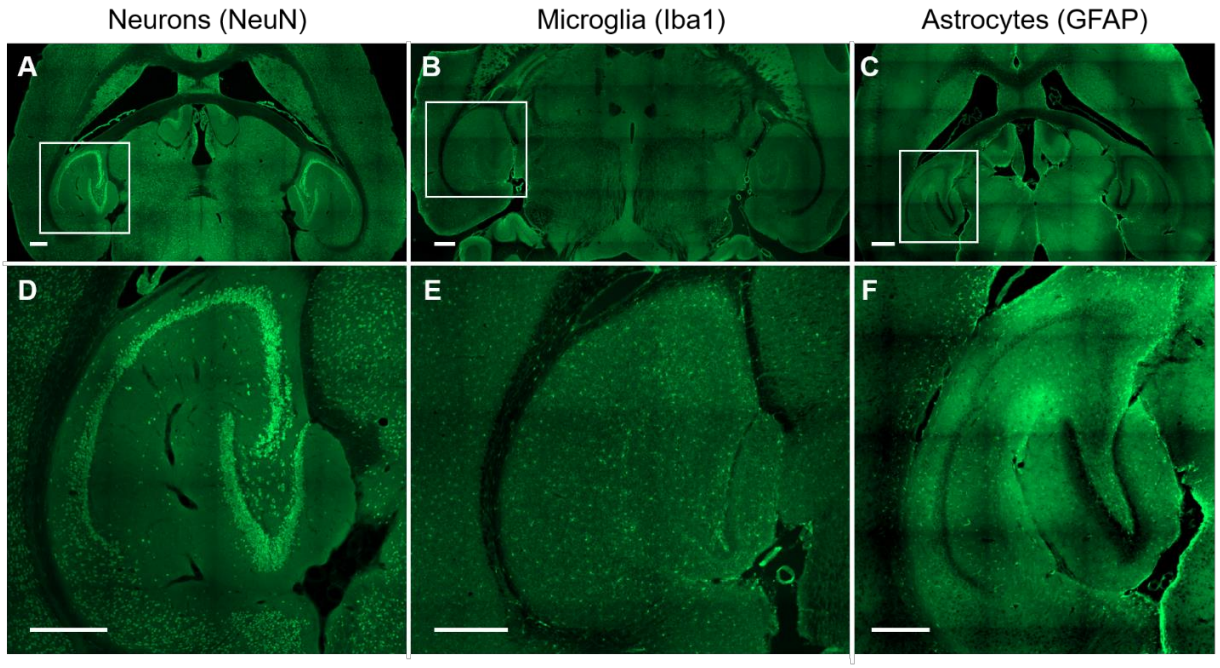

Figure 2.18. Brain slices stained for neurons, microglia and astrocytes. Fluorescence images (10x) of brain slices stained for **(A)** neurons, **(B)** microglia and **(C)** astrocytes with **(D-F)** respective zoomed in regions (20x) of the stained hippocampus, which is the area of the brain that we targeted with focused ultrasound. The scale bars indicate 500 μm.

Neurons were stained by targeting the neuronal marker NeuN (neuronal nuclei antigen), a protein found exclusively in the nervous tissue, predominantly in the nucleus and perinuclear regions of mature neurons (Figure 2.18 A, D). Neuronal uptake was detected in all brains, although in different amounts at the different time points. A significant difference in neuronal uptake was observed between RaSP and long-pulse-treated brains

at 0 h ($P < 0.05$; Figure 2.19 and 2.20). In RaSP-treated brains, dextran uptake was observed particularly in the granule cells of the dentate gyrus (Figure 2.19 A-F), which was not found as much with long pulses. Preferential uptake was observed in the neurogenic layer of neurons of the dentate gyrus. At later time points, within the first 24 hours, higher neuronal uptake was detected in RaSP-treated brains compared to long-pulse-treated brains ($P < 0.05$, Figure 2.20 and 2.21). At 24 and 48 h, however, little dextran uptake was observed in neurons with both ultrasound sequences and, at 48 h, the difference between the two sequences was not significant (Figure 2.21).

Neuronal uptake in RaSP-treated brains remained at a similar level at 0 and 2 h and then decreased significantly from 24 h onwards ($P < 0.05$), indicating that most dextran was cleared from the brain within this time frame (Figure 2.20). With long pulses, neuronal uptake levels were not only lower, but also decreased at an earlier time point (2 h) compared to the RaSP-treated brains (24 h), indicating an earlier clearing of the dextran from long-pulse-treated brains (Figure 2.20 and 2.21). A significant difference in neuronal uptake was observed between 0 h and all other time points in long-pulse-treated brains ($P < 0.05$).

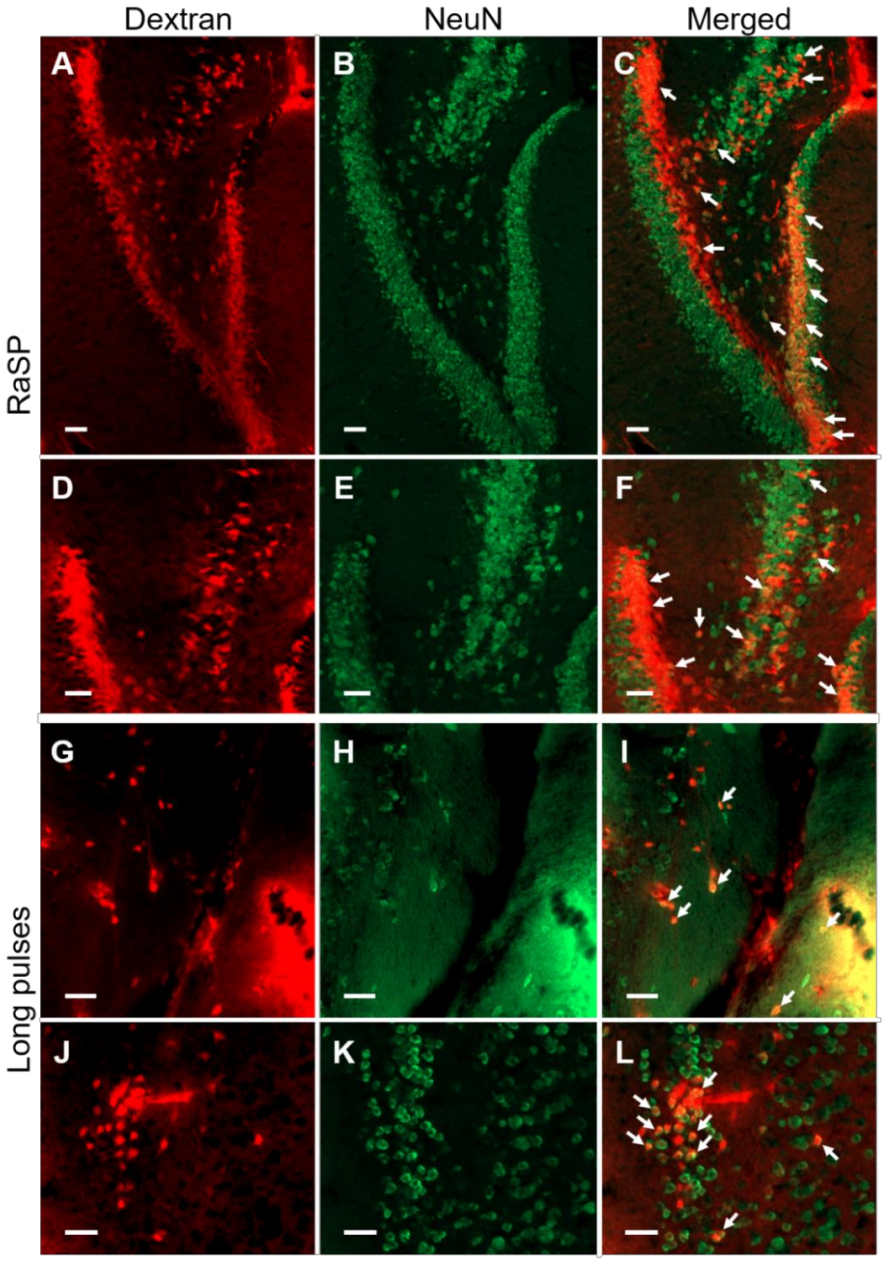

Figure 2.19. Uptake of dextran within neurons in RaSP and long-pulse-treated brains at 0 h. Fluorescence images (10x) show dextran delivery in **(A, D)** RaSP-treated brains and **(G, J)** long-pulse-treated brains, with respective **(B, E, H, K)** neuronal staining and **(C, F, I, L)** merged channels. Neuronal uptake was higher in **(C, F)** RaSP-treated brains than **(I, L)** long-pulse-treated brains. White arrows highlight examples of dextran uptake within neurons. In RaSP-treated brains, dextran uptake was found particularly in the **(C, F)** granule cells of the dentate gyrus. The scale bars indicate 50 μm.

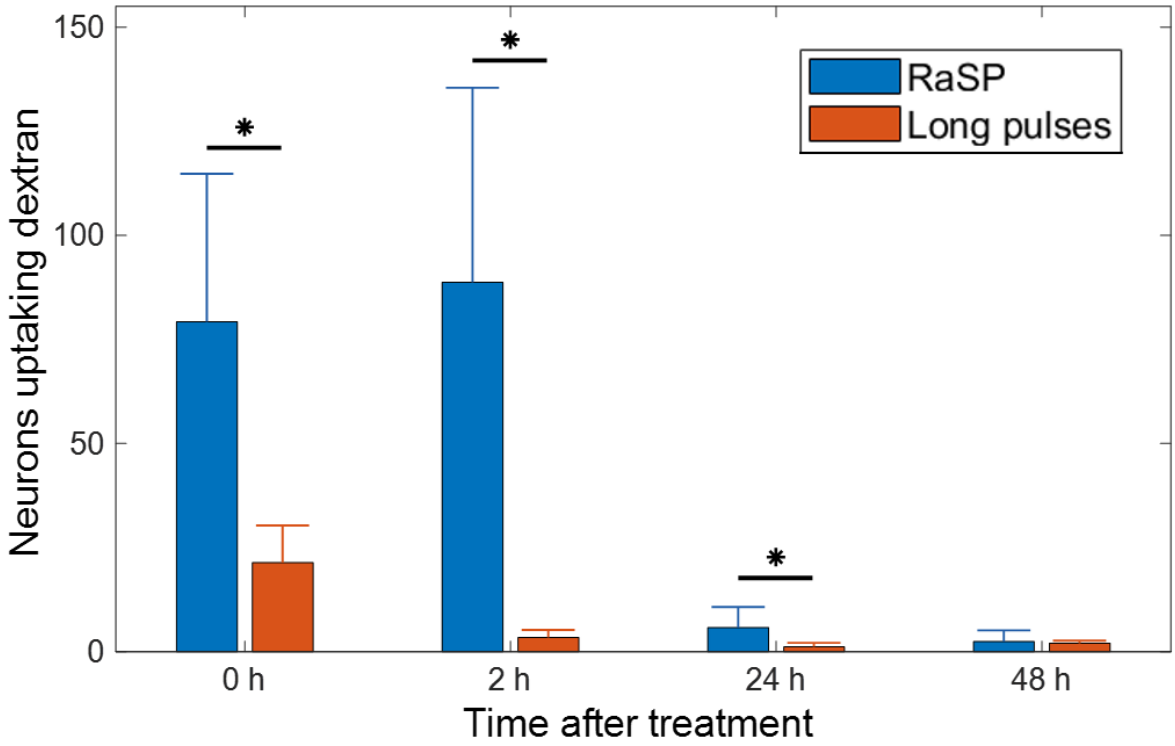

Figure 2.20. Number of neurons with dextran uptake in brains treated with RaSP or long pulses observed at 0 h, 2 h, 24 h and 48 h after ultrasound treatment. A significantly higher number of neurons uptaking dextran was found in RaSP-treated brains at 0 h, 2 h and 24 h compared to long-pulse brains at the same time points ($P < 0.05$). In RaSP-treated brains, higher neuronal uptake was observed at the earlier time points (0 h, 2 h) than at later ones (24 h, 48 h; $P < 0.05$). In long-pulse-treated brains, there was a significant difference in neuronal uptake between 0 h and all the time points ($P < 0.05$), with a decrease starting at 2 h, which is earlier than with the RaSP-treated brains. For clarity, significance bars were only shown between RaSP and long pulse results at the same time point and not between different time points.

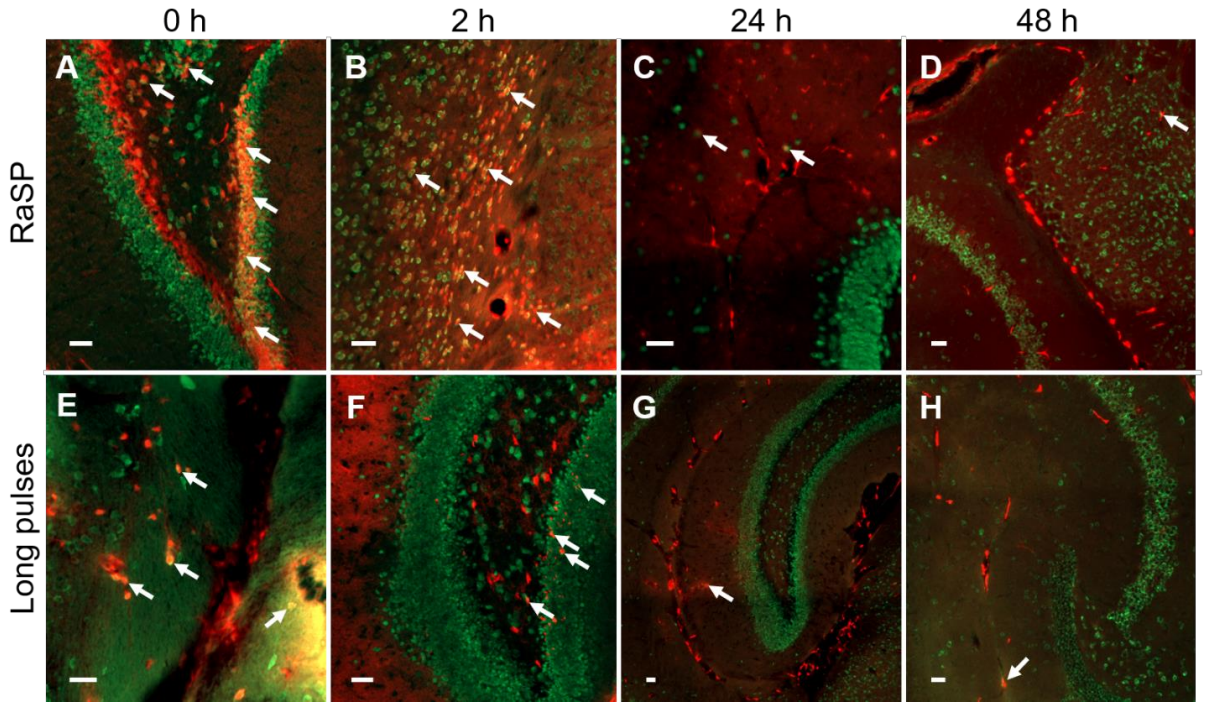

Figure 2.21. Neuronal uptake in RaSP and long-pulse-treated brains at 0 h, 2 h, 24 h and 48 h after ultrasound treatment. Fluorescence images (10x) show examples of dextran uptake in neurons for **(A-D)** RaSP and **(E-H)** long pulses at 0 h **(A, E)**, 2 h **(B, F)**, 24 h **(C, G)** and 48 h **(D, H)**. White arrows show examples of cellular uptake, which is found to be higher in RaSP-treated brains than long-pulse-treated brains at 0 h, 2 h and 24 h. The decrease in neuronal uptake starts at 24 h for RaSP and at 2 h for long pulses. The scale bars indicate 50 μm.

Microglia, the innate immune cells of the brain, were stained by using antibodies targeting ionised calcium binding adaptor molecule 1 (Iba1), a protein specifically expressed in microglia/macrophages [117]. Dextran uptake within microglia was significantly higher in all long-pulse-treated brains compared to all RaSP brains at all time points ($P < 0.01$; Figure 2.22-24). Microglial uptake was observed in every brain slice in long pulse brains, whilst in RaSP-treated brains, uptake was low and, in some slices, there was no uptake at all. The significantly higher microglial uptake with long pulses persisted over time, with the difference being more prominent at the later 24 and 48 h time points ($P < 0.001$; Figure 2.23). There was no significant difference in the number of microglia with dextran

uptake between the RaSP (lower uptake)-treated brains at different time points and between long-pulse (higher uptake)-treated brains at different time points (Figure 2.23-24).

In response to insult to the brain, microglia rapidly transform from a resting state to an activated state, proliferate, migrate to sites of interest, release cytokines and become phagocytotic. When activated, microglia undergo a characteristic change in cell morphology. At rest, microglia exhibit a ramified morphology with numerous processes extending tens of microns away from their cell body (soma); when activated, on the other hand, these processes are drawn back into the soma, leading to a rounded amoeboid-like appearance [118]. Activation also leads to a shift in the gene expression profile of the microglia, with an upregulated expression of Iba1. In long-pulse-treated brains, this characteristic change to an activated cell morphology was observed specifically in the microglia with dextran uptake (Figure 2.22 I-J). On the other hand, in RaSP-treated brains, the few microglia that had dextran uptake did not have a more rounded shape but were instead ramified, with processes elongating away from the somas (Figure 2.22 G-H). This difference in morphology of the microglia with dextran uptake in RaSP and long pulse brains was observed consistently over time. Such difference suggests that the long pulse treatment leads to a stronger response from the innate immune cells of the brain compared with the RaSP treatment.

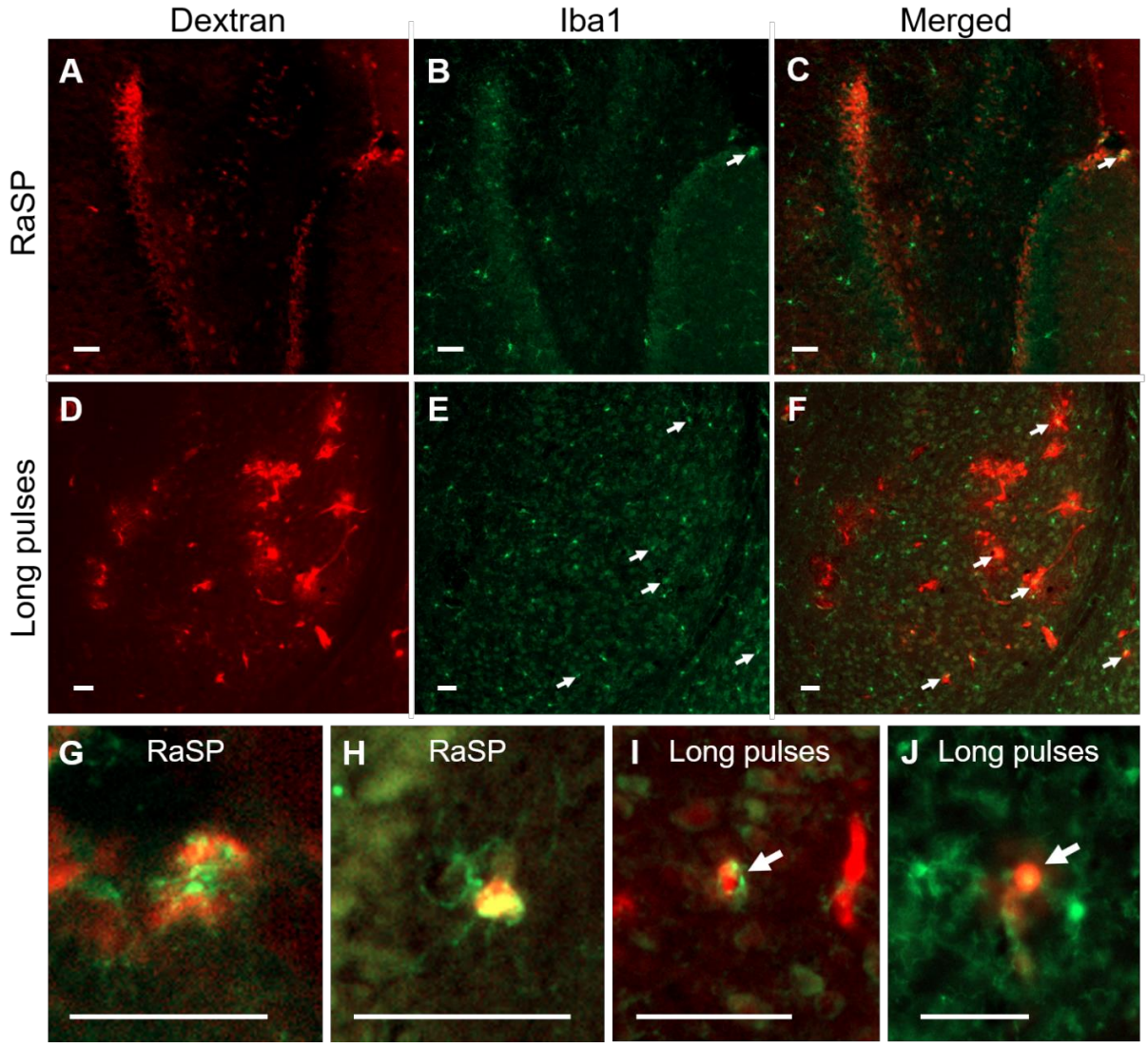

Figure 2.22. Dextran uptake within microglia in RaSP and long-pulse-treated brains at 0 h. Fluorescence images (10x) show dextran delivery in **(A)** a RaSP-treated brain and **(D)** a long-pulse-treated brain, with respective **(B, E)** microglial staining (Iba1) and **(C, F)** merged channels. Microglial uptake was higher with **(E)** long pulses compared to **(B)** RaSP. Arrows highlight where dextran uptake is occurring, as well as the rounded amoeboid-like shape of these microglia, a sign of activation. **(G-J)** These images highlight the difference in the shape of the microglia with dextran uptake, which is **(G-H)** ramified with processes in the RaSP brains, and **(I-J)** rounded with no processes in long-pulse-treated brains. The scale bars indicate 50 µm.

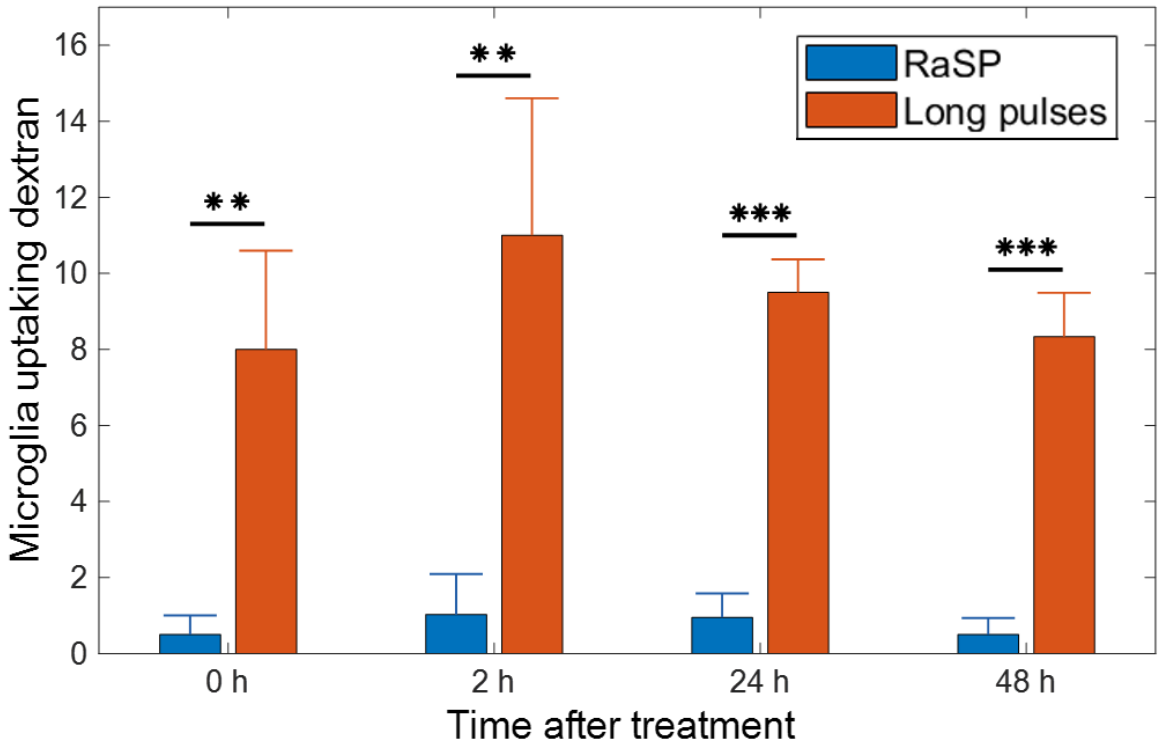

Figure 2.23. Number of microglia with dextran uptake in brains treated with RaSP or long pulses observed at 0 h, 2 h, 24 h and 48 h after ultrasound treatment. In all RaSP-treated brains, dextran uptake within microglia was significantly lower than in long-pulse-treated brains ($P < 0.01$), a difference that was more prominent at 24 h and 48 h ($P < 0.001$). The number of microglia with uptake in RaSP brains at all time points was also significantly different from long pulse brains at all time points ($P < 0.01$). For clarity, significance bars were only shown between RaSP and long pulse results at the same time point, and not between different time points.

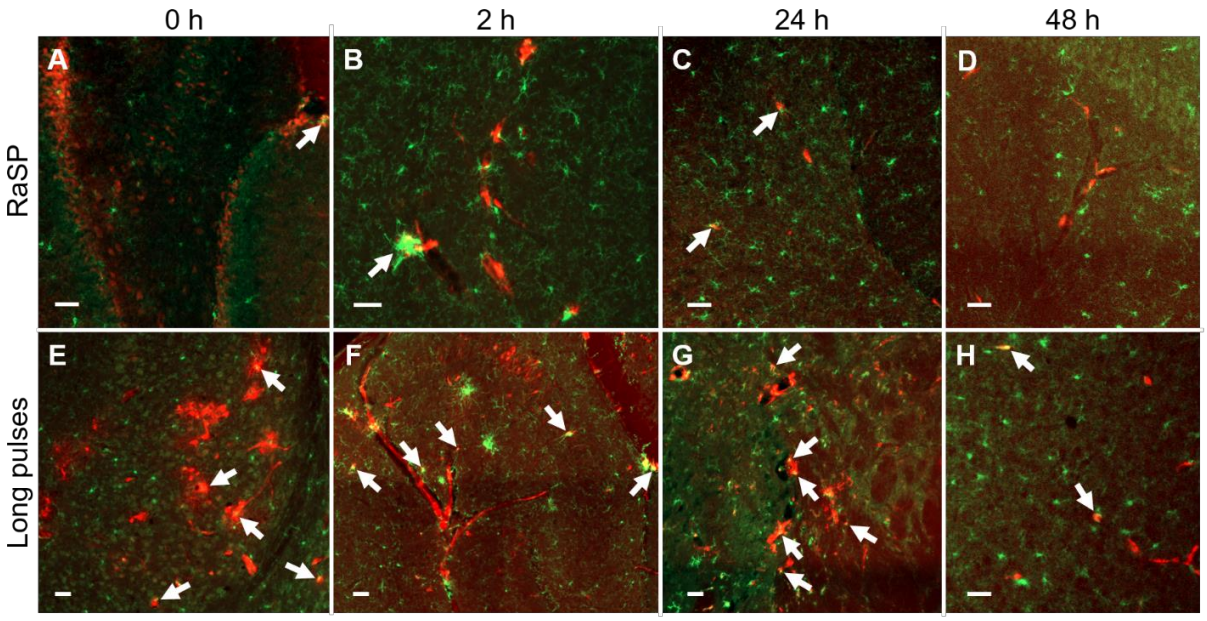

Figure 2.24. Dextran uptake within microglia in RaSP and long-pulse-treated brains at 0 h, 2 h, 24 h and 48 h after ultrasound treatment. Fluorescence images (10x) show examples of dextran uptake in microglia for **(A-D)** RaSP and **(E-H)** long-pulse-treated brains at 0 h **(A, E)**, 2 h **(B, F)**, 24 h **(C, G)** and 48 h **(D, H)**. Arrows highlight where dextran uptake is occurring, which is found to be higher in long-pulse-treated brains than RaSP-treated brains at all time points. In long pulse brains, the microglia uptaking the dextran appear to have a more rounded amoeboid-like shape, a sign of activation, while in the RaSP brains the cells were ramified with more processes. The scale bars indicate 50 μm.

Astrocytes are specialised glial cells in the brain that have a number of functions, including maintaining the neuronal microenvironment and regulating the permeability of the blood-brain barrier [50], [119]. Astrocytes were stained using antibodies targeting the glial fibrillary acidic protein (GFAP), which is an intermediate filament protein specifically found in glial cells that forms a major component of the astrocytic cytoskeleton [120]. In situations where brain damage occurs, astrocytes become reactive, increasing the size of their processes (hypertrophy) and the expression levels of GFAP [120], which is considered a sensitive and reliable marker for reactive astrocytes.

Dextran uptake within astrocytes was significantly higher in all long pulse brains compared to all RaSP brains at all time points ($P < 0.01$; Figure 2.25-27). Uptake within astrocytes was observed in every brain slice in long pulse brains, whilst in RaSP-treated brains, uptake was low with mostly no uptake at all. This significantly higher uptake in long-pulse-treated brains persisted over time, with the biggest difference observed at 2 h ($P < 0.001$; Figure 2.26). No significant difference in the number of astrocytes with dextran uptake was found between the RaSP brains and the long pulse brains over time (Figure 2.26-27). The astrocytes that had dextran uptake did not display any observable increases in the size of their cell processes, which is what would be expected from reactive astrocytes (Figure 2.25 I, L and Figure 2.27 E-H).

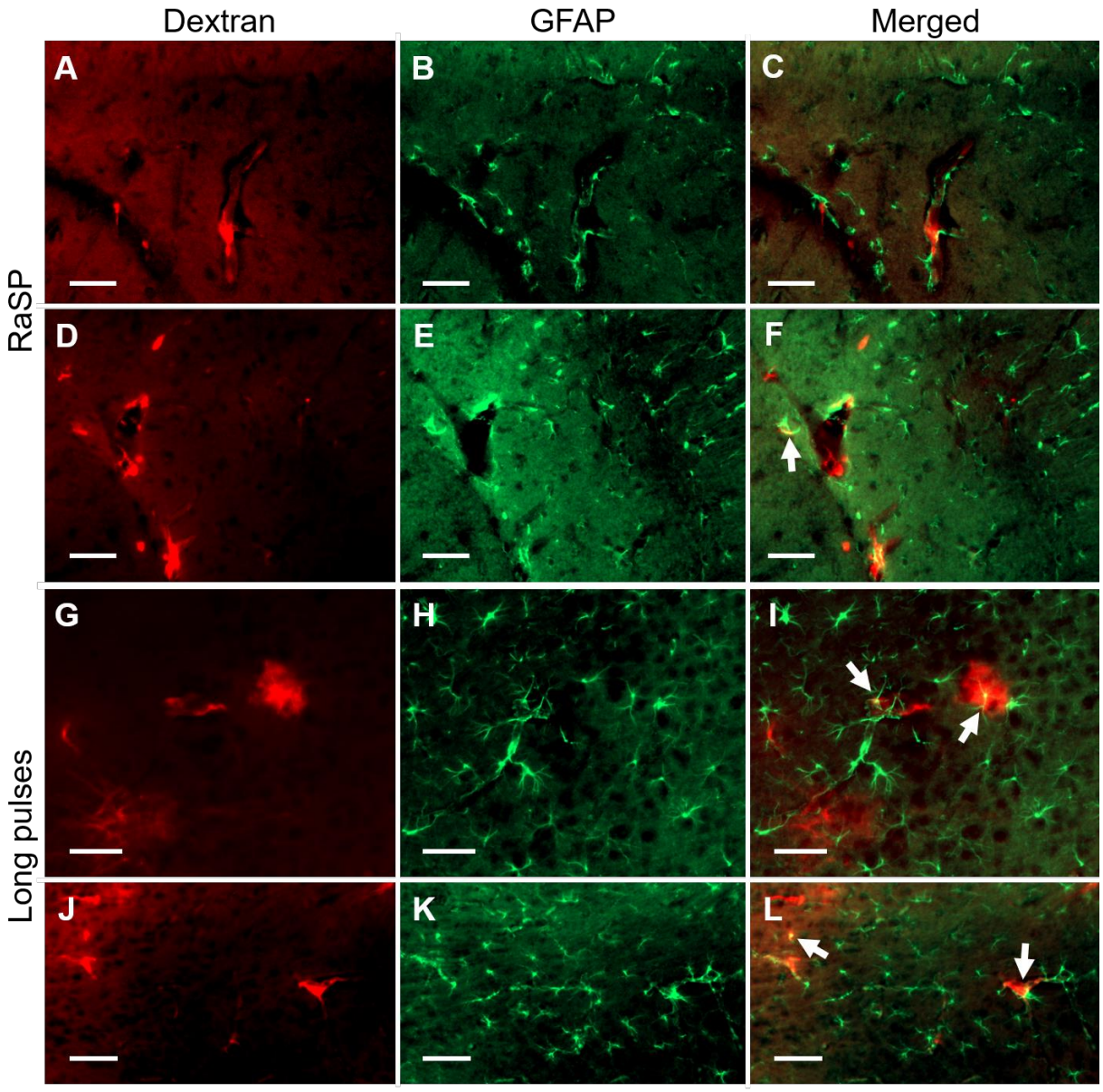

Figure 2.25. Dextran uptake within astrocytes in RaSP and long-pulse-treated brains at 0 h. Fluorescence images (10x) show dextran delivery in **(A, D)** a RaSP-treated brain and **(G, J)** a long-pulse-treated brain with respective **(B, E, H, K)** astrocyte staining (GFAP) and **(C, F, I, L)** merged channels. Astrocyte uptake was not detected in **(C, F)** RaSP-treated brains; however, in **(I, L)** long-pulse-treated brains, some dextran uptake in astrocytes was observed. Arrows highlight where astrocytes with dextran uptake are present. The scale bars indicate 50 µm.

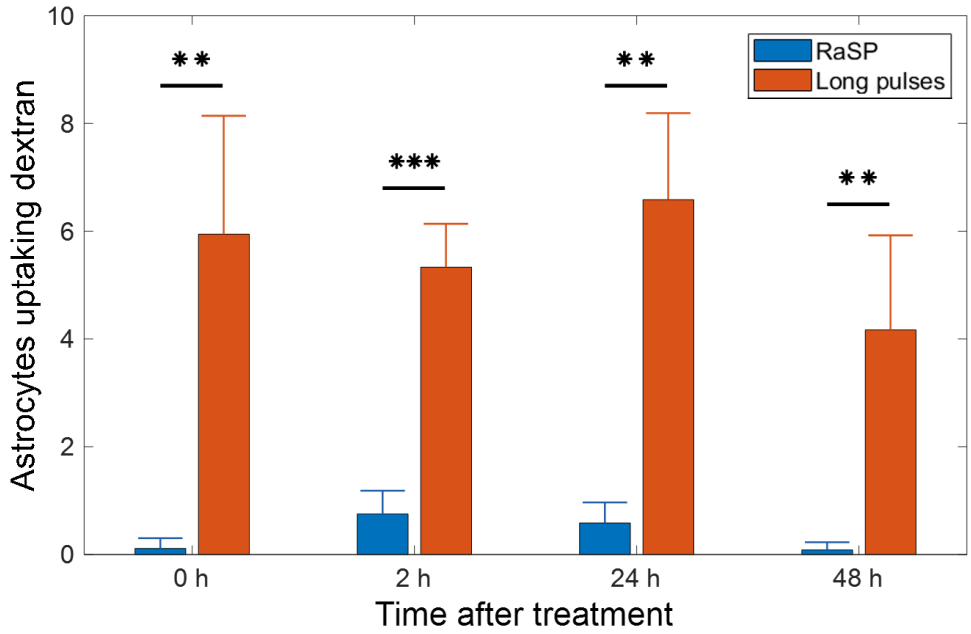

Figure 2.26. Number of astrocytes with dextran uptake in brains treated with RaSP or long pulses observed at 0 h, 2 h, 24 h and 48 h after ultrasound treatment. In all RaSP-treated brains, dextran uptake within astrocytes was significantly lower than in long-pulse-treated brains ($P < 0.01$), a difference that was most prominent at 2 h ($P < 0.001$). The number of astrocytes with uptake in RaSP brains at all time points was also significantly different from long pulse brains ($P < 0.01$). For clarity, significance bars were only shown between RaSP and long pulse results at the same time point, and not between different time points.

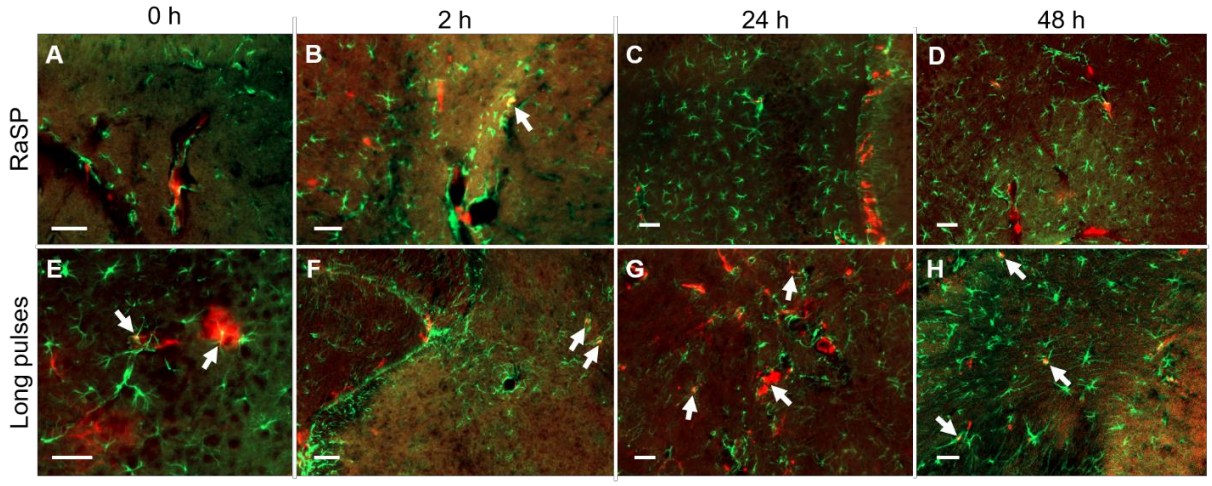

Figure 2.27. Dextran uptake within astrocytes in RaSP and long-pulse-treated brains at 0 h, 2 h, 24 h and 48 h after ultrasound treatment. Fluorescence images (10x) show examples of

dextran uptake in astrocytes for **(A-D)** RaSP and **(E-H)** long-pulse-treated brains at 0 h **(A, E)**, 2 h **(B, F)**, 24 h **(C, G)** and 48 h **(D, H)**. Arrows highlight where dextran uptake is occurring, which is found to be higher in long-pulse-treated brains than RaSP-treated brains at all time points. The scale bars indicate 50 μm.

2.4.4 Time window for molecular delivery

To determine for how long the blood-brain barrier permeability was affected after treatment with RaSP and long pulses, dextran was injected during the treatment (0 min, n = 5), 10 minutes (n = 3) or 20 minutes (n = 3) after ultrasound exposure. Three additional mice were injected with dextran, but not treated with ultrasound and were used as controls for the NOD quantification. When dextran was injected during the ultrasound treatment, fluorescence was detected in all RaSP and long pulse brains (Figure 2.28 A, D). However, when dextran was administered 10 or 20 minutes after exposure to a RaSP sequence, dextran was not detected in the brain, suggesting that delivery is occurring either during or within 10 minutes of ultrasound exposure (Figure 2.28 B-C). In long-pulse-treated brains, on the other hand, dextran was detected at 10 and 20 minutes, indicating a prolonged increase in the permeability of the BBB, which confirms previous reports (Figure 2.28 E-F).

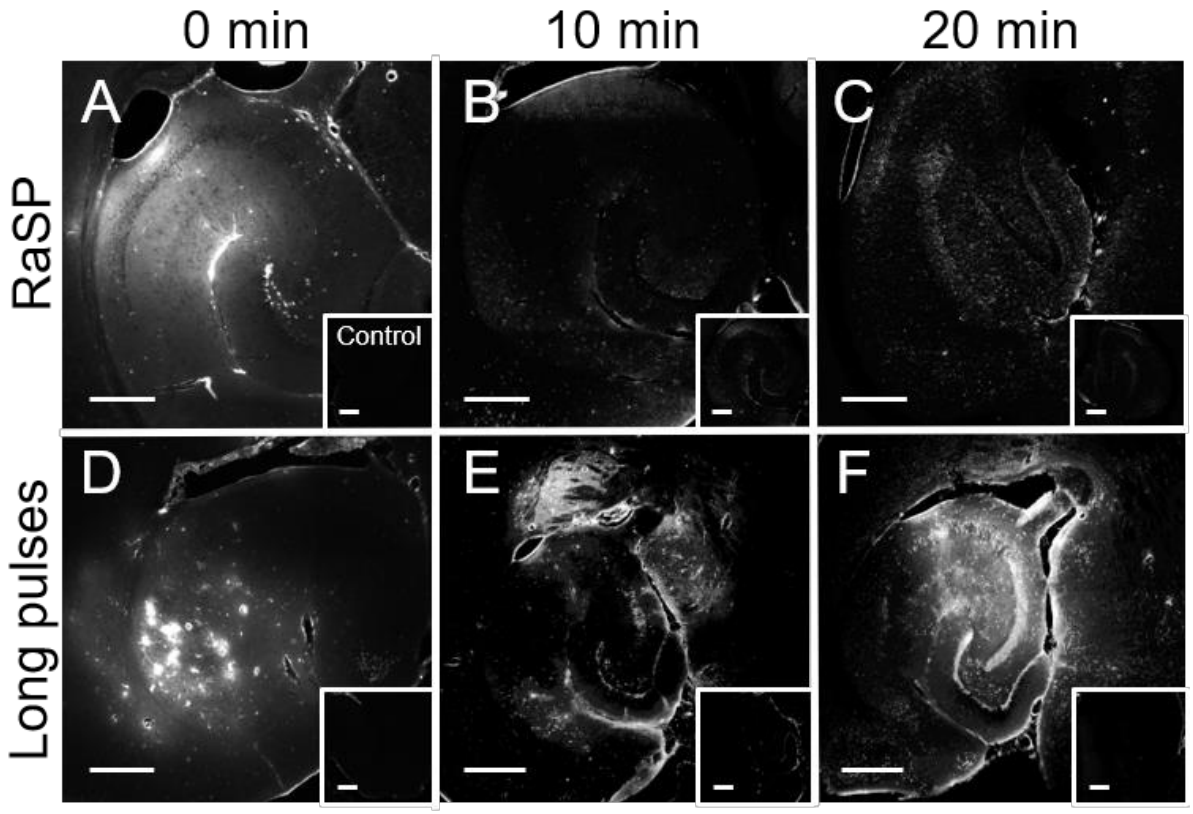

Figure 2.28. Dextran delivery at 0, 10 and 20 min after ultrasound treatment with RaSP and long pulse sequences. Fluorescence images (10x) of brains with dextran injected at **(A, D)** 0 min, **(B, E)** 10 min and **(C, F)** 20 min after ultrasound exposure with either a **(A-C)** RaSP or **(D-F)** long pulse sequence treatment. With RaSP, the BBB permeability decreases, such that dextran does not enter the brain at 10 minutes, while with long pulses, dextran still enters the brain 10 and 20 minutes after the ultrasound treatment. The scale bars indicate 500 μm. Image modified from Morse et al, *Radiology*, 2019, 291:459-466.

The results obtained from the fluorescence images were confirmed by quantifying the NOD, which showed continued delivery of dextran with long pulses at the later time points. In RaSP brains, on the other hand, at 10 and 20 minutes the NOD levels dropped to values within the control region (shaded region; Figure 2.29). At 10 and 20 minutes, NOD values were significantly different between RaSP and long pulses ($P < 0.05$). A significant difference was also found between RaSP brains at 0 min and those at 10 and

20 minutes, and between long pulse brains at 0 min and those at 20 min ($P < 0.05$). Thus, these results show that the increase in permeability of the blood-brain barrier is shorter following a RaSP ultrasound treatment compared to a long pulse treatment.

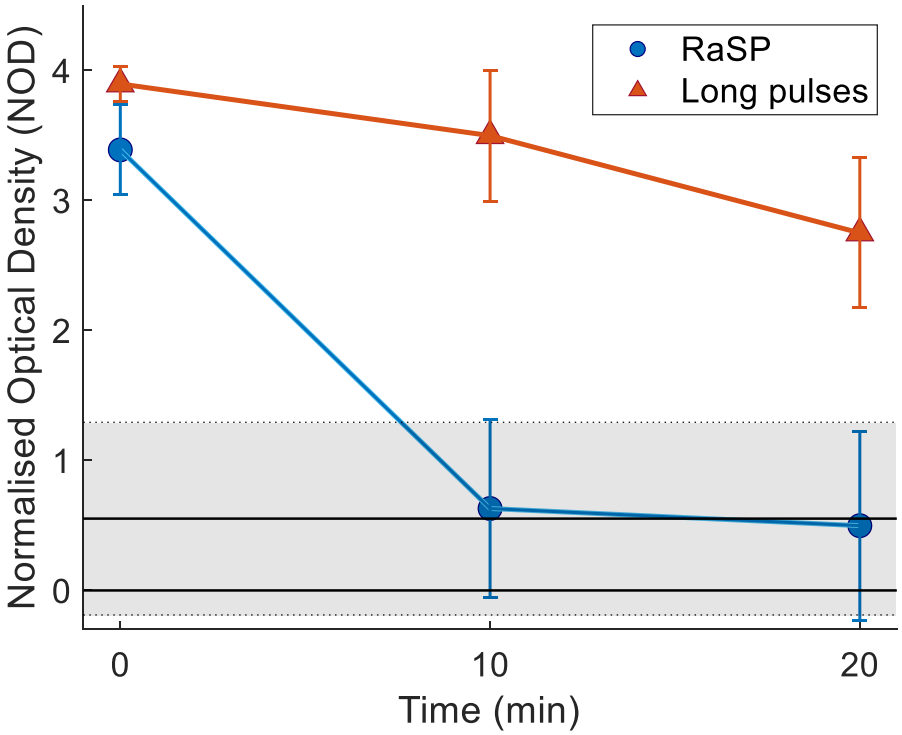

Figure 2.29. BBB closing timeline with RaSP and long pulse sequences. The detected dose of dextran was quantified with the normalised optical density (NOD) on brains where dextran was injected at 0, 10 and 20 minutes after ultrasound exposure using RaSP (blue) and long pulse (orange) sequences. With RaSP, the NOD decreased down to control levels (shaded region) within 10 minutes, indicating that the BBB is closing within this timeframe, not allowing dextran to enter the brain. With long pulses, however, the NOD was still above control levels at 20 minutes, indicating that the BBB still had an increased permeability and was allowing dextran into the brain. At 10 and 20 minutes, the NOD was found to be statistically significant between RaSP and long pulses ($P < 0.05$). The NOD for RaSP-treated brains at 0 min was also found to be significantly different from that of RaSP brains at 10 and 20 min, with a significant difference also found between the NOD of long pulse brains at 0 min and at 20 min ($P < 0.05$). The shaded region

denotes the mean ± standard deviation NOD of the control mice, which were injected with dextran but not treated with ultrasound. Image from Morse et al, *Radiology*, 2019, 291:459-466.

2.4.5 Extravasation of endogenous proteins into the brain

To investigate the extent of the increased permeability of the BBB when treated with RaSP and long pulses, brain slices at all three time points were stained for endogenous albumin and immunoglobulin. These two proteins, the most abundant proteins circulating in the bloodstream, have a significantly larger size (67 kDa and 150 kDa) than the delivered dextran (3 kDa) [63], [64] and are normally not present in the brain [65]. Staining with fluorescently labelled antibodies bound to the albumin showed that albumin extravasation occurred with both pulse sequences at 0 min, although less was detected in RaSP-treated brains (Figure 2.30 A, D). At the later time points, with RaSP, little or no albumin extravasation was observed (Figure 2.30 B-C), while with long pulses albumin was still detected at 10 and 20 minutes after ultrasound exposure (Figure 2.30 E-F). The NOD quantification confirmed these observations, showing a 4.7-fold decrease in the amount of albumin extravasating into the brain at 0 min with the RaSP treatment ($P < 0.0001$; Figure 2.31). At 10 and 20 minutes, the NOD values decreased down to control levels (shaded region) in RaSP brains, with no significant difference between NOD values at 10 and 20 minutes ($P > 0.05$). On the other hand, with long pulses, the NOD was still above control levels at these later time points. All other comparisons between different time points of the same sequence type and between RaSP and long pulse brains at the same time points were found to be significant ($P < 0.01$).

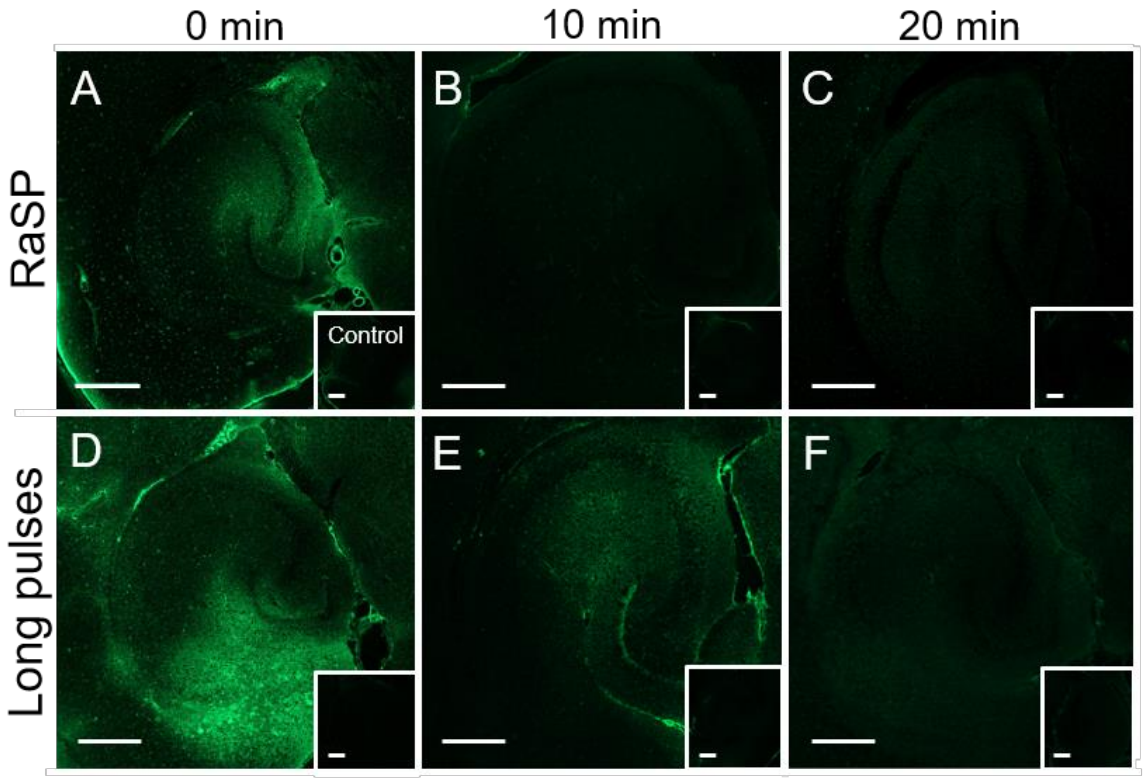

Figure 2.30. Albumin extravasation into the brain at 0, 10 and 20 min after ultrasound exposure with RaSP and long pulse sequences. Fluorescence images (10x) of brain slices stained for albumin show the extent of albumin extravasation into the brain at **(A, D)** 0 min, **(B, E)** 10 min and **(C, F)** 20 min after ultrasound exposure with either a **(A-C)** RaSP or **(D-F)** long pulse sequence treatment. With RaSP, less albumin extravasation was observed compared to the long pulse brains and at 10 and 20 minutes, hardly any albumin was detected. With long pulses, albumin was still detected 10 and 20 minutes after the ultrasound exposure. The scale bars indicate 500 µm.

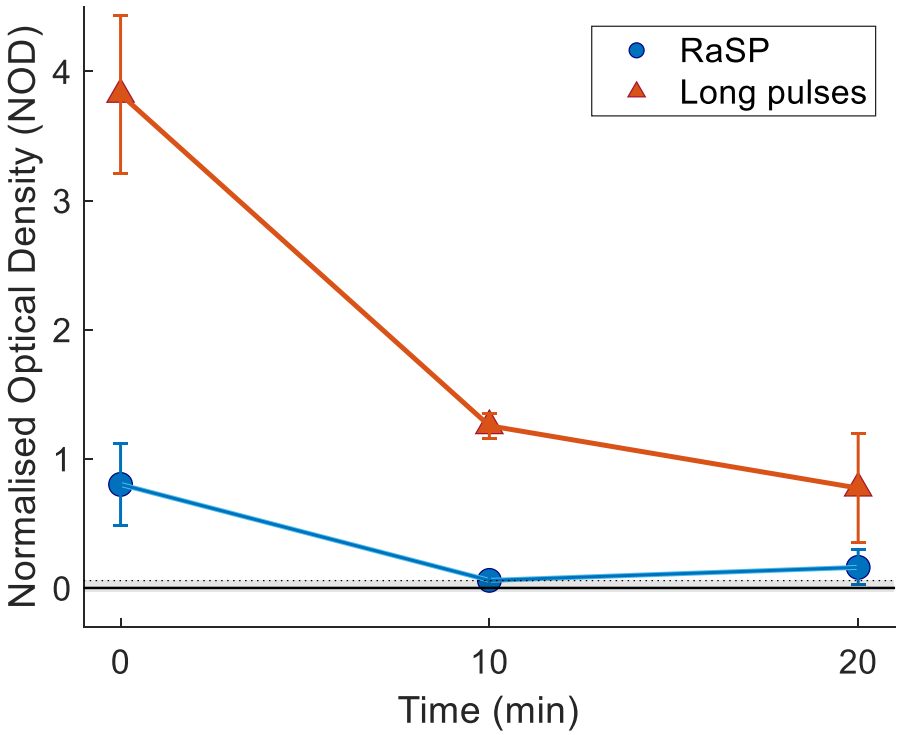

Figure 2.31. Albumin extravasation with RaSP and long pulse sequences. The detected dose of albumin was quantified with the normalised optical density (NOD) on brains where dextran was injected at 0, 10 and 20 minutes after ultrasound exposure using RaSP (blue) or long pulse (orange) sequences. In RaSP-treated brains, the NOD decreased down to control levels (shaded region) at 10 minutes, and little was detected at 20 minutes. With the long pulses, the NOD was still above control levels at 10 and 20 minutes. At all time points, the NOD was found to be significantly different between RaSP and long pulse brains ($P < 0.01$), as well as the NOD between the different time points for each sequence time ($P < 0.01$), with the exception of the NOD for RaSP brains at 10 min and 20 min ($P > 0.05$). The shaded region denotes the mean ± standard deviation NOD of the control mice injected with dextran but not treated with ultrasound, which were stained for albumin.

Immunoglobulin, on the other hand, was hardly detected in RaSP-treated brains at all time points (Figure 2.32 A-C), while with long pulses it was detected in all brains over time (Figure 2.32 D-F). These results were confirmed by the NOD quantification, which showed significant difference between RaSP and long pulse NODs at all time points ($P < 0.05$),

with the greatest difference being at 20 minutes ($P < 0.0001$; Figure 2.33). Over time, NOD values in RaSP brains were not significantly different from each other and the same was found for long pulse brains over time ($P > 0.05$). Overall, the extravasation of albumin and immunoglobulin was lower in RaSP compared to long-pulse-treated brains.

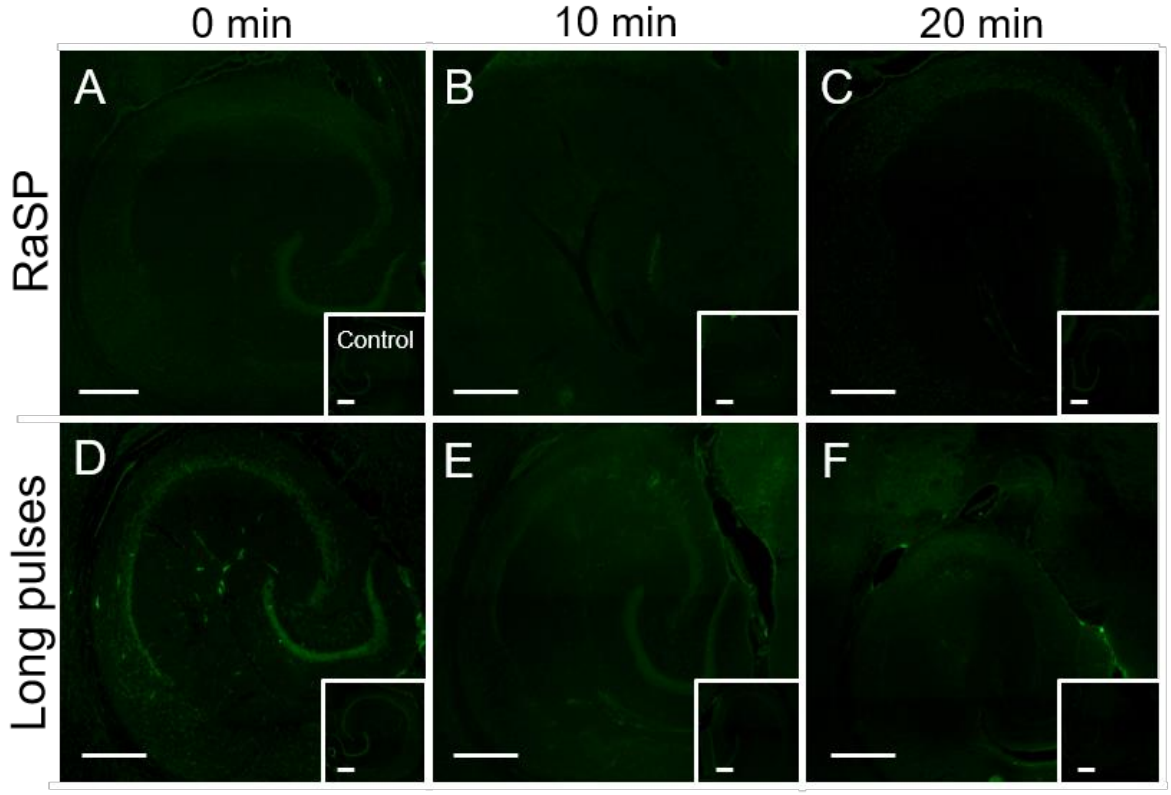

Figure 2.32. Immunoglobulin extravasation into the brain at 0, 10 and 20 min after ultrasound exposure with RaSP and long pulse sequences. Fluorescence images (10x) of brain slices stained for immunoglobulin show the extent of immunoglobulin extravasation into the brain at **(A, D)** 0 min, **(B, E)** 10 min and **(C, F)** 20 min after ultrasound exposure with either **(A-C)** a RaSP or **(D-F)** long pulse sequence treatment. With RaSP, less immunoglobulin extravasation was observed compared to the long pulse brains at all time points, with no immunoglobulin staining visible in almost all brain slices. With long pulses, immunoglobulin was detected in most slices at all time points. The scale bars indicate 500 μm.

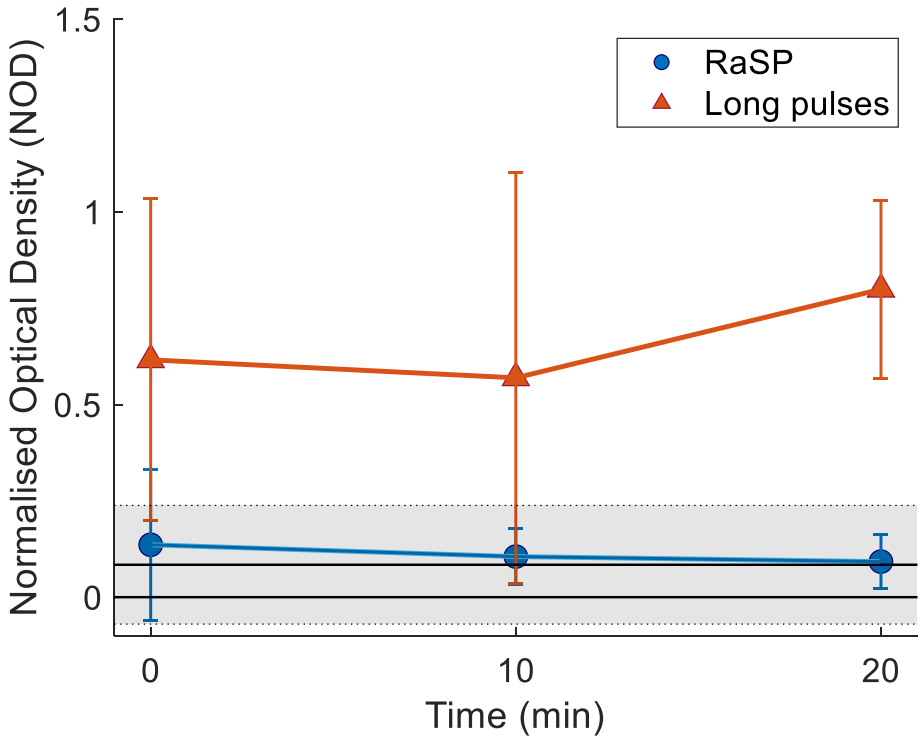

Figure 2.33. Immunoglobulin extravasation with RaSP and long pulse sequences. The detected dose of immunoglobulin was quantified with the normalised optical density (NOD) on brains where dextran was injected at 0, 10 and 20 minutes after ultrasound exposure using RaSP (blue) and long pulse (orange) sequences. In RaSP-treated brains, the NOD values were within control levels (shaded region) at all time points, with a higher variation at 0 min. In long-pulse brains, NOD values varied between brain slices, but levels were mostly above control levels, indicating continued extravasation of immunoglobulin at 10 and 20 minutes with long pulses. At each time point, a significant difference was found between RaSP and long pulse NOD values ($P < 0.05$) with the largest difference being at 20 min ($P < 0.0001$). Within the same sequence type, neither RaSP nor long pulse NOD values were significantly different from each other over time. The shaded region denotes the mean ± standard deviation NOD of the control mice injected with dextran but not treated with ultrasound, which were stained for immunoglobulin.

To investigate whether albumin and immunoglobulin were being delivered to similar regions as the dextran, qualitative observations were made by comparing the fluorescence dextran images with their corresponding stained images. In regions where

albumin and immunoglobulin were delivered, dextran was also found, even if just a uniform spread of dextran was present (Figure 2.34-35). However, dextran was present in regions where albumin and immunoglobulin were not, suggesting that the delivery pattern is dependent on the properties of the molecule. In addition, cellular uptake of both dextran and albumin or immunoglobulin was observed within the same cells in long-pulse-treated brains (Figure 2.34 I, L and 2.35 I, L). Such uptake was observed in neuronal-like cells, glial-like cells and endothelial cells. In RaSP brains, uptake of dextran and these proteins within the same cell was not observed.

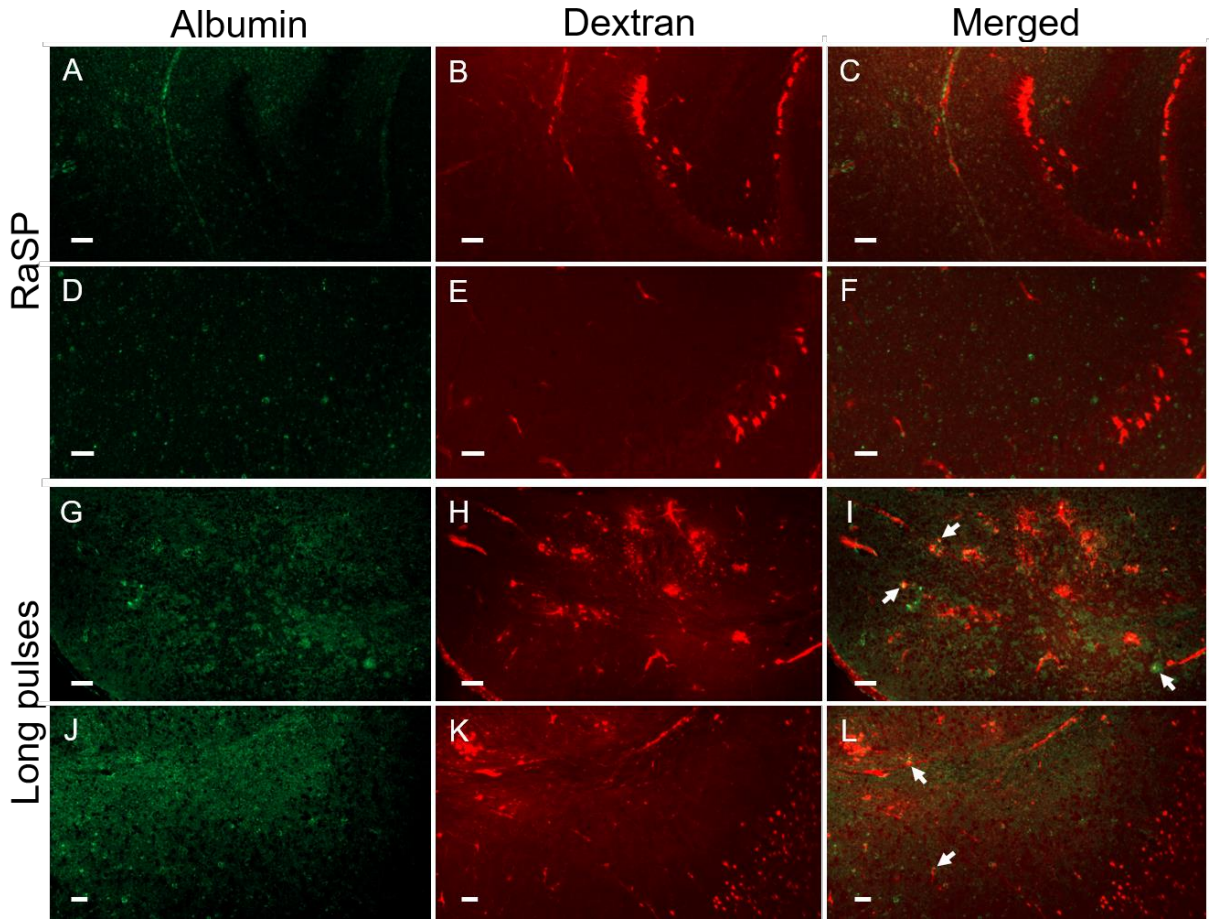

Figure 2.34. Distribution of albumin and dextran in RaSP and long-pulse-treated brains at 0 min. Fluorescence images (10x) show **(A, D, G, J)** brain regions stained for albumin with their corresponding **(B, E, H, K)** dextran distribution and **(C, F, I, L)** merged channels treated with either **(A-F)** RaSP or **(G-L)** long pulses (two examples shown per sequence type). In regions where

albumin was delivered, dextran was also found in the brain, however, regions with just dextran delivery and no albumin were also observed. Cellular uptake of both albumin and dextran within the same cells was observed only **(I, L)** in long-pulse-treated brains within neuronal, glial and endothelial-like cells (white arrows). The scale bars indicate 50 μm.

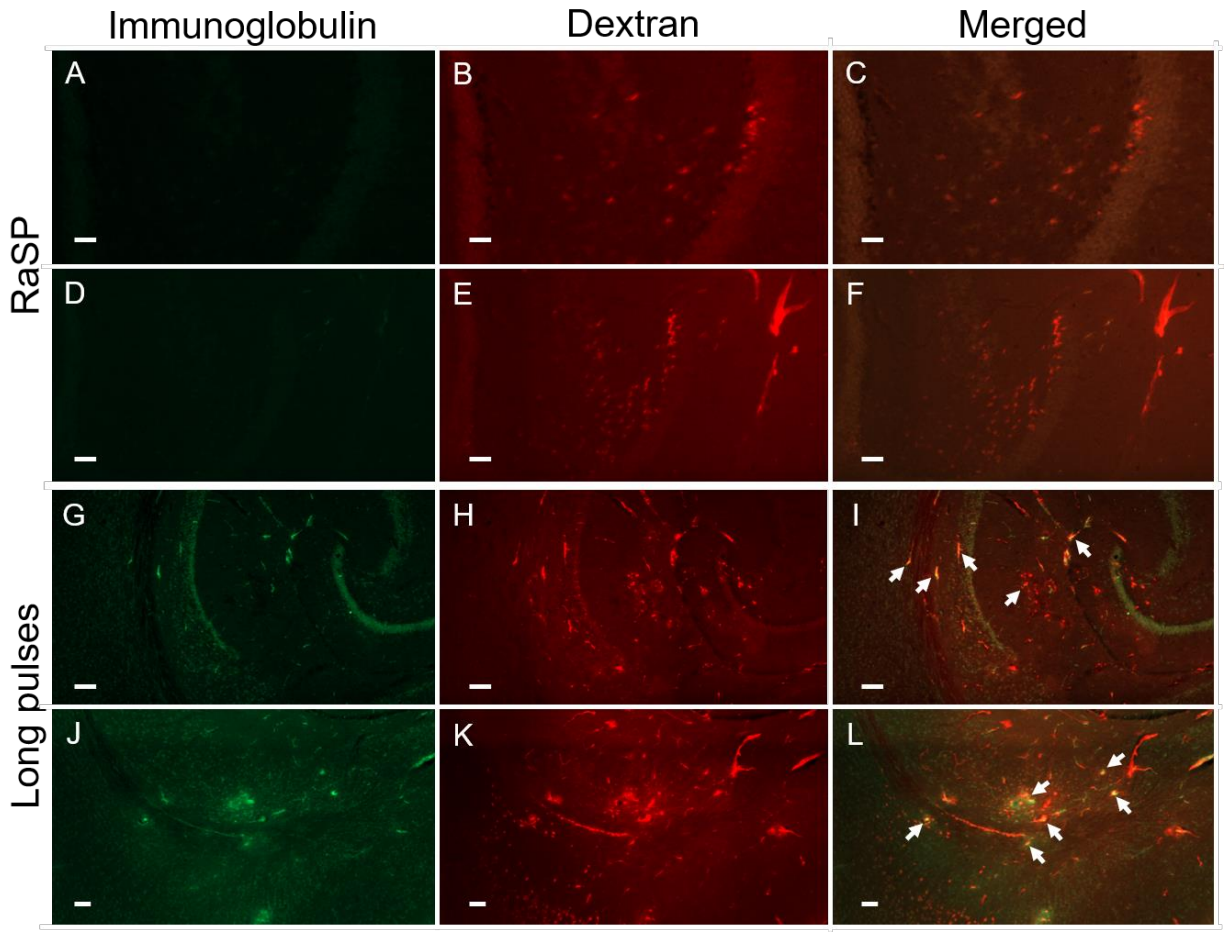

Figure 2.35. Distribution of immunoglobulin and dextran in RaSP and long-pulse-treated brains at 0 min. Fluorescence images (10x) show **(A, D, G, J)** brain regions stained for immunoglobulin with their corresponding **(B, E, H, K)** dextran distribution and **(C, F, I, L)** merged channels treated with either **(A-F)** RaSP or **(G-L)** long pulses (two examples shown per sequence type). In regions where immunoglobulin was delivered, dextran was also found in the brain, however, regions with just dextran and no immunoglobulin were observed. Cellular uptake of both immunoglobulin and dextran within the same cells was observed only in **(I, L)** long-pulse-

treated brains within neuronal, glial and endothelial-like cells (white arrows). The scale bars indicate 50 μm.

2.4.6 Safety profile

Sections were stained with H&E to investigate potential damage caused by the ultrasound exposure. As expected, all control right hippocampi showed no damage (Figure 2.36-37 D-F). The targeted left hippocampi in RaSP-treated brains also showed no evidence of damage (Figure 2.36 A-C), while in long-pulse-treated brains, tissue damage was observed (Figure 2.37 A-C; dextran images shown in Appendix Figure 6.14-15). To quantify the damage, three histological measures were used: the number of areas with more than five extravasated red blood cells, the number of microvacuolation sites and the number of dark neurons. Microvacuolation sites consisted of large and small microvacuolations with the appearance of inhomogeneous pores in focal regions of the parenchyma. Dark neurons were identified as darkly stained triangulated and shrunken cell bodies. Nine H&E stained slices were analysed per brain (n = 3 per sequence type). In long pulse brains, sites with more than five extravasated RBCs were detected in 67% of the analysed sections, microvacuolations in 63% of sections and dark neurons in 37%. In RaSP-treated brains, however, no sites with any of these three histological measures were found. In long-pulse-treated brains, red blood cell extravasation sites were identified around blood vessels in the hippocampus. Microvacuolations occurred mostly around microvessels, often found in areas that also exhibited red blood cell extravasation; when these sites occurred in proximity to the neuronal cell bodies of the hippocampus, neuronal damage was found. Neuronal damage was observed mainly in the pyramidal and granular layers of the hippocampus. Although sites of damage were only observed in long-pulse-treated brains and not in RaSP brains, the difference between the two sequence types was not found to be statistically significant, due to the large variation in the quantified values for the long-pulse-treated brains.

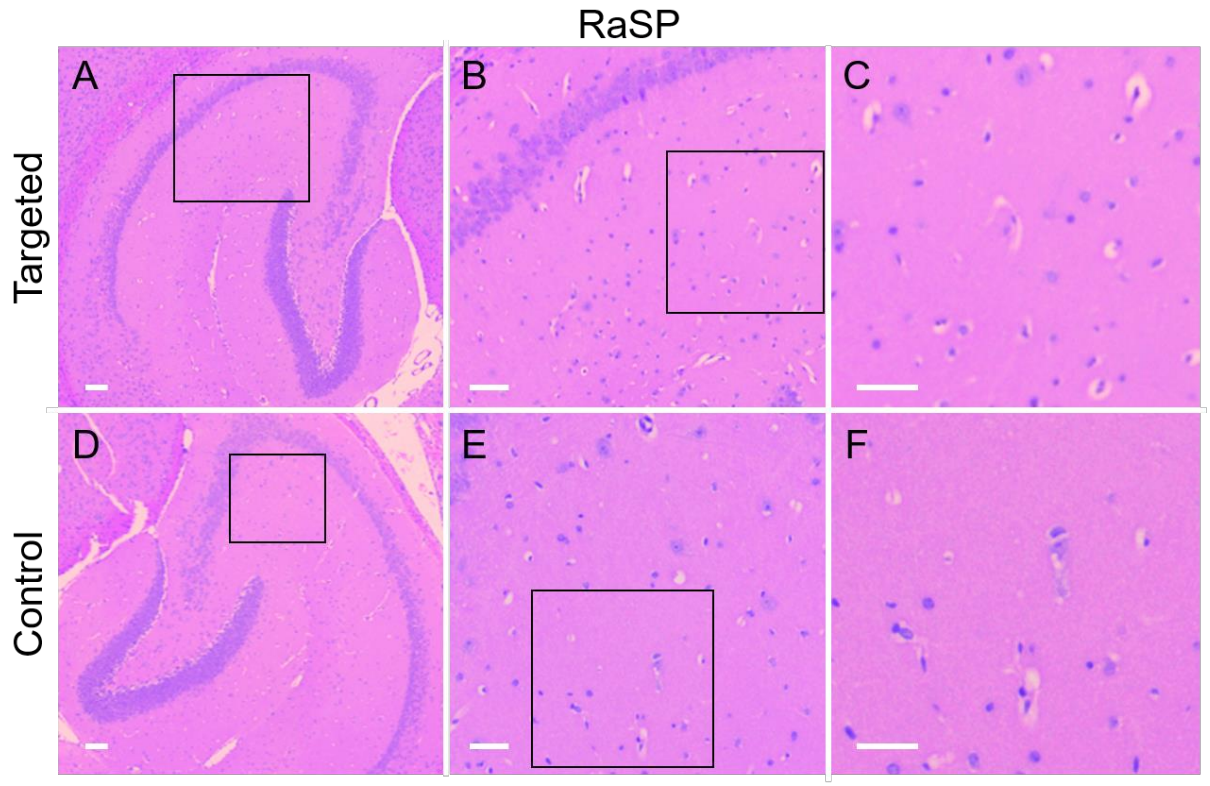

Figure 2.36. H&E staining on RaSP-treated brains to assess tissue damage. Microscopic examination of H&E stained **(A-C)** left (targeted) and **(D-F)** right (control) hippocampi of RaSP-treated brains show no histological damage. The black boxes inside the left and middle column images show which regions are enlarged in the middle and right columns respectively. The scale bars indicate 50 μm.

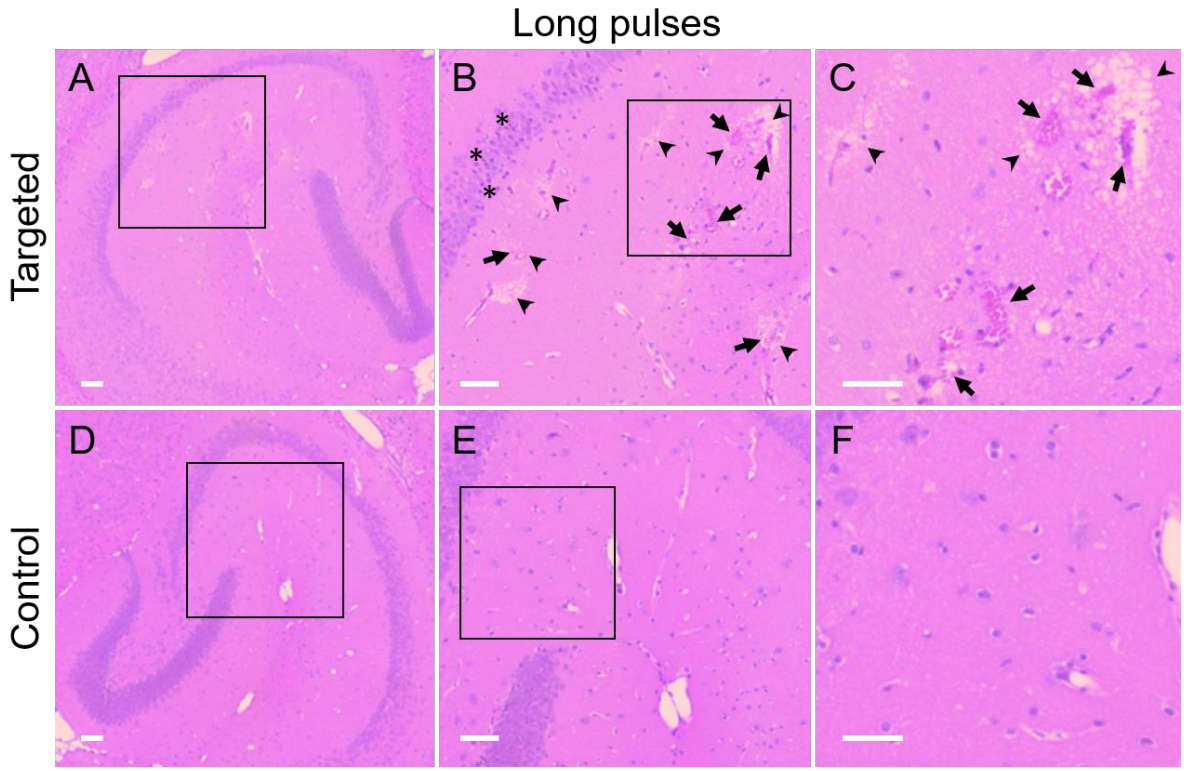

Figure 2.37. H&E staining on long-pulse-treated brains to assess tissue damage. Microscopic examination of H&E-stained **(A-C)** left (targeted) and **(D-F)** right (control) hippocampi of long-pulse-treated brains show histological damage at multiple sites within the ultrasound targeted hippocampus. The arrows point to red blood cell (RBC) extravasations, the arrowheads highlight areas of microvacuolations, and asterisks mark damaged neurons. The black boxes inside the left and middle column images show which regions are enlarged in the middle and right columns respectively. The scale bars indicate 50 μm.

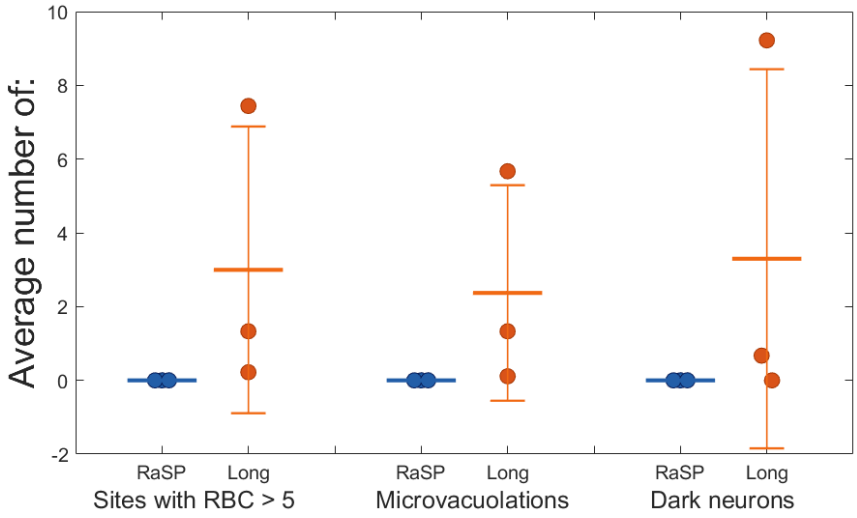

Figure 2.38. Number of sites with red blood cell extravasations, microvacuolations and dark neurons in RaSP and long pulse brains. The average number of sites with more than five extravasated red blood cells (RBCs), number of microvacuolations and number of dark neurons is shown for (blue) RaSP and (orange) long-pulse-treated brains. This quantification was performed on nine H&E-stained slices per brain. In all RaSP brains, no sites with more than five extravasated RBCs, microvacuolations or dark neurons were observed, whereas in long pulse brains, damaged sites were found in all brains. However, no statistical significance was found, due to the small sample size and high variation between brains.

2.4.7 Dextran excretion from the brain

To investigate how the distribution of dextran changed over time as it was excreted from the brain, fluorescence images of RaSP and long pulse brains, with dextran injected before the ultrasound treatment, were compared between 0 and 48 hours. In both RaSP and long-pulse-treated brains, over time, dextran was increasingly found in and around blood vessels rather than within the parenchyma (Figure 2.39-40). Uptake within cells also decreased over time, as previously shown (Figure 2.20). A similar trend was observed in both RaSP and long pulse brains, although the latter displayed a greater number of vessels with dextran uptake. Such movement of dextran from the parenchyma towards the blood vessels was expected, as the interstitial fluid clears compounds out of the brain by moving

them towards the perivenular space to postglymphatic sites, such as the subarachnoid CSF and meningeal lymphatics.

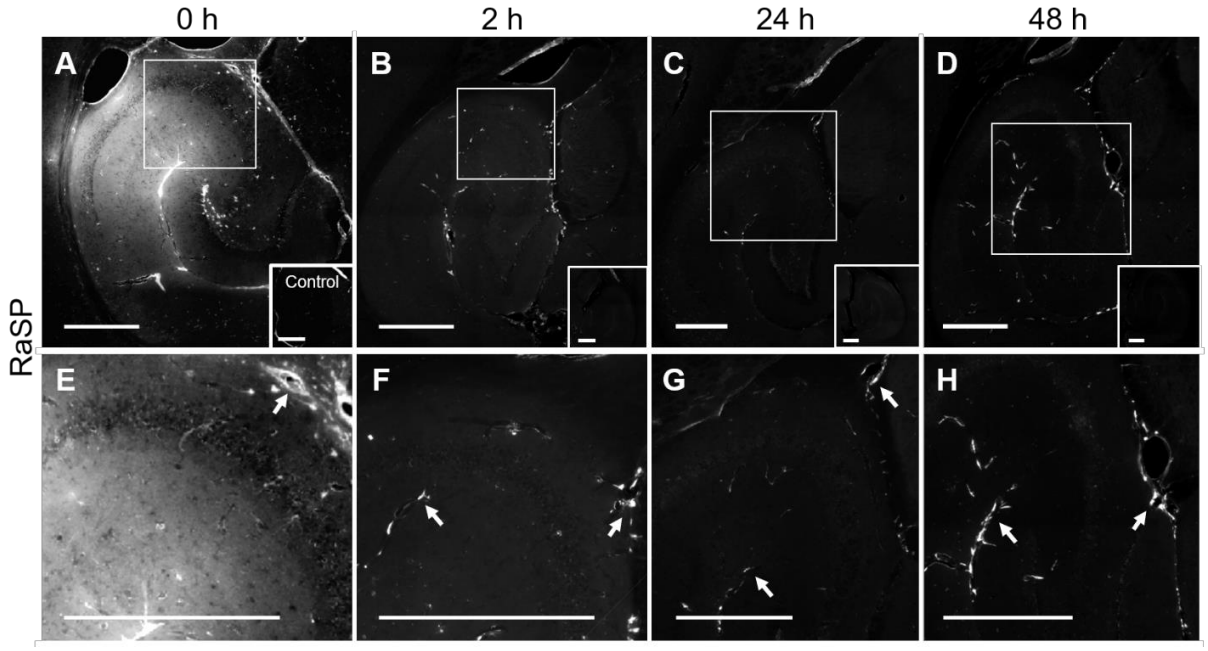

Figure 2.39. Dextran excretion from RaSP-treated brains between 0 and 48 h. Fluorescence images (10x) show the distribution of dextran throughout the hippocampus at **(A, E)** 0 h, **(B, F)** 2 h, **(C, G)** 24 h and **(D, H)** 48 h after ultrasound exposure with a RaSP sequence. Respective control right hippocampi are shown in the bottom right corner. Over time, dextran was increasingly found in and nearby blood vessels (white arrows), possibly in the perivenular space, rather than in the parenchyma. The white boxes inside images highlight **(E-H)** the enlarged regions in the row below. The scale bars indicate 500 µm.

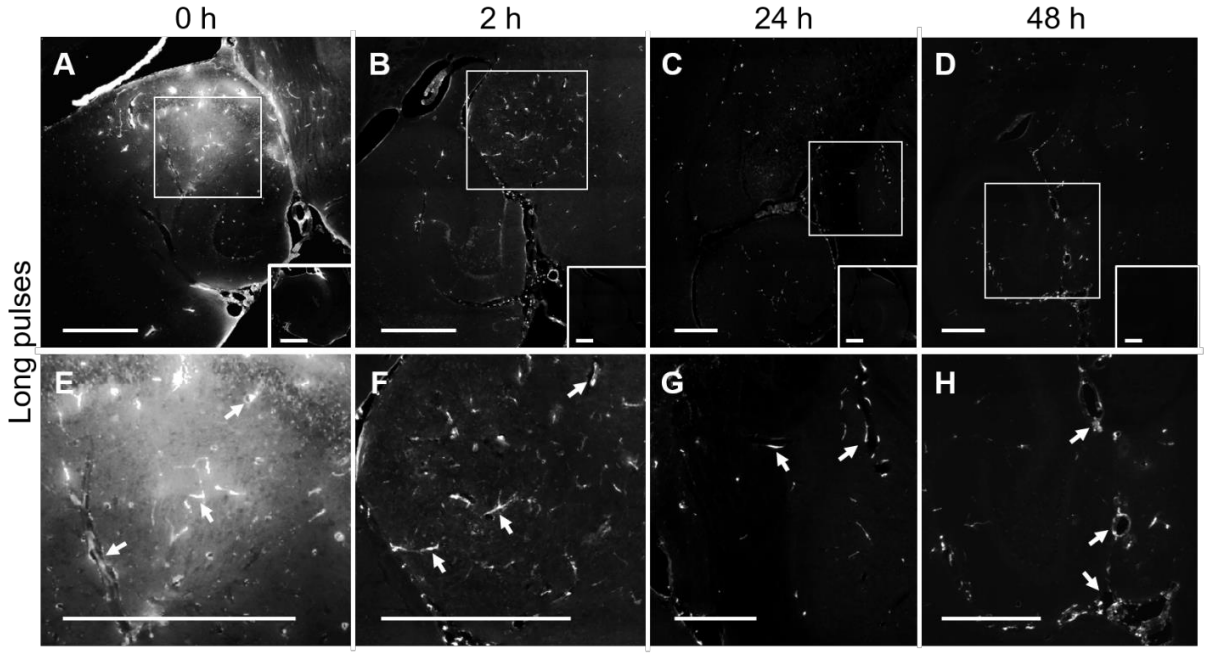

Figure 2.40. Dextran excretion from long-pulse-treated brains between 0 and 48 h. Fluorescence images (10x) show the distribution of dextran throughout the hippocampus at **(A, E)** 0 h, **(B, F)** 2 h, **(C, G)** 24 h and **(D, H)** 48 h after ultrasound exposure with a long pulse sequence. Respective control right hippocampi are shown in the bottom right corner. Over time, dextran was increasingly found in and nearby blood vessels (white arrows), possibly in the perivenular space, rather than in the parenchyma. The white boxes inside images highlight **(E-H)** the enlarged regions in the row below. The scale bars indicate 500 µm.

2.4.8 Predictability

To investigate whether the detected dose of dextran could be predicted from the energy of the acoustic emissions generated by the microbubbles, the normalised optical density was plotted against the sum of the acoustic energy from the microbubble emissions during the ultrasound treatment, which were recorded with the passive cavitation detector. With the RaSP sequence, the energy of the acoustic emissions correlated with the delivered dextran dose ($r = 0.97$), while with the long pulses, only a weak correlation was found ($r = 0.21$; Figure 2.41). Although lower sums of energy were detected from the microbubbles during RaSP treatments (duty cycle = 0.0000025%), dextran doses similar

to those delivered with long pulses (duty cycle = 0.005%) were achieved. The RaSP sequence was also found to be more efficient at delivering dextran to the brain than the long pulse sequence. While long pulses deposited 150 times more acoustic energy (cumulative energy over one burst) into the brain, only 70 times more energy was returned from the stimulated microbubbles to the passive cavitation detection system. This implied that a cycle in the RaSP sequence produced 2.2 times more acoustic energy than a cycle in the long pulse sequence.

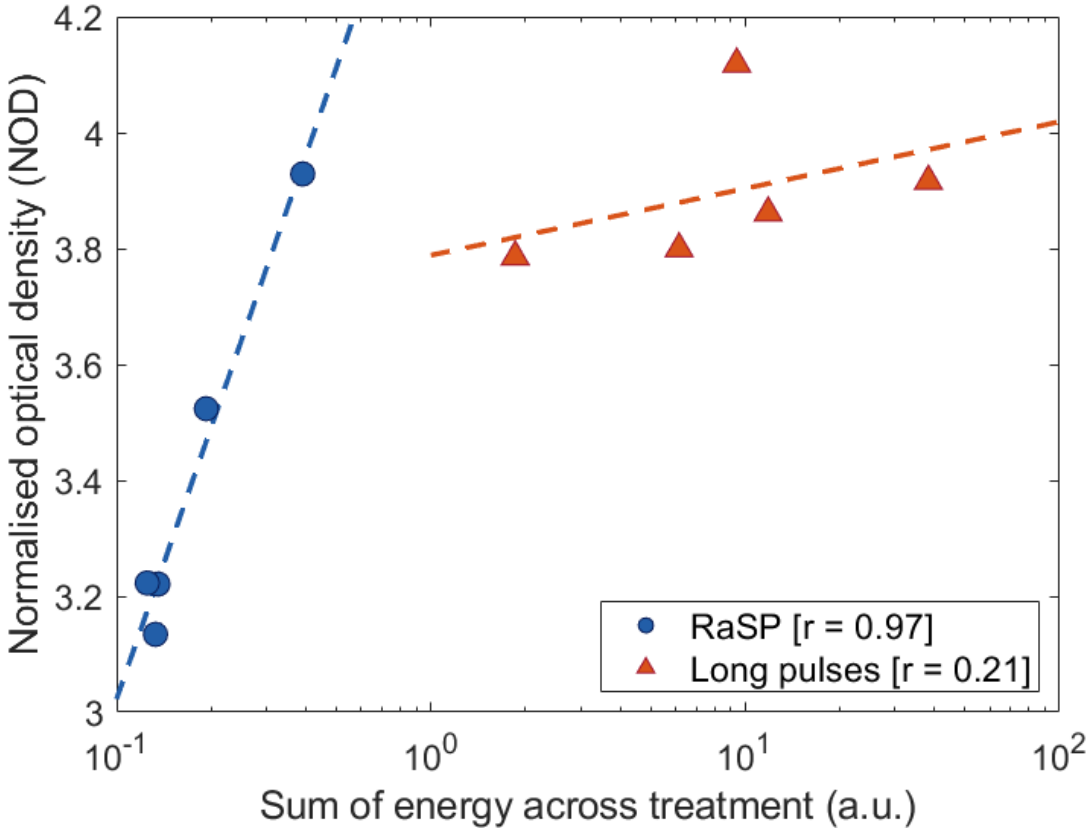

Figure 2.41. Predicting the detected dextran dose based on the energy of the acoustic emissions. The relationship between the detected dose of dextran and the energy of the acoustic emissions was found by plotting the normalised optical density (NOD) versus the sum of the uncalibrated acoustic energy from the microbubbles, generated during either a rapid short-pulse (RaSP, blue circles) or a long pulse (orange triangles) sequence. A strong correlation was found

with the RaSP sequence (r = 0.97), while with the long pulses, a weak linear relationship was observed (r = 0.21). Image from Morse et al, *Radiology*, 2019, 291:459-466.

2.4.9 Energy and lifetime of microbubble activity

The acoustic emissions generated by the microbubbles were analysed to understand how the microbubbles behaved in the brain. As expected, the uncalibrated energy of the acoustic emissions across the ultrasound treatment decreased over time (Figure 2.42). After being intravenously injected, microbubbles clear from the blood supply within a few minutes [96], [97] and during ultrasound excitation, the stimulated microbubbles can be destroyed. However, with the RaSP sequence, the acoustic emissions from the microbubbles maintained energies above the noise level for longer durations than the long pulse sequence did (Figure 2.42). The energy of the emissions did not return to the control level by the end of the treatment in all RaSP-treated brains, unlike with the long pulses. The time needed for the energy to reach 80% of its cumulative value (t_{80} constant) was twice as long for RaSP than for long pulses (Figure 2.43). These results could be due to a reduced level of microbubble destruction with the RaSP sequence, which deposits 150 times less acoustic energy into the tissue compared to the long pulse sequence.

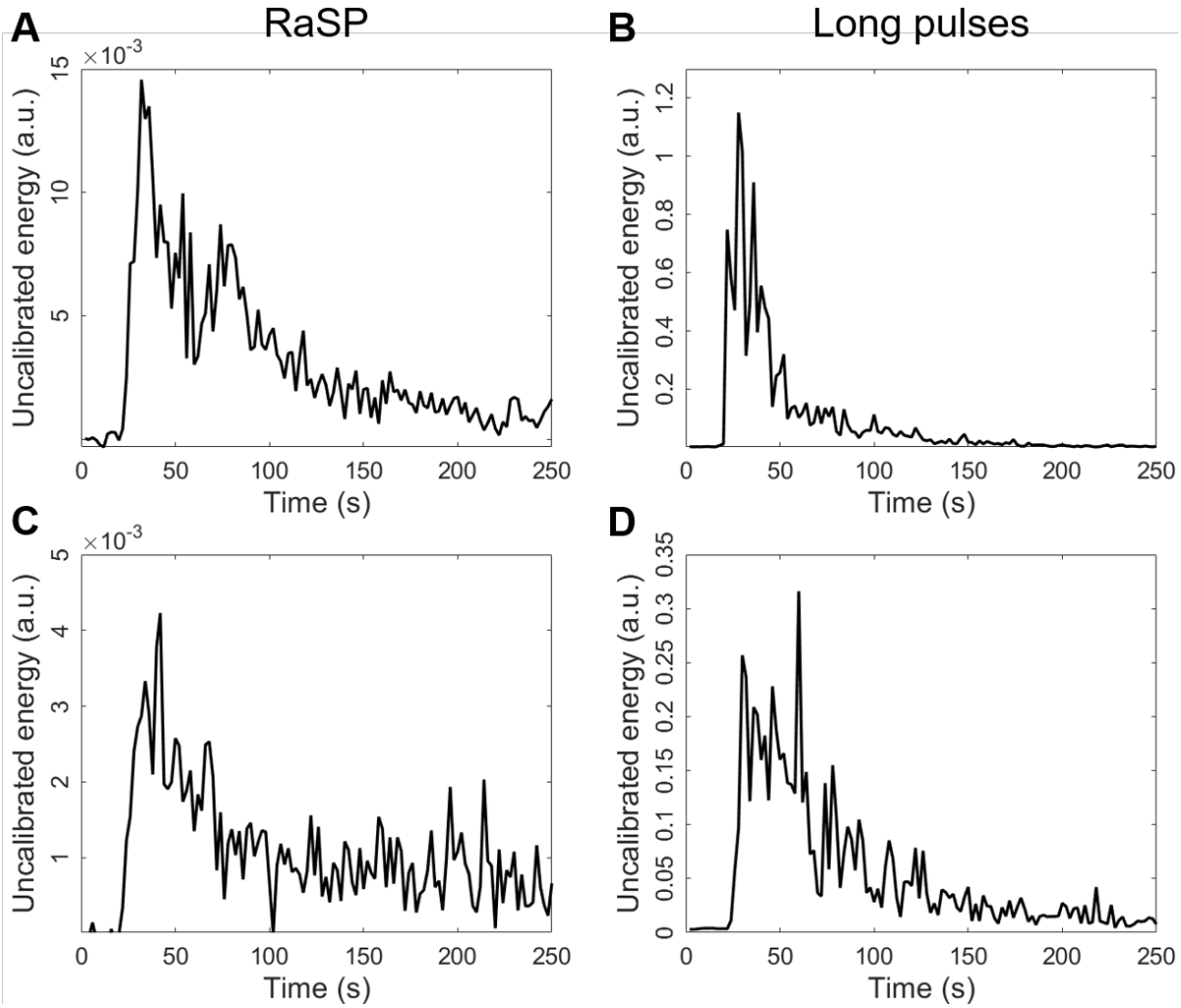

Figure 2.42. Energy from acoustic emissions during RaSP and long pulse sequence treatment. The uncalibrated energy (a.u.) during RaSP and long pulse ultrasound treatments (two examples shown per sequence type) shows the strength of the microbubble activity over time. The energy decreased with both sequences, as there were less microbubbles present in the bloodstream. However, with the RaSP sequence, the energy stayed above the control levels for a longer period of time. By the end of the RaSP treatment, the energy had not returned to the control level, while with the long pulses, it had. Image modified from Morse et al, *Radiology*, 2019, 291:459-466.

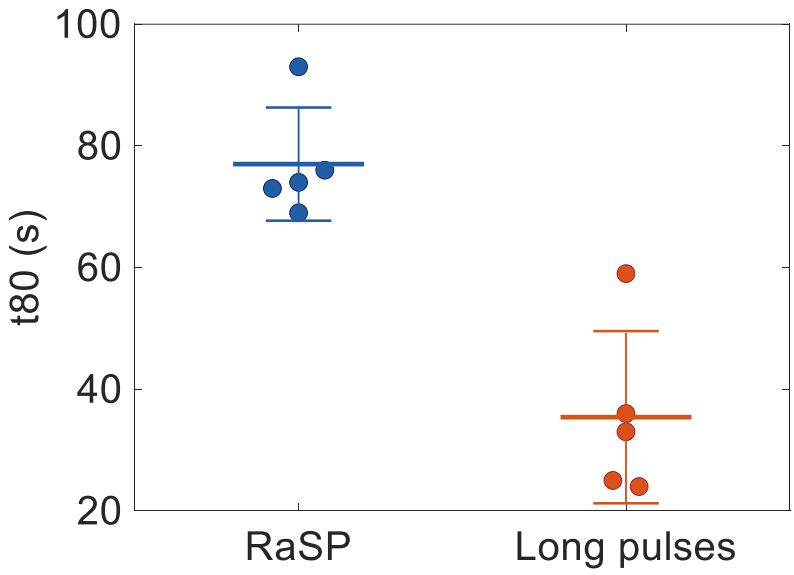

Figure 2.43. Lifetime of acoustic emissions from microbubbles. The time period taken for the energy to reach 80% of its cumulative value (t_{80}) was quantified to represent how long the microbubble activity was maintained, with the two pulse sequences. The t_{80} was twice as long for RaSP compared to the long pulses ($P < 0.001$). This image was modified from Morse et al, *Radiology*, 2019, 291:459-466.

In RaSP sequences, 13 pulses are rapidly emitted in a burst. From the acoustic emissions received in RaSP brains, the first of these pulses produced the highest energy, while the energy of subsequent pulses decreased (Figure 2.44). Energy levels, however, were maintained above the noise level within bursts across the entire sonication. The standard deviation of the energy from the initial pulses in the burst was higher than later pulses and a plateau was reached towards the end of the burst, with the energy of those pulses being more similar between each other and between bursts (Figure 2.44). Similar trends were observed by looking at the energy of each pulse throughout the ultrasound treatment, with the first pulse producing the highest energy during the treatment, although decreasing over time (Figure 2.45). The following few pulses maintained energy levels above the noise during the ultrasound treatment.

Overall, higher energy values – both the energy summed across the treatment and the maximum energy – were received by the PCD from long pulses than from RaSP (Table 2.7). The average sum of energy was 70x higher and the maximum energy 48x higher for long pulses than for RaSP. Energy values displayed more variation within long-pulse-treated brains, with some brains achieving much higher values than others.

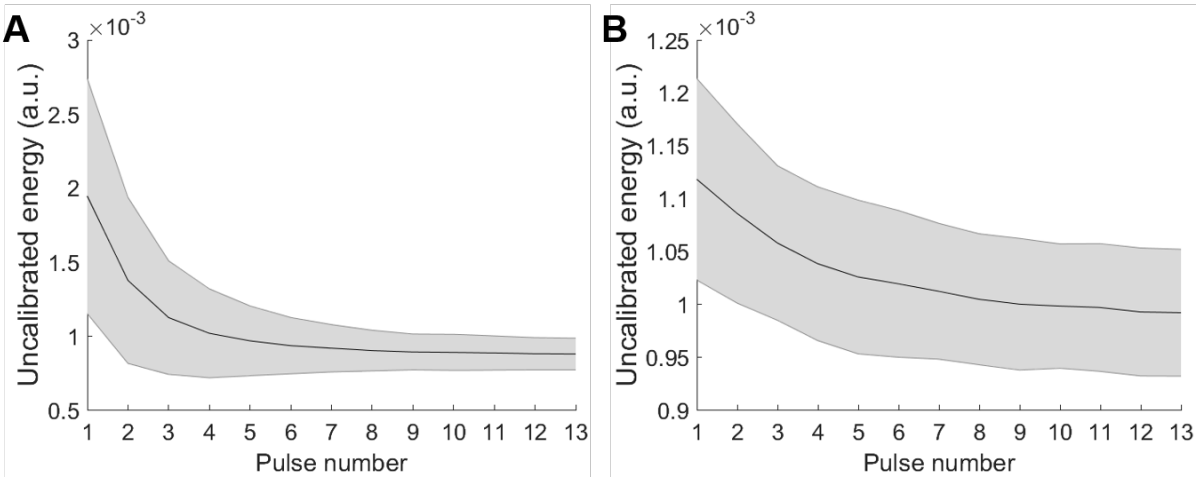

Figure 2.44. Average energy of each pulse within a burst during a RaSP treatment. (A-B) Two examples of the uncalibrated energy from the acoustic emissions for each pulse within a burst throughout the RaSP treatment show the average decrease in energy during a burst. The first pulse of each burst produced the highest energy and subsequent pulses decreased in energy within each burst. Energy levels were maintained above the noise level across the entire sonication. The data is presented as the mean ± standard deviation; the shaded area represents one standard deviation.

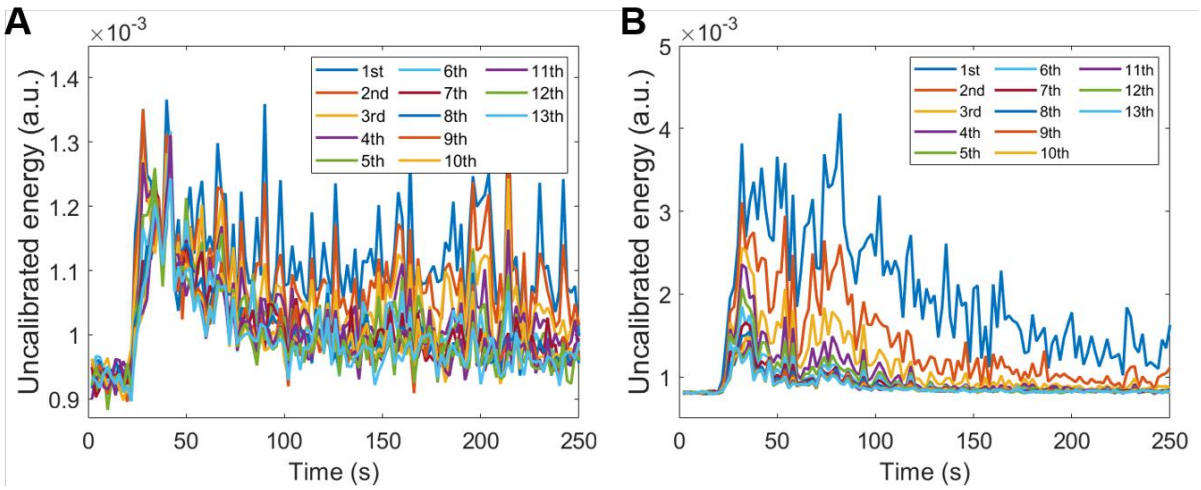

Figure 2.45. Energy of each pulse across the ultrasound treatment emitting a RaSP sequence. (A-B) Two examples of the uncalibrated energy from the acoustic emissions of each pulse (1^{st} – 13^{th}) throughout the ultrasound treatment with a RaSP sequence are shown. The energy of the first pulse produced the highest energy throughout the ultrasound treatment, with a decrease over time. Following pulses had lower energy and at least the first few pulses in the burst maintained energy levels above the noise throughout the ultrasound treatment.

Table 2.7. Sum and maximum uncalibrated energies from the acoustic emissions for all RaSP and long-pulse-treated brains. Average sum and maximum energy values are shown for each brain sonicated with both sequence types (energy unit: mV^2s).

Sequence type	Brain	Energy Sum	Energy max
RaSP	1st	0.193	0.005
	2nd	0.133	0.004
	3rd	0.391	0.146
	4th	0.135	0.005
	5th	0.125	0.004
	Average:	0.195 ± 0.113	0.0328 ± 0.063
Long pulses	1st	1.855	0.238
	2nd	6.163	0.313
	3rd	11.832	1.149
	4th	9.398	0.643
	5th	38.265	5.263
	Average:	13.503 ± 14.338	1.521 ± 2.122

2.4.10 Frequency content of microbubble emissions

To determine the type of microbubble activity generated during the ultrasound treatments, the spectral content of the microbubble emissions was analysed. The type of cavitation generated by the RaSP treatment was milder compared to that of the long pulses. With the long pulse sequence, broader emissions were observed in a few pulses in four out of the five brains, while such broadening was completely absent during RaSP treatments (Figure 2.46, Appendix Figure 6.16). These broader emissions suggest that higher magnitudes of inertial cavitation were being generated during the long pulse

treatment, possibly causing microbubbles to damage the surrounding tissue. Strong harmonic and ultraharmonic emissions were also observed with long pulses. The RaSP sequence, on the other hand, produced low magnitude harmonic emissions and very low magnitude ultraharmonic emissions, suggesting the microbubbles were undergoing stable non-inertial or low magnitude inertial cavitation. Broader harmonic emissions were observed compared to the long pulse sequence, due to the shorter pulse length in the time domain.

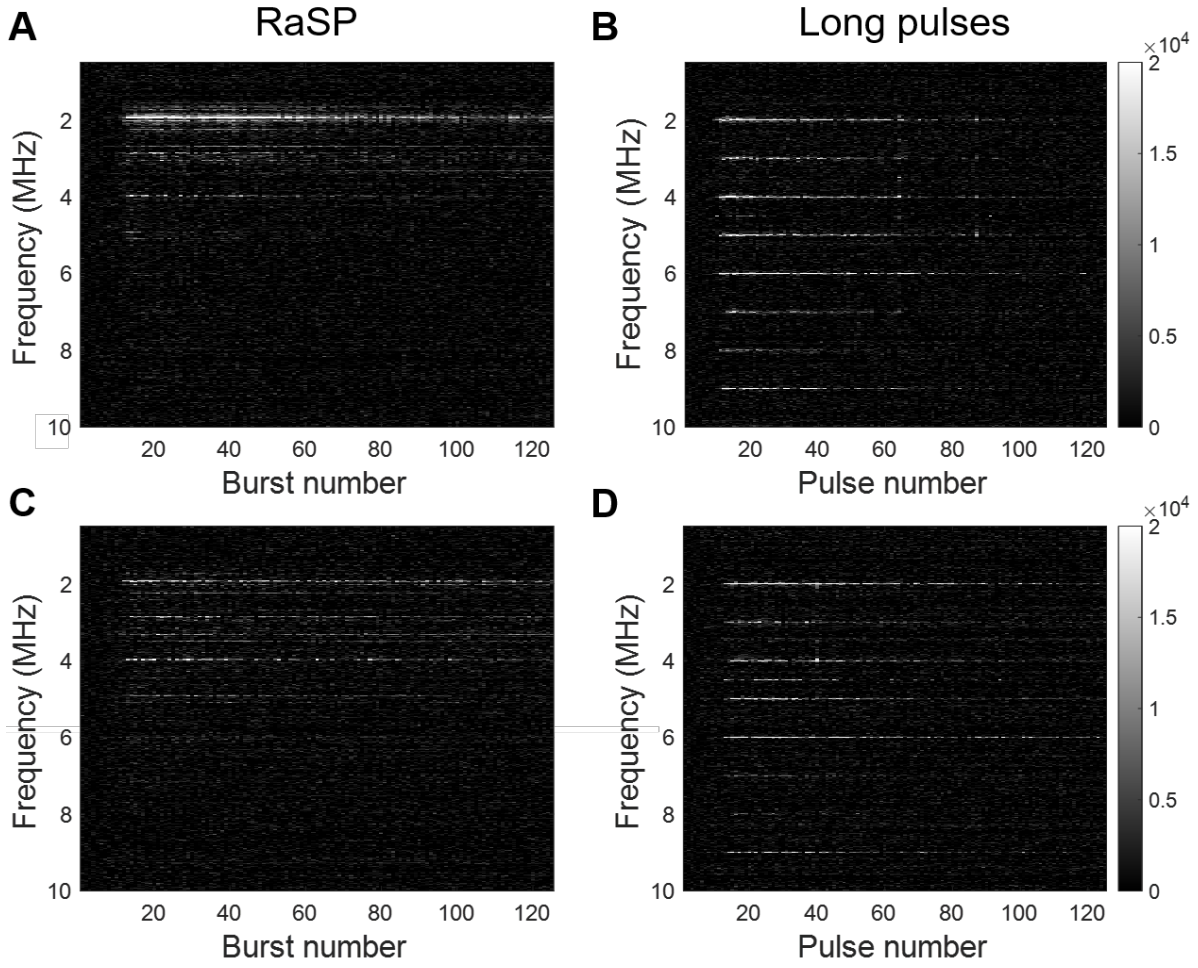

Figure 2.46. Spectral content of the acoustic emissions produced by RaSP and long pulse sequences. Spectral analysis of the acoustic emissions during treatment describes the type of cavitation produced with **(A, C)** RaSP and **(B, D)** long pulse sequences. Two examples are shown for each sequence type. The RaSP sequence produced lower magnitude harmonic emissions and

very low magnitude ultraharmonic emissions, while the long pulses produced broader emissions in some pulses and high magnitudes of high order harmonics and ultraharmonics. The harmonic emissions with RaSP were broader than those observed with the long pulses, due to the shorter pulse length. The colour bar indicates the magnitude of the Fourier Transform (F.T.). Image modified from Morse et al, *Radiology*, 2019, 291:459-466.

2.5 Discussion

In this chapter, ultrasound emitted in a RaSP sequence is shown to deliver a model drug homogeneously throughout the brain parenchyma, with reduced alterations to the normal BBB function. The BBB returned to its normal permeability within minutes and had a low level of endogenous proteins released into the brain. Uptake of our model drug was observed in neurons, and less so in microglia and astrocytes, which did not appear to have an activated morphology. The delivered dose could be predicted from the acoustic energy emitted from the stimulated microbubbles ($r = 0.97$) and no tissue damage was observable with H&E staining. This simultaneous improvement of efficacy and safety suggests that previous trade-offs in performance and safety with ultrasound drug delivery, as shown in numerous optimisation studies [2], [12], [17], [19], [75], [121], could be overcome by moving beyond traditional long pulse sequence designs.

The RaSP sequence was designed to have a short, low energy pulse and a rapid emission rate; these two characteristics need to be balanced to produce the improved drug delivery and safety shown here. Short pulses emitted at a slow rate have previously been shown to deliver drugs to the brain [2], [16], [17], [19]; however, they have either required higher acoustic peak-rarefactional pressures or produced a low probability and low dose of drug delivery. Short pulses emitted rapidly have been shown to deliver drugs in a diffuse pattern [17]. However, high peak-rarefactional pressures were used, no safety benefits were described and no direct comparison between short and long pulse sequences was provided. The RaSP sequence used here was optimised *in vitro* in previous work [13], [14],

[95], minimising the pulse energy and optimising the emission rate so microbubbles could be gently stimulated, allowing them to freely flow within the vasculature between pulses.

2.5.1 Delivery

Ultrasound emitted in a RaSP sequence achieved a more uniform drug delivery distribution compared to the long pulse sequence (Figure 2.14-15). The observed improvement in distribution with RaSP is thought to be the consequence of an improvement in the distribution of the stimulated microbubble activity within the vasculature, as well as a reduction in the magnitude and diversity of the microbubble activity [13], [14], [122]. Rather than increasing the probability and dose of drug delivery by increasing the magnitude of stress exerted by a microbubble on the capillary wall, a low magnitude of stress by the microbubbles was maintained by distributing this stress throughout the capillary network. To distribute the stress at a given capillary site, the microbubbles were stimulated with ultrasound pulses with low energy to reduce microbubble destruction so these bubbles could be stimulated again microseconds later. Short pulses alone, without being emitted at a high repetition frequency or being grouped into bursts, have not been able to produce better drug delivery because they have either required high pressures or delivered a low drug dose [2], [15], [16], [18], [19].

Despite applying 150 times less acoustic energy into the brain, the amount of drug detected was not significantly different between the two sequences ($P > 0.05$; Figure 2.15). This is thought to be due to the dextran not being concentrated in specific regions but being spread out within the parenchyma, reaching more cells and being uptaken by them. The distribution, on the other hand, was found to be significantly different ($P < 0.001$), showing less variation in the drug delivery in RaSP brains, an indication of this more uniform spread. With long pulses, a higher concentration of dextran was observed around blood vessels, which is likely caused by strong microbubble activities (e.g., inertial cavitation). The RaSP sequence was designed to stimulate the microbubbles more gently

and for a shorter duration, avoiding high drug accumulation around the blood vessels. RaSP is also thought to cause less microbubble aggregation, due to shorter periods of sound that cause bubble-to-bubble attractive interactions (secondary radiation forces). In previous *in vitro* work, long pulses were shown to increase the number and size of microbubble clusters [123], which could explain the greater vascular effects produced by the long pulses.

The pressure with which the pulses were emitted in both sequences was chosen based on the pressure threshold experiment, where long pulses were emitted at three different pressures. Delivery was only observed at the two higher pressures within both the main ultrasound focus and the upper side lobe region (Figure 2.12-13). These results show that when emitting long pulses, a pressure between 0.18 and 0.35 MPa is necessary to observe dextran delivery. The pressure in the side lobe is lower than in the main focus and is positioned 2 mm from the main lobe, which is exactly the distance observed between delivery regions in the fluorescence images at the two highest pressures with long pulses. If intermediate pressures between 0.18 and 0.35 MPa were tested, a more accurate threshold for delivery could be found. In addition, this threshold value will vary depending on the delivered compound; smaller compounds may only need lower pressures to deliver them across the BBB [3], [11]. This pressure threshold experiment was performed by emitting conventionally used long pulses and our findings are in agreement with previously reported studies [90], [124]–[126]. If this experiment were to be repeated at intermediate pressures using RaSP sequences, then the pressure threshold may have been found to be higher than for long pulses. With RaSP, delivery was indeed observed within the main ultrasound focus at 0.35 MPa but not in the upper side lobe. This could be considered advantageous as there is more control over where exactly the drug is being delivered. If these experiments were to be repeated with a different ultrasound setup, this pressure threshold experiment would need to be repeated, as it is dependent on the specific setup used.

Within the fluorescence images of the hippocampi, high intensity regions were not only observed within the brain parenchyma, but also at the edges of the brain and within the ventricles. These areas lit up due to the cerebrospinal fluid, which surrounds the brain, flowing in the subarachnoid space and within the ventricles. The model dextran drug was present in the CSF as well as in the blood vessels, as this fluid regulates the extracellular environment of the neurons, removing dextran from the brain.

2.5.2 Cellular uptake

When emitting ultrasound with a RaSP sequence, not only was the distribution of the drug delivery more uniform, but more cellular uptake was also observed (Figure 2.16-17). We hypothesise that this is the natural outcome of dextran being more uniformly delivered throughout the brain parenchyma at a high dose using RaSP, therefore reaching more of the brain cells. This distribution is advantageous when treating a diseased region, as it is ideal to have drugs and imaging agents reach all of the targeted parenchymal regions or cells, rather than having overtreated and undertreated areas with high accumulations in some regions and little or none in others, as observed with the long pulses.

In RaSP-treated brains, dextran was detected within neurons in higher quantities than in long-pulse-treated brains (Figure 2.19-21). Dextran has previously been used as a neuronal tracer [127], [128] and its presence near neurons may simply increase the likelihood of uptake. With long pulses, most of the dextran was concentrated around the blood vessels and not as uniformly spread within the parenchyma, which could be the cause of the lower neuronal uptake. The presence of dextran within neurons, which has also previously been reported in the hippocampus following ultrasound treatment [17], indicates that this technology could deliver drugs to a wide range of therapeutic targets, such as those on the cell membrane. Uptake within the neuronal cell bodies and their axons also indicates that intracellular targets could be reached. However, whether the delivered drug enters cells or not will depend on the properties of the specific drug, such

as size, charge and lipophilicity. Molecules could be designed with more favourable molecular properties to increase their cellular uptake if necessary.

We are uncertain why some neurons are uptaking the dextran while others are not. It is possible that some of the neurons with no dextran uptake simply require more time for uptake to occur or for the dextran to reach that specific region. There may also be preferential uptake of dextran in specific categories of neurons. In our experiments, preferential uptake appeared to occur in the neurogenic layer of neurons of the dentate gyrus, which future staining could confirm. Uptake could also be correlated with changes in neuronal activity. Staining for the *c-FOS* protein, which is an indirect marker of neuronal activity, as it is expressed when neurons fire action potentials [129]–[131], could confirm whether this is occurring. Another possibility is that these cells are in areas where not enough dextran has been delivered, such as in the periphery of the focal region. The cells could also be in a different imaging plane. There is also a possibility that dextran may have been uptaken by some neurons and have already been excreted by the time they were imaged. In future experiments, we could explore trends in the number of neurons with dextran uptake at intermediate time intervals to the ones already investigated. This could give an indication as to when the rate of dextran uptake within neurons is exceeded by its excretion rate.

Higher neuronal uptake was observed at the earlier time points compared to the later ones, using both RaSP and long pulses (Figure 2.20-21). Specifically, higher uptake in RaSP brains was observed at 0 and 2 h compared to 24 and 48 h, and in long pulse brains at 0 h compared to later time points. It is possible that even though the BBB permeability is returning to normal within 10 minutes in RaSP brains, similar levels of dextran uptake are present at 0 and 2 h due to the model drug having had more time to diffuse within the parenchyma, reaching more of the cells and being uptaken. However, between 2 and 24 h, the excretion of dextran might be greater than any new uptake. Dextran could be

excreted first from the neurons via transporters [132], [133], and then from the brain via normal excretion pathways, such as via the cerebrospinal fluid, which clears compounds out of the parenchyma to the perivenular space, and then along draining veins to postglymphatic clearance sites [80]. However, with long pulses, even though there is a prolonged increase in the permeability of the BBB, neuronal uptake is not only lower, but clearance pathways also seem to be activated sooner, between 0 and 2 h compared to the RaSP, where the strongest decrease occurs later between 2 and 24 h (Figure 2.20). This could be due to the higher concentrations of dextran in certain regions initiating an earlier excretion involving immune cells to remove the dextran sooner than in RaSP-treated brains.

The above results and discussion are based on the NeuN stain, which is a widely established neuron-specific marker [112], [134]. This stain can also be used to determine differences in the expression of this protein within cells, depending on the intensity of the NeuN staining. However, the staining varied significantly between brain slices, depending on the exact orientation of the slides when performing each staining step and on how well distributed the solutions were on each brain slice. It was therefore not possible here to quantify differences in intensity of NeuN staining between brains, or between targeted and control sides of the brain.

Significantly less dextran uptake was observed within glial cells, both microglia and astrocytes, when the RaSP sequence was used compared to long pulses ($P < 0.01$; Figure 2.23 and 2.26). In long pulse brains, similar levels of uptake were maintained in both cell types over time (0-48 h), while in RaSP-treated brains, little or no uptake was observed. Microglia reside nearly uniformly throughout the entire brain and have an important role in defending the brain and repairing tissue damage. Increased microglial uptake could be due to the long pulses disrupting the BBB more than the short pulses. Such disruption could lead to microglial activation and phagocytosis of the dextran to remove it from the

brain. The RaSP sequence, on the other hand, allows for a gentler stimulation of the blood vessels, which is hypothesised to be the reason for the reduced glial cell uptake and the lack of glial cell activation.

The microglia uptaking dextran in long-pulse-treated brains displayed a rounded amoeboid-like shape, a sign of activation, while those in RaSP brains did not (Figure 2.22). Microglia are capable of exhibiting phagocytotic activity under both quiescent and reactive states [32], [135], [136]. Data has also suggested that when microglia are phagocytosing compounds, they are not activated in the same way as an inflammatory challenge would [135]. These findings could explain why with RaSP, the cells were ramified and not activated, yet still uptaking the dextran. With long pulses, on the other hand, there was not only uptake but also activation, which could be due to an inflammatory stimulus caused by the ultrasound treatment or by the high concentrations of dextran, rather than by the phagocytotic activity.

Previous studies have reported microglial processes to undergo changes within minutes, with morphological changes to the entire microglia occurring within an hour [32]. The brain parenchyma is thought to be screened by resting microglia once every few hours. However, depending on the stimulus, microglia have been shown to respond within different time frames. With laser-induced lesions, for example, a microglial response was observed within 20 minutes [32]. In ultrasound treated brains, microglia also responded within the first few minutes following treatment. Depending on the stimulus, microglial activation can last for days and if such activation is sustained, then it can result in chronic inflammation and damage to the brain tissue [44], [45]. In long-pulse-treated brains, the number of microglia uptaking the dextran did not decrease between 0 and 48 h. Future experiments will be done to assess at what time point such uptake and activation decreases.

In future work, it would be interesting to investigate the number of microglia within the targeted area that are activated rather than in a resting state. To do so, staining for CD68, a lysosomal membrane marker, will be performed, as it is expressed only in activated microglia and not in resting ones [137]. The Iba1 staining performed here, on the other hand, stains all microglia. In addition, to make quantification of activation possible, fluorescence images will need to be acquired with at least 20x magnification, or DAB (3,3'-diaminobenzidine) staining would need to be performed.

In a similar way to microglia, astrocytes were also found to uptake dextran more in long-pulse-treated brains. Little or no uptake was observed in RaSP brains (Figure 2.25-27). This could be due to similar reasons to those pointed out for microglial uptake differences: more disruption to the BBB or higher concentrations of dextran leading to an increased response of the astrocytes to phagocytose the dextran and remove it from the brain. Astrocytes not only play an essential role in regulating brain functions, supporting neuronal survival and controlling blood flow, but also have a strong phagocytic capacity [138]. The number of astrocytes uptaking dextran did not decrease significantly between 0 and 48 h. Therefore, future experiments are needed to establish for how long the astrocytes display this phagocytotic behaviour, which might depend on the length of time dextran stays in the brain.

Differently from microglia, the astrocytes uptaking dextran did not display observable morphological changes associated with reactivity, such as an increase in size of the cell processes, nor was the GFAP stain intensity stronger due to increased GFAP expression [120]. Astrocytes have been shown previously to display no morphological changes, which were instead observed in microglia [32]. Depending on the lesion, however, astrocyte reactivity has been detected in previous studies at different time points: in some cases a few hours, and in others, days after the lesion occurred [120]. Depending on the insult to the brain, the reactive state of astrocytes has been shown to persist for hours, days or

even years [139]. It is hypothesised that astrocytes might become reactive at later time points in our experiments, which will be explored in future experiments. It is also possible that dextran is being uptaken by astrocytes as a nutrient for neurons. Evidence in previous studies suggests that astrocytes uptake glucose, metabolise it and transport the lactate product to neighbouring neurons as their primary metabolic fuel [140], [141].

In future work, astrocyte staining will be performed not only with GFAP, but also S100β, a calcium binding protein, which stains all mature astrocytes [50], [142]. One of the limitations of GFAP staining is that it is not an absolute marker for all non-reactive astrocytes and is often not detectable in astrocytes in healthy tissue [50]. In addition, GFAP does not label all portions of astrocytes, as it is not present throughout the cytoplasm and only the main stem branches are labelled [50]. The extent of astrocyte branching could therefore be underestimated in our stained brain slices.

2.5.3 Time window for delivery

The BBB returned to its normal permeability within 10 minutes from the ultrasound treatment in RaSP-treated brains, which is the fastest reported so far (Figure 2.28-29). With long pulses, dextran still entered the brain 20 minutes after the treatment, indicating that the permeability was increased for longer periods of time. Previous studies have shown a reduction in the time the BBB permeability increase lasted by lowering the pulse lengths and reducing the peak rarefactional pressures emitted [60], [143]. Our results confirm these findings and show a significantly reduced return to normal BBB function compared to when long pulses were used. This reduction is thought to be due to the better spatio-temporal distribution of microbubble activity within the blood vessels and stable cavitation being maintained, which would reduce the probability of unnecessary tissue damage. With long pulses, the BBB has been shown to remain open for several hours (4-48 h), depending on the parameters used and the sensitivity of the permeability assessment method [60], [143]. The exact duration of enhanced BBB permeability, upon

emitting these long pulses with our setup, would need to be explored in the future. These prolonged opening times can be considered useful for the delivery of long-circulating drugs that require large drug doses to be delivered into the brain. However, it is important to consider the safety aspects of having a non-intact BBB for that duration of time, not only with more drugs getting into the brain, but also other toxic bloodborne substances. On the other hand, RaSP led to a very short increase in BBB permeability, providing a safer delivery profile. If the drugs to be delivered required long periods of enhanced extravasation to have a therapeutic effect, then longer sonication durations and longer microbubble infusions could be used.

Future work will explore whether we can adjust the duration of enhanced BBB permeability by changing the ultrasound pulse shape and sequence parameters. There will, however, be a trade-off between efficacy and safety – the longer the BBB is open for, the more time the delivered agent and other bloodborne substances have to extravasate into the brain. Particularly for some diseases, the side effects caused by a prolonged BBB enhancement might outweigh the beneficial effects of achieving a higher agent delivery. It may also be the case, that to achieve a longer opening time, parameters that provide less control over the type and magnitude of the microbubble activity occurring need to be used. These decisions will need to be made depending on the situation. Lastly, it is important to note that the duration of enhanced BBB permeability will also vary depending on the size of the molecule being delivered. The smaller the molecule, the more likely it is that the duration of BBB increase will be enough to allow its extravasation for longer. For example, the same sized opening may not allow a 3 kDa dextran molecule across, but it may allow a smaller MRI contrast agent into the brain. In addition, the less sensitive the technique used to assess the closing process is, the shorter the duration of the increased permeability is going to appear. As an example, *in vivo* magnetic resonance imaging is likely to be less sensitive compared to *ex vivo* fluorescence microscopy.

2.5.4 Extravasation of endogenous proteins

Overall, the extravasation of albumin and immunoglobulin was lower in RaSP-treated brains compared to those treated with long pulses. Albumin was detected at 0 minutes in RaSP brains in a 4.7 times lower dose compared with long pulses. However, no detectable levels above the control were found at later time points with RaSP. This result suggests that the albumin that entered the brain at 0 minutes was removed from the brain within 10-20 minutes. The presence of albumin within the brain parenchyma has been previously associated with the activation of microglia and astrocytes, as well as the production of molecules such as cytokines and chemokines, normally observed in a sterile inflammatory response to injury [25], [144]. The extravasation of albumin observed in RaSP brains at 0 minutes could be leading to a response from these phagocytic cells, encouraging its rapid removal from the brain. On the other hand, in long pulse brains, the amount of albumin extravasating into the brain is not only higher, but albumin is also still present within the brain 20 minutes after the sonication. This result could be due to the BBB not closing within that time frame as it does with RaSP, which would therefore allow more albumin to extravasate over this time period. In long-pulse-treated brains, the amount of albumin still entering the brain seems to be outweighing the rate at which the brain can remove the extravasated albumin from the brain within this time frame.

These albumin extravasation results could be linked to the amount of dextran uptake and activation of glial cells observed in the different brains. It is possible that the activation of microglia with long pulses is linked not only to possible tissue damage caused by the microbubbles within the vasculature, but also to the extravasation of albumin and dextran themselves. The higher albumin extravasation with long pulses could be a reason for the greater glial cell involvement and higher dextran uptake within glial cells observed, particularly since the clearance of albumin following focused ultrasound treatment has been previously shown to be mediated by glial rather than neuronal cells [71].

Although albumin (67 kDa) entered the brain at 0 minutes, immunoglobulin (150 kDa) did not, indicating that the increased permeability of the blood-brain barrier has a size threshold that will not allow the larger immunoglobulin proteins into the brain when emitting ultrasound with a RaSP sequence. With long pulses, however, both proteins extravasated into the brain at all time points, indicating a higher size threshold compared to that of the RaSP sequence. These results confirm previous studies that report a size-threshold in delivery using focused ultrasound [3], [11], [17], [111], [145]. However, this also means that the extravasation of other compounds with similar characteristics to albumin and immunoglobulin (such as large size) could also be limited when using RaSP. This limitation could both be an advantage or a disadvantage depending on whether the agent in question is a beneficial drug or imaging agent, or a harmful foreign substance that is not meant to be in the brain. Ideally, however, we want the barrier to be open enough for our delivered agent of interest to reach the brain in high enough quantities and for the extravasation of other bloodborne substances and larger agents to be minimal or avoided. If the delivered agent were to be an antibody of a similar size to albumin or immunoglobulin, ways to circumvent this problem could be found by delivering nanobodies instead, which will be tested in future work.

When comparing their distribution within the brain, dextran was detected in regions where albumin and immunoglobulin were not, suggesting that the delivery pattern is dependent on the properties of the molecule. In this case, dextran is significantly smaller than both endogenous proteins, which could be the reason for dextran reaching areas in the brain that albumin and immunoglobulin did not.

2.5.5 Safety profile

The lack of histological damage in RaSP-treated brains confirms the improved safety profile of this sequence compared to that of long pulses. Although both sequences were emitted at the same acoustic pressure, 150 times less energy was inputted by using RaSP.

The tissue damage observed in long pulse brains was mostly located around blood vessels, suggesting that these effects are caused by microbubble activity, most probably inertial cavitation, as a result of focused ultrasound exposure. Previous studies have reported similar findings regarding tissue damage at pressures comparable to ours, found to be around the threshold for inertial cavitation in such studies [146]–[149]. The dark necrotic neurons were mainly found in the pyramidal layers of the hippocampus and in locations thought to be ischemic, distal to severed vessels, which would reduce blood flow, leading to ischemic regions and acute necrosis.

Although we only assessed tissue damage in brains sacrificed immediately after the ultrasound treatment, we would expect microvacuolations to occur as an immediate consequence of the mechanical forces from the microbubbles. It is possible, that red blood cells extravasate and neurons become damaged at later time points. However, the effect of focused ultrasound on the vasculature and surrounding tissue has been suggested to be immediate and not progressive over time [12]. Future work will analyse tissue damage at later time points to assess whether long-term functional and behavioural changes that we have not quantified here are taking place. H&E staining alone is insufficient to fully understand histological damage, as inflammatory molecules, glial cells and axons cannot be identified. Here, we have analysed glial cell involvement in addition to H&E; however, other techniques will be performed in future studies, such as TUNEL to assess cell damage, and long-term behavioural and functional studies. Although no significant differences were observed between the H&E quantifications for RaSP and long pulses, a larger sample size would highlight the significance of such differences, as RaSP brains here showed no histological damage at all.

2.5.6 Dextran excretion

Across 48 h, in both RaSP and long-pulse-treated brains, dextran was found to be less distributed in the parenchyma and cells, but more around the blood vessels. These

observations could be explained by the bulk flow of interstitial fluid and cerebrospinal fluid through the parenchyma, which would move the dextran towards peri-venular spaces and eventually back into the subarachnoid space and clearance sites. This clearance pathway has recently been proven to occur in humans as well as in rodents [80], [150]–[152]. In general, dextran has been shown to be excreted from the bloodstream within hours, with the liver, spleen and lungs being the main organs involved in uptaking dextran, depending on its size [153]. However, we did not know how long to expect dextran to be present within the brain following ultrasound exposure.

A greater number of vessels showed dextran uptake with long pulses compared to RaSP-treated brains. First, this could be explained by the fact that the BBB remained open for longer periods of time in long-pulse-treated brains, allowing more dextran to extravasate into the brain while also being cleared. Second, our evidence suggests that the disruption in long-pulse-treated brains is higher than in RaSP brains. This higher disruption could lead to a slower clearance of the dextran from the vessels, which may be damaged due to the inertial cavitation activity of the microbubbles.

2.5.7 Acoustic emissions analysis and predictability

Detecting acoustic emissions with a passive cavitation detector during sonications can be a useful tool to create a real-time feedback system [154]–[156]. These systems can be used to predict the delivered dose and determine whether acoustic emissions associated with adverse effects have been avoided. In this study, the time traces of the acoustic emissions were plotted in real-time to evaluate whether microbubble activity was being detected. Whenever the uncalibrated energy from these microbubble emissions was higher than that of the control pulses, delivery was observed. Following the experiments, signals were processed to identify the magnitude, duration and type of cavitation activity occurring, to then link these results back to the delivered distributions observed and any adverse effects.

By analysing the energy of the acoustic emissions across the sonication, we found that in a RaSP sequence, the microbubble activity lasted for longer periods of time (Figure 2.42). Microbubble activity was not only maintained across the sonication but also across the 13 pulses emitted within a burst, with a more than double t_{80} value throughout all bursts compared to the long pulse sequence (Figure 2.43). The energy of each pulse across the sonication followed similar trends to the overall energy sum (Figure 2.44). However, it also highlighted that the first few short pulses within each burst had the highest energy, which did not decrease back down to control levels by the end of the sonication. These results were confirmed by analysing the average energy of each pulse within a RaSP burst (Figure 2.44). These findings are indicative of microbubble persistence and improved temporal distribution of the cavitation activity. With long pulses, however, the emissions decreased more rapidly, often reaching control levels before the end of the sonication (Figure 2.42 B, D), a trend that has been observed in previous studies [13], [14], [87], [88].

From the frequency domain analysis, we found that the received acoustic emissions during the RaSP sonications lacked broadband emissions, while long pulse treatments showed signs of broader signals around harmonics and ultraharmonics. This is likely due to the more gentle, low pressure, short pulse length stimulation by the RaSP sequence, which is less likely to generate inertial cavitation [7], [157], [158]. These results suggest that the increased control over the distribution of microbubble activity can lead to a more predictable drug delivery, as observed from our *in vivo* experiments.

Our acoustic emissions show that by emitting ultrasound in a RaSP sequence, we are improving the temporal distribution of microbubble activity *in vivo*. Despite emitting 150 times less energy overall, RaSP delivered a similar drug dose to the long pulse sequence. This result indicates that the higher energies inputted with the long pulses are unnecessary to create the desired bioeffect. If anything, the long pulses are delivering drugs inefficiently at high doses to certain regions only. We also found that the energy of

the acoustic emissions summed across the sonication correlated strongly with the amount of detected drug delivered. These preliminary results suggest that the acoustic emissions from the microbubbles exposed to a RaSP sequence may be a good predictor of the delivered drug dose. Previous studies have also reported correlations between acoustic emissions and the dose of delivered agents, specifically with emissions related to non-inertial cavitation [155], [156], [159]–[162]. The strong correlation found could be explained by our hypothesis that RaSP is more efficiently stimulating microbubble activity that is responsible for drug delivery across the BBB. By reducing bubble destruction emitting low-pressure short pulses, we believe a more uniform delivery is being achieved. This delivery is also thought to be easier to predict in comparison with the spotty pattern delivered with the long pulses.

In the future, a larger sample size will be needed to establish whether this correlation can be used to reliably predict the extent of permeability enhancement and drug delivery. This will also be useful to establish whether the correlation is much lower when emitting long pulses. The low correlation that was found here is mainly due to one of the brains displaying a much higher delivered drug dose (NOD) compared to the other brains. With a larger sample size, we will be able to establish whether this is an outlier.

To establish differences in the spatial distribution of the microbubble activity during RaSP and long pulse treatments, future work will focus on using passive acoustic mapping (PAM). PAM is a technique which uses a transducer array instead of a single element [163] and has previously been used to monitor cavitation activity during ultrasound-mediated BBB enhancement [91], [164], [165]. We will incorporate a linear array into our setup to analyse the spatial distribution of microbubble activity within the brain using both sequences.

2.4.8 Clinical relevance

The improved efficacy and safety of delivery achieved with our RaSP sequence could benefit the treatment of many neurological diseases, such as Alzheimer's disease, Parkinson's disease and brain tumours. These diseases are difficult to treat due to the disease developing and spreading throughout the healthy brain tissue while being protected by an intact BBB. Alzheimer's disease, for example, is characterised by an extensive distribution of plaques that affect large parts of the brain. The uniform delivery pattern obtained with RaSP allows the delivered drug to fully cover the intended region of the ultrasound focus, without over- or under-dosing certain regions. With RaSP, the BBB returns to its normal permeability within minutes, preventing large amounts of unwanted compounds into the brain, thereby reducing the likelihood of long-term side effects. For long-term chronic disorders, such as neurodegenerative diseases, that may need repeated drug delivery sessions, minimising these side effects is essential.

Cancer treatment would also benefit from this sequence, allowing a more uniform treatment of the core and periphery of tumours. Many brain tumours, such as glioblastoma, have a leaky tumour core but the margins are protected by an intact BBB. Focused ultrasound-mediated delivery has already been used to deliver adenoviruses, antibodies, genes and liposomes into tumours [166]–[169]. However, in these studies, long pulses were emitted, resulting in inhomogeneous drug distributions [167], [168]. The use of rapid, short-pulsed ultrasound could overcome the limitations of long pulses, reducing the damage to healthy brain tissue at tumour margins, allowing a safer and more efficient delivery of drugs.

RaSP could also be advantageous when delivering imaging agents for the diagnosis of brain diseases, such as Alzheimer's and metastases, or to study the brain and its disorders. In such applications, the process of delivering diagnostic or function-altering agents should not significantly modify the tissue being imaged. The RaSP treatment reduces the

disturbance to the delivered region when compared to the most common currently used ultrasound pulses and particularly in comparison with other delivery techniques, such as direct injections through the skull and healthy brain tissue [170].

Delivery with RaSP sequences is not limited to the brain and could also have uses in other applications involving ultrasound and microbubbles. For example, we expect that the improved distribution of microbubble activity stimulated with RaSP could be used to deliver molecules across the capillaries of other organs and diseases, to deliver drugs into cells (sonoporation) [171]–[173], and to release drugs from microbubbles and liposomes [167].

2.5.9 Limitations and future work

Despite the improved efficacy and safety that RaSP has enabled when delivering agents to the brain, the possibility of further improving these features remains.

Altering the BBB permeability, even if for a short duration, not only allows the drug of interest to enter the brain, but also unwanted bloodborne compounds. We have observed that both dextran (3 kDa) and albumin (67 kDa) extravasate into the brain when a RaSP sequence is emitted, but immunoglobulin (150 kDa) does not. This suggests that there is a molecular size threshold and possibly a different transfer rate for these molecules. The distribution of dextran and albumin was also found to be slightly different, with dextran delivered in regions where albumin was not, within the area targeted with ultrasound. This molecular size threshold could vary throughout the ultrasound beam, with differences also depending on the type, magnitude, duration and distribution of the cavitation activity. These results signify that if these exact ultrasound parameters were used, then only molecules below a certain size would be able to enter the brain, most probably with the threshold being between the size of albumin and immunoglobulin. Whether a molecule crosses the BBB or not, will not only depend on its size, but also on its overall net charge and lipophilicity. The molecule's affinity for carrier or receptor-mediated

transport, hydrogen bonding potential and affinity for efflux mechanisms are all factors to consider when delivering agents across the BBB [11].

In addition, due to the short duration of BBB permeability increase, over the course of hours, RaSP may deliver lower drug yields into the brain compared to long pulses. Thus, further refinement of the ultrasound technology, in terms of the RaSP sequence parameters, microbubbles administered and the device emitters and sensors [163], [174], [175], may provide better control over the cavitation activity generated *in vivo*, which could lead to greater control of the BBB permeability change. The ultrasound parameters in this new RaSP sequence, such as centre frequency, pressure, pulse length, repetition frequency and total number of pulses emitted, have not yet been optimised for delivery dose. Exploring the changes both in cavitation and drug delivery distribution caused by changing parameters such as the pulse repetition frequency will help gain a deeper understanding of the capabilities and mechanism of how these pulses work. It may be possible to alter the BBB permeability for a very narrow range of molecular sizes, which could prevent albumin and other foreign compounds from entering the brain. Equally, the sequence could be adjusted to enable the delivery of larger molecules, such as liposomes, antibodies and viruses, which with the current RaSP parameters are predicted to be difficult to deliver efficiently with a RaSP sequence.

A trade-off between efficacy and safety is most likely to still exist. By increasing parameters such as acoustic pressure, larger agents and higher doses will be delivered, although some safety aspects would likely be compromised. The RaSP sequence, however, can achieve higher drug doses with less compromise in safety compared to long pulses, due to higher doses being delivered to the parenchyma of the brain rather than being concentrated around blood vessels. Our results so far are related to the delivery of 3 kDa dextran, so future work will establish how the factors investigated here will change depending on the properties of the delivered compound.

In future work, we seek to understand how the rapid short-pulse sequence delivers compounds across the BBB and how this differs from delivery using long pulses. There could be a different mechanism of delivery, which currently is thought to be mostly due to paracellular rather than transcellular transport, as a consequence of the size threshold, as with the long pulses. However, the mechanism might actually be similar between the sequence types, with the difference being in the magnitude of mechanical stress exerted by the microbubbles on the vessel walls. Towards this aim, ongoing fundamental *in vitro* microscopy work is being performed during ultrasound exposure in live tissue sections, enabling both the microbubble activity and bioeffects to be observed and correlated.

We will also characterise the long-term effects of RaSP-mediated drug delivery, looking into whether we are causing cell death, triggering an inflammatory response at a gene and protein expression level, and behavioural effects. Blood samples could be analysed to establish how long the drug stays within the bloodstream. Any toxic side effects caused by the drug being delivered could be analysed by looking at the liver and kidneys.

We not only plan to optimise the RaSP sequence design, depending on the molecule to be delivered, but also the microbubbles and their protocol of administration. The findings in this study were obtained using polydisperse microbubbles. In the future, we will use monosized microbubbles, which may provide further control of the cavitation activity and type of bioeffects created. It may also be beneficial to infuse the microbubbles continuously rather than inject them as a bolus. Also, the microbubble concentration used in these experiments is higher than the clinical dose. Future experiments will establish whether this higher microbubble dose is necessary to achieve the improved efficacy and whether lower doses would improve the drug delivery process at all.

In terms of the ultrasound frequency used in this work, 1 MHz was chosen as it is an appropriate frequency to target all regions of a mouse brain. However, to target regions through a human skull, we will test RaSP with lower ultrasound frequencies in larger

animal models. At 1 MHz, ultrasound would be significantly attenuated when travelling through the thick human skull. However, lower frequencies will attenuate less, allowing deeper brain regions to be targeted. In this study, the mechanical index, which can be used to gauge the likelihood of mechanical bioeffects occurring [176], was calculated to be 0.35 ($MI = P_{neg}/\sqrt{f_c}$, Table 2.1, Appendix 6.1). When testing lower frequencies, this index will increase unless the pressure is also decreased. As a reference, when ultrasound contrast agents are used, the FDA has established that the MI should not exceed 0.8 [177], [178]. Lastly, in terms of heating effects, the maximum temperature increase during our sonication was calculated to be lower than 1 mK (Appendix 6.2). Temperature increases smaller than 1.5 °C (274.65 K) are not considered a hazard to human or animal tissue even if maintained indefinitely [179]. Since our temperature increase with both RaSP and long-pulse sequences was below 1 mK, it was considered negligible. The thermal index for cranial bone (TIC), which measures the likelihood of thermal bioeffects being created by the ultrasound beam on the skull, was calculated to be 1.8×10^{-5}. Since guidelines indicate that the TIC should be kept below 1 [180], we did not consider thermal effects on the skull to be an issue.

In terms of the methods used in this chapter, many future improvements have already been highlighted throughout the discussion. However, more generally, repeat experiments, will be performed in the future to increase sample sizes, which in some experiments such as H&E and duration of BBB enhancement did not reach a high enough power (80%).

Passive cavitation detection was used as an efficient and inexpensive method to verify the presence of microbubbles and identify the type of cavitation activity taking place. However, information regarding the spatial distribution of the microbubble activity cannot be provided by this technique. Methods such as passive acoustic mapping will be used instead in the future [163], [174], [175]. Regarding our frequency analysis, the fast

Fourier transform (FFT) was used to analyse both long pulse and RaSP emissions. However, this transform produces an average frequency amplitude across the duration of the inputted signal. For steady and long pulse signals this method works well, however, for short pulses the FFT will underestimate the frequency amplitude generated by the microbubbles, as it will average the short signal with the noise signal around it. Future work will explore the short time Fourier transform (STFT) or Stockwell transform (S-transform) as an alternative technique to better analyse the spectral content of the acoustic emissions captured during RaSP sonications.

It is also important to note the limitations of some of the quantification methods used throughout this study. The NOD and COV quantifications for the dose and distribution of the drug delivered are highly sensitive to the presence of any artefacts and therefore, to the selected regions of interest. Antibody staining can be very inhomogeneous, with some areas appearing brighter than others, which could be interpreted as a higher expression of the target. However, no conclusions were based on the level of intensity of the staining. Future work will focus on staining some of the target cells of interest, such as microglia and astrocytes, with alternative markers. To stain for all non-reactive astrocytes as well as reactive ones, brain slices will be stained for S100β, a calcium-binding protein [56]. To know how many microglia within the targeted area are in an activated rather than a resting state, staining for CD68, a lysosomal membrane marker, will be carried out [137]. Future staining will also be performed to assess the integrity of blood vessels and tight junction proteins.

Lastly, in this study, our new RaSP sequence was compared to long pulses emitted at the same acoustic pressure and with bursts of thirteen five cycle pulses being compared to the emission of 10,000 cycle pulses. This comparison was made to show how designing the pulse shape and sequence is important in terms of the drug delivery observed. We

were not aiming to compare exactly the same amount of energy being inputted by the two pulse sequences, although this could be explored in the future.

2.6 Conclusions

A rapid short-pulse sequence has been proposed as a method to deliver drugs non-invasively to the brain with improved efficacy and safety compared to conventionally used long pulse sequences. To our knowledge, we have used the lowest acoustic energy reported in the literature to deliver drugs across the BBB. RaSP sequences delivered drugs uniformly throughout the parenchyma and with comparable drug doses to a standard long pulse sequence. By prolonging the lifetime of the microbubbles, the RaSP sequence spreads the cavitation activity spatially and temporally, which is thought to avoid regions of tissue over-treatment, thus improving the therapeutic and safety outcome. High delivery efficiency was achieved while altering the permeability of the BBB for less than 10 minutes and minimising the levels of endogenous albumin and immunoglobulin released into the brain. These results support our hypothesis that the RaSP sequence increases our control over the cavitation distribution, with the lowest reported duration of BBB permeability increase to date, no histological damage observed and less involvement of immune responsive glial cells.

Real-time monitoring of the acoustic emissions showed good correlation between the microbubble energy and the detected amount of drug delivered. Such improvements were achieved with 150 times less acoustic energy deposited into the brain, suggesting that raising the energy does not always improve performance. The structure of the ultrasound sequence should be instead considered in concert with the tissue structure, its vascular flow and the ultrasound beam shape. We anticipate that the rapid short-pulse sequence can be designed and optimised for different purposes, such as for sonoporation and sonothrombolysis. As a delivery technique, rapid short-pulse ultrasound sequences

could be used to deliver compounds more efficiently and safely for the treatment, diagnosis and study of neurological diseases.

2.7 References

[1] J. J. Choi, M. Pernot, S. A. Small, and E. E. Konofagou, "Noninvasive, transcranial and localized opening of the blood-brain barrier using focused ultrasound in mice," *Ultrasound Med. Biol.*, vol. 33, no. 1, pp. 95–104, 2007.

[2] J. J. Choi, K. Selert, Z. Gao, G. Samiotaki, B. Baseri, and E. E. Konofagou, "Noninvasive and localized blood-brain barrier disruption using focused ultrasound can be achieved at short pulse lengths and low pulse repetition frequencies," *J. Cereb. Blood Flow Metab.*, vol. 31, no. 2, pp. 725–737, 2011.

[3] J. J. Choi, S. Wang, Y. S. Tung, B. Morrison, and E. E. Konofagou, "Molecules of Various Pharmacologically-Relevant Sizes Can Cross the Ultrasound-Induced Blood-Brain Barrier Opening in vivo," *Ultrasound Med. Biol.*, vol. 36, no. 1, pp. 58–67, 2010.

[4] K. Hynynen, N. McDannold, N. A. Sheikov, F. A. Jolesz, and N. Vykhodtseva, "Local and reversible blood-brain barrier disruption by noninvasive focused ultrasound at frequencies suitable for trans-skull sonications," *Neuroimage*, vol. 24, no. 1, pp. 12–20, 2005.

[5] N. McDannold, N. Vykhodtseva, S. Raymond, F. A. Jolesz, and K. Hynynen, "MRI-guided targeted blood-brain barrier disruption with focused ultrasound: Histological findings in rabbits," *Ultrasound Med. Biol.*, vol. 31, no. 11, pp. 1527–1537, 2005.

[6] D. McMahon, W. Oakden, and K. Hynynen, "Investigating the effects of dexamethasone on blood-brain barrier permeability and inflammatory response following focused ultrasound and microbubble exposure," *Theranostics*, vol. 10, no. 4, pp. 1604–1618, 2020.

[7] J. Tu, T. J. Matula, A. A. Brayman, and L. A. Crum, "Inertial cavitation dose produced in ex vivo rabbit ear arteries with Optison® by 1-MHz pulsed ultrasound," *Ultrasound Med. Biol.*, vol. 32, no. 2, pp. 281–288, 2006.

[8] H. L. Liu *et al.*, "Hemorrhage Detection During Focused-Ultrasound Induced Blood-Brain-Barrier Opening by Using Susceptibility-Weighted Magnetic Resonance Imaging," *Ultrasound Med. Biol.*, vol. 34, no. 4, pp. 598–606, 2008.

[9] J. H. Hwang, J. Tu, A. A. Brayman, T. J. Matula, and L. A. Crum, "Correlation between inertial cavitation dose and endothelial cell damage in vivo," *Ultrasound Med. Biol.*, vol. 32, no. 10, pp. 1611–1619, 2006.

[10] J. E. Chomas, P. Dayton, D. May, and K. Ferrara, "Threshold of fragmentation for ultrasonic contrast agents," *J. Biomed. Opt.*, vol. 6, no. 2, p. 141, 2001.

[11] H. Chen and E. E. Konofagou, "The size of blood-brain barrier opening induced by focused ultrasound is dictated by the acoustic pressure," *J. Cereb. Blood Flow Metab.*, vol. 34, no. 7, pp. 1197–1204, 2014.

[12] B. Baseri, J. J. Choi, Y. S. Tung, and E. E. Konofagou, "Multi-modality safety assessment of blood-brain barrier opening using focused ultrasound and definity microbubbles: A short-term study," *Ultrasound Med. Biol.*, vol. 36, no. 9, pp. 1445–1459, 2010.

[13] A. N. Pouliopoulos, C. Li, M. Tinguely, V. Garbin, M.-X. Tang, and J. J. Choi, "Rapid short-pulse sequences enhance the spatiotemporal uniformity of acoustically driven microbubble activity during flow conditions," *J. Acoust. Soc. Am.*, vol. 140, no. 4, pp. 2469–2480, 2016.

[14] A. N. Pouliopoulos, S. Bonaccorsi, and J. J. Choi, "Exploiting flow to control the in vitro spatiotemporal distribution of microbubble-seeded acoustic cavitation activity in ultrasound therapy," *Phys. Med. Biol.*, vol. 59, no. 22, pp. 6941–6957, 2014.

[15] B. Zhao *et al.*, "Blood-brain barrier disruption induced by diagnostic ultrasound combined with microbubbles in mice," *Oncotarget*, vol. 9, no. 4, pp. 4897–4914, 2018.

[16] K. Hynynen, N. McDannold, H. Martin, F. A. Jolesz, and N. Vykhodtseva, "The threshold for brain damage in rabbits induced by bursts of ultrasound in the presence of an ultrasound contrast agent (Optison®)," *Ultrasound Med. Biol.*, vol. 29, no. 3, pp. 473–481, 2003.

[17] J. J. Choi, K. Selert, F. Vlachos, A. Wong, and E. E. Konofagou, "Noninvasive and localized neuronal delivery using short ultrasonic pulses and microbubbles," *Proc. Natl. Acad. Sci. U. S. A.*, vol. 108, no. 40, pp. 16539–16544, 2011.

[18] K. F. Bing, G. P. Howles, Y. Qi, M. L. Palmeri, and K. R. Nightingale, "Blood-Brain Barrier (BBB) Disruption Using a Diagnostic Ultrasound Scanner and Definity® in Mice," *Ultrasound Med. Biol.*, vol. 35, no. 8, pp. 1298–1308, 2009.

[19] M. A. O'Reilly, A. C. Waspe, M. Ganguly, and K. Hynynen, "Focused-Ultrasound Disruption

of the Blood-Brain Barrier Using Closely-Timed Short Pulses: Influence of Sonication Parameters and Injection Rate," *Ultrasound Med. Biol.*, vol. 37, no. 4, pp. 587–594, 2011.

[20] J. Silburt, N. Lipsman, and I. Aubert, "Disrupting the blood–brain barrier with focused ultrasound: Perspectives on inflammation and regeneration," *Proceedings of the National Academy of Sciences of the United States of America*, vol. 114, no. 33. pp. E6735–E6736, 2017.

[21] D. Mcmahon, R. Bendayan, and K. Hynynen, "Acute effects of focused ultrasound-induced increases in blood-brain barrier permeability on rat microvascular transcriptome," *Sci. Rep.*, vol. 7, 2017.

[22] D. McMahon and K. Hynynen, "Acute inflammatory response following increased blood-brain barrier permeability induced by focused ultrasound is dependent on microbubble dose," *Theranostics*, vol. 7, no. 16, pp. 3989–4000, 2017.

[23] D. McMahon, E. Mah, and K. Hynynen, "Angiogenic response of rat hippocampal vasculature to focused ultrasound-mediated increases in blood-brain barrier permeability," *Sci. Rep.*, vol. 8, no. 1, 2018.

[24] Z. I. Kovacs, S. R. Burks, and J. A. Frank, "Reply to Silburt et al.: Concerning sterile inflammation following focused ultrasound and microbubbles in the brain," *Proceedings of the National Academy of Sciences of the United States of America*, vol. 114, no. 33. pp. E6737–E6738, 2017.

[25] Z. I. Kovacsa *et al.*, "Disrupting the blood-brain barrier by focused ultrasound induces sterile inflammation," *Proc. Natl. Acad. Sci. U. S. A.*, vol. 114, no. 1, pp. E75–E84, 2017.

[26] Z. I. Kovacs *et al.*, "MRI and histological evaluation of pulsed focused ultrasound and microbubbles treatment effects in the brain," *Theranostics*, vol. 8, no. 17, pp. 4837–4855, 2018.

[27] R. M. Ransohoff, "How neuroinflammation contributes to neurodegeneration," *Science*, vol. 353, no. 6301. pp. 777–783, 2016.

[28] T. H. Palpagama, H. J. Waldvogel, R. L. M. Faull, and A. Kwakowsky, "The Role of Microglia and Astrocytes in Huntington's Disease," *Front. Mol. Neurosci.*, vol. 12, 2019.

[29] R. Masgrau, C. Guaza, R. M. Ransohoff, and E. Galea, "Should We Stop Saying 'Glia' and 'Neuroinflammation'?," *Trends in Molecular Medicine*, vol. 23, no. 6. pp. 486–500, 2017.

[30] J. L. Frost and D. P. Schafer, "Microglia: Architects of the Developing Nervous System," *Trends in Cell Biology*, vol. 26, no. 8. pp. 587–597, 2016.

[31] L. J. Lawson, V. H. Perry, P. Dri, and S. Gordon, "Heterogeneity in the distribution and morphology of microglia in the normal adult mouse brain," *Neuroscience*, vol. 39, no. 1, pp. 151–170, 1990.

[32] A. Nimmerjahn, F. Kirchhoff, and F. Helmchen, "Neuroscience: Resting microglial cells are highly dynamic surveillants of brain parenchyma in vivo," *Science (80-.).*, vol. 308, no. 5726, pp. 1314–1318, 2005.

[33] C. N. Parkhurst *et al.*, "Microglia promote learning-dependent synapse formation through brain-derived neurotrophic factor," *Cell*, vol. 155, no. 7, pp. 1596–1609, 2013.

[34] H. Wake, A. J. Moorhouse, S. Jinno, S. Kohsaka, and J. Nabekura, "Resting microglia directly monitor the functional state of synapses in vivo and determine the fate of ischemic terminals," *J. Neurosci.*, vol. 29, no. 13, pp. 3974–3980, 2009.

[35] R. C. Paolicelli *et al.*, "Synaptic pruning by microglia is necessary for normal brain development," *Science (80-.).*, vol. 333, no. 6048, pp. 1456–1458, 2011.

[36] M. Ě. Tremblay, R. L. Lowery, and A. K. Majewska, "Microglial interactions with synapses are modulated by visual experience," *PLoS Biol.*, vol. 8, no. 11, 2010.

[37] A. Karperien, H. Ahammer, and H. F. Jelinek, "Quantitating the subtleties of microglial morphology with fractal analysis," *Frontiers in Cellular Neuroscience*, no. JANUARY 2013. pp. 1–34, 2013.

[38] C. T. Ekdahl, "Microglial activation-tuning and pruning adult neurogenesis," *Front. Pharmacol.*, 2012.

[39] D. Boche, V. H. Perry, and J. A. R. Nicoll, "Review: Activation patterns of microglia and their identification in the human brain," *Neuropathology and Applied Neurobiology*, vol. 39, no. 1. pp. 3–18, 2013.

[40] A. Crotti and C. K. Glass, "The choreography of neuroinflammation in Huntington's disease," *Trends in Immunology*, vol. 36, no. 6. pp. 364–373, 2015.

[41] E. E. Benarroch, "Microglia: Multiple roles in surveillance, circuit shaping, and response to injury," *Neurology*, vol. 81, no. 12. pp. 1079–1088, 2013.

[42] M. E. Lull and M. L. Block, "Microglial Activation and Chronic Neurodegeneration," *Neurotherapeutics*, vol. 7, no. 4, pp. 354–365, 2010.

[43] Y. Nakagawa and K. Chiba, "Role of microglial M1/M2 polarization in relapse and remission of psychiatric disorders and diseases," *Pharmaceuticals*, vol. 7, no. 12. pp. 1028–1048, 2014.

[44] M. L. Monje, H. Toda, and T. D. Palmer, "Inflammatory Blockade Restores Adult Hippocampal Neurogenesis," *Science (80-.).*, vol. 302, no. 5651, pp. 1760–1765, 2003.

[45] G. Ellrichmann, C. Reick, C. Saft, and R. A. Linker, "The role of the immune system in Huntington's disease," *Clinical and Developmental Immunology*, vol. 2013. 2013.

[46] J. Koenigsknecht-Talboo and G. E. Landreth, "Microglial phagocytosis induced by fibrillar β-amyloid and IgGs are differentially regulated by proinflammatory cytokines," *J. Neurosci.*, vol. 25, no. 36, pp. 8240–8249, 2005.

[47] X. Qiao, D. J. Cummins, and S. M. Paul, "Neuroinflammation-induced acceleration of amyloid deposition in the APPV717F transgenic mouse," *Eur. J. Neurosci.*, vol. 14, no. 3, pp. 474–482, 2001.

[48] M. Simard and M. Nedergaard, "The neurobiology of glia in the context of water and ion homeostasis," *Neuroscience*, vol. 129, no. 4, pp. 877–896, 2004.

[49] E. E. Benarroch, "Neuron-astrocyte interactions: Partnership for normal function and disease in the central nervous system," in *Mayo Clinic Proceedings*, 2005, vol. 80, no. 10, pp. 1326–1338.

[50] M. V. Sofroniew and H. V. Vinters, "Astrocytes: Biology and pathology," *Acta Neuropathol.*, vol. 119, no. 1, pp. 7–35, 2010.

[51] B. A. Macvicar and E. A. Newman, "Astrocyte regulation of blood flow in the brain," *Cold Spring Harb. Perspect. Biol.*, vol. 7, no. 5, pp. 1–15, 2015.

[52] A. Verkhratsky and M. Nedergaard, "Physiology of astroglia," *Physiol. Rev.*, vol. 98, no. 1, pp. 239–389, 2018.

[53] K. Govindpani *et al.*, "Vascular Dysfunction in Alzheimer's Disease: A Prelude to the Pathological Process or a Consequence of It?," *J. Clin. Med.*, vol. 8, no. 5, p. 651, 2019.

[54] J. L. Zamanian *et al.*, "Genomic analysis of reactive astrogliosis," *J. Neurosci.*, vol. 32, no. 18, pp. 6391–6410, 2012.

[55] U. Wilhelmsson *et al.*, "Redefining the concept of reactive astrocytes as cells that remain within their unique domains upon reaction to injury," *Proc. Natl. Acad. Sci. U. S. A.*, vol. 103, no. 46, pp. 17513–17518, 2006.

[56] M. V. Sofroniew, "Molecular dissection of reactive astrogliosis and glial scar formation," *Trends in Neurosciences*, vol. 32, no. 12. pp. 638–647, 2009.

[57] L. Ben Haim, M. A. Carrillo-de Sauvage, K. Ceyzériat, and C. Escartin, "Elusive roles for reactive astrocytes in neurodegenerative diseases," *Frontiers in Cellular Neuroscience*, vol. 9, no. AUGUST. 2015.

[58] A. Buffo, C. Rolando, and S. Ceruti, "Astrocytes in the damaged brain: Molecular and cellular insights into their reactive response and healing potential," *Biochemical Pharmacology*, vol. 79, no. 2. pp. 77–89, 2010.

[59] M. Pekny *et al.*, "Astrocytes: a central element in neurological diseases," *Acta Neuropathologica*, vol. 131, no. 3. pp. 323–345, 2016.

[60] G. Samiotaki and E. E. Konofagou, "Dependence of the reversibility of focused-ultrasound-induced blood-brain barrier opening on pressure and pulse length in vivo," *IEEE Trans. Ultrason. Ferroelectr. Freq. Control*, vol. 60, no. 11, pp. 2257–2265, 2013.

[61] N. Sheikov, N. McDannold, S. Sharma, and K. Hynynen, "Effect of Focused Ultrasound Applied With an Ultrasound Contrast Agent on the Tight Junctional Integrity of the Brain Microvascular Endothelium," *Ultrasound Med. Biol.*, vol. 34, no. 7, pp. 1093–1104, 2008.

[62] Z. Zea-Aragón, N. Terada, N. Ohno, Y. Fujii, T. Baba, and S. Ohno, "Effects of anoxia on serum immunoglobulin and albumin leakage through blood-brain barrier in mouse cerebellum as revealed by cryotechniques," *J. Neurosci. Methods*, vol. 138, no. 1–2, pp. 89–95, 2004.

[63] Merck, "Antibody Basics," *Merck products*, 2020. https://www.sigmaaldrich.com/technical-documents/articles/biology/antibody-basics.html (accessed Feb. 26, 2020).

[64] L. Biosolutions, "Albumin (ALB)," *Lee Biosolutions products*, 2020. https://www.leebio.com/product/1273/albumin-alb-mouse-serum-101-50 (accessed Feb. 26, 2020).

[65] K. M. Knudsen Sand, M. Bern, J. Nilsen, H. T. Noordzij, I. Sandlie, and J. T. Andersen, "Unraveling the interaction between FcRn and albumin: Opportunities for design of

albumin-based therapeutics," *Frontiers in Immunology*, vol. 6, no. JAN. 2015.

[66] P. G. Matz, A. Lewén, and P. H. Chan, "Neuronal, but not microglial, accumulation of extravasated serum proteins after intracerebral hemolysate exposure is accompanied by cytochrome c release and DNA fragmentation," *J. Cereb. Blood Flow Metab.*, vol. 21, no. 8, pp. 921–928, 2001.

[67] B. Arvin, L. F. Neville, F. C. Barone, and G. Z. Feuerstein, "The role of inflammation and cytokines in brain injury," *Neurosci. Biobehav. Rev.*, vol. 20, no. 3, pp. 445–452, 1996.

[68] B. M. Famakin, "The immune response to acute focal cerebral ischemia and associated post-stroke immunodepression: A focused review," *Aging and Disease*, vol. 5, no. 5. pp. 307–326, 2014.

[69] S. P. Gadani, J. T. Walsh, J. R. Lukens, and J. Kipnis, "Dealing with Danger in the CNS: The Response of the Immune System to Injury," *Neuron*, vol. 87, no. 1. pp. 47–62, 2015.

[70] R. Shechter and M. Schwartz, "CNS sterile injury: Just another wound healing?," *Trends in Molecular Medicine*, vol. 19, no. 3. pp. 135–143, 2013.

[71] A. Alonso, E. Reinz, M. Fatar, M. G. Hennerici, and S. Meairs, "Clearance of albumin following ultrasound-induced blood-brain barrier opening is mediated by glial but not neuronal cells," *Brain Res.*, vol. 1411, pp. 9–16, 2011.

[72] A. Alonso *et al.*, "Reorganization of gap junctions after focused ultrasound blood-brain barrier opening in the rat brain," *J. Cereb. Blood Flow Metab.*, vol. 30, no. 7, pp. 1394–1402, 2010.

[73] A. Alonso, E. Reinz, M. Fatar, J. Jenne, M. G. Hennerici, and S. Meairs, "Neurons but not glial cells overexpress ubiquitin in the rat brain following focused ultrasound-induced opening of the blood-brain barrier," *Neuroscience*, vol. 169, no. 1, pp. 116–124, 2010.

[74] M. Kinoshita, N. McDannold, F. A. Jolesz, and K. Hynynen, "Noninvasive localized delivery of Herceptin to the mouse brain by MRI-guided focused ultrasound-induced blood-brain barrier disruption," *Proc. Natl. Acad. Sci. U. S. A.*, vol. 103, no. 31, pp. 11719–11723, 2006.

[75] J. Shin *et al.*, "Focused ultrasound-mediated noninvasive blood-brain barrier modulation: Preclinical examination of efficacy and safety in various sonication parameters," *Neurosurg. Focus*, vol. 44, no. 2, p. E15, 2018.

[76] J. C. Weng, S. K. Wu, W. L. Lin, and W. Y. I. Tseng, "Detecting blood-brain barrier disruption within minimal hemorrhage following transcranial focused ultrasound: A correlation study with contrast-enhanced MRI," *Magn. Reson. Med.*, vol. 65, no. 3, pp. 802–811, 2011.

[77] C. H. Fan, H. L. Liu, C. Y. Huang, Y. J. Ma, T. C. Yen, and C. K. Yeh, "Detection of Intracerebral Hemorrhage and Transient Blood-Supply Shortage in Focused-Ultrasound-Induced Blood-Brain Barrier Disruption by Ultrasound Imaging," *Ultrasound Med. Biol.*, vol. 38, no. 8, pp. 1372–1382, 2012.

[78] H. C. Tsai, C. H. Tsai, W. S. Chen, C. Inserra, K. C. Wei, and H. L. Liu, "Safety evaluation of frequent application of microbubble-enhanced focused ultrasound blood-brain-barrier opening," *Sci. Rep.*, vol. 8, no. 1, 2018.

[79] N. McDannold, C. D. Arvanitis, N. Vykhodtseva, and M. S. Livingstone, "Temporary disruption of the blood-brain barrier by use of ultrasound and microbubbles: Safety and efficacy evaluation in rhesus macaques," *Cancer Res.*, vol. 72, no. 14, pp. 3652–3663, 2012.

[80] Y. Meng *et al.*, "Glymphatics Visualization after Focused Ultrasound-Induced Blood–Brain Barrier Opening in Humans," *Ann. Neurol.*, vol. 86, no. 6, pp. 975–980, 2019.

[81] D. Furtado, M. Björnmalm, S. Ayton, A. I. Bush, K. Kempe, and F. Caruso, "Overcoming the Blood–Brain Barrier: The Role of Nanomaterials in Treating Neurological Diseases," *Advanced Materials*, vol. 30, no. 46. 2018.

[82] A. Burgess, K. Shah, O. Hough, and K. Hynynen, "Focused ultrasound-mediated drug delivery through the blood-brain barrier.," *Expert Rev. Neurother.*, vol. 15, no. 5, pp. 477–91, 2015.

[83] A. Burgess and K. Hynynen, "Microbubble-assisted ultrasound for drug delivery in the brain and central nervous system," *Adv. Exp. Med. Biol.*, vol. 880, pp. 293–308, 2016.

[84] J. C. G. Bünzli and C. Piguet, "Lanthanide-containing molecular and supramolecular polymetallic functional assemblies," *Chem. Rev.*, vol. 102, no. 6, pp. 1897–1928, 2002.

[85] D. J. Begley, "ABC transporters and the blood-brain barrier," *Curr Pharm Des*, vol. 10, no. 12, pp. 1295–312, 2004.

[86] A. Armulik, G. Genové, and C. Betsholtz, "Pericytes: Developmental, Physiological, and Pathological Perspectives, Problems, and Promises," *Developmental Cell*, vol. 21, no. 2. pp.

193–215, 2011.

[87] C. Bing *et al.*, "Characterization of different bubble formulations for blood-brain barrier opening using a focused ultrasound system with acoustic feedback control," *Sci. Rep.*, vol. 8, no. 1, 2018.

[88] D. E. Goertz, C. Wright, and K. Hynynen, "Contrast agent kinetics in the rabbit brain during exposure to therapeutic ultrasound," *Ultrasound Med. Biol.*, vol. 36, no. 6, pp. 916–924, 2010.

[89] J. Deng *et al.*, "The role of caveolin-1 in blood-brain barrier disruption induced by focused ultrasound combined with microbubbles," *J. Mol. Neurosci.*, vol. 46, no. 3, pp. 677–687, 2012.

[90] T. Nhan, A. Burgess, E. E. Cho, B. Stefanovic, L. Lilge, and K. Hynynen, "Drug delivery to the brain by focused ultrasound induced blood-brain barrier disruption: Quantitative evaluation of enhanced permeability of cerebral vasculature using two-photon microscopy," *J. Control. Release*, vol. 172, no. 1, pp. 274–280, 2013.

[91] R. M. Jones, L. Deng, K. Leung, D. McMahon, M. A. O'Reilly, and K. Hynynen, "Three-dimensional transcranial microbubble imaging for guiding volumetric ultrasound-mediated blood-brain barrier opening," *Theranostics*, vol. 8, no. 11, pp. 2909–2926, 2018.

[92] M. A. O'Reilly and K. Hynynen, "Blood-brain barrier: Real-time feedback-controlled focused ultrasound disruption by using an acoustic emissions-based controller," *Radiology*, vol. 263, no. 1, pp. 96–106, 2012.

[93] M. A. Oreilly and K. Hynynen, "A PVDF receiver for ultrasound monitoring of transcranial focused ultrasound therapy," *IEEE Trans. Biomed. Eng.*, vol. 57, no. 9, pp. 2286–2294, 2010.

[94] C. D. Arvanitis, M. S. Livingstone, N. Vykhodtseva, and N. McDannold, "Controlled Ultrasound-Induced Blood-Brain Barrier Disruption Using Passive Acoustic Emissions Monitoring," *PLoS One*, vol. 7, no. 9, 2012.

[95] A. N. Pouliopoulos, "Controlling microbubble dynamics in ultrasound therapy," 2017.

[96] E. Quaia, "Classification and Safety of Microbubble-Based Contrast Agents," in *Contrast Media in Ultrasonography*, 2005, pp. 3–14.

[97] R. Senior *et al.*, "Contrast echocardiography: Evidence-based recommendations by European Association of Echocardiography," *European Journal of Echocardiography*, vol. 10, no. 2. pp. 194–212, 2009.

[98] G. M. Shepherd, *The Synaptic Organization of the Brain*. 2004.

[99] S. A. Small, S. A. Schobel, R. B. Buxton, M. P. Witter, and C. A. Barnes, "A pathophysiological framework of hippocampal dysfunction in ageing and disease," *Nature Reviews Neuroscience*, vol. 12, no. 10. pp. 585–601, 2011.

[100] Lenth Russ, "Java applets for power and sample size," *Computer Software*, 2006. http://homepage.stat.uiowa.edu/~rlenth/Power/index.html (accessed Mar. 28, 2020).

[101] R. G. Thorne and C. Nicholson, "In vivo diffusion analysis with quantum dots and dextrans predicts the width of brain extracellular space," *Proc. Natl. Acad. Sci. U. S. A.*, vol. 103, no. 14, pp. 5567–5572, 2006.

[102] M. A. Valdez, E. Fernandez, T. Matsunaga, R. P. Erickson, and T. P. Trouard, "Distribution and Diffusion of Macromolecule Delivery to the Brain via Focused Ultrasound using Magnetic Resonance and Multispectral Fluorescence Imaging," *Ultrasound Med. Biol.*, vol. 46, no. 1, pp. 122–136, 2020.

[103] S. Wanga, B. Baserib, J. J. Choib, Y. S. Tungb, B. Morrisonb, and E. E. Konofagoua, "Delivery of Fluorescent Dextrans through the Ultrasound-Induced Blood-Brain Barrier Opening in Mice," in *Proceedings - IEEE Ultrasonics Symposium*, 2008, pp. 1702–1705.

[104] W. M. Pardridge, "CNS drug design based on principles of blood-brain barrier transport," *J. Neurochem.*, vol. 70, no. 5, pp. 1781–1792, 1998.

[105] Z. Guo *et al.*, "Lipoxin A4 Reduces Inflammation Through Formyl Peptide Receptor 2/p38 MAPK Signaling Pathway in Subarachnoid Hemorrhage Rats," *Stroke*, vol. 47, no. 2, pp. 490–497, 2016.

[106] U. Motosugi, T. Ichikawa, and T. Araki, "Rules, Roles, and Room for Discussion in Gadoxetic Acid-enhanced Magnetic Resonance Liver Imaging: Current Knowledge and Future Challenges," *Magn. Reson. Med. Sci.*, vol. 6, no. 3, pp. 161–175, 2013.

[107] M. Schneider and D. Ph, "Characteristics of SonoVueTM," vol. 16, no. 7, pp. 743–746, 1999.

[108] U.S. Food and Drug Administration (FDA): Centre for Drug Evaluation and Research, "Ceritinib: clinical pharmacology and biopharmaceutics review," *Cent. drug Eval. Res.*, vol. 20, 2014, [Online]. Available: http://www.accessdata.fda.gov/drugsatfda_docs/nda/2012/203756Orig1s000ClinPharmR.

pdf%5Cnhttp://www.accessdata.fda.gov/drugsatfda_docs/nda/2014/205755Orig1s000ClinPharmR.pdf%5Cnhttp://www.accessdata.fda.gov/drugsatfda_docs/nda/2013/204819Orig1s000ClinPharm.

[109] V. V. V. Hira, A. L. de Jong, K. Ferro, M. Khurshed, R. J. Molenaar, and C. J. F. Van Noorden, "Comparison of different methodologies and cryostat versus paraffin sections for chromogenic immunohistochemistry," *Acta Histochem.*, vol. 121, no. 2, pp. 125–134, 2019.

[110] J. A. Ramos-Vara, "Technical aspects of immunohistochemistry," *Vet. Pathol.*, vol. 42, no. 4, pp. 405–426, 2005.

[111] T. Chan, "Synthesis, in vitro and in vivo evaluation of nanoparticles and metal complexes for the treatment of brain diseases," 2020.

[112] H. K. Wolf *et al.*, "NeuN: A useful neuronal marker for diagnostic histopathology," *J. Histochem. Cytochem.*, vol. 44, no. 10, pp. 1167–1171, 1996.

[113] R. J. Mullen, C. R. Buck, and A. M. Smith, "NeuN, a neuronal specific nuclear protein in vertebrates," *Development*, vol. 116, no. 1, pp. 201–211, 1992.

[114] D. Ito, Y. Imai, K. Ohsawa, K. Nakajima, Y. Fukuuchi, and S. Kohsaka, "Microglia-specific localisation of a novel calcium binding protein, Iba1," *Mol. Brain Res.*, vol. 57, no. 1, pp. 1–9, 1998.

[115] L. F. Eng, R. S. Ghirnikar, and Y. L. Lee, "Glial Fibrillary Acidic Protein: GFAP-Thirty-One Years (1969-2000)," *Neurochem. Res.*, 2000.

[116] Z. Yang and K. K. W. Wang, "Glial fibrillary acidic protein: From intermediate filament assembly and gliosis to neurobiomarker," *Trends in Neurosciences*. 2015.

[117] K. Ohsawa, Y. Imai, Y. Sasaki, and S. Kohsaka, "Microglia/macrophage-specific protein Iba1 binds to fimbrin and enhances its actin-bundling activity," *J. Neurochem.*, vol. 88, no. 4, pp. 844–856, 2004.

[118] G. W. Kreutzberg, "Microglia: A sensor for pathological events in the CNS," *Trends in Neurosciences*, vol. 19, no. 8. pp. 312–318, 1996.

[119] K. Li, J. Li, J. Zheng, and S. Qin, "Reactive Astrocytes in Neurodegenerative Diseases," *Aging Dis.*, vol. 10, no. 3, p. 664, 2019.

[120] R. Schmidt-Kastner, K. Wietasch, H. Weigel, and U. T. Eysel, "Immunohistochemical staining

for glial fibrillary acidic protein (GFAP) after deafferentation or ischemic infarction in rat visual system: Features of reactive and damaged astrocytes," *Int. J. Dev. Neurosci.*, vol. 11, no. 2, pp. 157–174, 1993.

[121] A. Carpentier *et al.*, "Clinical trial of blood-brain barrier disruption by pulsed ultrasound," *Sci. Transl. Med.*, vol. 8, no. 343, p. 343re2, 2016.

[122] J. J. Choi and C.-C. Coussios, "Spatiotemporal evolution of cavitation dynamics exhibited by flowing microbubbles during ultrasound exposure," *J. Acoust. Soc. Am.*, vol. 132, no. 5, pp. 3538–3549, 2012.

[123] C. Lazarus, A. N. Pouliopoulos, M. Tinguely, V. Garbin, and J. J. Choi, "Clustering dynamics of microbubbles exposed to low-pressure 1-MHz ultrasound," *J. Acoust. Soc. Am.*, vol. 142, no. 5, pp. 3135–3146, 2017.

[124] K. Hynynen, N. McDannold, N. Vykhodtseva, and F. A. Jolesz, "Noninvasive MR imaging-guided focal opening of the blood-brain barrier in rabbits," *Radiology*, vol. 220, no. 3, pp. 640–646, 2001.

[125] N. McDannold, N. Vykhodtseva, and K. Hynynen, "Blood-Brain Barrier Disruption Induced by Focused Ultrasound and Circulating Preformed Microbubbles Appears to Be Characterized by the Mechanical Index," *Ultrasound Med. Biol.*, vol. 34, no. 5, pp. 834–840, 2008.

[126] B. Zhao *et al.*, "Blood-brain barrier disruption induced by diagnostic ultrasound combined with microbubbles in mice," *Oncotarget*, vol. 9, no. 4, pp. 4897–4914, 2018.

[127] D. M. Nance and J. Burns, "Fluorescent dextrans as sensitive anterograde neuroanatomical tracers: Applications and pitfalls," *Brain Res. Bull.*, vol. 25, no. 1, pp. 139–145, 1990.

[128] N. Rajakumar, K. Elisevich, and B. A. Flumerfelt, "Biotinylated dextran: a versatile anterograde and retrograde neuronal tracer," *Brain Res.*, vol. 607, no. 1–2, pp. 47–53, 1993.

[129] M. Dragunow and R. Faull, "The use of c-fos as a metabolic marker in neuronal pathway tracing," *J. Neurosci. Methods*, vol. 29, no. 3, pp. 261–265, 1989.

[130] M. VanElzakker, R. D. Fevurly, T. Breindel, and R. L. Spencer, "Environmental novelty is associated with a selective increase in Fos expression in the output elements of the hippocampal formation and the perirhinal cortex," *Learn. Mem.*, vol. 15, no. 12, pp. 899–

908, 2008.

[131] A. S. Perrin-Terrin *et al.*, "The c-FOS protein immunohistological detection: A useful tool as a marker of central pathways involved in specific physiological responses in vivo and ex vivo," *J. Vis. Exp.*, vol. 2016, no. 110, 2016.

[132] A. M.S. Hartz and B. Bauer, "ABC Transporters in the CNS – An Inventory," *Curr. Pharm. Biotechnol.*, vol. 12, no. 4, pp. 656–673, 2011.

[133] M. Grube, P. Hagen, and G. Jedlitschky, "Neurosteroid transport in the brain: Role of ABC and SLC transporters," *Frontiers in Pharmacology*, vol. 9, no. APR. 2018.

[134] V. V. Gusel'nikova and D. E. Korzhevskiy, "NeuN as a neuronal nuclear antigen and neuron differentiation marker," *Acta Naturae*, vol. 7, no. 2. pp. 42–47, 2015.

[135] A. Sierra *et al.*, "Microglia shape adult hippocampal neurogenesis through apoptosis-coupled phagocytosis," *Cell Stem Cell*, vol. 7, no. 4, pp. 483–495, 2010.

[136] X. Zhao *et al.*, "Noninflammatory Changes of Microglia Are Sufficient to Cause Epilepsy," *Cell Rep.*, vol. 22, no. 8, pp. 2080–2093, 2018.

[137] G. A. Kozloski, "Microglia Markers," *Mater. Methods*, vol. 9, 2019.

[138] Y. J. Jung and W. S. Chung, "Phagocytic roles of glial cells in healthy and diseased brains," *Biomolecules and Therapeutics*, vol. 26, no. 4. pp. 350–357, 2018.

[139] S. A. Liddelow and B. A. Barres, "Reactive Astrocytes: Production, Function, and Therapeutic Potential," *Immunity*, vol. 46, no. 6. pp. 957–967, 2017.

[140] J. Chuquet, P. Quilichini, E. A. Nimchinsky, and G. Buzsáki, "Predominant enhancement of glucose uptake in astrocytes versus neurons during activation of the somatosensory cortex," *J. Neurosci.*, vol. 30, no. 45, pp. 15298–15303, 2010.

[141] M. K. Jha and B. M. Morrison, "Glia-neuron energy metabolism in health and diseases: New insights into the role of nervous system metabolic transporters," *Experimental Neurology*, vol. 309. pp. 23–31, 2018.

[142] Z. Zhang *et al.*, "The Appropriate Marker for Astrocytes: Comparing the Distribution and Expression of Three Astrocytic Markers in Different Mouse Cerebral Regions," *Biomed Res. Int.*, vol. 2019, 2019.

[143] G. Samiotaki, F. Vlachos, Y. S. Tung, and E. E. Konofagou, "A quantitative pressure and

microbubble-size dependence study of focused ultrasound-induced blood-brain barrier opening reversibility in vivo using MRI," *Magn. Reson. Med.*, vol. 67, no. 3, pp. 769–777, 2012.

[144] D. Shlosberg, M. Benifla, D. Kaufer, and A. Friedman, "Blood-brain barrier breakdown as a therapeutic target in traumatic brain injury," *Nature Reviews Neurology*, vol. 6, no. 7. pp. 393–403, 2010.

[145] Y. Shen *et al.*, "Delivery of liposomes with different sizes to mice brain after sonication by focused ultrasound in the presence of microbubbles," *Ultrasound Med. Biol.*, vol. 42, no. 7, pp. 1499–1511, 2016.

[146] K. Hynynen *et al.*, "Focal disruption of the blood-brain barrier due to 260-kHz ultrasound bursts: A method for molecular imaging and targeted drug delivery," *J. Neurosurg.*, vol. 105, no. 3, pp. 445–454, 2006.

[147] N. McDannold, N. Vykhodtseva, and K. Hynynen, "Use of Ultrasound Pulses Combined with Definity for Targeted Blood-Brain Barrier Disruption: A Feasibility Study," *Ultrasound Med. Biol.*, vol. 33, no. 4, pp. 584–590, 2007.

[148] N. McDannold, N. Vykhodtseva, and K. Hynynen, "Targeted disruption of the blood-brain barrier with focused ultrasound: Association with cavitation activity," *Phys. Med. Biol.*, vol. 51, no. 4, pp. 793–807, 2006.

[149] Y. S. Tung, J. J. Choi, B. Baseri, and E. E. Konofagou, "Identifying the inertial cavitation threshold and skull effects in a vessel phantom using focused ultrasound and microbubbles," *Ultrasound Med. Biol.*, vol. 36, no. 5, pp. 840–852, 2010.

[150] J. J. Iliff *et al.*, "A paravascular pathway facilitates CSF flow through the brain parenchyma and the clearance of interstitial solutes, including amyloid β," *Sci. Transl. Med.*, vol. 4, no. 147, 2012.

[151] A. Louveau *et al.*, "Structural and functional features of central nervous system lymphatic vessels," *Nature*, vol. 523, no. 7560, pp. 337–341, 2015.

[152] M. Absinta *et al.*, "Human and nonhuman primate meninges harbor lymphatic vessels that can be visualized noninvasively by MRI," *Elife*, vol. 6, 2017.

[153] S. Pustylnikov, D. Sagar, P. Jain, and Z. K. Khan, "Targeting the C-type lectins-mediated host-pathogen interactions with dextran," *J. Pharm. Pharm. Sci.*, vol. 17, no. 3, pp. 371–392, 2014.

[154] H. L. Liu *et al.*, "Design and Implementation of a Transmit/Receive Ultrasound Phased Array for Brain Applications," *IEEE Trans. Ultrason. Ferroelectr. Freq. Control*, vol. 65, no. 10, pp. 1756–1767, 2018.

[155] S. Y. Wu, C. S. Sanchez, G. Samiotaki, A. Buch, V. P. Ferrera, and E. E. Konofagou, "Characterizing Focused-Ultrasound Mediated Drug Delivery to the Heterogeneous Primate Brain in Vivo with Acoustic Monitoring," *Sci. Rep.*, vol. 6, 2016.

[156] J. Xia, P. H. Tsui, and H. L. Liu, "Low-pressure burst-mode focused ultrasound wave reconstruction and mapping for blood-brain barrier opening: A preclinical examination," *Sci. Rep.*, vol. 6, 2016.

[157] X. Guo, J. Tu, and D. Zhang, "Investigation on the inertial cavitation threshold of micro-bubbles," in *Proceedings of Meetings on Acoustics*, 2013, vol. 19, p. 075072.

[158] W. S. Chen, A. A. Brayman, T. J. Matula, L. A. Crum, and M. W. Miller, "The pulse length-dependence of inertial cavitation dose and hemolysis," *Ultrasound Med. Biol.*, vol. 29, no. 5, pp. 739–748, 2003.

[159] Y. Yang *et al.*, "Cavitation dose painting for focused ultrasound-induced blood-brain barrier disruption," *Sci. Rep.*, vol. 9, no. 1, 2019.

[160] T. Sun *et al.*, "Closed-loop control of targeted ultrasound drug delivery across the blood–brain/tumor barriers in a rat glioma model," *Proc. Natl. Acad. Sci. U. S. A.*, vol. 114, no. 48, pp. E10281–E10290, 2017.

[161] C. H. Fan *et al.*, "Submicron-bubble-enhanced focused ultrasound for blood-brain barrier disruption and improved CNS drug delivery," *PLoS One*, vol. 9, no. 5, 2014.

[162] N. McDannold, C. D. Arvanitis, N. Vykhodtseva, and M. S. Livingstone, "Temporary disruption of the blood-brain barrier by use of ultrasound and microbubbles: Safety and efficacy evaluation in rhesus macaques," *Cancer Res.*, vol. 72, no. 14, pp. 3652–3663, 2012.

[163] M. Gyöngy and C.-C. Coussios, "Passive cavitation mapping for localization and tracking of bubble dynamics," *J. Acoust. Soc. Am.*, vol. 128, no. 4, pp. EL175–EL180, 2010.

[164] C. D. Arvanitis and N. McDannold, "Integrated ultrasound and magnetic resonance imaging for simultaneous temperature and cavitation monitoring during focused ultrasound therapies," *Med. Phys.*, vol. 40, no. 11, 2013.

[165] C. D. Arvanitis, M. S. Livingstone, and N. McDannold, "Combined ultrasound and MR imaging to guide focused ultrasound therapies in the brain," *Phys. Med. Biol.*, vol. 58, no. 14, pp. 4749–4761, 2013.

[166] J. J. Choi, R. C. Carlisle, C. Coviello, L. Seymour, and C. C. Coussios, "Non-invasive and real-time passive acoustic mapping of ultrasound-mediated drug delivery," *Phys. Med. Biol.*, vol. 59, no. 17, pp. 4861–4877, 2014.

[167] S. M. Graham *et al.*, "Inertial cavitation to non-invasively trigger and monitor intratumoral release of drug from intravenously delivered liposomes," *J. Control. Release*, vol. 178, no. 1, pp. 101–107, 2014.

[168] A. H. Liao, H. Y. Chou, Y. L. Hsieh, S. C. Hsu, K. C. Wei, and H. L. Liu, "Enhanced therapeutic epidermal growth factor receptor (EGFR) antibody delivery via pulsed ultrasound with targeting microbubbles for glioma treatment," *J. Med. Biol. Eng.*, vol. 35, no. 2, pp. 156–164, 2015.

[169] N. Nomikou and A. P. McHale, "Microbubble-enhanced ultrasound-mediated gene transfer Towards the development of targeted gene therapy for cancer," *Int. J. Hyperth.*, vol. 28, no. 4, pp. 300–310, 2012.

[170] R. A. Kroll and E. A. Neuwelt, "Outwitting the blood-brain barrier for therapeutic purposes: Osmotic opening and other means," *Neurosurgery*, vol. 42, no. 5, pp. 1083–1100, 1998.

[171] Y. Hu, J. M. F. Wan, and A. C. H. Yu, "Membrane Perforation and Recovery Dynamics in Microbubble-Mediated Sonoporation," *Ultrasound Med. Biol.*, vol. 39, no. 12, pp. 2393–2405, 2013.

[172] F. E. Shamout *et al.*, "Enhancement of Non-Invasive Trans-Membrane Drug Delivery Using Ultrasound and Microbubbles During Physiologically Relevant Flow," *Ultrasound Med. Biol.*, vol. 41, no. 9, pp. 2435–2448, 2015.

[173] Y. Zhou, J. Cui, and C. X. Deng, "Dynamics of sonoporation correlated with acoustic cavitation activities," *Biophys. J.*, vol. 94, no. 7, pp. L51–L53, 2008.

[174] C. Coviello *et al.*, "Passive acoustic mapping utilizing optimal beamforming in ultrasound therapy monitoring," *J. Acoust. Soc. Am.*, vol. 137, no. 5, pp. 2573–2585, 2015.

[175] M. T. Burgess, I. Apostolakis, and E. E. Konofagou, "Power cavitation-guided blood-brain

barrier opening with focused ultrasound and microbubbles," *Phys. Med. Biol.*, vol. 63, no. 6, p. 065009, 2018.

[176] R. E. Apfel and C. K. Holland, "Gauging the likelihood of cavitation from short-pulse, low-duty cycle diagnostic ultrasound," *Ultrasound Med. Biol.*, vol. 17, no. 2, pp. 179–185, 1991.

[177] F. Ahmadi, I. V. McLoughlin, S. Chauhan, and G. ter-Haar, "Bio-effects and safety of low-intensity, low-frequency ultrasonic exposure," *Progress in Biophysics and Molecular Biology*, vol. 108, no. 3. pp. 119–138, 2012.

[178] FDA, "SUPRAX® safely and effectively," 2017. [Online]. Available: https://www.accessdata.fda.gov/drugsatfda_docs/label/2018/021064s022lbl.pdf.

[179] G. ter Haar, "Ultrasonic imaging: Safety considerations," *Interface Focus*, vol. 1, no. 4. pp. 686–697, 2011.

[180] "The new British Medical Ultrasound Society guidelines for the safe use of diagnostic ultrasound equipment," *Ultrasound*, vol. 18, no. 2, pp. 50–51, 2010.

3 | Delivery of liposomes to the brain with rapid short-pulse sequences

3.1 Background

Ultrasound emitted in a rapid short-pulse (RaSP) sequence improves the efficacy and safety of delivery of relatively small 3 kDa dextran molecules (~2-3 nm) into the brain (Chapter 2). However, it is uncertain whether these improvements translate when delivering much larger particles. In this chapter, we investigated whether RaSP could improve the delivery of 100 nm diameter liposomes into the brain.

3.1.1 Liposomes

Liposomes are drug carrier systems typically composed of a concentric phospholipid bilayer filled with an aqueous core. Their size varies between 50 and 1,000 nm in diameter [1] and they can be loaded with a variety of drugs and imaging agents (Figure 3.1) [2]. The bilayer can store hydrophobic molecules, while the aqueous core can be loaded with hydrophilic molecules. Particularly in cancer applications, liposomes are used to transport cytotoxic drugs. If these drugs are injected unencapsulated, they cause untargeted side effects, which limit their clinical application. Enclosing these drugs in liposome structures improves their therapeutic efficacy and blood circulation half-life, and reduces their systemic toxicity [3], [4].

Liposomes are among the most investigated structures for drug delivery due to their high drug loading capacity, low toxicity, biocompatibility, biodegradability and their ability to deliver both hydrophilic and hydrophobic molecules to targeted tissues of interest [5]. Their circulation half-life in blood can be prolonged by incorporating polyethyleneglycol-lipids (e.g. PEG) into the bilayer membrane (2-24 h in mice [6], [7]; Figure 3.1). With this incorporation, liposomes can evade the reticuloendothelial system and the absorption of blood proteins [8]. These favourable properties result in

a higher accumulation of liposomes at sites where the vasculature is leaky [9], such as in tumours and in brain diseases where the blood-brain barrier (BBB) is not intact.

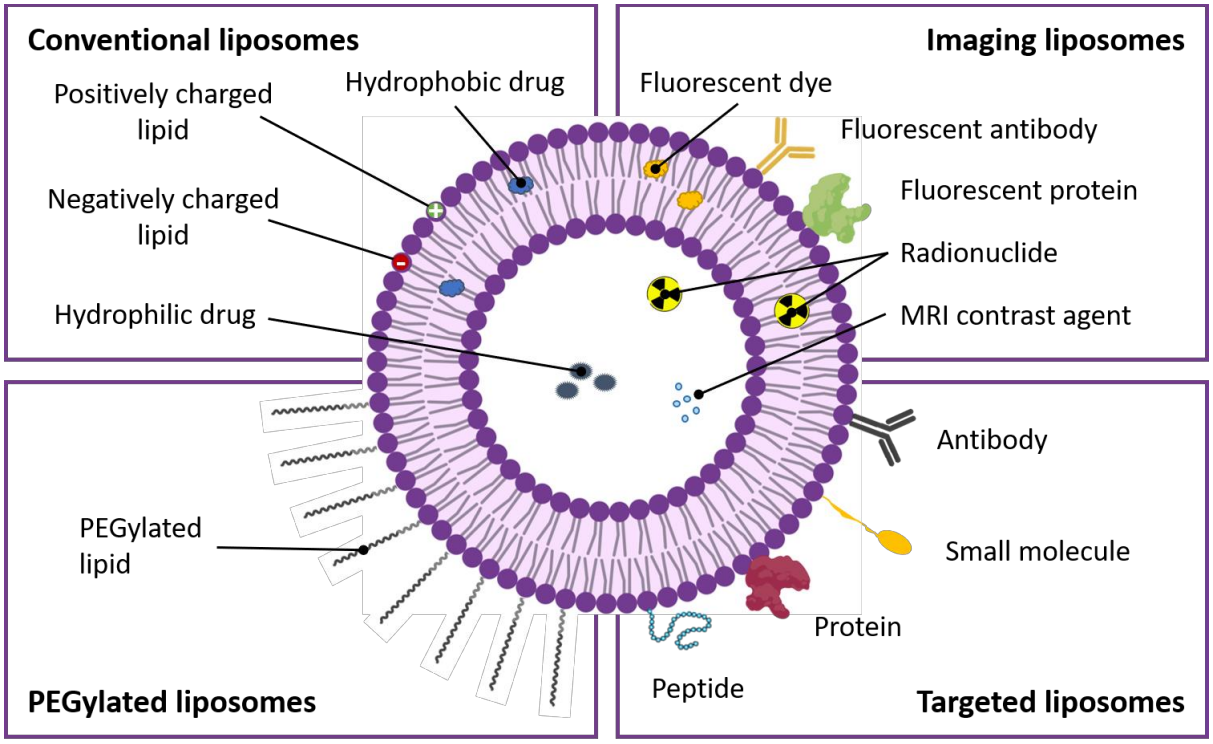

Figure 3.1. Schematic representation of different liposome delivery systems. Conventional liposomes are composed of a phospholipid bilayer, made of positively and negatively charged lipids, that encloses an aqueous core. Hydrophilic drugs can be loaded into the core and hydrophobic drugs into the bilayer where PEGylated lipids are used to stabilise the liposomes. Agents can be attached to the lipid surface or loaded within the core to enable imaging of the liposomes, including fluorescent dyes, antibodies and proteins, radionuclides and MRI contrast agents. Antibodies, proteins, peptides and small molecules can be attached to the lipid surface to allow for specific targeting.

Many brain diseases, however, require drugs to also be delivered through an intact BBB, such as in brain tumours and neurodegenerative diseases. Brain tumours, for example, tend to have a leaky tumour core but an intact vasculature at the tumour margins [10]–[12]. They represent a significant challenge due to their infiltrative nature and high probability of recurrence at the tumour margins [13], [14]. Therefore, drugs and imaging agents need to be delivered across these regions of intact BBB. So far, a few small molecules have shown modest improvements in the outcomes of clinical

trials [15]. Hydrophobic and larger molecules have suffered from their inability to cross this barrier. These larger molecules could instead be loaded into liposomes to mask their toxicity and improve their local delivery. However, due to their large size, liposomes cannot cross an intact BBB [16], [17]. Chemical modifications have been made to enhance liposome delivery into the brain. Positively charged liposomes have shown increased delivery across the BBB *in vivo* via absorption-mediated transcytosis, as endothelial cells have negatively charged membranes [18]–[20]. Liposomes can also be conjugated to antibodies and peptides (Figure 3.1) to enhance their receptor-mediated endocytosis to pass the BBB, which has been shown *in vitro* [21], [22]. However, reaching therapeutically relevant concentrations in the brain and avoiding nonspecific uptake in peripheral tissues are the main challenges with these techniques [23].

3.1.2 Liposome delivery with focused ultrasound

The use of focused ultrasound and microbubbles enables the delivery of liposomes into the brain in a local and non-invasive way. This technique has been shown to deliver liposomes into the brain in several *in vivo* studies (summarised in Appendix Table 6.9) [16], [17], [32]–[36], [24]–[31]. Different types of liposomes have been delivered, including ones loaded with genes [27], [30], [31] or chemotherapeutic drugs such as doxorubicin [16], [17], [28], [29], [33], [34] and paclitaxel [25], and ones labelled with imaging agents like quantum dots [29], rhodamine [26], [32], and gadolinium-based contrast agents together with rhodamine [35]. The size of the liposomes delivered with focused ultrasound and microbubbles ranges between 55 and 200 nm. Many have demonstrated delivery in healthy mice and rats [16], [26], [31], [32], [34], [35], although most liposomes have been loaded with drugs and delivered to brain tumour models [17], [24], [25], [27], [29], [33], showing improved outcomes [17], [37]–[39].

When using focused ultrasound to deliver liposomes, by increasing the size of the liposomes, lower delivered doses have been detected via both fluorescence and MRI [35]. This observation is due to the enhanced permeability of the BBB only allowing

substances below a certain size-threshold into the brain [26], [40]–[43]. This means that a higher delivery of small molecules that fall below this threshold will be achieved compared to larger molecules.

Once delivered into the brain, fluorescently labelled liposomes have shown heterogeneous spot-like patterns of delivery, similar to those of other large compounds, such as 2,000 kDa (54.4 nm) dextran [40] and magnetic resonance contrast agents (1-65 nm) [44]. This pattern was observed in brains where liposomes between 55-200 nm were delivered [26], [32], [35], [36]. Most delivery was observed around blood vessels. This confined delivery is thought to be due to the size of the pores within the extracellular matrix of the brain being 60 nm in diameter [45], which would limit the diffusion of most liposomes (> 60 nm) within the brain parenchyma once delivered across the BBB. However, the much smaller drugs loaded within the liposomes, once released, can be the ones diffusing through the electrostatically charged brain parenchyma to reach the desired target.

In many focused ultrasound-mediated liposome delivery studies, adverse effects have been observed in the form of intratumoural haemorrhage, scars with infiltrating macrophages, activated astrocytes, cysts and damage in the healthy tissue surrounding tumours [16], [17], [24], [26], [29]–[34]. However, all studies delivering liposomes with this technology have used long ultrasound pulses. Having shown that by emitting ultrasound in rapid short-pulses, damage can be avoided and the distribution of much smaller molecules can be improved (Chapter 2, [46]), we here sought to investigate whether these short pulses could improve the distribution of much larger liposomal compounds and improve the safety profile of their delivery.

3.2 Aims and objectives

The overall aim of this chapter was to investigate whether ultrasound emitted in a RaSP sequence could deliver liposomes across the BBB in a similar or improved manner to ultrasound emitted in a long pulse sequence. To achieve this aim, fluorescently labelled

liposomes (~ 100 nm diameter) were delivered across the BBB in mice using a RaSP or long pulse sequence.

To investigate how changing the ultrasound pressure affected liposome delivery, mice were treated with two acoustic pressures, either 0.4 or 0.6 MPa. The delivery and distribution of liposomes was compared qualitatively and quantitatively between brains treated with the two sequence types and both pressures.

We then investigated whether differences could be observed in the distribution of liposomes when waiting 0 h or 2 h after the ultrasound treatment, to see if the liposomes were able to diffuse within the parenchyma after crossing the BBB. These different recovery times were applied to mice treated with both ultrasound sequences and both pressures.

To determine whether liposomes were uptaken by neurons, microglia or astrocytes once delivered to the brain, immunohistochemical staining was performed. While uptake within neurons could tell us whether focused ultrasound can deliver liposomes to potential neuronal targets, uptake within microglia and astrocytes could indicate a pathway of excretion of the liposomes from the brain.

Lastly, tissue damage was investigated at a microscopic level in brains treated with both sequence types and both pressures at 0 h. These results were used to determine whether by emitting ultrasound in a RaSP sequence, an improved safety profile could be achieved when delivering liposomes to the brain.

3.3 Materials and methods

This section describes the experiments carried out to evaluate whether the efficacy and safety of liposome delivery could be improved by emitting ultrasound in a RaSP sequence. The brain of mice was treated with ultrasound emitted either in a RaSP or long pulse sequence, at 0.4 or 0.6 MPa and waiting either 0 h or 2 h after the ultrasound treatment. Brain tissue was collected and imaged to determine the detected amount and distribution of the delivered liposomes. Immunohistological staining was

performed to determine which cells were uptaking the liposomes, including whether glial cells were involved in removing liposomes from the brain. Staining for tissue damage was also carried out to determine whether liposomes could be delivered safely to the brain by emitting RaSP at a higher ultrasound pressure (0.6 MPa) than that used in our tissue damage assessment in Chapter 2 (Figure 2.36-38).

3.3.1 Ultrasound setup

Therapeutic ultrasound pulses were emitted from a single element spherical-segment focused ultrasound transducer (Figure 3.2; centre frequency: 1 MHz; active diameter: 90 mm; focal depth: 60.5 mm; part number: H-198; Sonic Concepts, Bothell, WA, USA) driven by one or two function generators (33500B Series; Agilent Technologies, Santa Clara, CA, USA) through a 50-dB power amplifier (2100L Electronics and Innovation, Rochester, NY) and an impedance matching box (Sonic Concepts, WA, USA). When ultrasound was emitted with a RaSP sequence, two function generators were used, one to define the pulse shape and the other to define the pulse sequence. For the long pulse sequence only one function generator was needed. The elevational, lateral and axial full width at half maximum (FWHM) at the ultrasound focus were 1 mm, 2 mm and 20 mm respectively (Appendix Figure 6.2). The acoustic pressures reported here are derated using an 11% attenuation, which was measured experimentally by placing the top layer of the mouse skull (post-mortem, n = 4) between the transducer and the focal point, where a hydrophone was positioned. The transducer, surrounded by a transparent casing, was mounted onto a three-dimensional positioning system (Velmex, Bloomfield, NY, USA) to move to the desired targeted location.

Acoustic emissions from microbubbles were passively captured during the ultrasound treatment using a passive cavitation detector (PCD; centre frequency: 7.5 MHz; diameter: 12.7 mm, focal length: 76.2 mm; Olympus Industrial, Essex, UK). The PCD was coaxially aligned through the rectangular central opening of the therapeutic transducer. The emissions were captured by the PCD, filtered by a 3-30 MHz band-pass filter, amplified by a 28-dB pre-amplifier and recorded by an 8-bit oscilloscope

(PicoScope 3205A). Time domain traces were displayed in real-time and were used to determine whether microbubble activity was occurring during the ultrasound treatment. Further processing of these signals was not carried out here, however, the data was saved for future off-line processing.

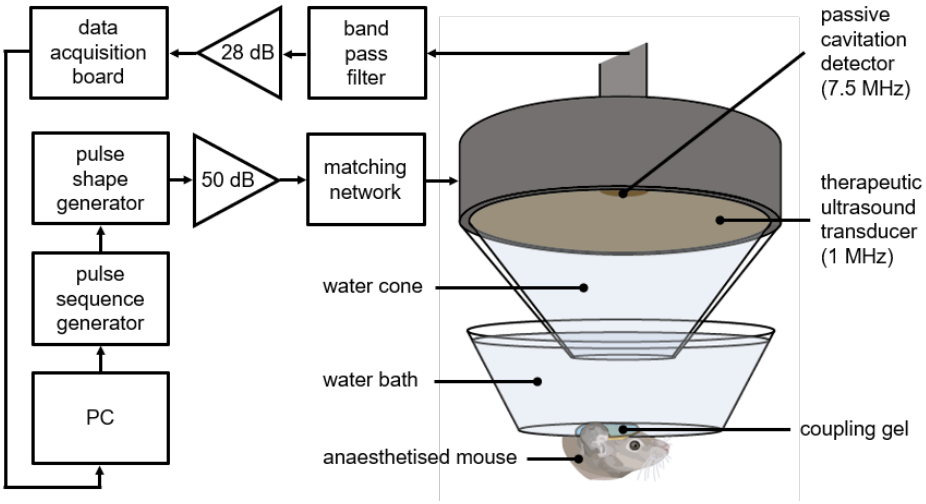

Figure 3.2. Ultrasound experimental setup. Ultrasound was focused through the intact scalp and skull onto the left hippocampus of the mouse's brain while the right hippocampus was used as a control (no ultrasound). Ultrasound pulses were emitted from the therapeutic transducer (1 MHz) driven by one or two function generators through a 50-dB amplifier and an impedance matching network. A 7.5 MHz passive cavitation detector captured the acoustic emissions from the microbubbles, which were filtered by a band pass filter, amplified by a 28-dB pre-amplifier and recorded by an 8-bit oscilloscope.

3.3.2 Animals

Thirty-six female C57bl/6 wild-type mice (8-12 weeks old, 19.9 g ± 0.6; Envigo, Huntingdon, UK) were used in this study (Table 3.1). All animal experiments were performed in approval with the UK Home Office and Imperial College London's animal facility committee.

Twenty-four mice were used to compare the dose and distribution of liposomes in brains treated with both sequence types (RaSP or long pulses), with two acoustic pressures (0.4 or 0.6 MPa) with either a 0 h or 2 h recovery period. Staining was

performed on these brains to determine which cells were uptaking the liposomes once delivered into the brain.

To assess damage, twelve mice were sonicated with both sequence types (RaSP or long pulses) at both acoustic pressures (0.4 or 0.6 MPa; n = 3 for each parameter group) with no recovery time following ultrasound treatment (0 h). These additional twelve mice were needed as haematoxylin and eosin (H&E) staining, used to assess damage, requires the brains to be processed with a paraffin-embedding technique rather than cryofreezing, which was used to assess the dose and distribution of the liposomes.

In all mice, the left hippocampus was treated with ultrasound while the right hippocampus was used as a no-ultrasound control. Variabilities caused by physiological differences between animals were reduced by using each animal as its own control.

Table 3.1. Summary of mice used in each study. Twenty-four mice were used to compare the delivery and distribution of liposomes with RaSP or long pulse sequences at 0.4 or 0.6 MPa either immediately or 2 h after the ultrasound treatment. Twelve mice were used to assess tissue damage with haematoxylin and eosin (H&E) staining at the two acoustic pressures and with the two sequence types at 0 h.

Study	Sequence type	Pressure	Recovery time	Number of mice
Delivery Comparison	RaSP	0.4 MPa	0 h	3
			2 h	3
		0.6 MPa	0 h	3
			2 h	3
	Long	0.4 MPa	0 h	3
			2 h	3
		0.6 MPa	0 h	3
			2 h	3
Tissue Damage Assessment	RaSP	0.4 MPa	0 h	3
		0.6 MPa		3
	Long	0.4 MPa		3
		0.6 MPa		3
Total				36

3.3.3 Liposomes and microbubbles

PEGylated liposomes labelled with a far-red DiD fluorophore (1,1′-dioctadecyl-3,3,3′,3′-tetramethylindodicarbocyanine, 4-chlorobenzensulfonate salt) were synthesized by Aishwarya Mishra (PhD student, Dr Rafael Torres' group; Figure 3.3; full experimental details of liposome synthesis in Appendix 6.3). PEGylated liposomes were chosen due to their clinically relevant size (~ 100 nm) and long blood half-life, to investigate the effect of molecule size on agent delivery with a RaSP sequence. The DiD fluorophore was selected as it has been shown to be robust and not leak from bilayer membranes for sustained periods of time *in vitro* [47]. DiD is also known to be weakly fluorescent in aqueous media but highly fluorescent in a lipid environment [48], [49]. This property favours the detection of the dye embedded within the lipid-membrane of liposomes, compared to the dye alone. In these experiments DiD was found to give no fluorescent signal when dissolved in water, confirming previous findings. The liposomes were synthesised with a diameter of 96.5 ± 1.1 nm and samples were found to be more than 96% stable in serum with no leakage of the dye across 48 hours (Appendix Figure 6.17). Due to the different concentrations of the lipids that were used to synthesise the bilayer, the liposomes had a slight-negative surface charge.

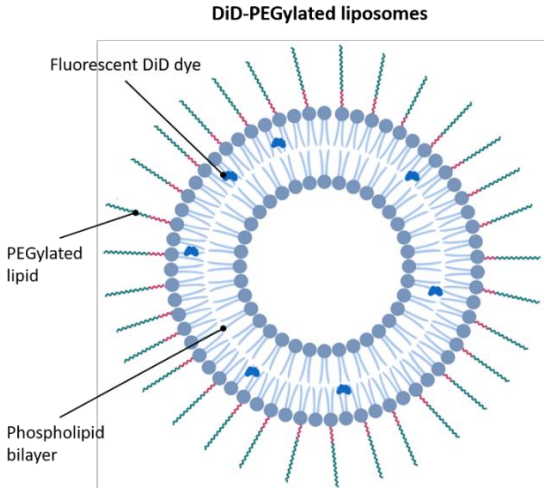

Figure 3.3. DiD-PEGylated liposome structure. The liposomes consist of a phospholipid bilayer with PEG brushes attached to the surface for biocompatibility and the DiD fluorophore embedded within the lipid bilayer to enable *ex vivo* fluorescence detection of the liposomes.

SonoVue (Bracco, Milan, Italy) microbubbles were used to deliver the above liposomes (concentration: 42.6 mg/ml) into the brain (concentration: 5 µl/g of body mass, volume: 100 µL, mean diameter: 2.5 µm [50], vial concentration: $3x10^8$/mL). A fresh vial of microbubbles was activated on each day of experiments and used within six hours from activation, following the manufacturer's instructions.

3.3.4 Experimental workflow

The experimental workflow was similar to that described in Chapter 2 (2.2.6, Figure 2.9). The mice were anesthetised, and the fur was shaved from the mouse's head. The mouse's head was then fixed within a stereotaxic frame and ultrasound gel was applied to the head. The water bath was lowered onto the gel so that a metal cross could be positioned in alignment with the skull sutures. Based on the position of this metal cross, the transducer was moved to target the left hippocampus (targeting method in section 2.2.3). Once the tail vein injection was in place, the liposomes were injected and the ultrasound treatment (RaSP or long pulse sequence) was started. Ten seconds into the treatment, the microbubbles were injected, allowing the initial ultrasound pulses to be used as control pulses for future acoustic emissions analysis. The microbubbles were injected over the course of 30 seconds through a 30-gauge home-made catheter.

At the end of the treatment, either immediately or after two hours of recovery, an overdose of pentobarbital was administered intraperitoneally and the mice were transcardially perfused with 20 mL ice cold phosphate-buffered saline with added heparin (20 units/mL; Sigma Aldrich, St Louis, MO, USA) and 10% formalin solution (Sigma Aldrich) to clear the vessels and fix the tissue. The brains were extracted and placed in 10 mL 10% formalin overnight, 15% sucrose for 6 h and then 30% sucrose overnight until the brains sunk to the bottom of the solution for cryoprotection. Brains used for H&E staining were instead kept in formalin and prepared by IQPath laboratory at University College London for paraffin-embedding and microtome sectioning (Appendix Table 6.7-6.8).

3.3.5 Histological staining

Brains used to observe the detected dose and distribution of the liposomes and cellular uptake were cryosectioned. Samples were snap-frozen by embedding the brains in optimal cutting temperature and placing them in a bath of isopentane and dry ice for five minutes. They were then sectioned into 30 µm horizontal slices using a cryostat (CryoStar NX70; Thermo Fisher, Waltham, MA, USA) at -12 to -14 °C. Initially, 1.5 mm of the embedded brain was trimmed from the bottom and then sixty 30 µm slices were cut to cover the entire hippocampus. Brain slices were collected on positively charged slides (Superfrost™ Ultra Plus Adhesion Slides, Thermo Fisher) and stored in the dark at 4 °C until imaged.

Immunostaining was performed on these brain slices to detect whether the liposomes were being uptaken by neurons, microglia or astrocytes. Only slices where cellular uptake was observed were stained for these cells and the antibodies used for each stain are shown in Table 3.2 (protocols in Appendix Tables 6.2-6.6). A DAPI mounting medium was applied before coverslipping the slides to stain the cell nuclei.

Table 3.2. Primary and secondary antibodies used to stain for neurons, microglia and astrocytes.

Stain	Primary Antibody	Secondary Antibody
Neurons	Recombinant anti-NeuN antibody [EPR12763] (ab177487) - 1:500	Goat anti-rabbit IgG H&L (Alexa Fluor® 488) (ab150077) - 1:500
Microglia	Anti-Iba1 antibody (ab5076) - 1:500	Donkey anti-goat IgG H&L (Alexa Fluor® 488) (ab150129) - 1:500
Astrocytes	GFAP monoclonal antibody (2.2B10) (13-0300) - 1:100	Mouse anti-rat IgG2a (FITC) (11-4817-82) - 1:500

3.3.6 Microscopy

Images were acquired using either a widefield microscope (10x; Zeiss Axio Observer, Oberkochen, Germany) or a confocal microscope (20x; Zeiss LSM-510 inverted, Oberkochen, Germany). Images were taken using both brightfield and fluorescent channels. The DiD fluorophore on the liposomes was imaged with the Cy5 channel, the Alexa 488 or FITC fluorophores on the antibodies to stain for cell uptake were imaged

with the GFP (green fluorescent protein) channel and the nuclei were imaged with the DAPI channel (Table 3.3). All imaging parameters, such as laser power and exposure time, were kept constant to allow more accurate quantitative measurements.

Table 3.3. Excitation and emission filters for the fluorophores. Excitation and emission filters are given as the centre wavelength and the bandwidth.

Fluorophore	Excitation	Emission
DAPI	390/40	450/40
Alexa 488, FITC	470/40	525/50
DiD	640/30	690/50

3.3.7 Analysis

Analysis on the acquired images was performed to determine the detected dose, distribution and areas of liposome delivery as well as tissue damage.

To compare the detected dose of liposomes delivered to the brain with the different parameters used, the normalised optical density (NOD) was calculated. Regions of interest (ROIs) were selected around the left and right hippocampus using Matlab R2019b (Mathworks, Natick, MA, USA). If present, artefacts, such as folds and air bubbles, were removed from these regions. The NOD is a normalised measurement of the detected dose of the liposomes [41]. Pixels with intensities above twice the standard deviation added to the mean of the control pixel intensities were summed in both ROIs. The sum in the targeted ROI was subtracted by that of the control ROI to obtain the NOD. Delivery was considered successful if the NOD was at least two standard deviations above the mean of the control region. The NOD was calculated on six slices for each quantified brain.

To quantify any differences in distribution between parameter sets, the coefficient of variation (COV) was calculated. The COV is defined as the ratio of the standard deviation over the mean fluorescence pixel intensity in the targeted region. The COV

quantification was performed on six sections for each brain and was not performed on brains that displayed no liposomal delivery.

To determine the number of spot-like areas where liposomes were delivered, the number of areas above 100 μm^2 was quantified. Larger areas of delivery were expected if the liposomes diffused further away from the blood vessels. Regions of interest were selected around all spots of liposome delivery in six sections per brain. An automatic threshold was applied equally to all images in ImageJ (dark triangle) to only select regions of liposome delivery. The area of each region was determined by using the automated 'Analyse Particles' tool in ImageJ.

To assess tissue damage, seven H&E stained slices were analysed per brain. First, adjacent unstained sections were imaged under a fluorescence microscope to identify the location of dextran delivery and therefore the ultrasound targeted brain region. Second, in the H&E stained slices, three histological measures were evaluated: number of sites with more than five extravasated red blood cells, number of microvacuolations and the number of dark neurons. The different values were plotted for RaSP and long-pulse-treated brains. Histological evaluation of the targeted and control hippocampi was performed without knowledge of which side was targeted with ultrasound.

3.3.8 Statistical analysis

A one-way analysis of variance (ANOVA) test was conducted to assess whether differences were present between the parameter sets in the NOD, COV and areas above 100 μm^2 results. *Post hoc* Bonferroni analysis was performed to estimate any significant differences in a pairwise manner ($P < 0.05$). A Wilcoxon rank sum test was performed to test whether differences between the H&E results were significant. All analysis was carried out in Matlab R2019b.

3.4 Results

To investigate whether rapid short-pulse sequences could deliver liposomes into the brain, the left hippocampus of mice was sonicated with either a RaSP or long pulse sequence while intravenously injecting microbubbles. Brains were treated with two different pressures and extracted either 0 or 2 h after the ultrasound treatment.

3.4.1 Detected dose

Liposomes were delivered to the brain with both RaSP and long pulse sequences (Figure 3.4). This is the first demonstration of liposomal delivery using a RaSP sequence. However, delivery was only observed at the higher acoustic pressure (0.6 MPa) with RaSP, with no delivery at 0.4 MPa at both 0 h and 2 h (Figure 3.4 A, C). Whereas long-pulse-treated brains showed delivery in 2 out of 3 brains at 0 h and in all brains at 2 h at this lower pressure (0.4 MPa). All other brains displayed liposomal delivery at the higher pressure (0.6 MPa), and, as expected, in the control right hippocampus no delivery was observed in any of the brains.

Higher fluorescence was detected with long pulses compared to RaSP and when the higher acoustic pressure was emitted compared to the lower one (Figure 3.4-3.5). In RaSP-treated brains, this higher pressure was needed to allow liposomes to be delivered to the brain (Figure 3.5). The NOD that was calculated from these fluorescence regions was 80-fold higher when ultrasound was emitted at 0.6 MPa compared to 0.4 MPa in RaSP-treated brains at 0 h. When long pulses were emitted, the NOD was found to be 23-fold higher at 0.4 MPa and 134-fold higher at 0.6 MPa compared to RaSP at 0.4 MPa at 0 h.

The two-hour recovery time did not influence the NOD significantly other than at 0.4 MPa in long-pulse-treated brains, where a 2-fold increase was observed with a longer recovery time ($P < 0.05$). A significant difference in the NOD was also found between the following groups: between RaSP at 0.4 MPa (0 h), and all higher pressures and long pulses; between RaSP at 0.4 MPa (2 h), and all higher pressures and long pulses at 0.4

MPa (2 h); between long pulses at 0.4 MPa (0 h) and both sequence types at 0.6 MPa (0 h); and lastly between long pulses at 0.4 MPa (2 h) and long pulses at 0.6 MPa (0 h; $P < 0.05$).

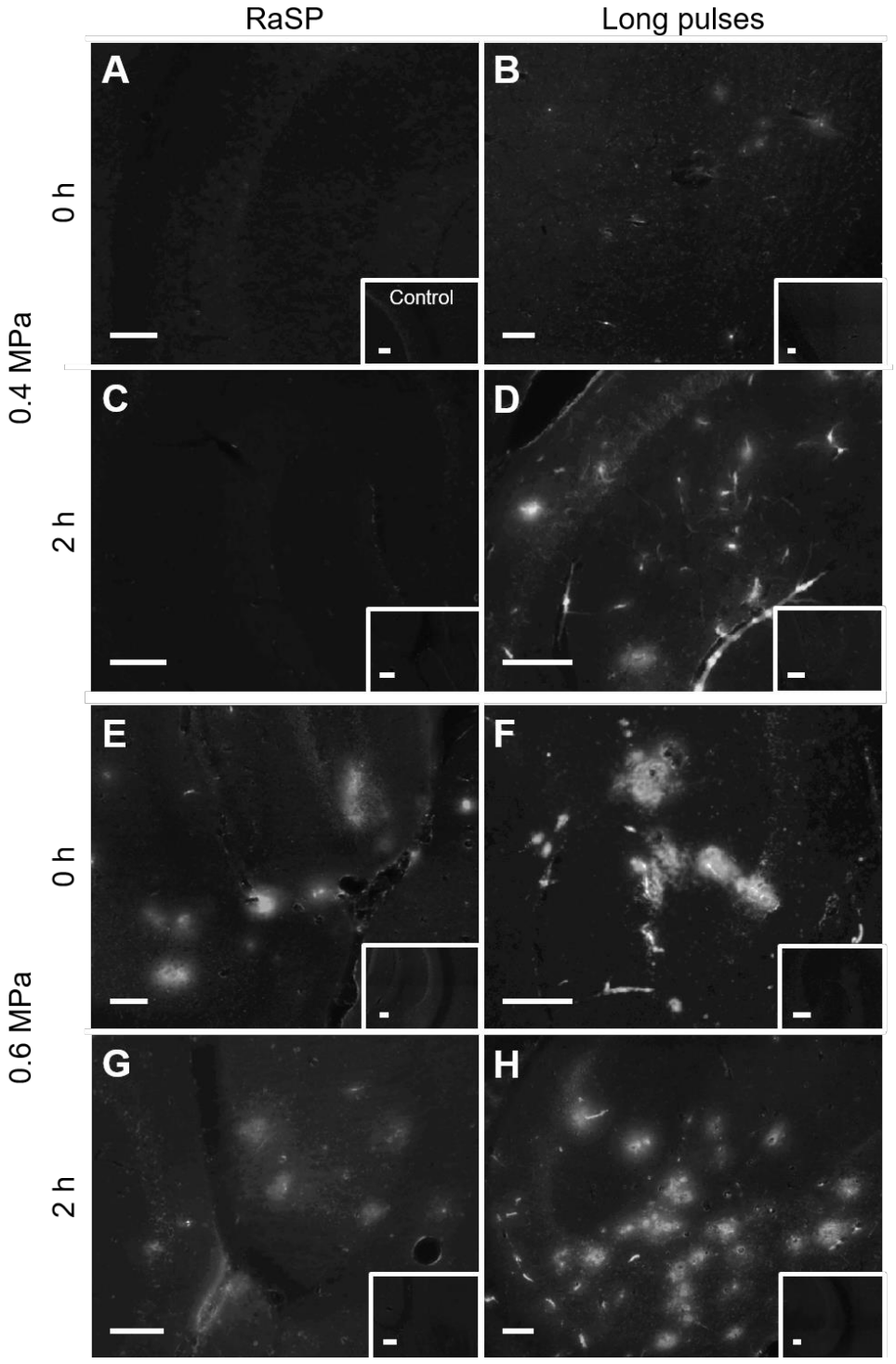

Figure 3.4. Liposomal delivery with rapid short-pulse (RaSP) and long pulse sequences at 0.4 and 0.6 MPa, and at 0 and 2 h after ultrasound treatment. Fluorescence images (10x)

show examples of liposomes delivered with **(A, C, E, G)** RaSP and **(B, D, F, H)** long pulse sequences at **(A-D)** 0.4 MPa and **(E-H)** 0.6 MPa, and at either **(A-B, E-F)** 0 h or **(C-D, G-H)** 2 h after the ultrasound treatment. Right hippocampus control regions are shown in white boxes in the bottom right corner of each image. **(A,C)** No delivery was observed at 0.4 MPa when brains were treated with a RaSP sequence. **(E-H)** At 0.6 MPa, delivery was observed in all brains. More spots of delivery were observed in long-pulse-treated brains compared to RaSP-treated brains. The scale bars indicate 50 μm.

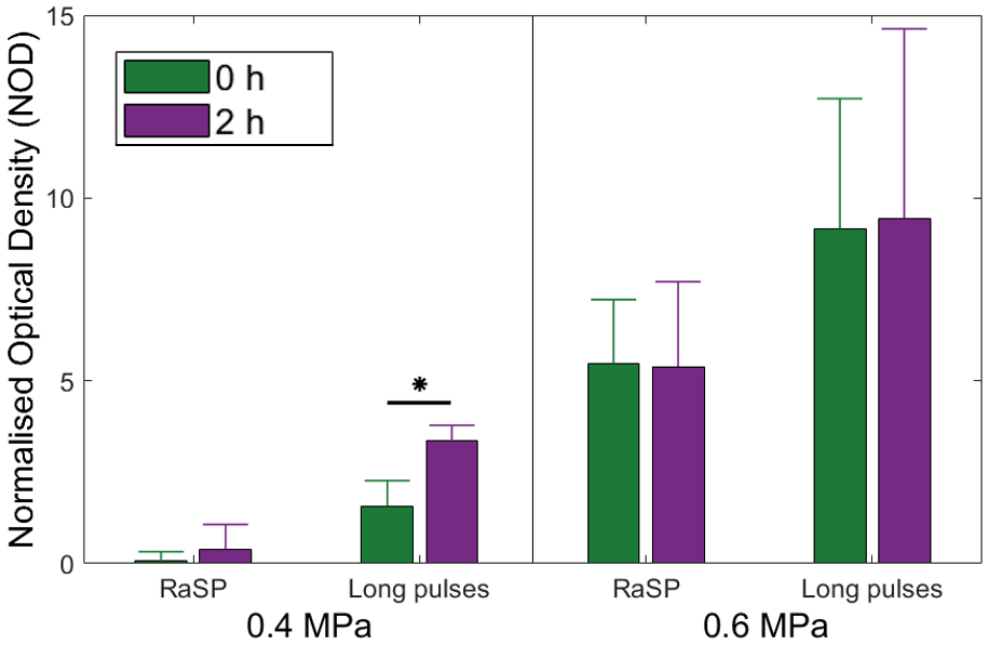

Figure 3.5. Detected dose of liposomes delivered with rapid short-pulse (RaSP) and long pulse sequences at 0.4 and 0.6 MPa, and at 0 h or 2 h after the ultrasound treatment. The threshold for liposomal delivery with RaSP was found to be between 0.4 and 0.6 MPa. The detected dose, quantified with the normalised optical density (NOD), was higher at 0.6 MPa for both RaSP and long pulse sequences ($P < 0.05$). No delivery was detected in RaSP brains at 0.4 MPa. The detected dose was only found to be significantly different between 0 h (green) and 2 h (purple) in long-pulse-treated brains at 0.4 MPa ($P < 0.05$). Significance was also found between RaSP 0.4 MPa (0 h) and all higher pressures and long pulse brains; between RaSP 0.4 MPa (2 h) and all higher pressures and long pulse 0.4 MPa (2 h) brains; between long 0.4 MPa (0 h) and brains treated with both sequence types at 0.6 MPa (0 h); and between long 0.4 MPa (2 h) and long 0.6 MPa (0 h) brains ($P < 0.05$). For clarity, significance bars were only shown between 0 h and 2 h results and not between different pressures or sequence types.

3.4.2 Delivery distribution

The distribution of the delivered liposomes was observed to be heterogeneous in all brains (Figure 3.4). This was observed equally in both RaSP and long-pulse-treated brains with the delivery sites being concentrated around blood vessels. Delivery was observed to be more densely concentrated around blood vessels in long pulse brains (Figure 3.4 D, F, H). Less variation (lower COV values) was quantified in RaSP brains, with significant differences between RaSP 0.6 MPa 0 h brains and long pulse brains at 0.4 MPa 0 h, and between RaSP brains at 0.6 MPa 0 and 2 h, and long pulse brains at 0.6 MPa 0 h ($P < 0.05$; Figure 3.6). The two-hour recovery time did not influence the COV, with no significant differences found between 0 h and 2 h brains within the same parameter sets ($P > 0.05$).

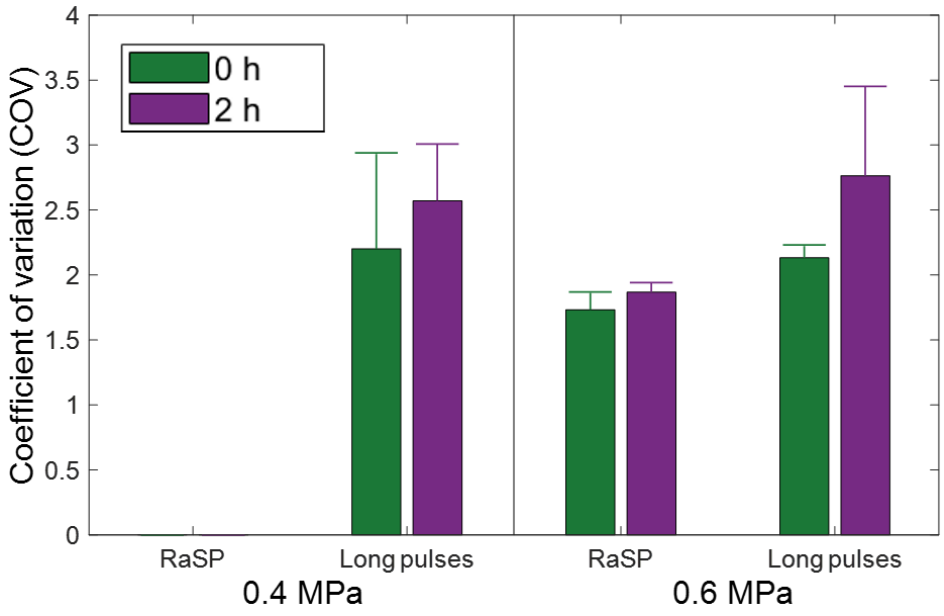

Figure 3.6. Distribution of liposomes delivered with rapid short-pulse (RaSP) and long pulse sequences at 0.4 and 0.6 MPa, and at 0 h or 2 h after the ultrasound treatment. A lower coefficient of variation (COV) was found in RaSP-treated brains compared to long-pulse-treated brains, which indicates less variation and therefore a more homogeneous distribution. The COV was not found to be significantly different between 0 h (green) and 2 h (purple) recovery times ($P > 0.05$). However, significant differences in COV were found between long pulse brains at 0.4 MPa (0 h) and RaSP brains at 0.6 MPa (0 h); and between RaSP brains at 0.6 MPa (0 h and 2 h), and long pulse brains at 0.6 MPa (0 h). The COV was not quantified for

RaSP-treated brains at 0.4 MPa as no liposomal delivery was observed in these brains. For clarity, significance bars were not shown between different pressures or sequence types.

To determine whether there were differences in the number and size of regions with liposome delivery between parameter sets, the number of areas above 100 μm^2 were quantified. The number of delivery regions above 100 μm^2 was found to be higher in long-pulse-treated brains compared to RaSP brains within the same parameter sets (Figure 3.7). Significant differences were found between all RaSP 0.6 MPa brains and long pulse brains at the same pressure at 2 h ($P < 0.05$). Increasing the acoustic pressure, led to an increase in the number of delivery sites. Significant differences were found by increasing the pressure for all parameter sets ($P < 0.05$) except at 0.4 MPa 0 h ($P > 0.05$). Allowing the liposomes two hours to extravasate into the brain and spread within the parenchyma, made most difference in long-pulse-treated brains, with a significant 21-fold increase at 0.4 MPa ($P < 0.01$).

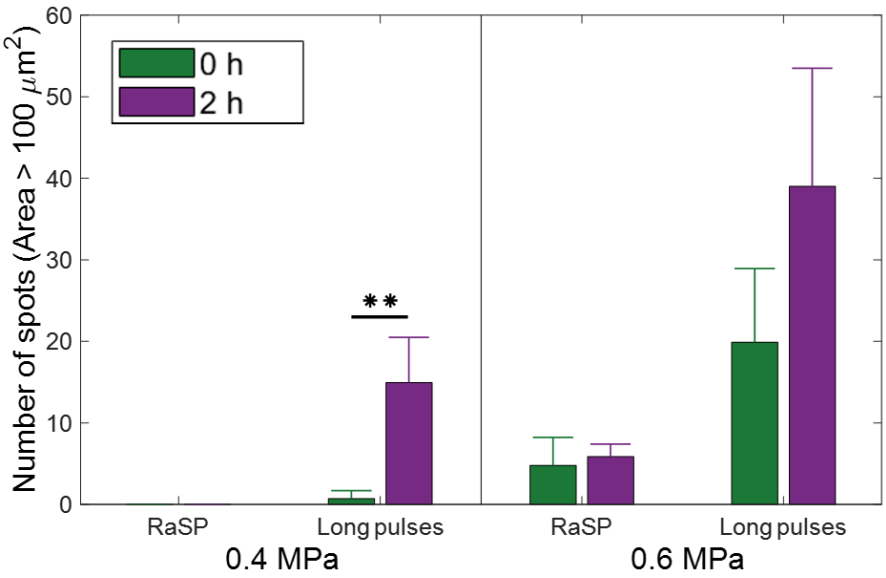

Figure 3.7. Number of areas with liposome delivery above 100 μm^2. The number of areas above 100 μm^2 with liposome delivery was found to be higher in long pulse compared to RaSP-treated brains with the same acoustic pressures. Increasing the acoustic pressure, increased the number of delivery regions. In addition, waiting 2 h instead of 0 h, led to an increase in the number of delivery spots only in long-pulse-treated brains. Significant differences were found between RaSP 0.6 MPa brains and long 0.6 MPa 2 h brains ($P < 0.05$).

The areas of delivery were not quantified for RaSP-treated brains at 0.4 MPa as no liposomal delivery was observed in these brains. For clarity, significance bars were not shown between different pressures or sequence types.

3.4.3 Subcellular localisation

By observing the fluorescence images, liposomes were not only found within the parenchyma but also within cells. To investigate the subcellular distribution of the liposomes within these cells, confocal images were acquired. Liposomes were found within the cytoplasm but not in the nucleus (Figure 3.8). Within the cytoplasm, the liposomes were not uniformly spread but instead small dots of fluorescence were visible. Most of the cells with liposome uptake were found to have a neuron-like morphology.

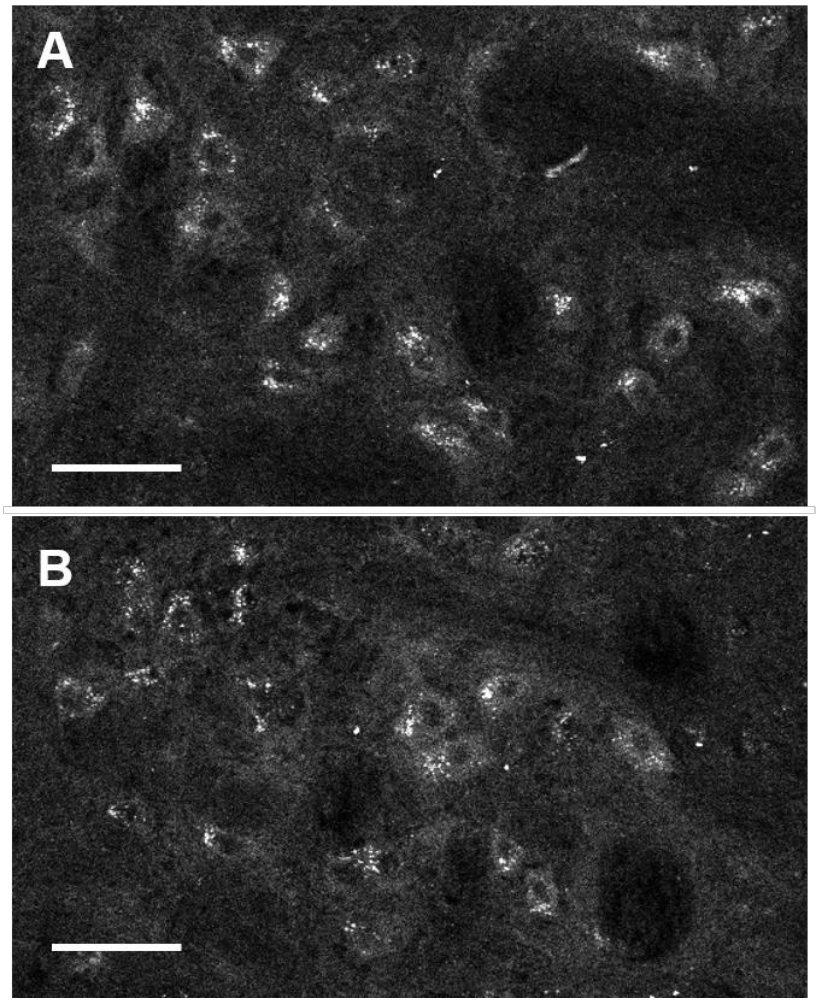

Figure 3.8. Subcellular localisation of liposomes. Confocal images (20x) show details of the subcellular localisation of the liposomes (DiD channel) within ultrasound-targeted regions.

These specific examples are from long-pulse-treated brains at 0.6 MPa and two hours after the ultrasound treatment. Fluorescence was observed within cells, specifically within the cytoplasm and not in the nucleus (darker circular centre within cells). Morphologically these cells with uptake appear to be neurons but staining is required for confirmation. The scale bars indicate 50 µm.

3.4.4 Cellular uptake

To identify the cells that were uptaking the liposomes, brain slices were stained for neurons, microglia and astrocytes. Staining was only performed on brains where cellular uptake was observed. Therefore, all brains treated with RaSP at 0.4 MPa, that did not display any cellular uptake, were not stained as well as one third of brains treated with RaSP at 0.6 MPa (0 h) and two thirds of brains treated with long pulses at 0.4 MPa (0 h).

Liposome uptake within neurons was observed in all brains where cellular uptake was detected (Figure 3.9-10). Although no statistical analysis could be performed due to the low sample size, higher neuronal uptake was observed in long-pulse-treated brains compared to RaSP-treated brains. Higher uptake was also observed in brains treated with the higher pressure (0.6 MPa) compared to the lower pressure (0.4 MPa; Figure 3.10).

Microglial uptake of liposomes was only observed at 0.6 MPa in brains extracted two hours after the ultrasound treatment (Figure 3.11-12). This uptake was higher in long-pulse-treated brains compared to RaSP ones (Figure 3.12). The microglia uptaking the liposomes appeared branched without a rounded shape, indicating a resting rather than an activated state.

No liposome uptake was observed within astrocytes in any RaSP or long-pulse-treated brains (Figure 3.13).

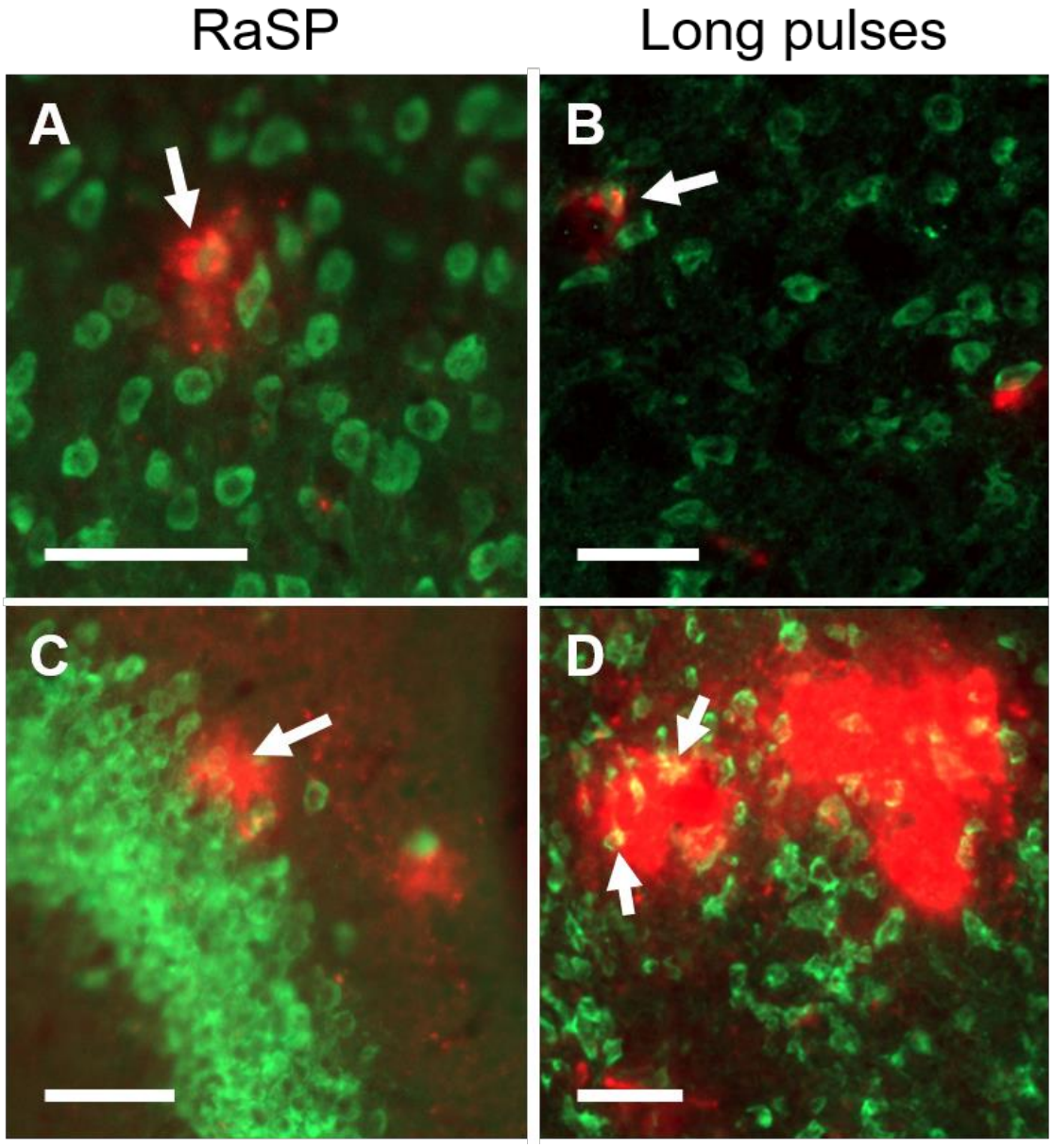

Figure 3.9. Uptake of liposomes within neurons in RaSP and long-pulse-treated brains. Fluorescence images (10x) show liposome (red) uptake (yellow) within neurons (green; NeuN staining) in **(A,C)** RaSP-treated brains and **(B,D)** long-pulse-treated brains. Uptake was higher in long-pulse-treated brains than RaSP ones. White arrows highlight examples of liposome uptake within neurons. The scale bars indicate 50 μm.

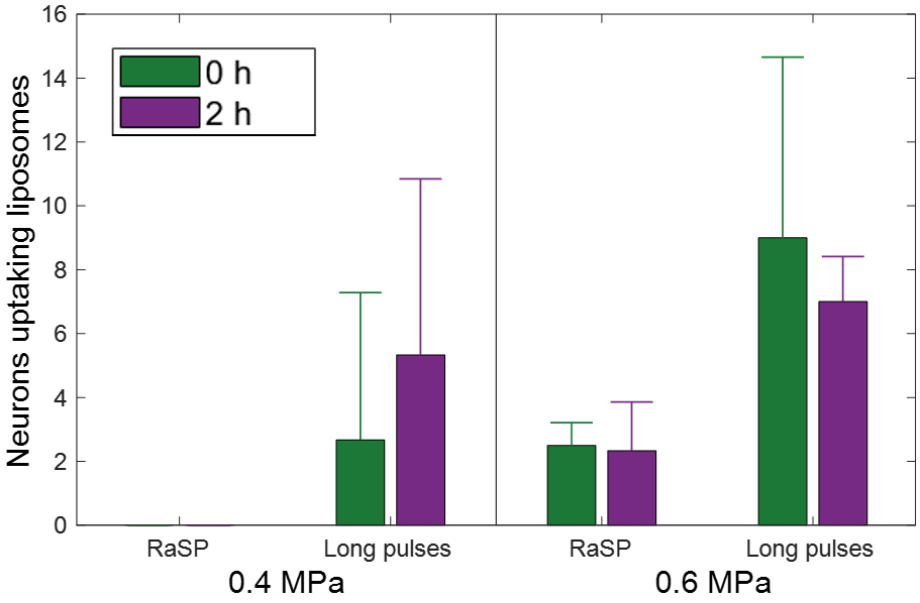

Figure 3.10. Number of neurons with liposome uptake in brains treated with RaSP or long pulses at 0.4 or 0.6 MPa, and at 0 h or 2 h after the ultrasound treatment. Neuronal uptake was observed in all brains where delivery was observed. However, more so in long-pulse-treated brains at 0.6 MPa than at 0.4 MPa and more than in RaSP-treated brains. This plot displays the average number of neurons with uptake across the evaluated brain slices. No statistical analysis was performed as the sample size was too small.

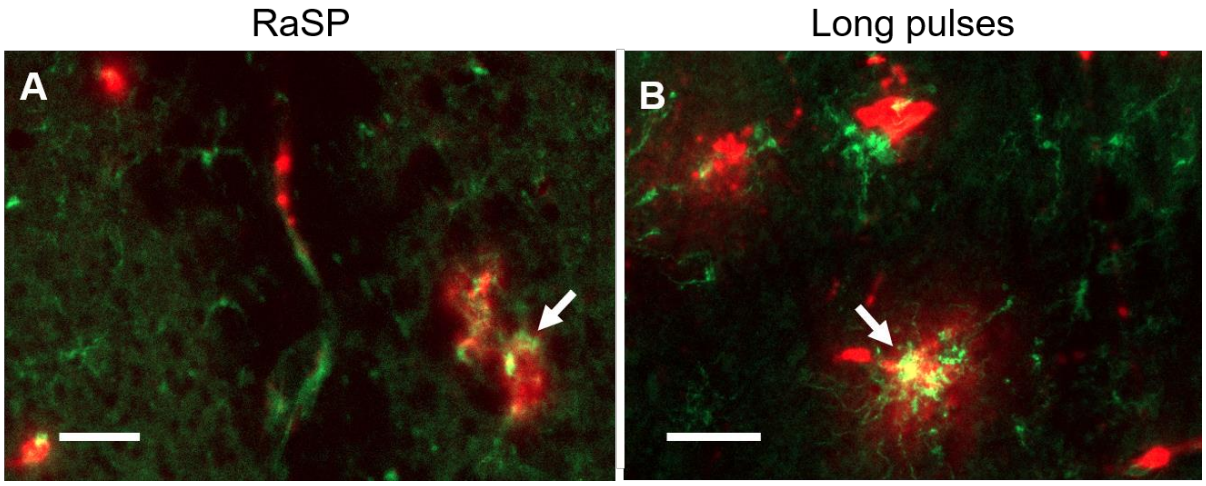

Figure 3.11. Uptake of liposomes within microglia in RaSP and long-pulse-treated brains. Fluorescence images (10x) show liposome (red) uptake (yellow) within microglia (green; Iba1 staining) in **(A)** a RaSP-treated brain slice and **(B)** a long-pulse-treated brain slice. White arrows highlight examples of liposome uptake within microglia. The scale bars indicate 50 µm.

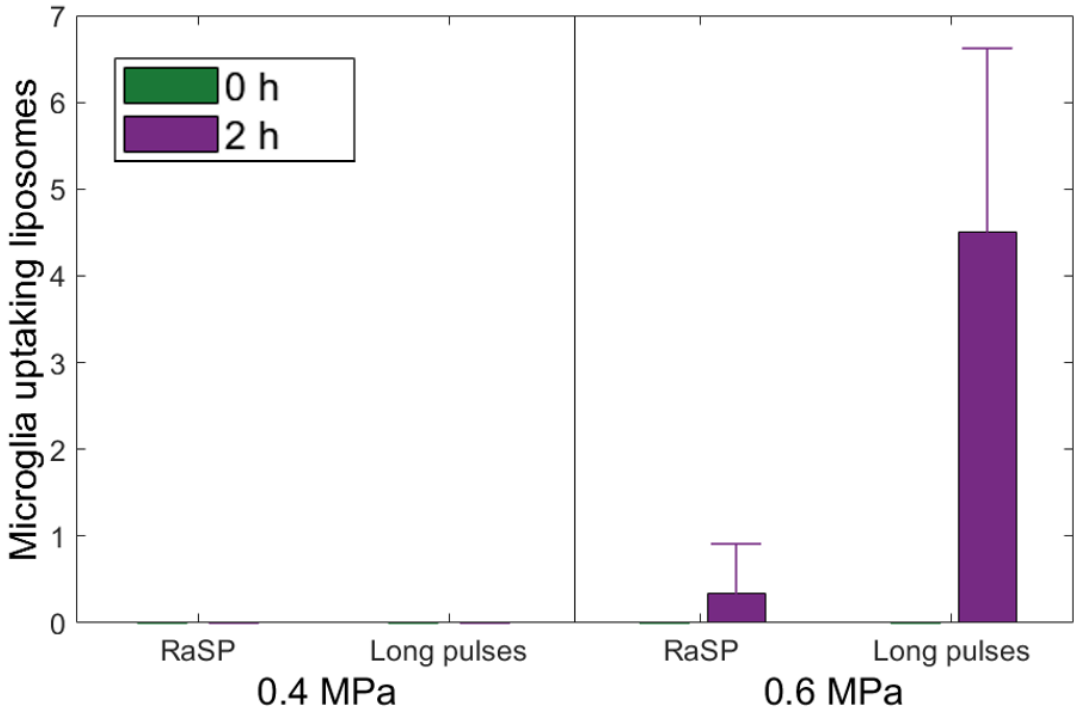

Figure 3.12. Number of microglia with liposome uptake in brains treated with RaSP or long pulses at 0.4 or 0.6 MPa, and at 0 h or 2 h after the ultrasound treatment. Microglial uptake was only observed in 0.6 MPa brains 2 h after ultrasound treatment. Higher uptake was observed in long-pulse-treated brains compared to RaSP ones. This plot displays the average number of microglia with uptake across the evaluated brain slices. No statistical analysis was performed as the sample size was too small.

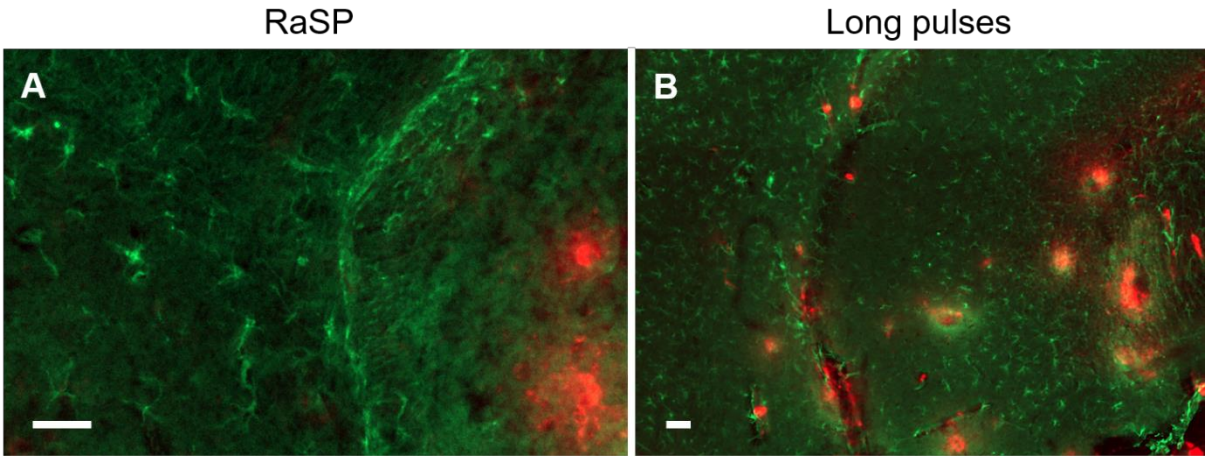

Figure 3.13. Uptake of liposomes within astrocytes in RaSP and long-pulse-treated brains. Fluorescence images (10x) show no liposome (red) uptake within astrocytes (green; GFAP staining) in **(A-B)** RaSP-treated brains and **(C-D)** long-pulse-treated brains. The scale bars indicate 50 μm.

3.4.5 Safety profile

To evaluate whether RaSP and long-pulse-treated brains displayed any histological damage at 0.6 MPa, sections were stained with H&E. As expected, all control right hippocampi showed no damage (Figure 3.14-15 D-F). The targeted left hippocampi in RaSP-treated brains showed no evidence of damage except for one site of red blood cell (RBC) extravasation in a single brain slice (Figure 3.14 C). No other sites of red blood cell extravasation and no microvacuolations or dark neurons were identified in the brain slices. In long-pulse-treated brains, however, sites with more than five extravasated RBCs were detected in 93% of analysed sections, microvacuolations in 93% of sections and dark neurons in 21% (Figure 3.15-16). No significant differences were found between RaSP and long-pulse-treated brains due to the large variations in numbers between brain slices ($P > 0.05$; Figure 3.16). Compared to H&E results performed on brains at 0.4 MPa (Chapter 2, section 2.3.6), the sites of histological damage were found to be larger at 0.6 MPa, with a higher number of red blood cells extravasating compared to brains treated with the lower pressure.

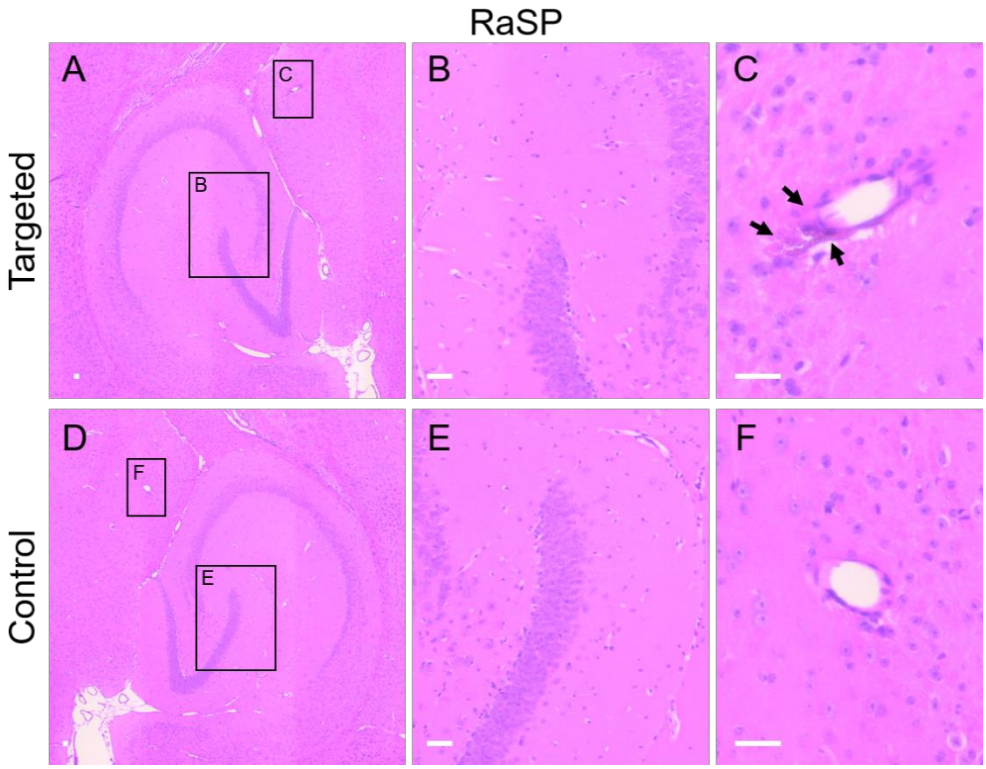

Figure 3.14. H&E staining on RaSP-treated brains at 0.6 MPa to assess tissue damage. Microscopic examination of H&E stained **(A-C)** left (targeted) and **(D-F)** right (control)

hippocampi of RaSP-treated brains show **(C)** a single site of red blood cell extravasation (arrows), but no histological damage in all other regions and brain slices. The black boxes show the enlarged regions in the middle and right columns respectively. The scale bars indicate 50 μm.

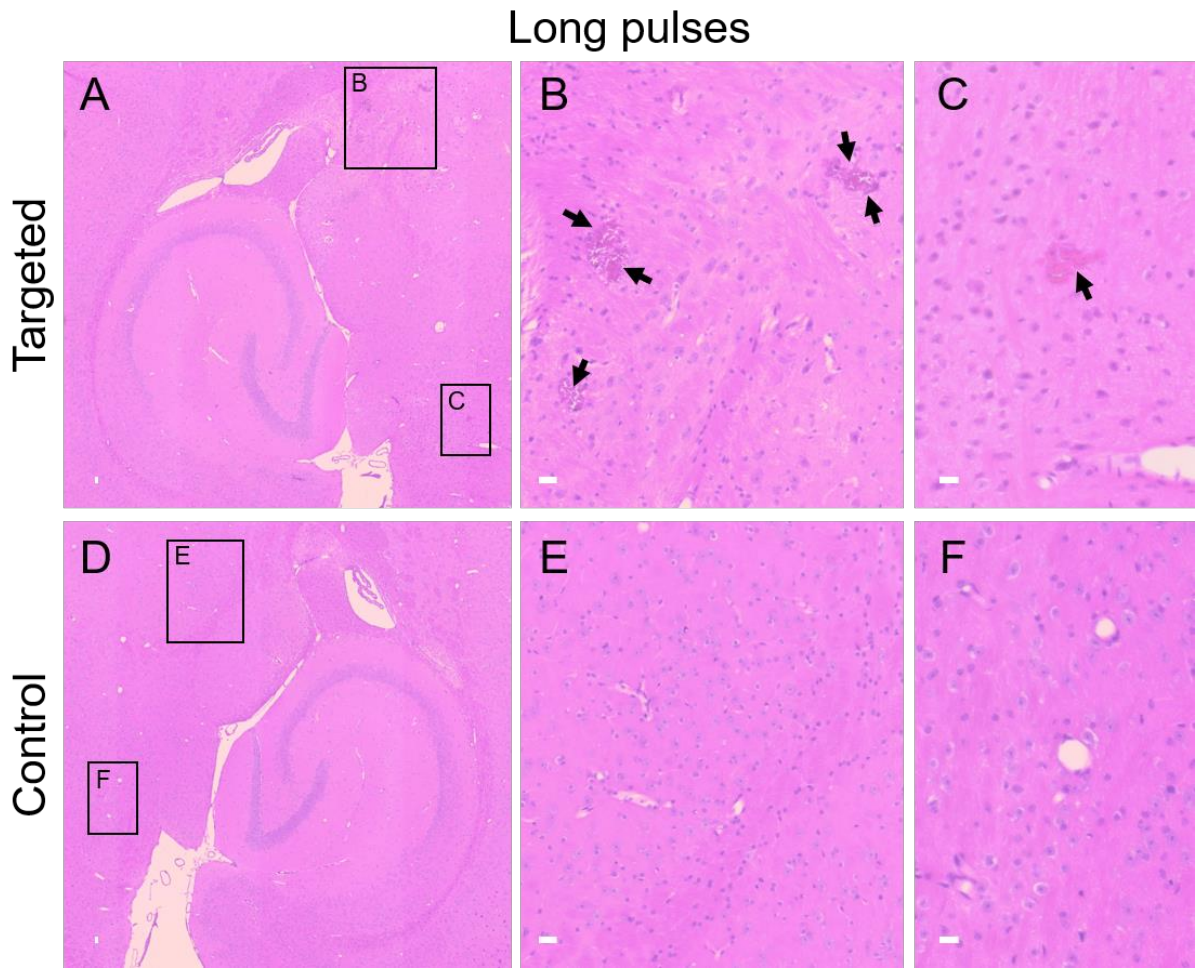

Figure 3.15. H&E staining on long-pulse-treated brains at 0.6 MPa to assess tissue damage. Microscopic examination of H&E stained **(A-C)** left (targeted) and **(D-F)** right (control) hippocampi of long-pulse-treated brains show **(B-C)** histological damage at multiple sites within the ultrasound targeted area (arrows): red blood cell extravasation, microvacuolations and dark neurons. The black boxes show the enlarged regions in the middle and right columns respectively. The scale bars indicate 50 μm.

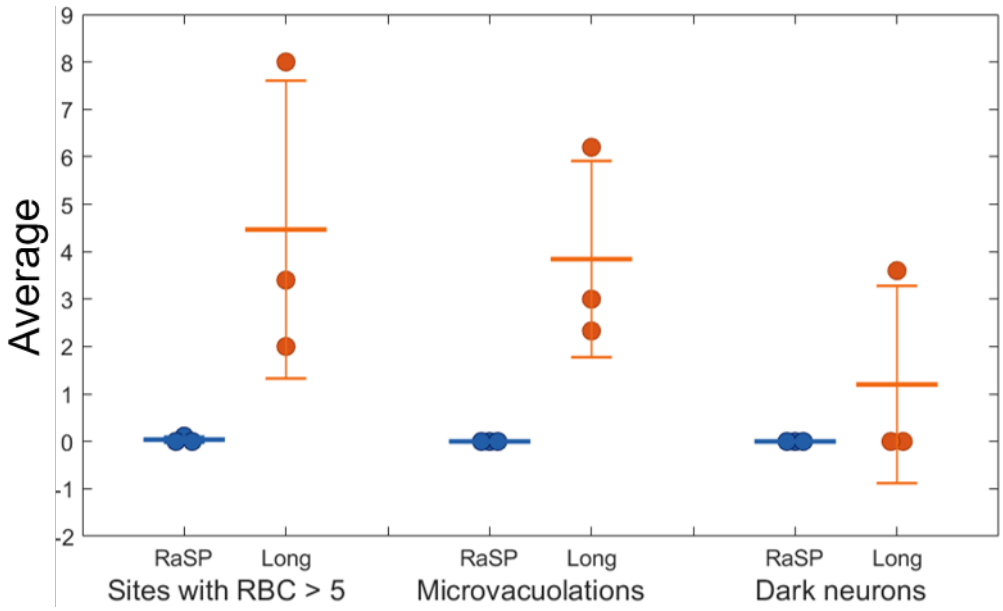

Figure 3.16. Average number of sites with red blood cell extravasations, microvacuolations and dark neurons in RaSP and long pulse brains at 0.6 MPa. The average number of sites with more than five extravasated red blood cells (RBCs), microvacuolations and dark neurons is shown for (blue) RaSP and (orange) long-pulse-treated brains. This quantification was performed on nine H&E stained slices per brain. In all RaSP brains, only one site with more than five extravasated RBCs and no sites with microvacuolations or dark neurons were observed. In long pulse brains, however, damaged sites were found in all brains. No significant differences were found between RaSP and long pulse brains ($P > 0.05$).

3.5 Discussion

3.5.1 Delivery

In this chapter, we have shown that 100 nm liposomes can be delivered to the brain when emitting ultrasound in a RaSP sequence. To the best of our knowledge, this is the first demonstration of liposome delivery when emitting short ultrasound pulses, as previous studies have only used long pulse sequences emitting pressures between 0.33 and 1.6 MPa [16], [17], [32]–[35], [24]–[31].

To investigate whether liposomes could be delivered with RaSP within a similar pressure range to the above long pulse studies, we tested delivery at 0.4 and 0.6 MPa. We found that with RaSP, a higher acoustic pressure (0.6 MPa) was required to achieve

delivery and the detected dose was lower than in long-pulse-treated brains (Figure 3.4-3.5). Therefore, with RaSP, the pressure threshold for liposomal delivery was higher than with long pulses.

This increased pressure threshold could be due to the reduced energy inputted into the brain when emitting RaSP, which would lead to a lower probability of disruptive microbubble activity occurring. Disruptive behaviour would more likely lead to the type of increase in BBB permeability that permits the passage of large liposomal agents into the brain. Our results showed that in long-pulse-treated brains, increasing the pressure led to an increase in delivery, both in terms of the overall detected fluorescence intensity and the number of delivery spots (Figure 3.4, 3.7). These results were expected based on previous work [26]. We have previously demonstrated that at 0.4 MPa smaller dextran molecules cross the BBB when emitting RaSP, but endogenous immunoglobulins (~ 15 nm x 9 nm x 4 nm [51], [52]) do not (Chapter 2). Based on these results, we did not expect larger 100 nm liposomes to enter the brain at this low acoustic pressure, as the larger the compound, the higher the pressure needed to deliver it across the BBB [40], [42].

In previous work, we have observed that the delivery and distribution of compounds delivered with focused ultrasound changes depending on the amount of time they are given to circulate and extravasate into the brain (Figure 2.39-2.40). Other groups have investigated liposomal delivery at 0 h, 2 h and 4 h after ultrasound exposure [26], [27], [32]. Here, we explored liposomal delivery at 0 h and 2 h timepoints. We found that in RaSP-treated brains, the detected fluorescence intensity and number of delivery spots were not significantly different between brains sacrificed immediately or two hours after ultrasound exposure (Figure 3.5, 3.7). However, in long-pulse-treated brains, a significant difference was found at 0.4 MPa. We hypothesise that these results could be explained by the difference in duration of increased BBB permeability. With long pulses, the increase in permeability lasts between 4-48 h depending on the ultrasound parameters used [53]–[56]. We would therefore expect the BBB permeability increase

to last the duration of the two-hour recovery period in our long-pulse-treated brains. In RaSP-treated brains, we have shown that the BBB permeability increase lasts for less than 10 minutes which will reduce the number of liposomes able to extravasate into the brain within a two-hour period (Chapter 2, Figure 2.28-29). We therefore hypothesise that the reason we see increased delivery only in long-pulse-treated brains and not in RaSP is due to the BBB being open for longer periods in these brains. This prolonged opening would allow more liposomes to extravasate into the brain within this time frame. On the other hand, at 0.6 MPa, the detected delivery was not significantly different between 0 and 2 h in long-pulse-treated brains. We hypothesise that this could be due to the BBB disruption being higher at this pressure, which would lead to the extravasation of most liposomes at 0 h. Due to the limited diffusion of the liposomes through the 60 nm pores of the extracellular matrix [45], two hours may not lead to a significant increase in the detected delivery, as liposomes will not travel far from the vessels.

3.5.2 Distribution

When delivering agents to the brain, a homogeneous distribution needs to be achieved to allow agents to reach as many targeted sites as possible, avoiding over or under-treating regions within the targeted brain parenchyma. In our experiments, we observed a heterogeneous distribution of liposomes in both RaSP and long-pulse-treated brains (Figure 3.4). However, the main purpose of these liposomes is to carry much smaller drugs or imaging agents, such as doxorubicin (~ 2 nm diameter [57]), to be released from the liposomes into the brain. Therefore, it is these smaller agents that will be diffusing through the brain parenchyma rather than the liposomes, which cannot diffuse far through the pores of the extracellular matrix. Although the distribution of the liposomes is not homogeneous, its delivery pattern could allow the agents loaded within them to be delivered more homogeneously.

Previous studies have shown similar heterogenous patterns of liposome delivery when emitting long pulse sequences [26]–[28], [32], which has also been observed when

delivering other large compounds such as dextran 2,000 kDa (54.4 nm) [40]. The spot-like pattern of confined liposome delivery is likely due to the slow diffusion of these large molecules through the 60 nm width of the extracellular matrix pores [58]. This pore size is the limiting factor in the diffusion of liposomes within the brain, making their delivery inefficient [59].

The uniformity of liposome distribution, quantified with the COV, was not found to be significantly different between brains. However, in RaSP-treated brains a slight decrease in heterogeneity was observed compared to long-pulse-treated brains. This is maybe due to a more uniform delivery around blood vessels in RaSP-treated brains, while with long pulses, delivery sites had a brighter centre with a more cloud-like periphery. A steeper drop-off in intensity around these vessels was observed compared to RaSP-treated brains. These qualitative observations indicate that the RaSP sequence is more likely to stimulate a gentler increase in BBB permeability with less disruptive events, which not only cause higher accumulation around vessels and more sites of delivery, but also tissue damage.

3.5.3 Cellular uptake

Liposomes can be synthesised to be taken up by specific cells within the brain or functionalised to bind specifically to receptors expressed by these cells. It is therefore important for us to know whether liposomes delivered with our focused ultrasound system can reach the areas within the brain where these cells are present. We first investigated whether our liposomes reached neurons, which are important targets for therapeutic and neuroprotective drugs as well as imaging agents. We also looked at whether our liposomes were being uptaken by microglia and astrocytes, which would indicate a pathway of excretion.

Without ultrasound, liposome uptake within neurons has previously been shown both *in vitro* [60]–[63] and *in vivo* [62]–[64]. *In vitro*, fluorescently labelled liposomes have been detected in hippocampal [61], cerebellar [62], mammalian [60] and peripheral neurons [63], while *in vivo*, fluorescence has been detected in neurons of the

hypothalamus and the cerebellum [62], [64]. However, our results showed that focused ultrasound can deliver liposomes to neurons of the hippocampus, proving that liposome uptake within neurons in the targeted region of the brain parenchyma can be achieved without an invasive procedure.

The location of liposomes within neurons can provide us with information regarding their method of uptake. In our experiments, liposomes were detected within the cytoplasm of neurons in a spot-like distribution but were not observed within the nucleus. This specific distribution has been reported with both cationic and anionic liposomes [61]–[63]. It suggests that liposomes are being taken up within lipid-rich compartments in the cytoplasm, such as endosomes or lysosomes. This information, which can be obtained by staining for these compartments, helps identify the pathway of liposome uptake, which has previously been shown to be via clathrin dependent or independent endocytosis depending on the type of liposome delivered [60]–[63]. Future staining will determine whether the anionic liposomes used in this study were compartmentalised, which could provide insight into their pathway of uptake and excretion. If liposome uptake were to be confirmed in lysosomes, this would indicate a pathway of excretion from the neurons.

The higher neuronal uptake observed in long-pulse-treated brains compared to RaSP-treated brains is hypothesised to be due to the higher liposomal delivery within the brain parenchyma as well as the higher number of delivery sites. In future work, later time points (> 2 h) will be explored to investigate whether the number of neurons uptaking liposomes changes over time and to study the pathway of excretion of these liposomes from the brain.

In addition to neurons, liposome uptake was investigated in microglia, which are the primary defence system of the brain. Previous studies have shown liposome uptake in microglia, with varying results depending on the composition of the liposomes. Liposomes with phosphatidylserine phospholipids, for example, have been shown to have neuroprotective roles, inhibiting microglial activation [65], [66]. Although

liposomes have also been synthesised to target microglia [67], non-targeted liposomes have also been observed within these cells [67]. Here, microglial uptake of liposomes was expected as a method of excretion from the brain.

Our results only showed liposome uptake within microglia in brains treated with the higher pressure and two hours after ultrasound treatment. This uptake was higher in long-pulse-treated brains than with RaSP. This could be due to the higher delivery of liposomes at more sites compared to RaSP-treated brains. It is also possible that the microglia in long-pulse-treated brains were more phagocytic due to more disruptive microbubble activity within the vasculature compared to the RaSP sonication. This activity, as well as the higher delivery of liposomes, could also explain why microglial uptake was observed at the higher 0.6 MPa pressure and not at 0.4 MPa.

Microglial response often requires time to manifest, which could explain why liposome uptake was only observed two hours after the ultrasound treatment. We have previously shown that dextran delivery via focused ultrasound led to an immediate response from microglia, which phagocytosed the dextran and displayed a more activated morphology (Chapter 2, Figure 2.22-24). The slower microglial response observed following liposome delivery could be due to the slower extravasation of these liposomes into the regions of the brain parenchyma where microglia are located. However, it could also be related to the type of compound being delivered, its size, biocompatibility and other properties. Future work will focus on exploring intermediate time points between 0 and 2 h, to establish when microglia start to phagocytose liposomes, but also later time points to explore how the microglial involvement develops over time.

In the dextran study described in Chapter 2, microglia appeared to have a more rounded activated morphology in long pulse brains at 0.4 MPa (Chapter 2, Figure 2.22). Here, the few microglia that displayed overlap with the liposome fluorescence did not appear to have a rounded morphology, which indicates that they are in a resting state. This could be due to differences in the probes delivered and in the timing of detection.

The amount of dextran delivered in Chapter 2 is thought to be higher compared to the number of much larger liposomes being delivered here, which could be a reason for the different microglial reaction observed at 0.4 MPa between these two studies. Future work will focus on quantitatively determining with DAB staining (3,3'-diaminobenzidine) whether the microglia uptaking dextran and liposomes are activated or not. This would help to establish whether the differences in activation state observed are due to the ultrasound treatment or the compounds being delivered across the BBB. To gain a better understanding of the microglial response of the brain to these treatments, future work will also establish where and how many activated microglia are within the targeted and control sides of the brain by staining for activated microglia only with CD68 antibody staining.

Lastly, liposome uptake was investigated within astrocytes, which would indicate a pathway of excretion from the brain as with microglia. No liposome uptake was observed within astrocytes in RaSP or long-pulse-treated brains. Previous studies have only shown uptake of targeted liposomes within astrocytes and only *in vitro* [68]–[71]. *In vivo*, the BBB is thought to be the main reason why many of these targeted liposomes have failed to reach astrocytes within the brain. Here, where untargeted liposomes were delivered, the lack of uptake within astrocytes could be due to their slower reaction compared to microglia [72], [73], with which a response was only observed two hours after ultrasound exposure in these experiments. Future work will therefore test whether astrocytes are involved at later time points. When delivering dextran, uptake in astrocytes was seen immediately, although in small amounts (Chapter 2). However, it is possible that astrocytes were uptaking dextran due to it being a sugar molecule, which astrocytes transport to neurons as a source of fuel. Liposomes are also much larger compounds and will respond differently regarding astrocyte uptake. Future work will also involve staining for all astrocytes and not just reactive ones, as was the case with the GFAP stain used in this study.

3.5.4 Safety profile

While investigating the efficiency of liposome delivery to the brain, it is equally important to maintain safety. In our previous work, we have shown that no tissue damage is caused by emitting a RaSP sequence at 0.4 MPa. However, here delivery of liposomes was only achieved at 0.6 MPa with RaSP. Therefore, we sought to investigate the safety profile at this higher pressure in comparison with that of the lower pressure and brains treated with long pulses. H&E staining showed no damage in RaSP-treated brains at 0.4 or 0.6 MPa, except for a single site of red blood cell extravasation at the higher pressure (Figure 3.14 and 3.16). In long-pulse-treated brains, damage was observed in all brains in the form of red blood cell extravasations, microvacuolations and dark neurons (Figure 3.15-16). Our long pulse results reflect findings from other studies that have shown similar H&E results [26], [31], [32]. With RaSP we expected the higher pressure to lead to a higher chance of tissue damage occurring; however, the safety profile was found to be improved compared to that of long pulses.

When emitting ultrasound at the higher pressure, larger sites of tissue damage were observed in long-pulse-treated brains, which has also been shown previously [74], [75]. This damage is thought to be due to the inertial cavitation of microbubbles [76]; however, it may not have long term effects [53], [77]. This type of treatment may be suitable when sonicating tumour cores, for example, whereas at tumour margins, a gentler sonication would be preferred to avoid the unnecessary disruption of any healthy tissue.

In our experiments, tissue damage was assessed on brains that were extracted immediately after the ultrasound exposure without any recovery time, as we expected this to be the worst-case scenario time point. Although we would expect repair processes to occur during the following hours, it is possible that the number of red blood cells extravasating increases over time. In the future, a two-hour assessment will be performed to investigate this further.

3.5.5 Limitations and future work

Although ultrasound emitted in a RaSP sequence has been shown here to deliver liposomes across the BBB, a lower delivery efficacy was achieved compared to long-pulse-treated brains. However, when emitting RaSP, the safety profile of liposome delivery was improved. We have yet to investigate whether therapeutically relevant concentrations of drugs carried by liposomes can be reached when emitting RaSP sequences. Such investigation will influence whether RaSP sequences can be used to efficiently deliver liposomes into the brain, which we plan on testing with doxorubicin-loaded liposomes in future work.

Despite a lower delivery efficacy and a single site of tissue damage being found in RaSP-treated brains, the RaSP sequence has yet to be optimised for liposomal delivery. Currently, the main limitation of the RaSP parameters used in this study is the lower efficacy of delivery. It is widely believed that the magnitude and number of sites of increased BBB permeability are related to the degree of microbubble-vessel interactions in the ultrasound field [78]–[80]. In future work, experiments emitting an increased number of pulses within the period of highest microbubble presence (first few minutes), might lead to an increase in the number of liposome delivery sites. This could be done by increasing the pulse repetition frequency, burst repetition frequency and the number of pulses per burst. These changes could improve the efficacy of delivery while continuing to monitor its safety, to see if efficient damage-free delivery can be achieved with RaSP at this higher pressure (0.6 MPa). Ultimately, depending on whether an improved RaSP sequence can demonstrate delivery of therapeutically relevant drug concentrations in the brain, the choice of ultrasound sequence will depend on the targeted disease and tissue region to be treated, with trade-offs in efficacy and safety depending on this choice.

Here, we have shown liposome delivery in a healthy mouse brain. However, liposomes are generally used to deliver drugs to diseased tissue, with the treatment of tumours being the most common application. A tumour environment has different

permeability, interstitial pressure and vasculature heterogeneity compared to the normal brain [81], [82]. In future work, doxorubicin-loaded liposomes would be delivered in a glioma mouse model to establish how these factors change the delivery patterns observed in this study. In terms of vascular permeability, the normal brain has an intact BBB, while many tumours have a leakier BBB. Therefore, we expect the intact BBB permeability of the healthy mice used in these experiments to be the worst-case scenario.

In this study, we used the fluorescent DiD dye to assess the location of liposome delivery in the brain with the assumption that the dye stays embedded in the liposomal membrane throughout the experiment. The DiD fluorophore was chosen as it dissociated to a very limited extent compared to other commonly used fluorescently labelled lipids [47]. In addition, in agreement with the literature, we found that the DiD fluorophore was not fluorescent when in water, but was strongly fluorescent when located within the liposome bilayer [48], [49]. Therefore, we assumed that the fluorescence signal detected was most probably from the DiD within the liposome bilayer rather than free within the brain. However, we cannot exclude the possibility that some of the detected fluorescence is due to the fluorophore dissociating from the liposomal membrane and entering a different lipid membrane, such as a cell membrane where it would be fluorescent. By staining for cell membranes in future work, we could explore whether they colocalise with the dye, which would indicate a dye exchange between liposomal and cellular lipid membranes.

Future work will also involve looking into the effect of ultrasound and microbubbles on liposome release. Fluorophores and drugs embedded within the liposome bilayer or loaded within the liposome core could be released within the bloodstream due to the ultrasound or microbubble activity. *In vitro* work has previously shown that drugs can be released when emitting ultrasound with microbubbles at 0.17 and 1.5 MPa (at 1 MHz), with more release at the lowest pressure [83]. In high intensity focused ultrasound applications, on the other hand, temperature increases are used to release

drugs from thermally sensitive liposomes [84]–[86]. However, most of these studies either injected liposomes that were more sensitive to ultrasound or attached the liposomes to the microbubbles themselves to encourage release during the oscillation of these microbubbles.

If drugs were to be released within the vasculature of the ultrasound targeted region, a more targeted delivery of drugs would still occur compared to the systemic administration of the drug alone. However, toxicity values would need to be assessed. In our case, if free DiD dye was being released into the bloodstream, it would not be fluorescent. Therefore, the likelihood of us interpreting the fluorescent signal as being from free dye extravasating into the brain is unlikely. In the future, we plan to perform biodistribution studies to investigate how ultrasound affects accumulation in the brain in comparison with other organs such as the heart, liver, spleen, lungs and kidneys. This could also give us a better idea of whether the dye or drugs loaded within the liposomes are being released into the bloodstream and then being excreted via other organs.

Overall, we are unsure how an oscillating microbubble affects neighbouring liposomes. In future work, our ultrasound parameters will be tested on microbubbles and liposomes *in vitro*, to see whether in this simplistic scenario the microbubbles induce the release of DiD from the liposomes. Recent studies have also shown that lipid exchange between microbubbles and cells can occur [87], which could also be taking place between microbubbles and liposomes.

In our experiments, SonoVue polydisperse microbubbles were used. In the future, monosized microbubbles will be tested to see whether this can give more control over the bioeffects that were observed. Larger sample sizes will also be needed as currently no statistical analysis could be performed on our cellular uptake quantification, due to their being a limited number of brain slices with cellular uptake and multiple stains to be performed on this limited number of brain slices.

The duration of increased BBB permeability has only been assessed for RaSP at 0.4 MPa (Chapter 2). However, in the future we will investigate how this duration changes by increasing the pressure. We would expect the time window for delivery to decrease if larger liposome were delivered instead of dextran [44]. The duration of increased BBB permeability will therefore be investigated with dextran to have a direct comparison with our previous work.

Future work will focus on investigating further whether inflammation occurs and whether any cell death is taking place. Staining for blood vessels could confirm whether any liposome uptake is occurring within endothelial cells. Lastly, by staining for lysosomes, we could confirm whether liposomes are taken up within these structures in the cytoplasm of neurons and further experiments could be performed to investigate the mechanisms of liposome uptake within cells and of delivery across the BBB.

3.6 Conclusion

Rapid short ultrasound pulses are here shown to allow the delivery of 100 nm PEGylated liposomes into the brain. Although the efficacy of liposome delivery with this specific RaSP sequence was lower than in long-pulse-treated brains, an improved safety profile was observed. The detected dose and number of delivery spots was lower than with long pulses and a higher acoustic pressure was required to enable liposomes across the BBB. On the other hand, only a single site of red blood cell extravasation was observed in RaSP brains at the higher pressure tested, while in long pulse brains signs of tissue damage were detected in all brains. The reduced delivery and safer profile of RaSP results are probably due to the lower energy inputted and due to a gentler stimulation of the vasculature.

In terms of cellular uptake, neurons were observed to uptake liposomes using RaSP, although to a lower degree compared to long-pulse-treated brains. Within neurons, liposomes were observed in spot-like patterns within the cytoplasm, but not within the

nucleus, which could, with further investigation, give an indication regarding the pathway of cellular uptake and excretion. Microglial uptake was only observed in brains treated with the higher pressure and after a two-hour recovery period, while no astrocyte uptake was observed in any of the brains. Lower glial cell involvement was observed in RaSP compared to long-pulse-treated brains. These results indicate that liposomes can be delivered non-invasively and safely across the BBB with a RaSP ultrasound sequence, which could allow drugs that target neurons and glial cells to reach desired regions in the brain.

3.7 References

[1] P. Sapra and T. M. Allen, "Ligand-targeted liposomal anticancer drugs," *Progress in Lipid Research*, vol. 42, no. 5. pp. 439–462, 2003.

[2] M. Alavi, N. Karimi, and M. Safaei, "Application of various types of liposomes in drug delivery systems," *Advanced Pharmaceutical Bulletin*, vol. 7, no. 1. pp. 3–9, 2017.

[3] P. Crosasso, M. Ceruti, P. Brusa, S. Arpicco, F. Dosio, and L. Cattel, "Preparation, characterization and properties of sterically stabilized paclitaxel-containing liposomes," *J. Control. Release*, vol. 63, no. 1–2, pp. 19–30, 2000.

[4] A. K. Singla, A. Garg, and D. Aggarwal, "Paclitaxel and its formulations," *Int. J. Pharm.*, vol. 235, no. 1–2, pp. 179–192, 2002.

[5] Y. Zhou, Z. Peng, E. S. Seven, and R. M. Leblanc, "Crossing the blood-brain barrier with nanoparticles," *Journal of Controlled Release*, vol. 270. pp. 290–303, 2018.

[6] T. M. Allen, "Long-circulating (sterically stabilized) liposomes for targeted drug delivery," *Trends in Pharmacological Sciences*, vol. 15, no. 7. pp. 215–220, 1994.

[7] S. M. Moghimi, A. C. Hunter, and J. C. Murray, "Long-circulating and target-specific nanoparticles: Theory to practice," *Pharmacological Reviews*, vol. 53, no. 2. pp. 283–318, 2001.

[8] P. Milla, F. Dosio, and L. Cattel, "PEGylation of Proteins and Liposomes: a Powerful and Flexible Strategy to Improve the Drug Delivery," *Curr. Drug Metab.*, vol. 13, no. 1, pp. 105–119, 2011.

[9] V. Torchilin, "Tumor delivery of macromolecular drugs based on the EPR effect,"

Advanced Drug Delivery Reviews, vol. 63, no. 3. pp. 131–135, 2011.

[10] J. N. Sarkaria *et al.*, "Is the blood-brain barrier really disrupted in all glioblastomas? A critical assessment of existing clinical data," *Neuro. Oncol.*, vol. 20, no. 2, pp. 184–191, 2018.

[11] B. J. Umlauf and E. V. Shusta, "Exploiting BBB disruption for the delivery of nanocarriers to the diseased CNS," *Current Opinion in Biotechnology*, vol. 60. pp. 146–152, 2019.

[12] N. Humle, K. Johnsen, G. Arendt, R. Nielsen, T. Moos, and L. Thomsen, "Targeted Vascular Drug Delivery in Cerebral Cancer," *Curr. Pharm. Des.*, vol. 22, no. 35, pp. 5487–5504, 2016.

[13] T. S. Surawicz, F. Davis, S. Freels, E. R. Laws, and H. R. Menck, "Brain tumor survival: Results from the national cancer data base," *J. Neurooncol.*, vol. 40, no. 2, pp. 151–160, 1998.

[14] A. Bhowmik, R. Khan, and M. K. Ghosh, "Blood brain barrier: A challenge for effectual therapy of brain tumors," *BioMed Research International*, vol. 2015. 2015.

[15] R. Stupp *et al.*, "Effects of radiotherapy with concomitant and adjuvant temozolomide versus radiotherapy alone on survival in glioblastoma in a randomised phase III study: 5-year analysis of the EORTC-NCIC trial," *Lancet Oncol.*, vol. 10, no. 5, pp. 459–466, 2009.

[16] L. H. Treat, N. McDannold, N. Vykhodtseva, Y. Zhang, K. Tam, and K. Hynynen, "Targeted delivery of doxorubicin to the rat brain at therapeutic levels using MRI-guided focused ultrasound," *Int. J. Cancer*, vol. 121, no. 4, pp. 901–907, 2007.

[17] L. H. Treat, N. McDannold, Y. Zhang, N. Vykhodtseva, and K. Hynynen, "Improved Anti-Tumor Effect of Liposomal Doxorubicin After Targeted Blood-Brain Barrier Disruption by MRI-Guided Focused Ultrasound in Rat Glioma," *Ultrasound Med. Biol.*, vol. 38, no. 10, pp. 1716–1725, 2012.

[18] F. Helm and G. Fricker, "Liposomal conjugates for drug delivery to the central nervous system," *Pharmaceutics*, vol. 7, no. 2, pp. 27–42, 2015.

[19] J. M. Scherrmann, "Drug delivery to brain via the blood-brain barrier," *Vascul. Pharmacol.*, vol. 38, no. 6, pp. 349–354, 2002.

[20] A. W. Vorbrodt, "Ultracytochemical characterization of anionic sites in the wall of brain capillaries," *J. Neurocytol.*, vol. 18, no. 3, pp. 359–368, 1989.

[21] E. Salvati *et al.*, "Liposomes functionalized to overcome the blood-brain barrier and to target amyloid-β peptide: The chemical design affects the permeability across an in vitro

model," *Int. J. Nanomedicine*, vol. 8, pp. 1749–1758, 2013.

[22] C. C. Visser *et al.*, "Targeting liposomes with protein drugs to the blood-brain barrier in vitro," *Eur. J. Pharm. Sci.*, vol. 25, no. 2–3, pp. 299–305, 2005.

[23] D. B. Vieira and L. F. Gamarra, "Getting into the brain: Liposome-based strategies for effective drug delivery across the blood–brain barrier," *International Journal of Nanomedicine*, vol. 11. pp. 5381–5414, 2016.

[24] F. Y. Yang *et al.*, "Pharmacokinetic Analysis of 111In-Labeled Liposomal Doxorubicin in Murine Glioblastoma after Blood-Brain Barrier Disruption by Focused Ultrasound," *PLoS One*, vol. 7, no. 9, 2012.

[25] Y. Shen *et al.*, "Enhanced delivery of paclitaxel liposomes using focused ultrasound with microbubbles for treating nude mice bearing intracranial glioblastoma xenografts," *Int. J. Nanomedicine*, vol. 12, pp. 5613–5629, 2017.

[26] Y. Shen *et al.*, "Delivery of liposomes with different sizes to mice brain after sonication by focused ultrasound in the presence of microbubbles," *Ultrasound Med. Biol.*, vol. 42, no. 7, pp. 1499–1511, 2016.

[27] A. Papachristodoulou *et al.*, "Chemotherapy sensitization of glioblastoma by focused ultrasound-mediated delivery of therapeutic liposomes," *J. Control. Release*, vol. 295, pp. 130–139, 2019.

[28] J. N. May *et al.*, "Multimodal and multiscale optical imaging of nanomedicine delivery across the blood-brain barrier upon sonopermeation," *Theranostics*, vol. 10, no. 4, pp. 1948–1959, 2020.

[29] Q. Lin *et al.*, "Brain tumor-targeted delivery and therapy by focused ultrasound introduced doxorubicin-loaded cationic liposomes," *Cancer Chemother. Pharmacol.*, vol. 77, no. 2, pp. 269–280, 2016.

[30] C. Y. Lin *et al.*, "Focused ultrasound-induced blood brain-barrier opening enhanced vascular permeability for GDNF delivery in Huntington's disease mouse model," *Brain Stimul.*, vol. 12, no. 5, pp. 1143–1150, 2019.

[31] C. Y. Lin *et al.*, "Focused ultrasound-induced blood-brain barrier opening for non-viral, non-invasive, and targeted gene delivery," *J. Control. Release*, vol. 212, pp. 1–9, 2015.

[32] J. Guo *et al.*, "Passive delivery of liposomes to mouse brain after blood-brain barrier opening induced by focused ultrasound with microbubbles," 2015.

[33] M. Aryal, N. Vykhodtseva, Y. Z. Zhang, J. Park, and N. McDannold, "Multiple treatments

with liposomal doxorubicin and ultrasound-induced disruption of blood-tumor and blood-brain barriers improve outcomes in a rat glioma model," *J. Control. Release*, vol. 169, no. 1–2, pp. 103–111, 2013.

[34] M. Aryal, N. Vykhodtseva, Y. Z. Zhang, and N. McDannold, "Multiple sessions of liposomal doxorubicin delivery via focused ultrasound mediated blood-brain barrier disruption: A safety study," *J. Control. Release*, vol. 204, pp. 60–69, 2015.

[35] M. Aryal, I. Papademetriou, Y. Z. Zhang, C. Power, N. McDannold, and T. Porter, "MRI Monitoring and Quantification of Ultrasound-Mediated Delivery of Liposomes Dually Labeled with Gadolinium and Fluorophore through the Blood-Brain Barrier," *Ultrasound Med. Biol.*, vol. 45, no. 7, pp. 1733–1742, 2019.

[36] Z. Kovacs, P. Luciani, P. Roth, J.-C. Leroux, E. Martin, and B. Werner, "Blood-brain barrier opening-based local delivery of 80 nm-sized liposomes in mice using pulsed focused ultrasound," *J. Ther. Ultrasound*, vol. 3, no. S1, 2015.

[37] H. L. Liu *et al.*, "Blood-brain barrier disruption with focused ultrasound enhances delivery of chemotherapeutic drugs for glioblastoma treatment," *Radiology*, vol. 255, no. 2, pp. 415–425, 2010.

[38] J. Mei *et al.*, "Experimental study on targeted methotrexate delivery to the rabbit brain via magnetic resonance imaging-guided focused ultrasound," *J. Ultrasound Med.*, vol. 28, no. 7, pp. 871–880, 2009.

[39] E. J. Park, Y. Z. Zhang, N. Vykhodtseva, and N. McDannold, "Ultrasound-mediated blood-brain/blood-tumor barrier disruption improves outcomes with trastuzumab in a breast cancer brain metastasis model," *J. Control. Release*, vol. 163, no. 3, pp. 277–284, 2012.

[40] H. Chen and E. E. Konofagou, "The size of blood-brain barrier opening induced by focused ultrasound is dictated by the acoustic pressure," *J. Cereb. Blood Flow Metab.*, vol. 34, no. 7, pp. 1197–1204, 2014.

[41] J. J. Choi, K. Selert, F. Vlachos, A. Wong, and E. E. Konofagou, "Noninvasive and localized neuronal delivery using short ultrasonic pulses and microbubbles," *Proc. Natl. Acad. Sci. U. S. A.*, vol. 108, no. 40, pp. 16539–16544, 2011.

[42] J. J. Choi, S. Wang, Y. S. Tung, B. Morrison, and E. E. Konofagou, "Molecules of Various Pharmacologically-Relevant Sizes Can Cross the Ultrasound-Induced Blood-Brain Barrier Opening in vivo," *Ultrasound Med. Biol.*, vol. 36, no. 1, pp. 58–67, 2010.

[43] T. Chan, "Synthesis, in vitro and in vivo evaluation of nanoparticles and metal complexes

for the treatment of brain diseases," 2020.

[44] B. Marty *et al.*, "Dynamic study of blood-brain barrier closure after its disruption using ultrasound: A quantitative analysis," *J. Cereb. Blood Flow Metab.*, vol. 32, no. 10, pp. 1948–1958, 2012.

[45] C. D. Arvanitis, G. B. Ferraro, and R. K. Jain, "The blood–brain barrier and blood–tumour barrier in brain tumours and metastases," *Nature Reviews Cancer*, vol. 20, no. 1. pp. 26–41, 2020.

[46] S. V. Morse *et al.*, "Rapid short-pulse ultrasound delivers drugs uniformly across the murine blood-brain barrier with negligible disruption," *Radiology*, vol. 291, no. 2, pp. 459–466, 2019.

[47] R. Münter, K. Kristensen, D. Pedersbæk, J. B. Larsen, J. B. Simonsen, and T. L. Andresen, "Dissociation of fluorescently labeled lipids from liposomes in biological environments challenges the interpretation of uptake studies," *Nanoscale*, vol. 10, no. 48, pp. 22720–22724, 2018.

[48] B. B. Bhowmik, S. Basu, and D. Ray, "Photophysical studies of 3,3′ dioctadecyloxacarbocyanine dye in model biological membranes and different solvents," *Chem. Phys. Lipids*, vol. 109, no. 2, pp. 175–183, 2001.

[49] B. S. Packard and D. E. Wolf, "Fluorescence Lifetimes of Carbocyanine Lipid Analogues in Phospholipid Bilayers," *Biochemistry*, vol. 24, no. 19, pp. 5176–5181, 1985.

[50] M. Schneider and D. Ph, "Characteristics of SonoVueTM," vol. 16, no. 7, pp. 743–746, 1999.

[51] H. Bagçi, F. Kohen, U. Kusçuoglu, E. A. Bayer, and M. Wilchek, "Monoclonal anti-biotin antibodies simulate avidin m the recognition of biotin," *FEBS Lett.*, vol. 322, no. 1, pp. 47–50, 1993.

[52] Y. H. Tan, M. Liu, B. Nolting, J. G. Go, J. Gervay-Hague, and G. Y. Liu, "A nanoengineering approach for investigation and regulation of protein immobilization," *ACS Nano*, vol. 2, no. 11, pp. 2374–2384, 2008.

[53] K. Hynynen, N. McDannold, N. A. Sheikov, F. A. Jolesz, and N. Vykhodtseva, "Local and reversible blood-brain barrier disruption by noninvasive focused ultrasound at frequencies suitable for trans-skull sonications," *Neuroimage*, vol. 24, no. 1, pp. 12–20, 2005.

[54] N. Sheikov, N. McDannold, S. Sharma, and K. Hynynen, "Effect of Focused Ultrasound

Applied With an Ultrasound Contrast Agent on the Tight Junctional Integrity of the Brain Microvascular Endothelium," *Ultrasound Med. Biol.*, vol. 34, no. 7, pp. 1093–1104, 2008.

[55] G. Samiotaki and E. E. Konofagou, "Dependence of the reversibility of focused-ultrasound-induced blood-brain barrier opening on pressure and pulse length in vivo," *IEEE Trans. Ultrason. Ferroelectr. Freq. Control*, vol. 60, no. 11, pp. 2257–2265, 2013.

[56] B. Zhao *et al.*, "Blood-brain barrier disruption induced by diagnostic ultrasound combined with microbubbles in mice," *Oncotarget*, vol. 9, no. 4, pp. 4897–4914, 2018.

[57] P. Bilalis, L. A. Tziveleka, S. Varlas, and H. Iatrou, "pH-Sensitive nanogates based on poly(l-histidine) for controlled drug release from mesoporous silica nanoparticles," *Polym. Chem.*, vol. 7, no. 7, pp. 1475–1485, 2016.

[58] R. G. Thorne and C. Nicholson, "In vivo diffusion analysis with quantum dots and dextrans predicts the width of brain extracellular space," *Proc. Natl. Acad. Sci. U. S. A.*, vol. 103, no. 14, pp. 5567–5572, 2006.

[59] P. A. Netti *et al.*, "Enhancement of fluid filtration across tumor vessels: Implication for delivery of macromolecules," *Proc. Natl. Acad. Sci. U. S. A.*, vol. 96, no. 6, pp. 3137–3142, 1999.

[60] H. M. E. Azzazy, K. Hong, M. C. Wu, and G. W. Gross, "Interaction of cationic liposomes with cells of electrically active neuronal networks in culture," *Brain Res.*, vol. 695, no. 2, pp. 231–236, 1995.

[61] A. Lakkaraju, Y. E. Rahman, and J. M. Dubinsky, "Low-density lipoprotein receptor-related protein mediates the endocytosis of anionic liposomes in neurons," *J. Biol. Chem.*, vol. 277, no. 17, pp. 15085–15092, 2002.

[62] Z. Chu, Y. Sun, C. Y. Kuan, G. A. Grabowski, and X. Qi, "Saposin C: Neuronal effect and CNS delivery by liposomes," in *Annals of the New York Academy of Sciences*, 2005, vol. 1053, pp. 237–246.

[63] S. Lee, A. T. Ashizawa, K. S. Kim, D. J. Falk, and L. Notterpek, "Liposomes to target peripheral neurons and Schwann cells," *PLoS One*, vol. 8, no. 11, 2013.

[64] I. E. Thunnissen, E. Marani, and W. J. Rietveld, "'Homing' of Lucifer Yellow liposomes into hypothalamic neurons: a combined neuroanatomical Golgi and tracing technique," *J. Neurosci. Methods*, vol. 12, no. 2, pp. 113–123, 1984.

[65] S. Hashioka *et al.*, "Phosphatidylserine and phosphatidylcholine-containing liposomes inhibit amyloid β and interferon-γ-induced microglial activation," *Free Radic. Biol. Med.*,

vol. 42, no. 7, pp. 945–954, 2007.

[66] S. Hashioka *et al.*, "Phospholipids modulate superoxide and nitric oxide production by lipopolysaccharide and phorbol 12-myristate-13-acetate-activated microglia," *Neurochem. Int.*, vol. 50, no. 3, pp. 499–506, 2007.

[67] N. J. Wiley *et al.*, "Lipopolysaccharide Modified Liposomes for Amyotropic Lateral Sclerosis Therapy: Efficacy in SOD1 Mouse Model," *Adv. Nanoparticles*, vol. 01, no. 03, pp. 44–53, 2012.

[68] B. dos Santos Rodrigues, H. Oue, A. Banerjee, T. Kanekiyo, and J. Singh, "Dual functionalized liposome-mediated gene delivery across triple co-culture blood brain barrier model and specific in vivo neuronal transfection," *J. Control. Release*, vol. 286, pp. 264–278, 2018.

[69] B. dos Santos Rodrigues, A. Banerjee, T. Kanekiyo, and J. Singh, "Functionalized liposomal nanoparticles for efficient gene delivery system to neuronal cell transfection," *Int. J. Pharm.*, vol. 566, pp. 717–730, 2019.

[70] P. Madhusudanan, S. Reade, and S. A. Shankarappa, "Neuroglia as targets for drug delivery systems: A review," *Nanomedicine: Nanotechnology, Biology, and Medicine*, vol. 13, no. 2. pp. 667–679, 2017.

[71] F. Zhang, Y. A. Lin, S. Kannan, and R. M. Kannan, "Targeting specific cells in the brain with nanomedicines for CNS therapies," *J. Control. Release*, vol. 240, pp. 212–226, 2016.

[72] S. A. Liddelow and B. A. Barres, "Reactive Astrocytes: Production, Function, and Therapeutic Potential," *Immunity*, vol. 46, no. 6. pp. 957–967, 2017.

[73] R. Schmidt-Kastner, K. Wietasch, H. Weigel, and U. T. Eysel, "Immunohistochemical staining for glial fibrillary acidic protein (GFAP) after deafferentation or ischemic infarction in rat visual system: Features of reactive and damaged astrocytes," *Int. J. Dev. Neurosci.*, vol. 11, no. 2, pp. 157–174, 1993.

[74] R. Chopra, N. Vykhodtseva, and K. Hynynen, "Influence of exposure time and pressure amplitude on blood-brain-barrier opening using transcranial ultrasound exposures," *ACS Chem. Neurosci.*, vol. 1, no. 5, pp. 391–398, 2010.

[75] N. McDannold, N. Vykhodtseva, and K. Hynynen, "Blood-Brain Barrier Disruption Induced by Focused Ultrasound and Circulating Preformed Microbubbles Appears to Be Characterized by the Mechanical Index," *Ultrasound Med. Biol.*, vol. 34, no. 5, pp. 834–840, 2008.

[76] N. McDannold, N. Vykhodtseva, and K. Hynynen, "Targeted disruption of the blood-brain barrier with focused ultrasound: Association with cavitation activity," *Phys. Med. Biol.*, vol. 51, no. 4, pp. 793–807, 2006.

[77] N. McDannold, N. Vykhodtseva, S. Raymond, F. A. Jolesz, and K. Hynynen, "MRI-guided targeted blood-brain barrier disruption with focused ultrasound: Histological findings in rabbits," *Ultrasound Med. Biol.*, vol. 31, no. 11, pp. 1527–1537, 2005.

[78] M. Aryal, C. D. Arvanitis, P. M. Alexander, and N. McDannold, "Ultrasound-mediated blood-brain barrier disruption for targeted drug delivery in the central nervous system," *Advanced Drug Delivery Reviews*, vol. 72. pp. 94–109, 2014.

[79] E. E. Cho, J. Drazic, M. Ganguly, B. Stefanovic, and K. Hynynen, "Two-photon fluorescence microscopy study of cerebrovascular dynamics in ultrasound-induced blood-brain barrier opening," *J. Cereb. Blood Flow Metab.*, vol. 31, no. 9, pp. 1852–1862, 2011.

[80] Y.-S. Tung, F. Vlachos, J. A. Feshitan, M. A. Borden, and E. E. Konofagou, "The mechanism of interaction between focused ultrasound and microbubbles in blood-brain barrier opening in mice," *J. Acoust. Soc. Am.*, vol. 130, no. 5, pp. 3059–3067, 2011.

[81] D. F. Baban and L. W. Seymour, "Control of tumour vascular permeability," *Advanced Drug Delivery Reviews*, vol. 34, no. 1. pp. 109–119, 1998.

[82] Y. Boucher, H. Salehi, B. Witwer, G. R. Harsh, and R. K. Jain, "Interstitial fluid pressure in intracranial tumours in patients and in rodents," *Br. J. Cancer*, vol. 75, no. 6, pp. 829–836, 1997.

[83] F. T. H. Yu, X. Chen, J. Wang, B. Qin, and F. S. Villanueva, "Low Intensity Ultrasound Mediated Liposomal Doxorubicin Delivery Using Polymer Microbubbles," *Mol. Pharm.*, vol. 13, no. 1, pp. 55–64, 2016.

[84] A. Schroeder, J. Kost, and Y. Barenholz, "Ultrasound, liposomes, and drug delivery: principles for using ultrasound to control the release of drugs from liposomes," *Chemistry and Physics of Lipids*, vol. 162, no. 1–2. pp. 1–16, 2009.

[85] M. B. C. De Matos *et al.*, "Ultrasound-sensitive liposomes for triggered macromolecular drug delivery: Formulation and in vitro characterization," *Front. Pharmacol.*, vol. 10, 2019.

[86] S. Dromi *et al.*, "Pulsed-high intensity focused ultrasound and low temperature - Sensitive liposomes for enhanced targeted drug delivery and antitumor effect," *Clin. Cancer Res.*, vol. 13, no. 9, pp. 2722–2727, 2007.

[87] M. Aron, O. Vince, M. Gray, C. Mannaris, and E. Stride, "Investigating the Role of Lipid Transfer in Microbubble-Mediated Drug Delivery," *Langmuir*, vol. 35, no. 40, pp. 13205–13215, 2019.

4 | Neuron labelling with an optical-MRI dual-modal imaging agent delivered to the brain via focused ultrasound

4.1 Background

In the field of neuroscience there is a growing need for methods to study neural systems *in vivo* for basic research purposes [1], [2]. Magnetic resonance imaging (MRI) is of particular interest for these purposes due to its unlimited penetration depth, which allows entire organisms to be scanned non-invasively, and its high spatial resolution, which can reach 10 µm with high field scanners [2]. MRI contrast agents can improve the contrast in magnetic resonance (MR) images; such contrast agents can be targeted to specific cells or made sensitive to specific brain activity [1]. One area of interest is the labelling of neurons to study aspects of their physiology, such as changes in neuronal density during development and in disease states [3]–[5]. This information, however, can only be provided non-invasively if the MRI contrast agents are able to cross the blood-brain barrier (BBB) and, once inside the brain, either cross the cell membrane of neurons or target neuronal surface markers.

4.1.1 MRI and Gd-based MRI contrast agents

MRI uses the inherent magnetic properties of endogenous nuclei inside of our body. More than 60% of our body weight is made up of water and each hydrogen atom in these water molecules (H_2O) has a nucleus containing a single positive charge - a proton. Each proton acts like a tiny magnet, spinning around its own axis (Figure 4.1 A-B). MRI aligns these nuclei with a strong magnetic field (B_0) from the MRI scanner (Figure 4.1 C) and then applies perpendicular radio frequency (RF) pulses that tilt the nuclei out of alignment (Figure 4.1 D). The sum of the magnetic properties of these individual nuclei in our body averaged together creates what is called a magnetisation (M), which has a longitudinal (Mz) and a transverse (Mxy) component with respect to the main magnetic field (B0) (Figure 4.1 E). Once these RF pulses are turned off, the

nuclei will realign with the main magnetic field of the scanner, a process which is referred to as relaxation. During this relaxation process the nuclei lose energy and emit their own RF signals. These signals are measured and then used to reconstruct MR images.

In such images, tissues are distinguished based on differences in the water molecule concentrations and on the time taken by the protons in these water molecules to relax in the magnetic field. The time taken for the protons to relax is measured in two different ways. The first is called T_1 relaxation, or longitudinal relaxation, and is the process by which the magnetic vector returns to its initial maximum value parallel to the main magnetic field - its resting state. Graphically, T_1 can be viewed as the time needed for the longitudinal magnetisation to recover 63% of its maximum value (Figure 4.1 F). The second is called T_2 relaxation, or transverse magnetisation, and is the process by which the transverse components of magnetisation decay, returning to their resting state. T_2 is defined as the time taken by the transverse magnetisation to fall to 37% of its initial value (Figure 4.1 F). Images where the contrast and brightness are predominantly determined by T_1 or T_2 properties of the tissue lead to T_1 or T_2-weighted MR images. Such weighting will depend on the MR pulse sequences employed to generate the images.

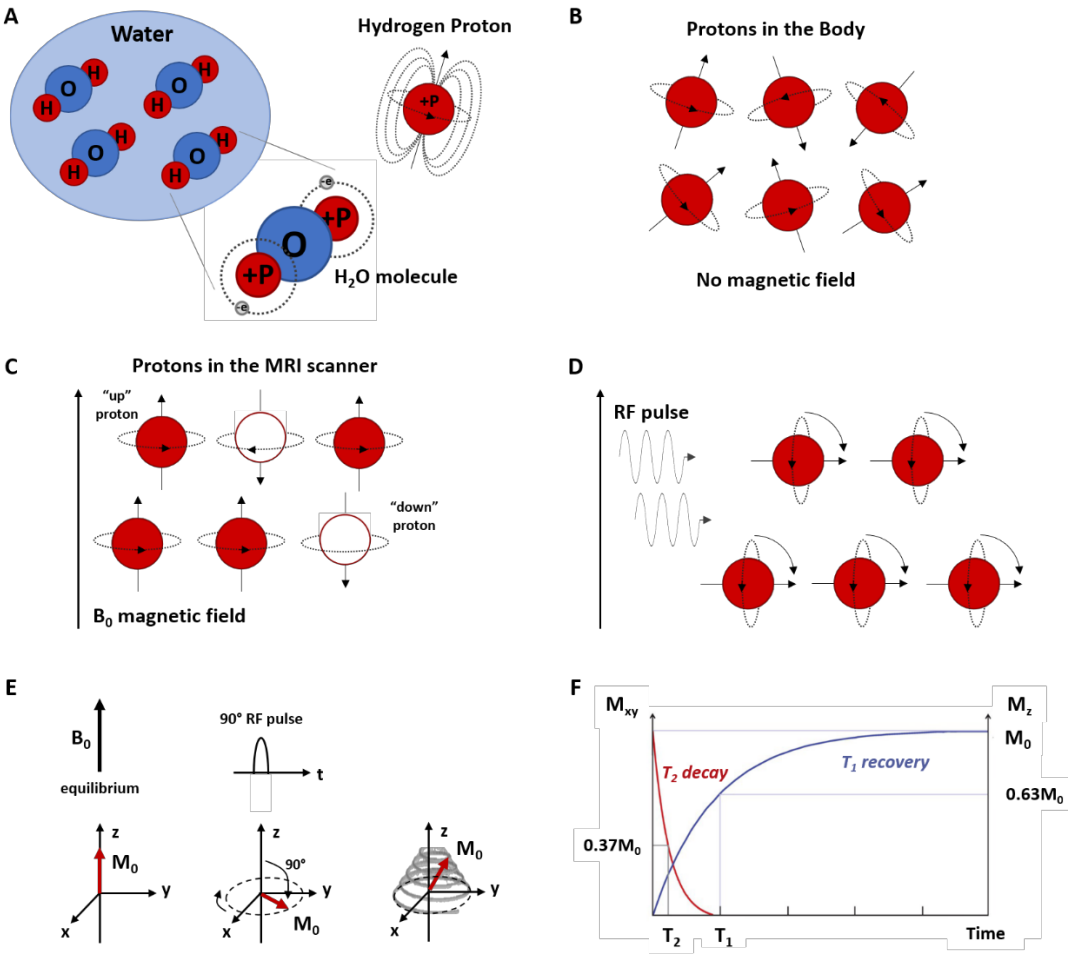

Figure 4.1. Hydrogen atom behaviour in a magnetic field and magnetisation changes over time. (A) Water molecules in the body have two hydrogen atoms that contain a positively charged proton that spins around its own axis, acting like a tiny magnet. **(B)** These protons in the body are all in random positions. **(C)** When in the MRI scanner the protons will align with the magnetic field (B_0). More protons will be aligned in parallel (red) than anti-parallel (white), generating a magnetic field that can be measured via MRI. **(D)** When a perpendicular radio frequency (RF) pulse is applied, the protons will flip away from the main B_0 field, absorbing the RF energy which will then be released as the protons relax back in alignment with the main magnetic field. This signal is measured and used to reconstruct MR images. **(E)** At equilibrium the magnetisation is aligned in the z direction, with just a longitudinal component (M_z), but when a 90° RF pulse is applied, the direction flips so that the magnetisation only has a transverse component (M_{xy}). As the nuclei realign with the main magnetic field, the longitudinal magnetisation component is recovered. **(F)** The time taken for the protons to relax is measured in two different ways: T_1, which is the time it takes the longitudinal magnetisation (M_{xy}) to recover 63% of its maximum value and T_2, which is the time taken by

the transverse magnetisation (M_z) to fall to 37% of its initial value. The figure was redrawn from Broadhouse et al., *Front. Young Minds*, 2019, 7 [6].

To increase the contrast between normal and abnormal tissue, MRI contrast agents are widely used, the majority of which are either paramagnetic gadolinium complexes or superparamagnetic iron oxide particles [7]. Gadolinium(III) complexes are the most commonly used as they make MR images brighter in the regions where they accumulate. Gadolinium(III) has a high magnetic moment and seven unpaired electrons, due to which it possesses paramagnetic properties. Gadolinium(III) complexes also have a free coordination site to which water molecules can bind directly (Figure 4.2). The interaction of these complexes with neighbouring water protons leads to a shortening in the longitudinal relaxation time (T_1), which results in an increase in the signal intensity of T_1-weighted images and therefore a brightening in the MR image (Figure 4.3 A) [8], [9]. Free Gd^{3+} ions are toxic due to their ionic radius being similar to that of Ca^{2+}, which leads to Gd^{3+} interfering with calcium-dependent processes, such as binding to Ca^{2+} binding enzymes and affecting voltage-gated calcium channels [10]. These processes can have adverse biological effects. Gd^{3+} ions are therefore stabilised by chelating ligands, forming stable complexes that are hydrophilic, thermodynamically stable and kinetically inert (Figure 4.2) [11]. One of the most common ligands used in MRI contrast agents for gadolinium is DOTA (tetraazacyclododecane-1,4,7,10-tetraacetic acid).

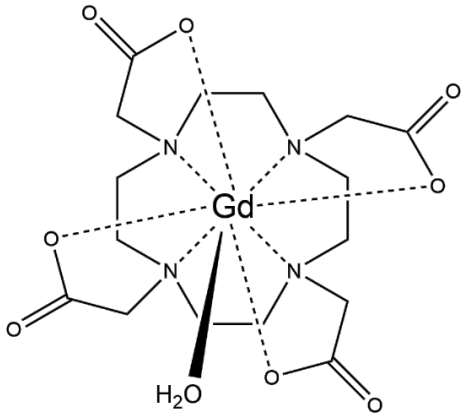

Figure 4.2. Structure of the gadolinium(III) complex Gd(DOTA). Gadolinium(III) is strongly paramagnetic and is stabilised in MRI contrast agents by chelating ligands, such as DOTA.

These Gd(III) complexes have a free coordination site to which water molecules bind directly, which shortens the T_1 relaxation time of these water protons.

Clinically, gadolinium(III) agents are administered intravenously and are rapidly excreted through the kidneys into the urine. Patients with advanced kidney disease cannot be administered Gd-based agents due to its association with nephrogenic systemic fibrosis. In addition to such adverse effects, Gd(III) deposits have also been found in the brain, bones and skin of other patients, months or years after their last contrast-enhanced MRI scan [11]. Due to these possible adverse effects, work has also been carried out on superparamagnetic iron oxide particles that shorten the transverse T_2 relaxation times, resulting in a darkening of the MR image (Figure 4.3 B). Such change in contrast, however, is not favoured by clinicians for diagnosis. In the future, work on Gd(III)-free contrast agents is expected to increase as clinicians become cautious regarding the long-term safety of Gd(III)-based agents for patients.

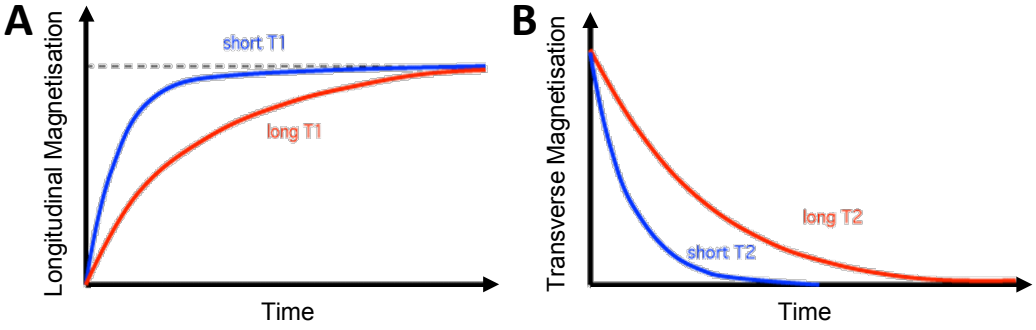

Figure 4.3. Longitudinal and transverse relaxation times. MRI contrast agents shorten the **(A)** longitudinal (T_1) and **(B)** transverse (T_2) relaxation times of neighbouring water protons, leading to an increase in signal intensity and a positive contrast effect. Gd(III)-based agents normally lead to a shortening in T_1 relaxation times (left), which makes the region where they are present brighter, while superparamagnetic particles shorten T_2 relaxation times, making the region darker (right). Figure was redrawn from [12].

Gd(III)-based agents are commonly used for clinical diagnosis, with over 10 million contrast scans performed every year [11]. However, Gd(III)-based MRI contrast agents can also be useful for *in vivo* imaging in basic research to investigate biological processes at the preclinical level, such as developmental events and changes in pH,

metabolic activity and gene expression [13]–[16]. Labelling neurons with Gd(III)-based agents is of interest to study aspects of neuronal physiology. However, the main barrier to the development of MRI contrast agents for the investigation of such biological questions is the delivery of these agents across cell membranes. As these agents are highly hydrophilic, the presence of the cell membrane restricts them to extracellular domains, preventing their internalisation [9]. Due to this hydrophilicity, these agents are also unable to cross an intact blood-brain barrier and for this reason are used to highlight lesions and tumours in the brain where the BBB is compromised [17].

4.1.2 Enhancing cellular uptake of Gd(III)-based contrast agents

To enhance the cellular permeability of Gd(III)-based contrast agents, a series of molecules that allow charged and uncharged agents across cell membranes have been investigated. The conjugation of cell-penetrating peptides (CPPs), short polycationic amino acid sequences, to Gd(III)-based contrast agents has been the most explored option to facilitate their cellular internalisation [18]–[23]. Although effective, CPP-conjugated complexes have been found to leak easily from cells [24] and cause quenched MRI signals due to endosomal or lysosomal entrapment [25]. Gd(III)-based agents have also been loaded into liposome structures in high concentrations to promote cell delivery [26], [27]. However, few of these have been shown to promote intracellular localisation in intact tissue.

Another approach involves attaching hydrophobic fluorescent dyes, such as rhodamine, fluorescein isothiocyanate (FITC), cyanine 7 (Cy7) and boron dipyrromethene (BODIPY) to gadolinium(III) complexes [28]–[30]. These dyes easily cross the cell membrane by themselves but can also make other complexes more cell permeable when conjugated to them. Furthermore, fluorescent dyes are advantageous as they are cheaper than CPPs, easier to conjugate and provide an additional way of imaging the probes via fluorescence microscopy as well as MRI. None of the fluorescent dye-Gd(III) complex conjugates reported so far have been used to label neurons.

Rhodamine B is a commonly used fluorescent dye that has been used by itself to label neurons *in vivo* [31]–[33]. It is biocompatible, is known not to be toxic to neurons and possesses a high quantum yield [31]. In addition, it has been reported not to leak from labelled cells and is resistant to histological fixation procedures [31]. Gd(III)-based contrast agents have previously been conjugated to rhodamine to permeate cells both *in vitro* and *in vivo* [29], [30]. Gd(III)-rhodamine complexes based on a macrocyclic, DOTA (tetraazacyclododecane-1,4,7,10-tetraacetic acid) scaffold (Gd(Rhoda-DOTA), Figure 4.2) have been reported to enter HeLa cells *in vitro* [29], Xenopus embryos *in vivo* [30], and have also been used as dual-modal probes to image tumours in mice (Gd(rhodamine-DO3A)) [34]. In HeLa cells, efficient cell permeation of this complex was demonstrated, but a significant change in the MR signal was not observed, although fluorescence was. Rhodamine B, in all the above-mentioned complexes delivered *in vitro* and *in vivo,* interconverts between a non-fluorescent form and a fully conjugated ring-opened fluorescent form upon activation of the carbonyl group (Figure 4.4). This is a property that has been exploited for pH and heavy metal ion sensing [35], [36]. Gd(rhodamine-DO3A) has, in fact, been used as a dual-modal probe to image tumours, as under acidic tumour conditions the rhodamine moiety exists in its highly fluorescent ring-opened form, making it a pH sensitive probe [34]. However, to label neurons for preclinical basic research, a probe with cell penetrating properties that is always fluorescent would be preferred to allow for both MRI and optical detection independent of pH.

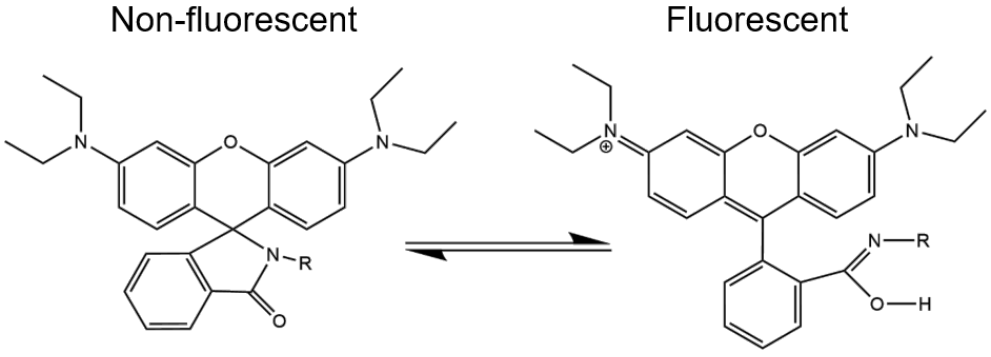

Figure 4.4. Rhodamine B interconverting between a non-fluorescent and a fluorescent form. The structure of both these forms of rhodamine is shown here.

4.1.3 Brain extravasation of Gd(III)-based contrast agents

Before reaching the neuronal cell membrane, intravenously injected probes first need to be able to cross the BBB. Since the BBB prevents most molecules above 400 Da from entering the brain to maintain homeostasis [37], [38], fluorescent dye-Gd(III) conjugates cannot enter the brain under normal conditions [39]. Although complexes can be delivered into the brain via direct injections through the skull or by injecting osmotic solutions intravenously, these procedures are either invasive, with possible complications such as haemorrhage and infection, or non-targeted [40], [41]. However, focused ultrasound and microbubbles can deliver these compounds across the BBB non-invasively and locally to the brain region of interest [42]. This ultrasound technology has been used to deliver many Gd(III)-based MRI contrast agents into the brain [42]–[46], as well as fluorescent dextran molecules into neurons [47], [48]. Recently, liposomes labelled with both gadolinium(III) and rhodamine have also been delivered with focused ultrasound through the BBB to verify liposome delivery, both optically and via MRI [49]. However, no optical-MRI probe designed to image neurons has yet been delivered using focused ultrasound and microbubbles. The delivery of such dual-modal agents into neurons could facilitate basic neuroscience research in preclinical models, combining the advantages of fluorescence imaging with those of MRI.

4.2 Aims and objectives

In this chapter, an 'always on' fluorescent rhodamine probe combined with a macrocyclic gadolinium complex (Gd(rhodamine-pip-DO3A)), synthesised by PhD students in Prof Nicholas Long's group, was used to label neurons. The probe was delivered non-invasively into the left hemisphere of mice using focused ultrasound and microbubbles. The distribution and cellular uptake of the compound was evaluated with fluorescence microscopy within the parenchyma and was compared to that of an optical probe, Texas-red dextran, conventionally used to assess BBB

permeability enhancement following ultrasound-mediated delivery. The cellular uptake of these two probes was analysed in neurons, microglia and astrocytes to check whether Gd(rhodamine-pip-DO3A) specifically labelled neurons and to see whether there was any glial cell-mediated immune response. *Ex vivo* MRI images were acquired to evaluate whether the Gd(III)-rhodamine probe could be detected via MRI as well as fluorescence. A binding assay was also performed to assess whether the probe was binding to albumin in the bloodstream and, lastly, H&E staining was carried out to evaluate the safety of the ultrasound parameters used to deliver this dual-modal probe to the brain.

4.3 Materials and methods

This section describes the different experiments that were carried out to achieve the above mentioned aims. The ultrasound setup and experimental protocol used are first described, with details regarding the microbubbles and probes delivered. The histological and microscopy work performed to assess whether this Gd-rhodamine probe can be used to label neurons is reported, followed by details regarding the *ex vivo* MRI scans and the binding assay to albumin, with statistical analysis relevant to the entire study.

4.3.1 Animals

Nineteen female wild-type C57bl/6 mice (8-12 weeks old, 19.07 ± 1.56 g; Envigo, Huntingdon, UK) were used in this study (Table 4.1). Ten mice were intravenously injected with Gd(rhodamine-pip-DO3A) and nine mice were injected with Texas Red® 3 kDa dextran during ultrasound treatment. Of the ten mice to which Gd(rhodamine-pip-DO3A) was delivered, three were used to detect the probe via MRI, as well as fluorescence microscopy. Of the nine mice to which dextran was delivered, six were used to compare the delivery, distribution and cellular uptake of dextran to that of the Gd-rhodamine probe, and three were used to assess the safety of the ultrasound parameters used by performing H&E staining. All procedures were performed after an

acclimatization period of seven days and mice were kept in standard conditions following a normal diet. All experimental protocols were approved by the institutional animal facility committee and the UK Home Office regulatory establishments.

Table 4.1. Summary of mice used in each experiment. Ten mice were used to assess the delivery and distribution of Gd(rhodamine-pip-DO3A) detected via fluorescence imaging (n = 7) or MRI (n = 3) *ex vivo*. Nine mice were used to deliver 3 kDa Texas Red dextran to compare the distribution of the MRI-optical probe (~ 1 kDa) to that of a larger dextran probe (3 kDa) and to assess damage with H&E staining.

Study	Type of Imaging	Number of mice
Gd(Rhodamine-pip-DO3A) delivery	Fluorescence imaging	7
	MRI	3
Texas Red dextran delivery	Fluorescence imaging	6
Tissue damage assessment with Texas Red dextran delivery		3
Total		19

4.3.2 Ultrasound setup and experimental conditions

Mice were anaesthetised with 1.5-2.0% vaporised isoflurane mixed with oxygen, using an anaesthesia vaporiser (Harvard Apparatus, Cambridge, UK). The fur was removed from the mouse's head with an electric trimmer and depilatory cream and the head was then fixed in a stereotaxic frame (45° ear bars; World Precision Instruments, Hertfordshire, UK). A water bath covered by transparent parafilm membrane and filled with degassed water was lowered onto the head where ultrasound gel had been placed, making the sutures of the skull clear for targeting. A 1-mm thick metallic cross was placed in alignment with the sagittal and lambdoid sutures and the ultrasound

transducer, mounted with a water-filled cone, was lowered into the water bath (Figure 4.5). The transducer was placed 3 mm laterally from the sagittal suture, 0.5 mm anterior to the lambdoid suture and 3 mm inferior to the skull to target the left hemisphere of the brain with the ultrasound focus positioned on the left hippocampus [48]. The opposite right hemisphere was used as a no ultrasound control side. When targeting the metallic cross, the transducer was used in pulse-echo mode, by connecting it to a pulser-receiver (DPR300; Insidix, Seyssins, France) and moving it with a 3D computer-controlled positioning system (Velmex Inc., Bloomfield, NY, USA) to create a raster scan of the cross.

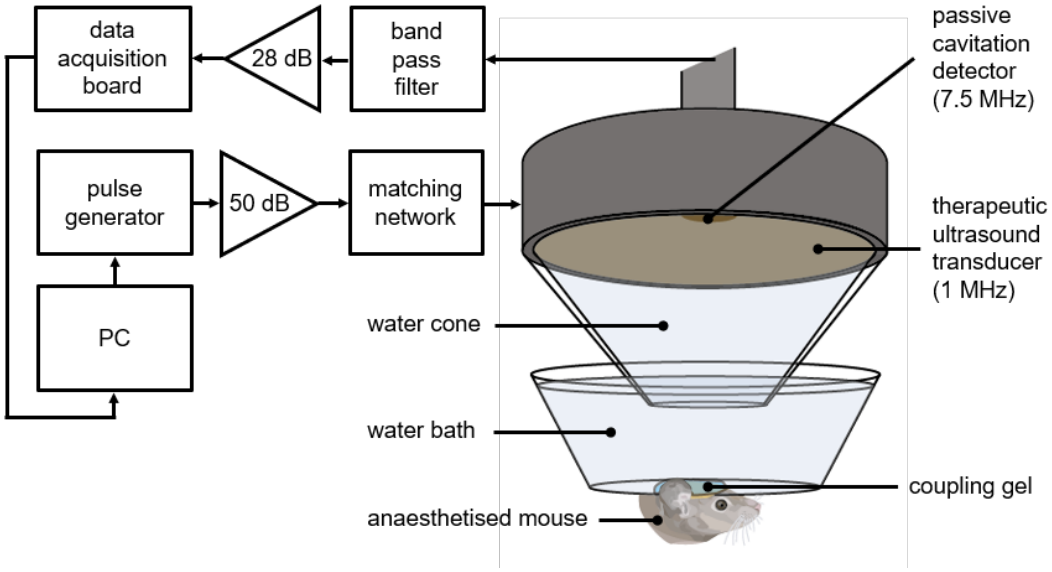

Figure 4.5. Ultrasound experimental setup. The mouse brain was exposed to 1-MHz ultrasound using a long pulse sequence, composed of 10,000 cycle pulses emitted at a slow rate of 0.5 Hz, at a peak negative pressure (P_{neg}) of 0.35 MPa. Ultrasound was emitted onto the left hemisphere through the intact scalp and skull, while the right hemisphere was used as a control, with no ultrasound focused onto it. A 7.5-MHz passive cavitation detector (PCD) was used to verify the presence of microbubble signals. PC = personal computer and dB values refer to the level of amplification. Image from Morse et al, *Theranostics*, 2020, 10(6):2659-2674.

After targeting, therapeutic ultrasound pulses were emitted from the single-element spherical-segment focused ultrasound transducer (centre frequency: 1 MHz, focal depth: 60.5 mm, diameter: 90 mm; Sonic Concepts, Bothell, WA, USA). A function generator (33500B Series; Agilent Technologies, Santa Clara, CA, USA) was used to

generate the pulses, which were passed through a 50-dB power amplifier (2100L Electronics and Innovation, Rochester, NY). Ultrasound pulses were emitted at a peak-negative pressure of 0.35 MPa with a pulse length of 10 ms at a repetition frequency of 0.5 Hz (125 pulses). The pressure amplitude reported was measured with a needle hydrophone (needle diameter: 0.2 mm, Precision Acoustics Ltd., Dorchester, Dorset, UK) prior to *in vivo* experiments in a degassed water tank. Peak-negative values were calculated and attenuated by 11% to correct for skull attenuation, which was measured through the parietal bone (n = 4). The axial, lateral and elevational full width at half maximum intensities of the ultrasound beam were 20 mm, 2 mm and 1 mm respectively.

The presence of microbubble emissions in the targeted region was verified by a passive cavitation detector (PCD, centre frequency: 7.5 MHz, focal length: 76.2 mm; Olympus Industrial, Essex, UK). This detector was positioned through the central opening of the therapeutic transducer with the foci aligned. Acoustic emissions were filtered by a 3-30 MHz bandpass filter (Mini circuits, Brooklyn, NY, USA), amplified by a 28-dB pre-amplifier (Stanford Research Systems, Sunnyvale, CA, USA), and recorded by an 8-bit oscilloscope sampling at 250 MHz (Picoscope 3205A; Pico Technology, Cambridgeshire, UK). Time domain traces were displayed in real-time to determine whether microbubble activity was occurring during the ultrasound treatment. Further processing of these signals was not carried out here, however, the data was saved for future off-line processing.

4.3.3 Microbubble and probe delivery

During the ultrasound treatment, following the first five ultrasound pulses that were used as controls, SonoVue® microbubbles (Bracco, Milan, Italy) were injected intravenously through a 30G home-made catheter over a period of 30 s (volume: 100 µl, concentration: 5 µl/g). The microbubbles were activated following the manufacturer's instructions and were used within 6 h from activation. One minute into the ultrasound treatment, Gd(rhodamine-pip-DO3A) (molecular weight: 1 kDa,

concentration: 5.6 mg/ml; n = 10) or lysine-fixable Texas Red® 3 kDa dextran (concentration: 5 mg/ml; Life Technologies, Paisley, UK; n = 6) were injected. The probes were diluted in 100 µl phosphate-buffered saline (PBS) and were not expected to cross the intact BBB due to their size being above the 400 Da threshold [50]. Details of the synthesis and characterisation of Gd(rhodamine-pip-DO3A) made by Tamara Boltersdorf and Bethany Harriss (PhD students, Prof. Nicholas Long's group) can be found in Appendix 6.4 and Figure 6.18. Very briefly, the structure of rhodamine B was modified to give an 'always on' fluorescent probe by adding a piperazine unit to the amide, locking it in its ring-opened form. This also creates a positive charge on the dye, facilitating its cell permeability. The modified rhodamine was then combined with a macrocyclic gadolinium complex to form a compound that enabled both the accumulation of a Gd-based contrast agent in neurons and simultaneous fluorescence imaging.

4.3.4 Histological staining

Following the ultrasound treatment, the mice were euthanised with an overdose of pentobarbital and were transcardially perfused with 20 mL PBS and 20 mL 10% formalin (Sigma Aldrich, St Louis, MO, USA). The brains were extracted, fixed in formalin overnight, and then cryoprotected before frozen sectioning by placing them in 15% sucrose for six hours and then 30% sucrose overnight. Brains were then placed in optimal cutting temperature compound (OCT; Agar Scientific, Stansted, UK) and sectioned into 30 µm horizontal sections to cover the entire hippocampus using a cryostat (CryoStar NX70; Thermo Fisher, Waltham, MA, USA).

Immunohistochemistry was performed on twelve sections from each brain to determine whether the probe was being uptaken by neurons (NeuN), microglia (Iba1) or astrocytes (GFAP). The antibodies and dilutions used to perform these staining procedures are shown in Table 4.2 and relevant protocols can be found in Appendix Tables 6.2-6.6. A DAPI mounting medium was applied before coverslipping the slides to stain for cell nuclei.

To assess tissue damage when emitting the ultrasound parameters used to deliver the probes, H&E staining and analysis was performed as described in Chapter 2 (section 2.3.7). Nine sections from each of the three brains were analysed for sites with more than five red blood cell extravasations, microvacuolations and dark neurons.

Table 4.2. Primary and secondary antibodies used to stain for neurons, microglia and astrocytes. The type of primary and secondary antibodies and their dilution are indicated.

Stain	Primary Antibody	Secondary Antibody
Neurons	Recombinant anti-NeuN antibody [EPR12763] (ab177487) - 1:500	Goat anti-rabbit IgG H&L (Alexa Fluor® 488) (ab150077) - 1:500
Microglia	Anti-Iba1 antibody (ab5076) - 1:500	Donkey anti-goat IgG H&L (Alexa Fluor® 488) (ab150129) - 1:500
Astrocytes	GFAP monoclonal antibody (2.2B10) (13-0300) - 1:100	Mouse anti-rat IgG2a (FITC) (11-4817-82) - 1:500

4.3.5 Microscopy and analysis

To analyse the detected dose, distribution and cellular uptake with both probes, images of brain slices were acquired with a fluorescence microscope (10x; Zeiss Axio Observer; Oberkochen, Germany) and a confocal microscope (20x; Zeiss LSM-510 inverted; Oberkochen, Germany). Gd(rhodamine-pip-DO3A) and Texas Red dextran were excited at 562/40 nm and emissions were filtered at 624/40 nm. Secondary antibody fluorophores (Alexa Fluor 488 and FITC) from the staining procedures were excited at 470/40 nm and emissions were filtered at 525/50 nm.

The detected dose of the delivered probes was quantified with the normalised optical density (NOD), which was performed on seven slices per brain [47]. All pixel intensities above the mean of the control region plus twice its standard deviation were summed for both targeted and control regions of interest. The sum of the pixels in the targeted region was then subtracted by that of the control region to find the NOD. To quantify the distribution of the probe, the coefficient of variation (COV) was calculated, defined as the standard deviation of the targeted region over the average fluorescence intensity in that region. These measurements were calculated for six slices of each treated brain by selecting regions around the targeted left hippocampus using

Matlab® (2018a, Mathworks, Natick, MA, USA). The stained slices, four slices for each stain in each brain, were used to quantify the number of neurons, microglia and astrocytes overlapping with the delivered probe.

4.3.6 Binding of Gd(rhodamine-pip-DO3A) to endogenous albumin

To assess whether Gd(rhodamine-pip-DO3A) might interact with endogenous albumin in the blood, since many Gd-based agents are known to do so, a binding assay was performed by Tiffany Chan (PhD student, Prof Ramon Vilar's group). Binding of Gd-based agents with albumin can slow down the motion of these agents, thereby enhancing T_1 relaxation times [51]. Increasing concentrations of Gd(rhodamine-pip-DO3A) (1 μM to 10 μM; 0.1 to 1 equivalents) were titrated into a solution of 10 μM bovine serum albumin (BSA), which has its own intrinsic fluorescence. Following each addition, the fluorescence emission was recorded between 310-450 nm using a Cary Eclipse Fluorescence Spectrophotometer with an excitation wavelength of 295 nm. The emission values at 345 nm (λ_{max}) were normalised to the emission recorded for BSA without any complex added. Triplicates were measured for each sample.

4.3.7 *Ex vivo* MRI

Ex vivo MRI scans of three brains were performed in a pre-clinical 9.4 T scanner (94/20 USR Bruker BioSpec; Bruker Biospin, Ettlingen, Germany) by Dr Nicoleta Baxan (MR physicist at Imperial College Biological Imaging centre). The scanner was equipped with a 40 mm inner diameter volume transmit/receive quadrature coil and the data was acquired with Paravision 6.0.1 (Bruker, BioSpin). T_1 weighted images were obtained with a 3D gradient echo-base FLASH sequence with the field of view selected to cover the entire mouse brain. The acquisition parameters were the following: T_R/T_E = 50/7.2 ms (T_R = repetition time; T_E = echo time), flip angle = 32°, spatial resolution = (100×100×100) μm^3, 14 averages with a total scan time of 7 h. The 3D volume reconstruction of the acquired images and smoothing was performed in Paravision 6.0.1 to show the brain surface (Figure 4.6). Maximum intensity projections were taken

across a 1 mm thickness to highlight the targeted left hemisphere and its contralateral side in sagittal, axial and coronal orientations (Figure 4.6). The signal intensity in the targeted side was compared to that of the control side by calculating the normalised signal intensity, using the same calculation as that used for the NOD.

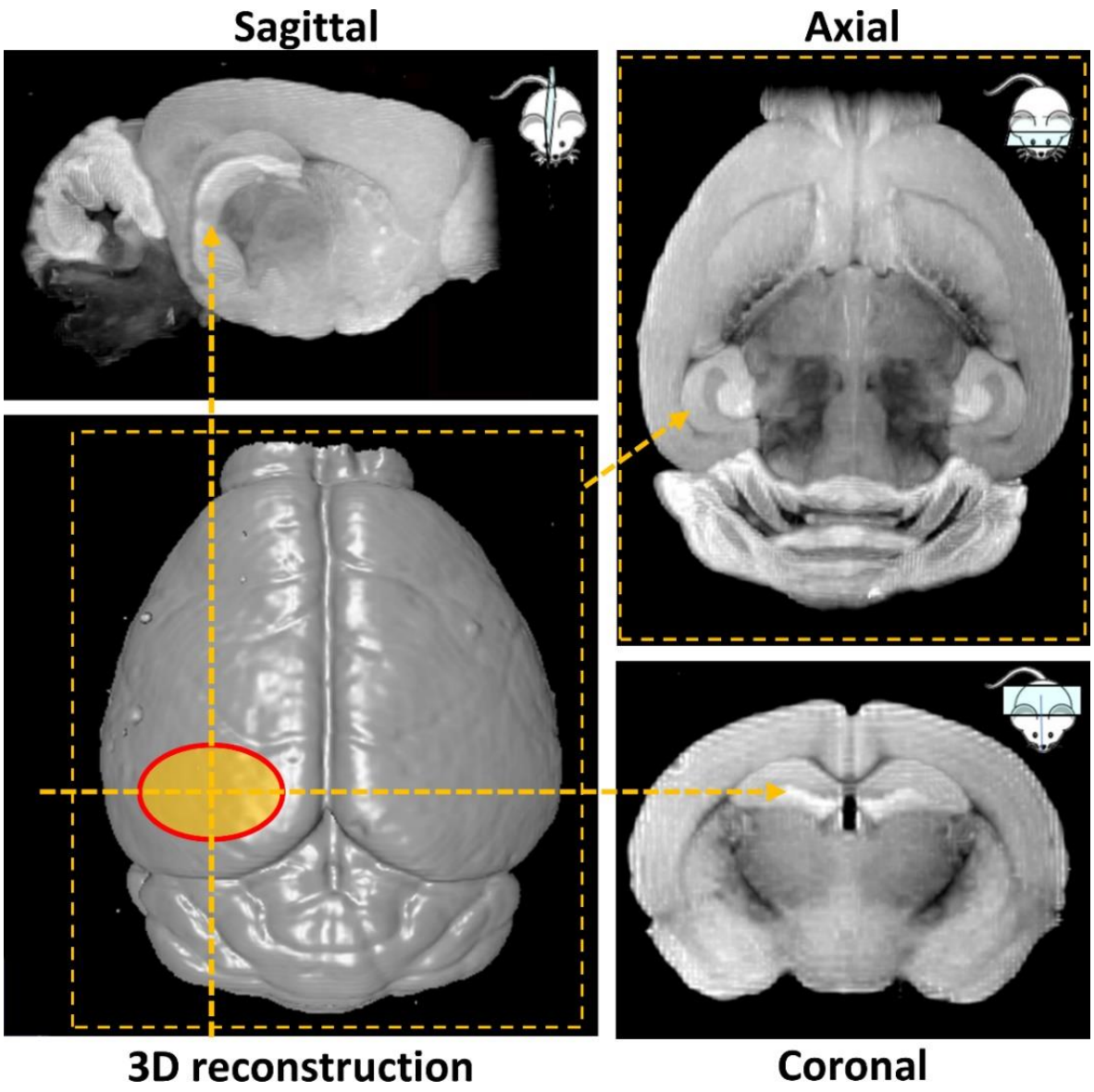

Figure 4.6. 3D reconstruction of the mouse brain from the MRI images and sagittal, axial and coronal brain slices. The MRI-based 3D volume reconstruction of one of the mouse brains with the targeted left hemisphere highlighted (red oval). Sagittal, axial and coronal orientations show with the yellow arrows the targeted hemisphere. The brain slices are maximum intensity projections (MIP) of 1 mm thickness volumes of the brain. Image modified Morse et al, *Theranostics*, 2020, 10(6):2659-2674.

4.3.8 Statistical analysis

To determine whether the NOD values were significantly different between brains injected with Gd(rhodamine-pip-DO3A), whether COV values were significantly different between brains injected with Gd(rhodamine-pip-DO3A) and dextran, and whether the number of neurons, microglia and astrocytes overlapping with the delivered probes differed from each other, a two-sided Student t-test was performed. A value of $p < 0.05$ was considered statistically significant.

4.4 Results

4.4.1 Delivery of Gd(rhodamine-pip-DO3A) to the brain

Rhodamine fluorescence was detected in the left hemisphere of all mice where Gd(rhodamine-pip-DO3A) was delivered (Figure 4.7 and 4.8). In the opposite right hemisphere, where no ultrasound was applied, no fluorescence was detected (Figure 4.8 right dashed circles). This result confirmed that Gd(rhodamine-pip-DO3A) does not cross the BBB by itself, but requires focused ultrasound combined with circulating microbubbles to enter the brain. Quantitatively, this was demonstrated by the normalised optical density (NOD), a measure of the detected dose, being at least two standard deviations above the mean of the control region in all seven brains (NOD > 0) (Figure 4.7). This criterion for the delivery to be considered successful was set beforehand. The detected dose, calculated with the NOD, did not vary substantially between brains. Only the NOD of the 7th brain was considered significantly different from the other six, and the 1st brain from the 6th ($P < 0.01$). All other NODs were not significantly different from each other ($P > 0.01$).

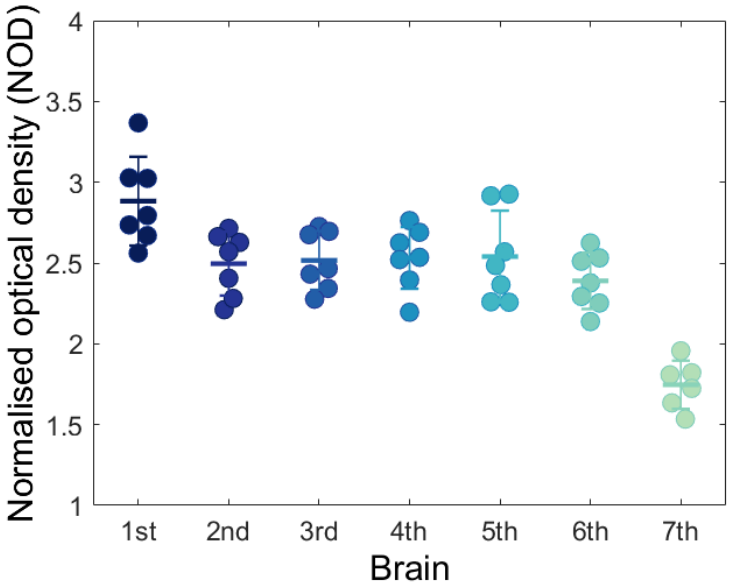

Figure 4.7. Successful delivery of Gd(rhodamine-pip-DO3A) to the left hemisphere of all seven mouse brains. Normalised optical density (NOD) measurements from the fluorescence images (performed on seven slices per brain) show that the signal detected in the targeted left hemisphere was always higher than that in the right control hemisphere (zero-line, NOD = 0). The NOD was calculated by first summing all pixels with intensities higher than the mean of the control region plus twice its standard deviation in both the targeted and control regions; the sum of the control region was then subtracted from the sum of the targeted region to obtain the NOD. If the NOD was at least two standard deviations above the mean of the control (NOD > 0) then the delivery was considered successful, as was the case in all seven brains. The NOD of the 7th brain was significantly different from the other six, as well as the 1st brain from the 6th ($P < 0.01$), but the NODs of all other brains were not significantly different from each other ($P > 0.01$).

The probe was delivered homogeneously throughout the targeted region in all brains (Figure 4.8 A-B left dashed circles). Cellular uptake of Gd(rhodamine-pip-DO3A) was also observed in all mouse brains (Figure 4.8 bright spots inside left dashed circles). The few bright regions observed in the right control hemispheres correspond to ventricles lighting up, autofluorescence or folds in the tissue at the edges of the brain.

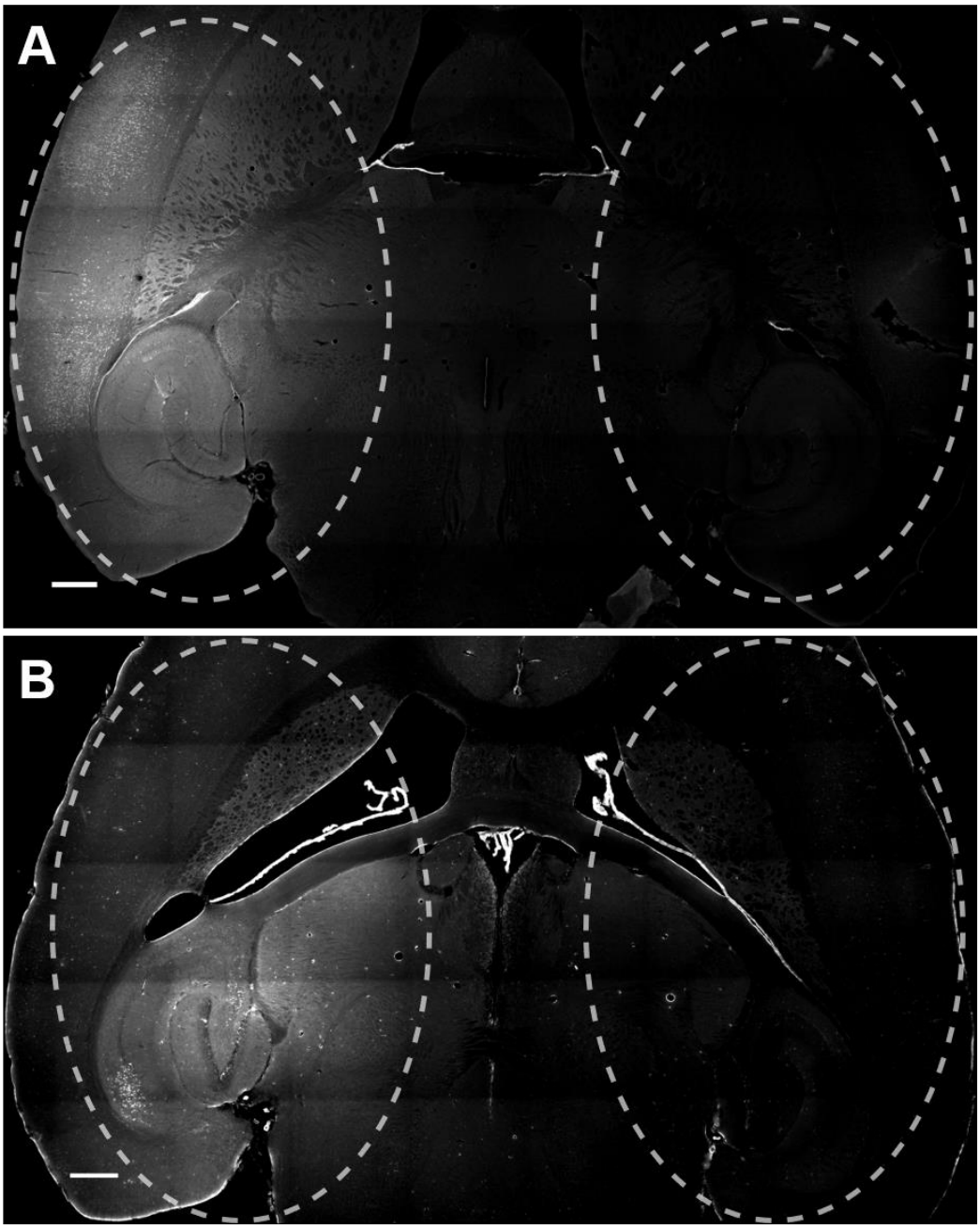

Figure 4.8. Delivery of Gd(rhodamine-pip-DO3A) to the left hemisphere of the mouse brain. (A-B) These fluorescence images (10x) show detected Gd(rhodamine-pip-DO3A) in the left hemisphere where ultrasound was focused (left dashed circle). No fluorescence was detected in the opposite right hemisphere (right dashed circle) where no ultrasound was applied (control region). The probe, which can be seen in the high intensity regions of these fluorescence images (white), was delivered homogeneously within the ultrasound-targeted regions. Cellular uptake of the probe within these regions was observed in all brains (dots with high intensity). The white scale bars indicate 500 μm. Image modified from Morse et al, *Theranostics*, 2020, 10(6):2659-2674.

4.4.2 Cellular uptake of Gd(rhodamine-pip-DO3A) in the brain

Cells that showed uptake of the dual-modal probe appeared, based on their cellular morphology, to only be neuron-like cells. This was confirmed by staining brain slices, where cellular uptake was observed for the detection of neurons (NeuN; Figure 4.9), microglia (Iba1; Figure 4.10) and astrocytes (GFAP; Figure 4.11). Overlap between the probe's fluorescence and the immunohistological staining was only observed in neurons (Figure 4.9 C, F), whereas no uptake was detected in microglia (Figure 4.10 C, F) or astrocytes (Figure 4.11 C, F). The number of neurons uptaking Gd(rhodamine-pip-DO3A) was found to be significantly different from the number of microglia and astrocytes overlapping with the probe, given that no uptake was observed in these cells ($P < 0.01$; Figure 4.12).

Although no uptake was observed in glial cells, some microglia in the ultrasound targeted regions appeared more rounded with shorter processes, an indication that they may be in an activated state (Figure 4.10 B, E, G). Any reactive morphological features of astrocytes, such as hypertrophy with an increase in size of the processes and increased GFAP expression levels, on the other hand, were difficult to identify (Figure 4.11 B, E, G).

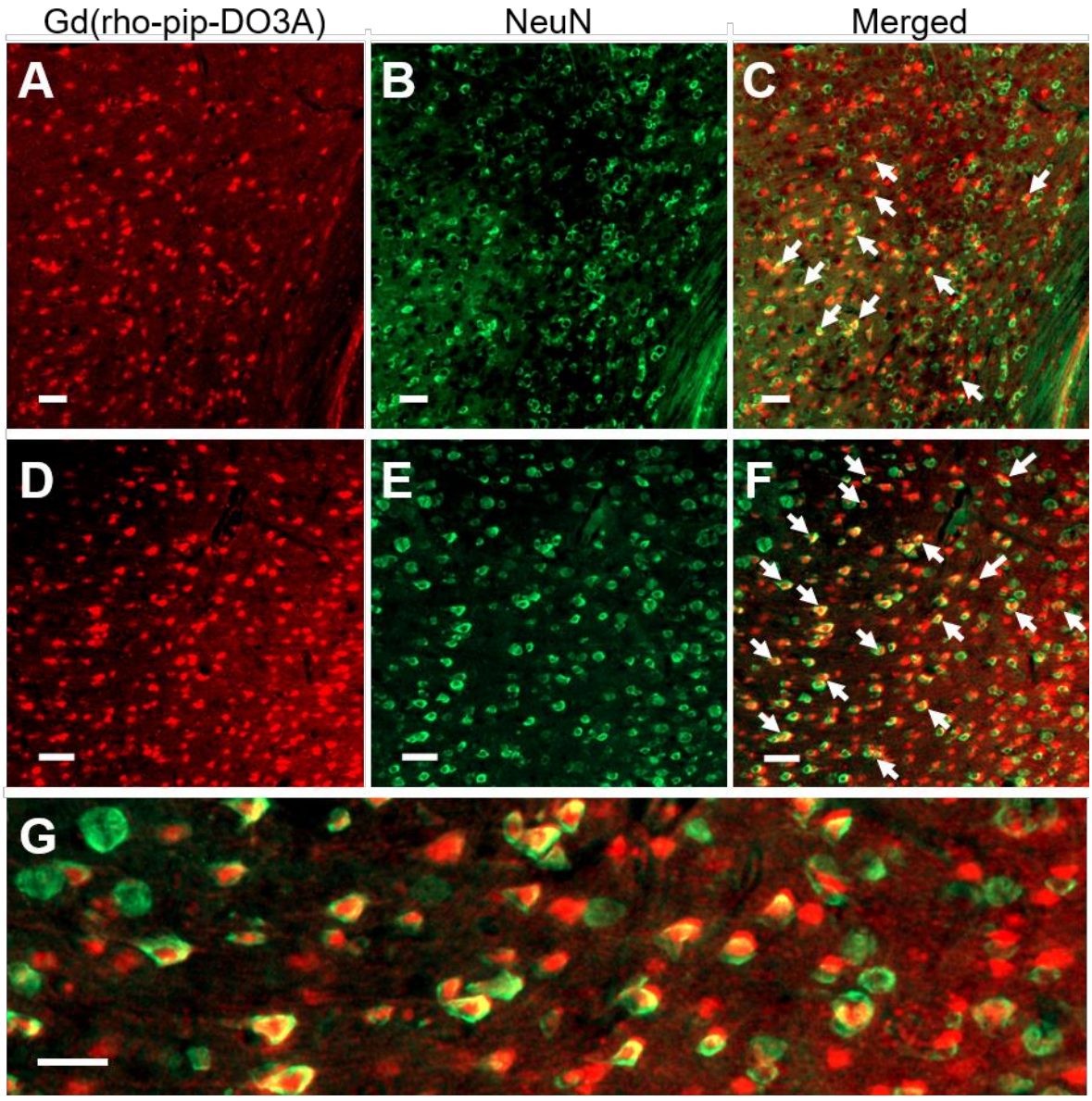

Figure 4.9. Neuronal staining of brain slices with Gd(rhodamine-pip-DO3A) delivery. Fluorescence images (10x) show **(A, D)** Gd(rhodamine-pip-DO3A) in the brain and **(B, E)** immunohistological staining of neurons using NeuN with **(C, F)** respective merged channels. The white arrows point to examples of colocalisation between the probe and the neuronal staining. This uptake of the probe within neurons was observed in all brains (four brain slices from each brain were stained with NeuN). **(G)** This zoomed-in region highlights uptake of the probe within neurons (yellow). The white scale bars indicate 50 μm. Image modified from Morse et al, *Theranostics*, 2020, 10(6):2659-2674.

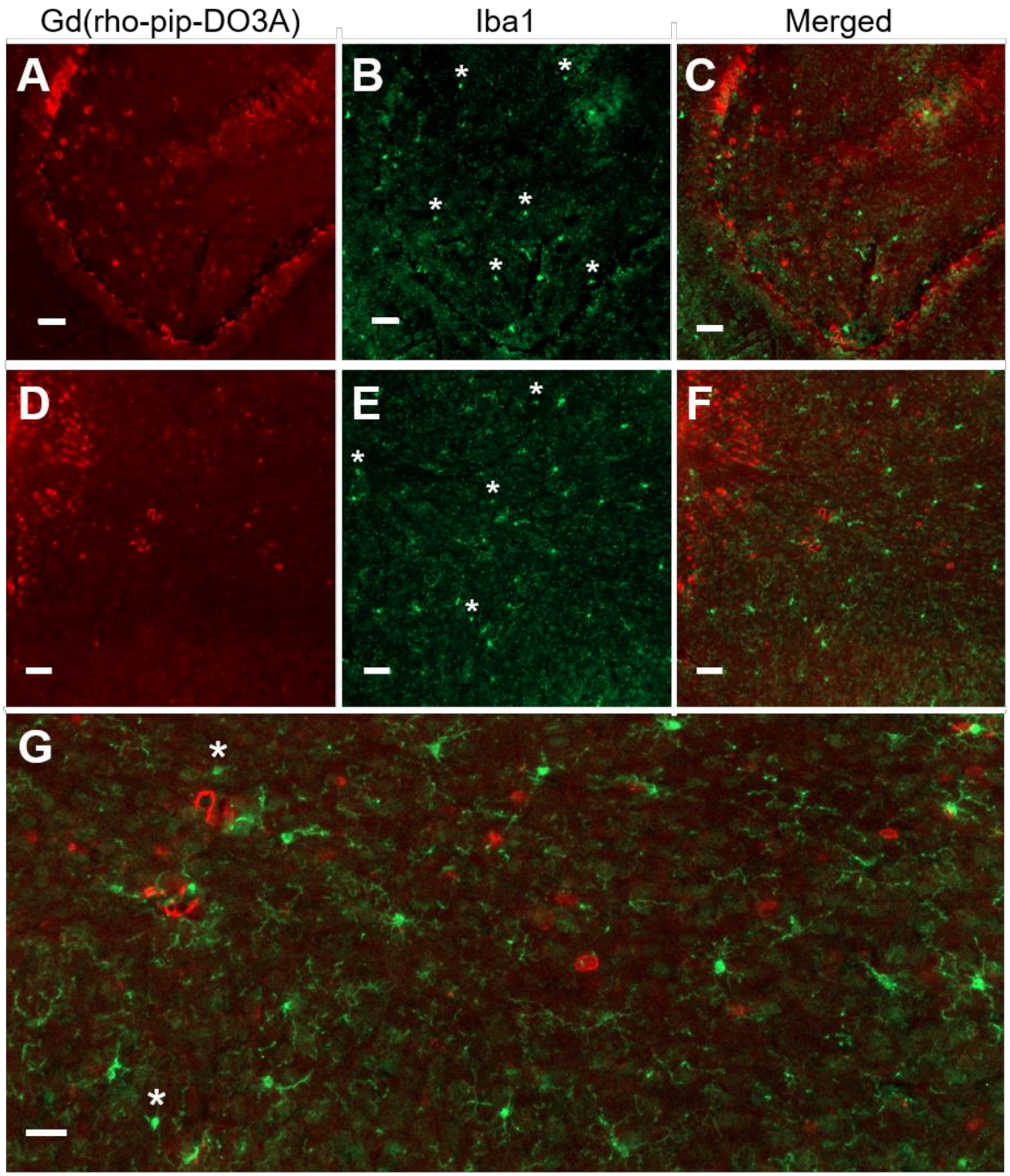

Figure 4.10. Microglia staining of brain slices with Gd(rhodamine-pip-DO3A) delivery. Fluorescence images (10x) show **(A, D)** Gd(rhodamine-pip-DO3A) in the brain and **(B, E)** immunohistological staining of microglia using Iba1 with **(C, F)** respective merged channels. No overlap between the microglial staining and the probe was observed in any of the brains (four brain slices stained from each brain). **(G)** Zoomed-in region shows in more detail the microglia stained with Iba1. The white asterisks are positioned above some of the microglia which, in this imaging plane, appear to be rounded with shorter processes, an indication of possible activation. The white scale bars indicate 50 μm.

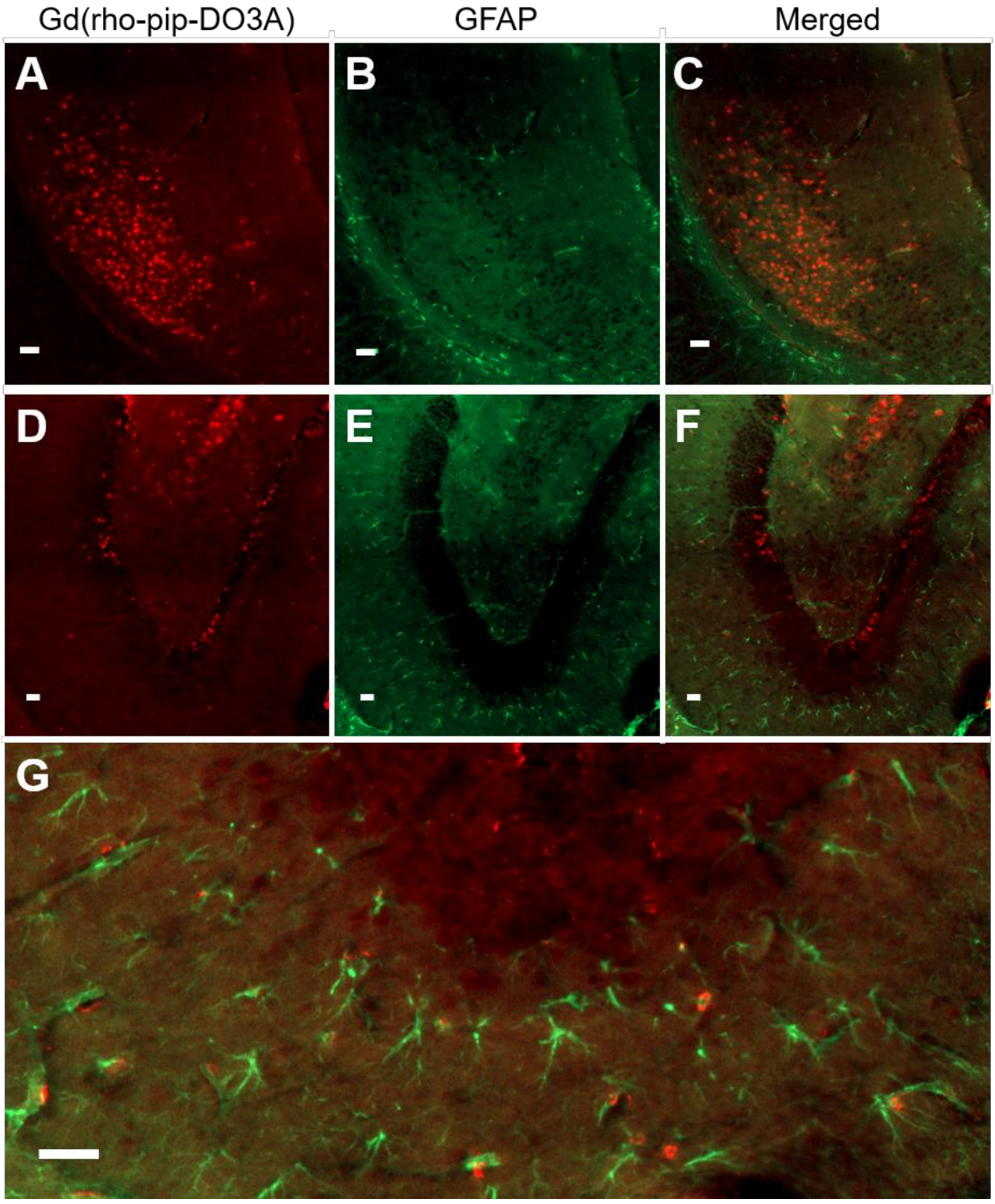

Figure 4.11. Astrocyte staining of brain slices with Gd(rhodamine-pip-DO3A) delivery. Fluorescence images (10x) show **(A, D)** Gd(rhodamine-pip-DO3A) in the brain and **(B, E)** immunohistological staining of astrocytes using GFAP with **(C, F)** respective merged channels. No overlap between the astrocyte staining and the probe was observed in any of the brains (four brain slices stained from each brain). **(G)** Zoomed-in region shows in more detail the astrocytes stained with GFAP. The white scale bars indicate 50 μm.

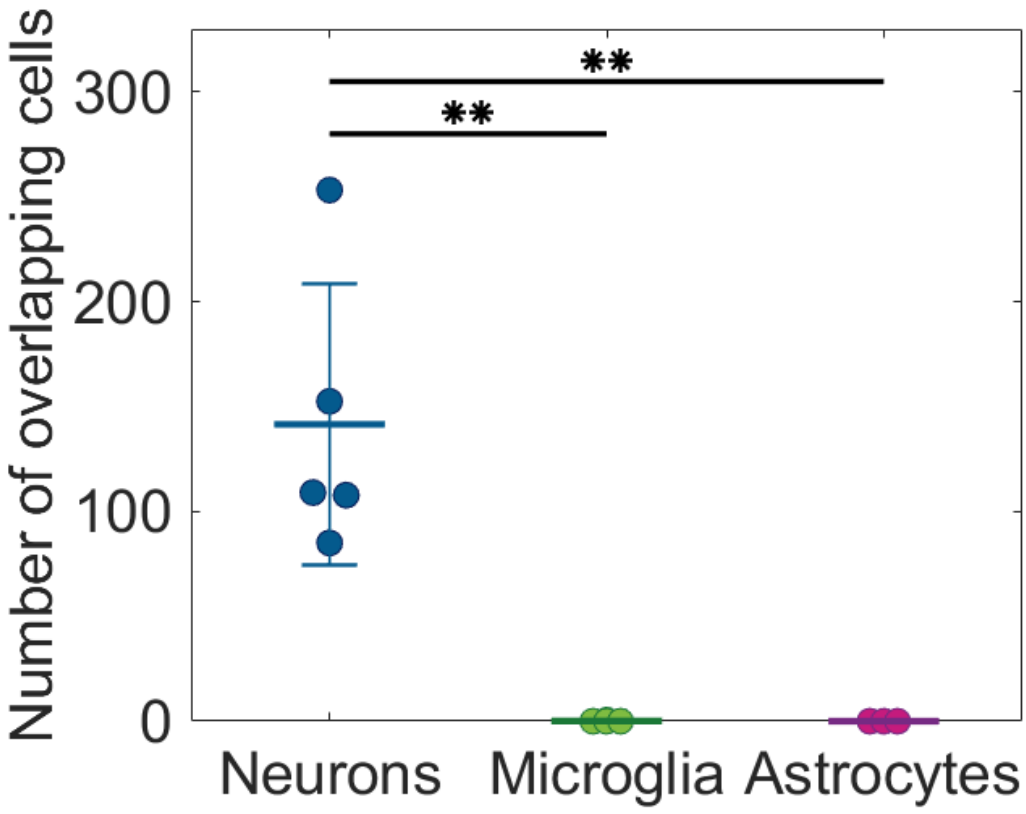

Figure 4.12. Number of neurons, microglia and astrocytes overlapping with Gd(rhodamine-pip-DO3A). Quantification was performed on the merged images, with both the fluorescence of the probe and the staining showing the number of cells with uptake. Overlap was only observed in neurons; therefore the number of neurons with uptake was significantly different from the number of microglia and astrocytes overlapping with the probe ($P < 0.01$).

4.4.3 Distribution of Gd(rhodamine-pip-DO3A) compared to Texas Red dextran in the brain

The distribution and cellular uptake of the 1 kDa Gd(rhodamine-pip-DO3A) probe within the brain was compared to that of a larger molecule, Texas Red 3 kDa dextran. In the second chapter of this thesis, dextran was used as our model drug and has often been used in the literature to assess the permeability enhancement of the BBB following focused ultrasound and microbubble treatment [52]–[54].

Gd(rhodamine-pip-DO3A) was found to distribute uniformly within the targeted area, homogeneously spreading within the parenchyma (Figure 4.13). This probe was not

only found to spread in between cells, but was also found inside cells, which we have confirmed to be specifically neurons. In terms of the subcellular localisation of the probe, Gd(rhodamine-pip-DO3A) was observed both within the nucleus and the cytoplasm of these neurons in confocal images (Figure 4.14). Some high intensity regions, approximately 1-3 μm in size, can also be observed, indicating higher accumulations of the probe in certain regions within the cells. In addition, Gd(rhodamine-pip-DO3A) was not only more homogeneously distributed, but was also detected across a much larger region of the brain compared to the dextran (Figure 4.13 A and 4.15 A).

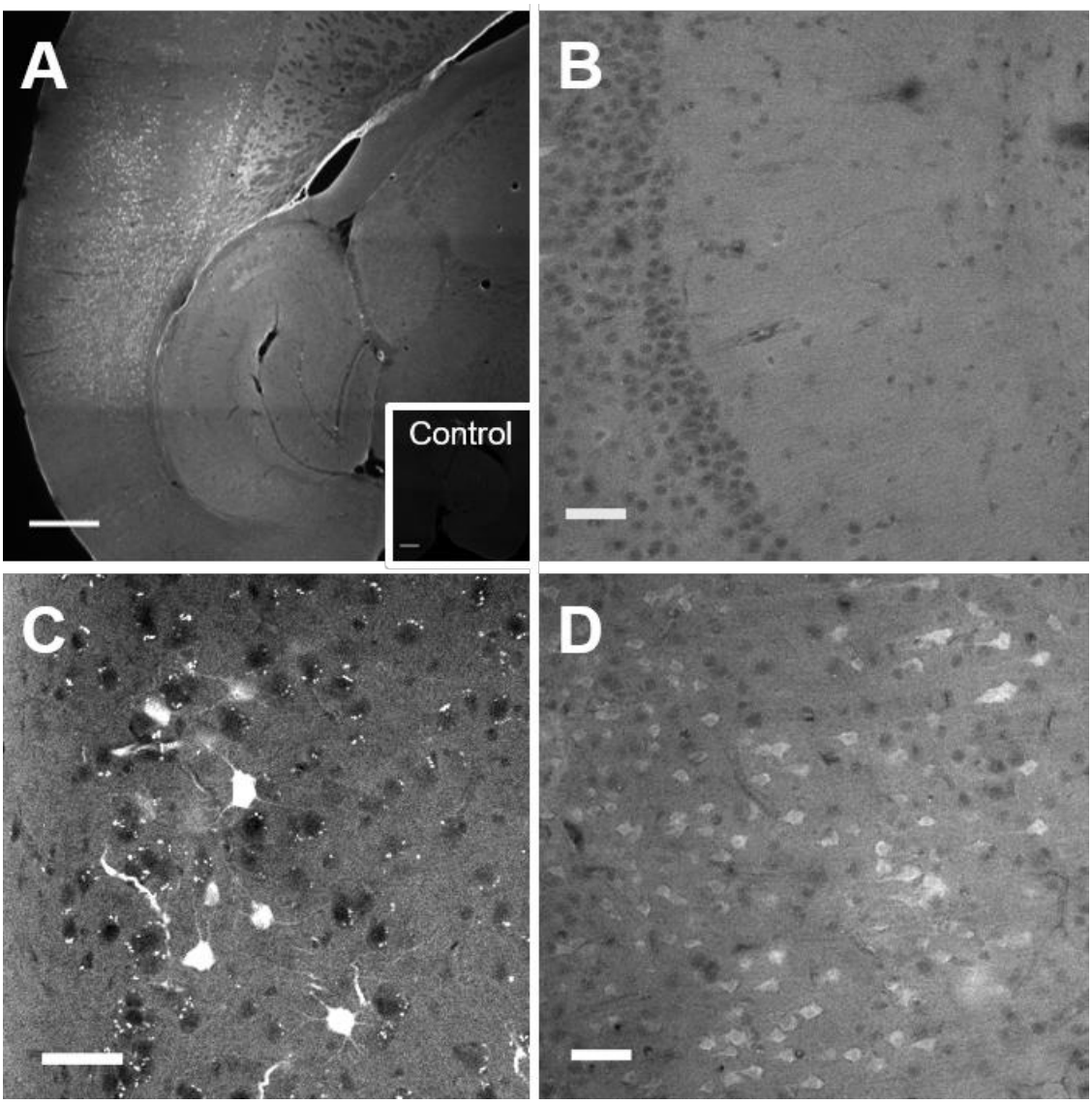

Figure 4.13. Distribution of Gd(rhodamine-pip-DO3A) within the brain. (A) This fluorescence image (10x) shows a typical distribution of Gd(rhodamine-pip-DO3A) in the

targeted left hemisphere of the brain. In the corresponding right control hemisphere, displayed in the small white box at the bottom right, no fluorescence was detected. The scale bar indicates 500 μm. **(B-D)** Confocal microscopy images (20x) highlight in more detail the **(B)** homogeneous distribution of Gd(rhodamine-pip-DO3A) throughout the parenchyma and **(C-D)** the cell uptake observed in neurons. The scale bars indicate 50 μm. Image modified from Morse et al, *Theranostics*, 2020, 10(6):2659-2674.

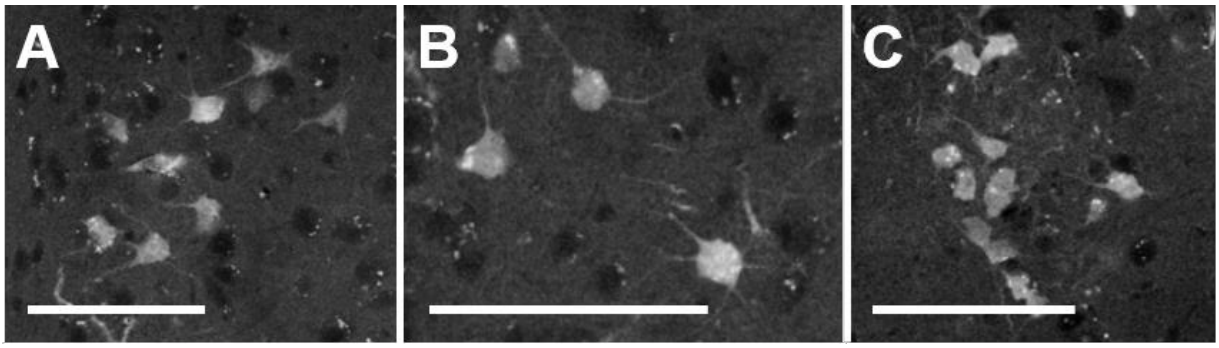

Figure 4.14. Subcellular localisation of Gd(rhodamine-pip-DO3A) within neuron-like cells. (A-C) Confocal microscopy images (20x) of brain regions with Gd(rhodamine-pip-DO3A) delivery highlight that the probe is found within the nucleus and cytoplasm. Small high intensity regions are also visible within the cells. The scale bars indicate 100 μm. Image modified from Morse et al, *Theranostics*, 2020, 10(6):2659-2674.

When the larger dextran molecule was delivered with the same ultrasound parameters, a more heterogeneous pattern of distribution within the brain was observed (Figure 4.15). High accumulation of the probe was identified around blood vessels and cell uptake was also observed. These cells, however, were identified morphologically to be not only neuron-like cells, but also glial-like cells. Immunohistochemistry confirmed dextran uptake within neurons and more so within microglia, but not in astrocytes (Figure 4.16), while Gd(rhodamine-pip-DO3A) was only found in neurons. With both probes, more rounded microglia with shorter processes were detected in the ultrasound-targeted region, a sign of immune cell activation.

The difference in distribution between the two delivered probes was quantified using the coefficient of variation (COV), defined as the standard deviation over the average fluorescence intensity in the targeted region. The COV showed that there is less

variation in the distribution of the dual-modal probe (COV = 0.4 ± 0.05) compared to that of dextran (COV = 1.23 ± 0.04), providing a better coverage of the tissue (Figure 4.17).

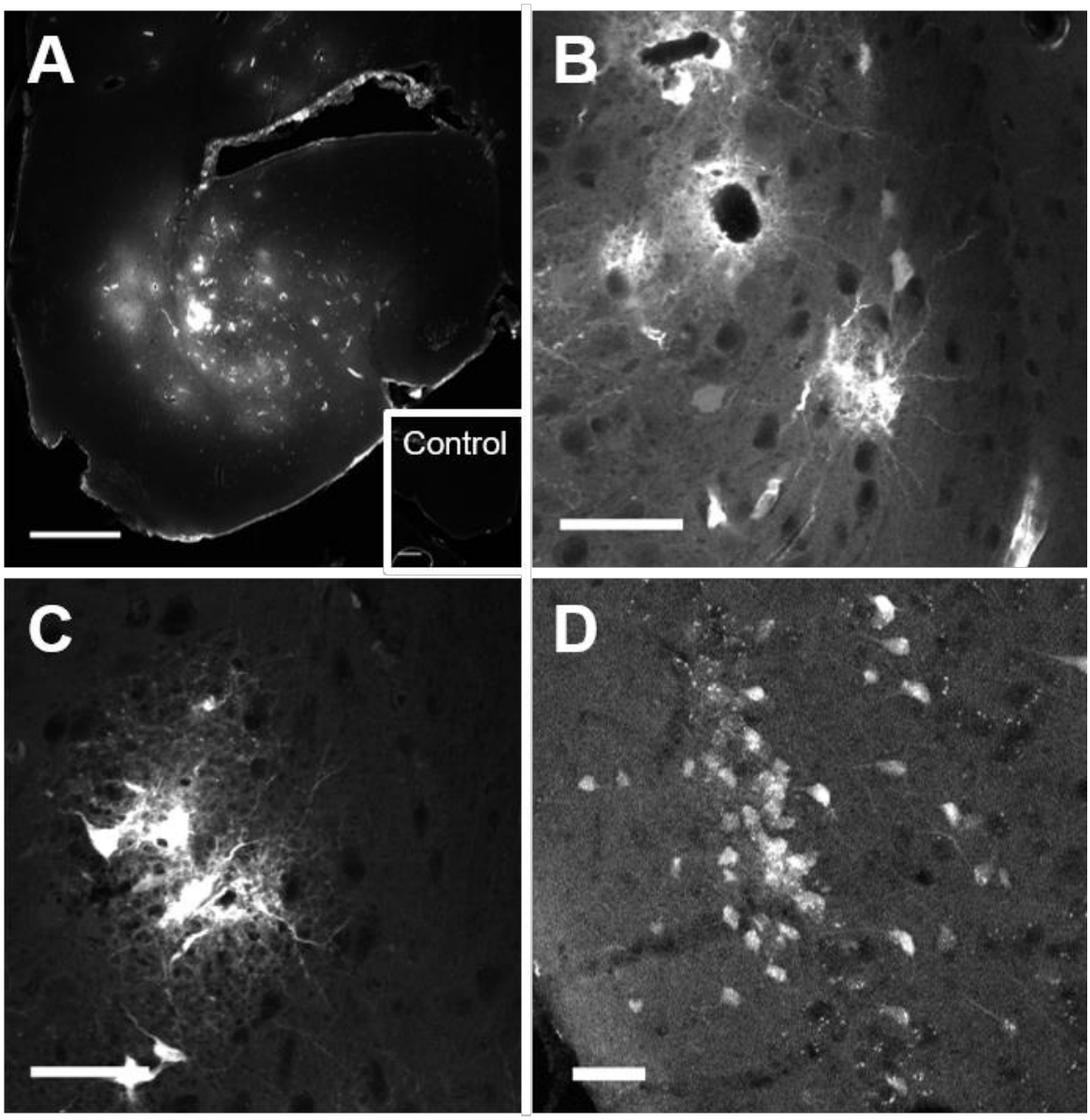

Figure 4.15. Distribution of dextran within the brain. (A) This fluorescence image (10x) shows a typical distribution of dextran in the targeted left hemisphere of the brain. In the corresponding right control hemisphere, displayed in the small white box at the bottom right, no fluorescence was detected. The scale bar indicates 500 μm. **(B-D)** Confocal microscopy images (20x) highlight in more detail the **(B)** accumulation of dextran around the blood vessels and the cell uptake observed in **(C)** glial-like cells and **(D)** neurons. The scale bars indicate 50 μm. Image modified from Morse et al, *Theranostics*, 2020, 10(6):2659-2674.

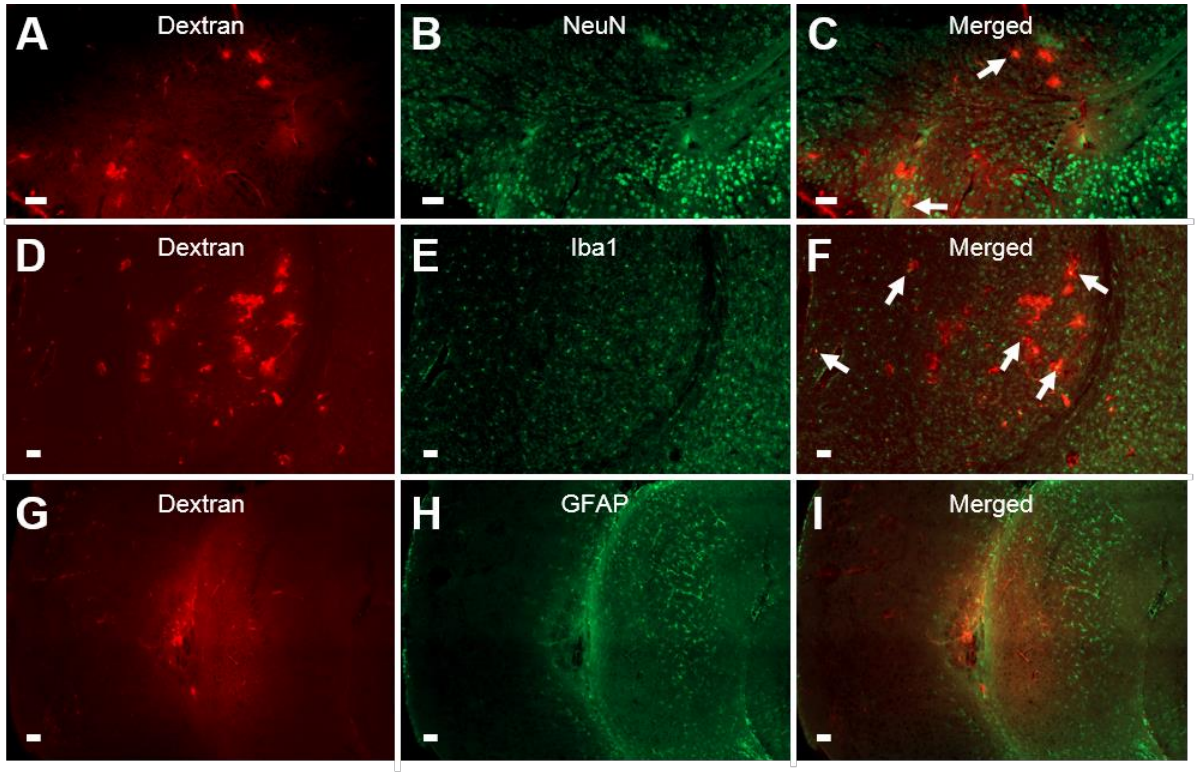

Figure 4.16. Neuronal, microglial and astrocyte staining of brain slices with dextran delivery. Fluorescence images (10x) of **(A, D, G)** dextran delivery and of immunohistological staining for **(B)** neurons with NeuN, **(E)** microglia with Iba1 and **(H)** astrocytes with GFAP, with **(C, F, I)** respective merged channels. The white arrows indicate the overlap between dextran and cells, which was mostly observed with neurons and more so with microglia. No overlap was observed with astrocytes. The white scale bars indicate 50 μm. Image taken from Morse et al, *Theranostics*, 2020, 10(6):2659-2674.

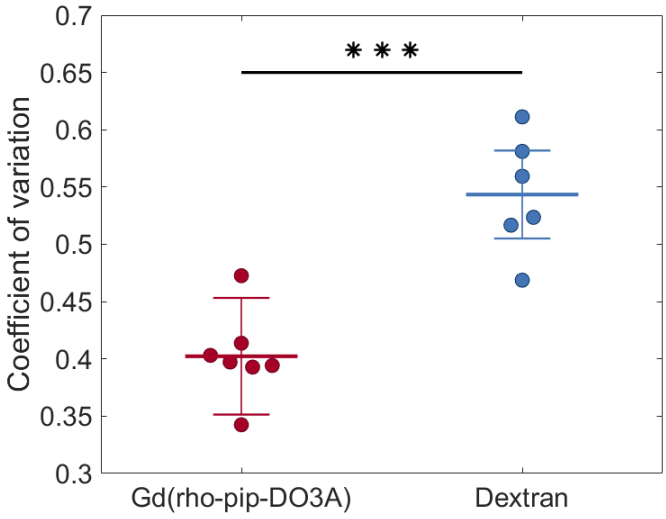

Figure 4.17. Quantified distribution of Gd(rhodamine-pip-DO3A) and dextran within the brain. The coefficient of variation (COV) was quantified as a measure of distribution

heterogeneity. A significant difference in the COV was quantified ($n = 6$; $P < 0.001$), as the distribution of Gd(rhodamine-pip-DO3A) was found to be more homogeneous (less variation) than that of dextran. Image modified from Morse et al, *Theranostics*, 2020, 10(6):2659-2674.

4.4.4 Detection of Gd(rhodamine-pip-DO3A) with MRI

Ex vivo MRI scans were performed on three of the mouse brains where Gd(rhodamine-pip-DO3A) was delivered to check whether the probe could be detected by MRI as well as fluorescence microscopy. An increase in the brightness of T_1 weighted MR images was observed in the left hippocampus where the probe had been delivered (Figure 4.18). The amount of probe detected in the left hippocampus was compared to the control right hippocampus, that was quantified with the normalised signal intensity. This quantification showed a higher intensity being detected in the left hippocampus compared to the control regions in all quantified images (Figure 4.19). Following the MRI scans, the brains were sectioned and imaged to visualise the location of the fluorescence compared to the increased MRI contrast. A higher signal was detected in similar regions of the brain in both MRI (Figure 4.18) and fluorescence (Figure 4.20) images. However, the distribution of the amount of probe that could still be detected via fluorescence, following the processing and MRI scanning, was different from that detected in the brains that were imaged immediately with fluorescence.

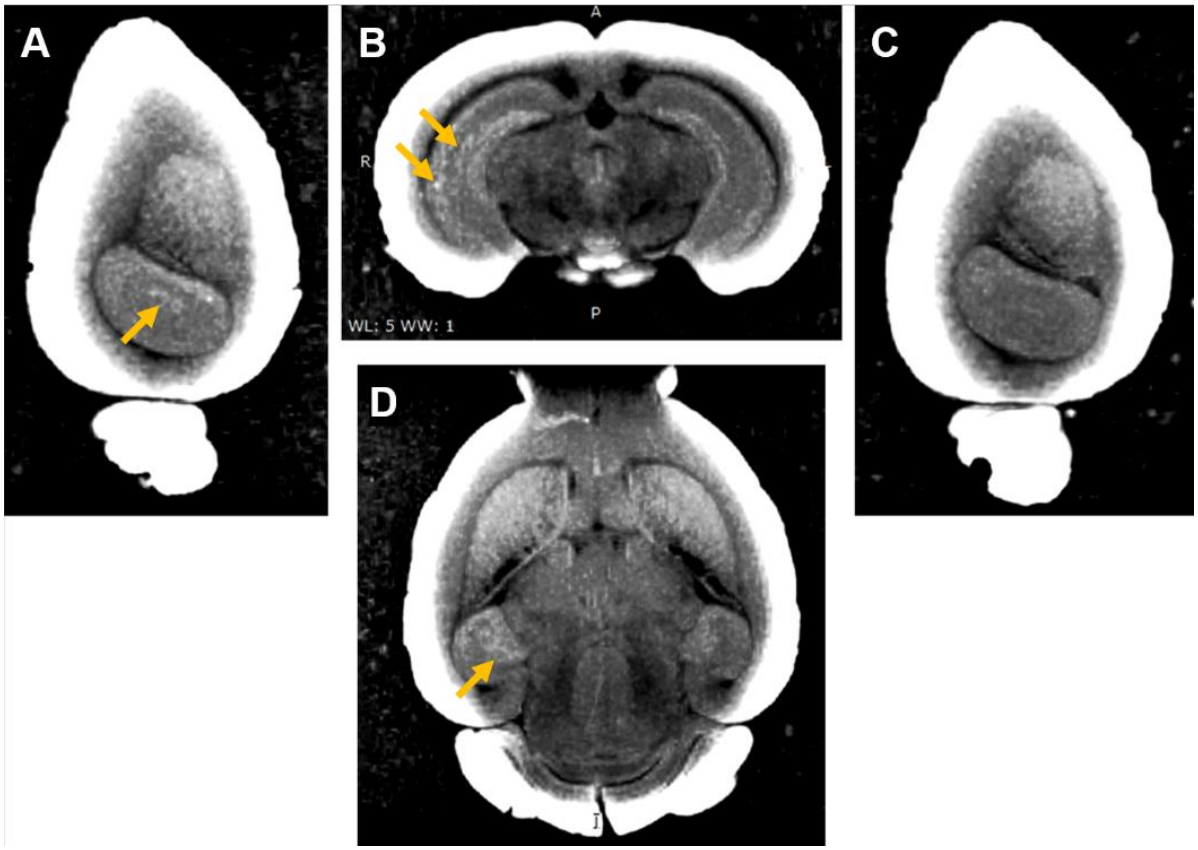

Figure 4.18. *Ex vivo* MRI images of Gd(rhodamine-pip-DO3A) delivery to the left hemisphere. (A) Sagittal, **(B)** coronal and **(D)** axial MR views show an enhancement in T_1 contrast in the left hippocampus compared to the **(C)** contralateral side. The yellow arrows highlight the localised distribution of the probe. The periphery of the brain slices has a high intensity due to the increased contrast applied to the images to visualise the probe. Image taken from Morse et al, *Theranostics*, 2020, 10(6):2659-2674.

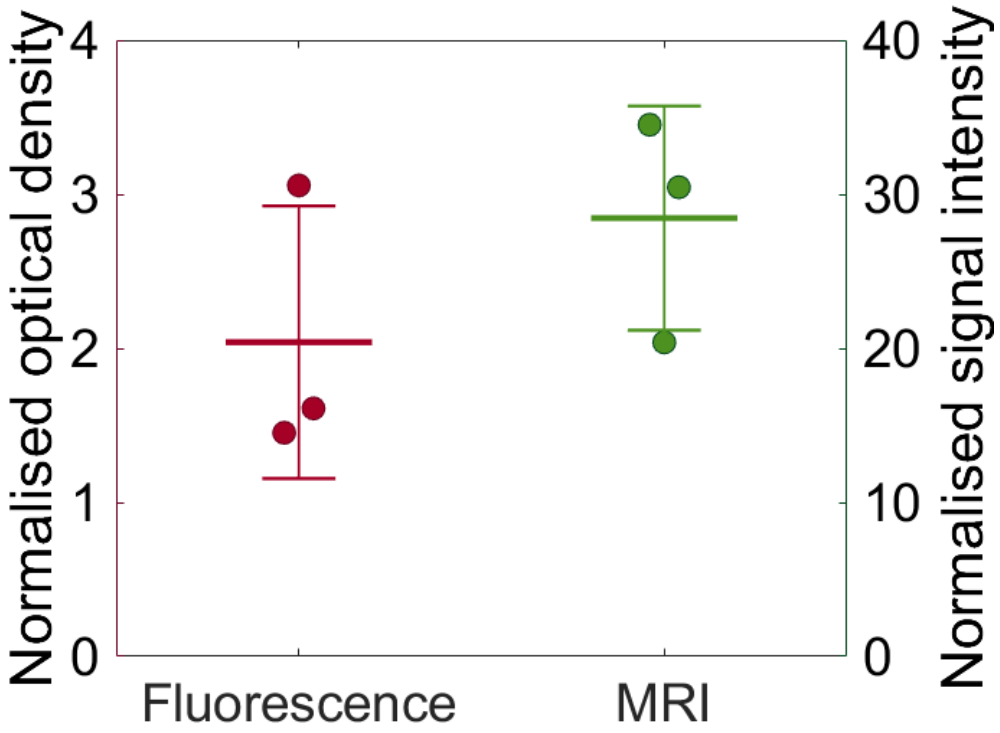

Figure 4.19. Increase in fluorescence and MRI signal in the left hemisphere. From the fluorescence images, the normalised optical density (NOD) was quantified (on six slices per brain) and from the MRI images, the normalised signal intensity was quantified (on five slices per brain). These measurements show that the signal detected was always higher in the left targeted hemisphere compared to the right control hemisphere (zero line). Measurements were taken on the same three brains.

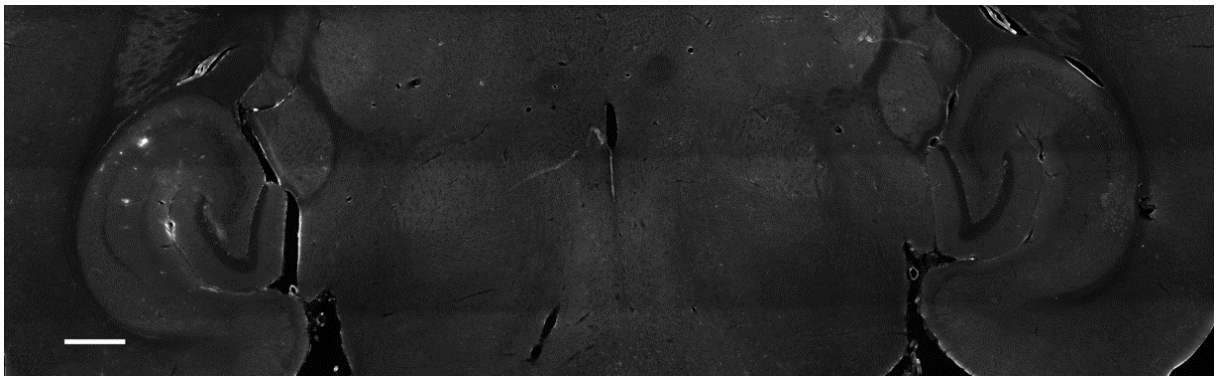

Figure 4.20. Fluorescence detection of Gd(rhodamine-pip-DO3A) in brain scanned with MRI. This example fluorescence image (10x) shows where Gd(rhodamine-pip-DO3A) is being detected optically in similar regions to those detected by MRI in the left hippocampus (see Figure 4.18). In the right control hippocampus, no compound is detected. The white scale bar indicates 500 µm. Image from Morse et al, *Theranostics*, 2020, 10(6):2659-2674.

4.4.5 Gd(rhodamine-pip-DO3A) binding to albumin

To assess whether our dual-modal complex interacted with endogenous albumin (most common bloodborne serum protein) within the blood, a binding assay of Gd(rhodamine-pip-DO3A) against serum albumin was performed. This was investigated because binding to albumin increases the relaxivity of Gd-based contrast agents. From this assay, Gd(rhodamine-pip-DO3A) was found to interact with albumin as the intrinsic fluorescence of serum albumin was quenched upon increasing titrations of the probe (Figure 4.21).

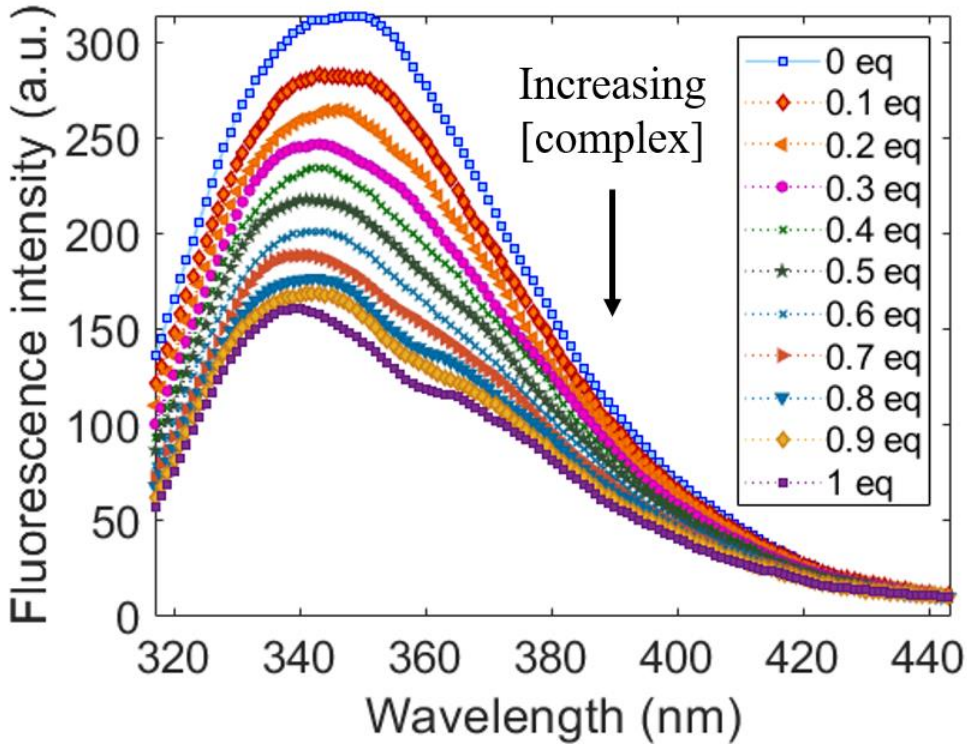

Figure 4.21. Binding of Gd(rhodamine-pip-DO3A) to albumin. These emission spectra show how the endogenous fluorescence intensity of albumin decreases with increasing titrations of Gd(rhodamine-pip-DO3A), indicating that an interaction between albumin and the complex is taking place (a.u. = arbitrary units; eq = equivalents). Image modified from Morse et al, *Theranostics*, 2020, 10(6):2659-2674.

4.4.6 Safety of ultrasound delivery parameters

To assess the safety of the ultrasound parameters used in this study, haematoxylin and eosin (H&E) staining was performed on three brains (nine slices per brain; same

experiments performed for the long pulse sequence safety comparison in Chapter 2 - Section 2.4.6). From the staining, sites of red blood cell extravasation, microvacuolations and dark neurons were observed in all brains (Figure 4.22). Red blood cell extravasation sites (with more than five extravasated cells) were observed in 67% of the analysed sections, microvacuolations in 63% and dark neurons in 37%. Sites of red blood cell extravasation were identified around blood vessels in the hippocampus and microvacuolation sites occurred mostly around microvessels, often in areas with red blood cell extravasation as well. When microvacuolations occurred close to neuronal cell bodies in the hippocampus, neuronal damage was also found, mainly in the pyramidal and granular layers of the hippocampus.

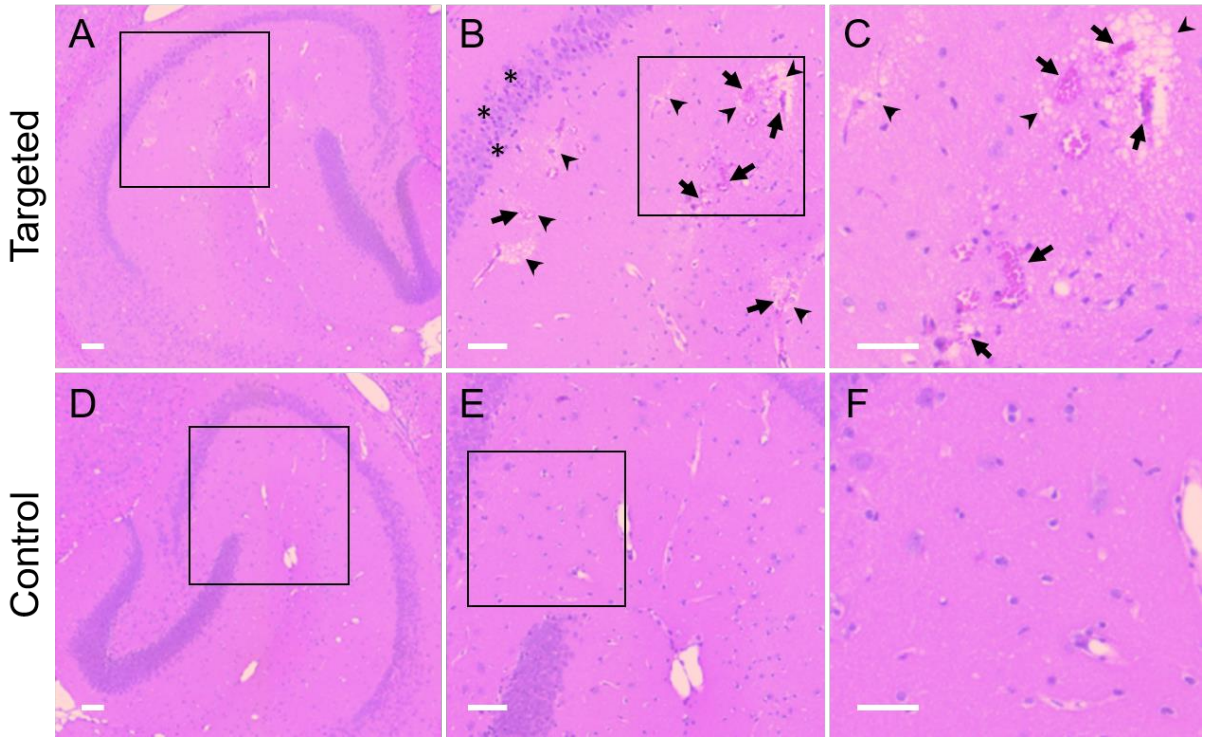

Figure 4.22. H&E staining to assess damage. (A-C) Histological damage was observed in multiple sites within the ultrasound targeted hippocampi, while **(D-F)** in the right control hippocampi none was observed. The arrows point to red blood cell extravasations (bright pink), the arrowheads highlight areas of microvacuolations, and asterisks mark damaged neurons in the H&E stained brain sections. The black boxes inside the left and middle column images highlight regions that were enlarged in the middle and right columns respectively. The scale bars indicate 50 μm.

4.5 Discussion

In this study we show that a dual-modal optical-MRI probe, Gd(rhodamine-pip-DO3A), can be delivered non-invasively and locally to the brain with focused ultrasound to label neurons within the targeted region. The probe was synthesised to have an 'always on' fluorescence and was found to distribute uniformly within the ultrasound-targeted region (COV = 0.4 ± 0.05). The cells where Gd(rhodamine-pip-DO3A) was taken up were all confirmed to be neurons and not microglia or astrocytes. Compared to a larger Texas-Red dextran molecule, our smaller probe was delivered more uniformly and led to less involvement from immune related cells, whereas dextran was uptaken by microglia. Lastly, the probe was detected via both fluorescence and MRI *ex vivo*, enabling the advantages of both imaging modalities to be exploited to facilitate the study of neuronal physiology.

Our aim was to enable labelling of neurons with a Gd-based MRI contrast agent. We chose a DOTA-derived macrocyclic ligand system, as they are known to be thermodynamically stable, and kinetically inert complexes [55], ensuring the Gd^{3+} ions were not released into the physiological system, that have been shown to be toxic [56]. Due to their hydrophilic nature, however, Gd-based contrast agents are extracellular probes. Therefore, based on previous studies [29], we hypothesised that by adding a cationic rhodamine derivative to a Gd-DO3A complex, we would be able to enhance its neuronal uptake. Molecules that are lipophilic and positively charged typically permeate cellular membranes, which is what we sought to achieve by incorporating a positive charge with the attached rhodamine [57], [58]. In previous studies, fluorophores have been attached to Gd-based agents to enhance their cellular uptake, but these probes interconverted between non-fluorescent and fluorescent forms, a property which is exploited for pH and heavy metal ion sensing. To allow fluorescence imaging independent of the surrounding environment, here the rhodamine B was specifically attached in a ring-open fluorescent form, creating an 'always on' probe. By adding the rhodamine to enhance cellular uptake, we also enabled the labelled

neurons to be imaged with both microscopy and MRI, which can provide complimentary information regarding neuronal physiology. In preclinical research, the high anatomical resolution and depth penetration achieved with MR imaging can be used synergistically with the high sensitivity of optical imaging [59], [60].

In addition to crossing the cellular membrane, the probe also needs to cross the blood-brain barrier to reach neurons. Focused ultrasound was used as a non-invasive and localised method to deliver this imaging agent into the brain. This delivery method has previously been used to transport Gd-based contrast agents into the brain to visualise the increase in BBB permeability following ultrasound treatment [42]–[46]. Recently, ultrasound has also been utilised to aid the delivery of liposomes across the BBB, labelled with both gadolinium and rhodamine to verify their delivery both optically and via MRI [49]. However, to the best of our knowledge, this is the first study to deliver an optical-MRI probe via focused ultrasound to image neurons.

4.5.1 Delivery and cellular uptake

Gd(rhodamine-pip-DO3A) was found to accumulate within the brain only in the regions targeted with focused ultrasound, with no delivery being observed in control regions. Within all such targeted brain regions, Gd(rhodamine-pip-DO3A) was taken up by cells. At the edges of the treated regions less uptake was observed, confirming that the lower ultrasound pressure present at the edges leads to less probe being delivered [48]. The cellular uptake of Gd(rhodamine-pip-DO3A) was only observed in neurons, while microglia and astrocytes did not colocalise with the probe. Whether a probe is taken up by neurons or not depends on the properties of the probe itself. We hypothesise that this rhodamine probe is labelling neurons due to its cationic and lipophilic properties.

Microglia and astrocytes participate in the removal of unwanted molecules to maintain optimal neuronal function, so they will uptake probes if they recognise them as being foreign [61]. Microglia are the resident immune cells of the brain and one of their roles is to phagocytose unwanted molecules or dead cells to maintain homeostasis in the

brain [62], [63]. Astrocytes also participate in this process, driving the phagocytic activity of microglia and phagocytosing debris within the brain [64]–[66]. However, our results show that microglia and astrocytes are not uptaking the probe, which indicates that neurons are being labelled without these glial cells phagocytosing the probe to remove it from the brain.

Although these glial cells are not taking up the probe, some microglia within the treated regions do appear to have a more rounded shape and shorter processes, which is an indication of the microglia being activated [62]. Staining in this study was performed by targeting Iba1, which is specifically expressed in resting and activated microglia and macrophages. In the future, staining for CD68 will be performed to specifically identify the number of activated microglia alone within the targeted region. Astrocytes, on the other hand, were not found to have a reactive morphology and were stained for GFAP, a standard method to visualise reactive astrocytes [65]. This staining technique highlights all reactive, but not all non-reactive, astrocytes. In our results, GFAP staining was brighter in all ultrasound-targeted regions of the brain but was not always in the opposite control sides. This difference could indicate that the astrocytes are in a reactive state in the targeted brain region. Further staining for non-reactive astrocytes, targeting S100β, could elucidate whether the astrocytes in the ultrasound targeted region are in a reactive state. In the future, image analysis on higher magnification images will classify whether these cells are activated or not.

Such a response from these glial cells could be due to the presence of an unknown probe in the brain or could be due to the microbubble stimulation of the microvasculature disrupting the permeability of the blood-brain barrier. However, when the larger 3 kDa dextran molecule was delivered, not only was it delivered to the neurons, but it was also taken up by glial cells, which had an activated morphology. This did not happen when delivering the 1 kDa Gd(rhodamine-pip-DO3A). One hypothesis is that the larger dextran molecule is recognised faster by the immune system as being foreign, due to its size and other properties. This could, however, be

a time sensitive process. In our experiments we only investigated the delivery and uptake immediately after the ultrasound treatment. In the future, uptake will be explored at later time points to see whether glial cell uptake occurs later, and to also see whether neuronal uptake increases or not. Not all neurons in the targeted region were labelled with Gd(rhodamine-pip-DO3A). Exploring later time points could elucidate whether more neurons are labelled as the probe is allowed more time to diffuse within the parenchyma.

4.5.2 Delivery comparison with 3 kDa dextran

As expected, our smaller 1 kDa dual-modal probe was delivered more homogeneously and across a larger region compared to 3 kDa dextran. This finding agrees with the size-threshold effect observed with this ultrasound technology [52], [67], [68]. At the edges of the ultrasound treated region, the ultrasound pressure is lower, which would allow the dual-modal probe across, but not the larger dextran, making the delivery region of the dextran smaller. The distribution of these two probes was also found to be significantly different. Gd(rhodamine-pip-DO3A) was distributed more uniformly across the treated region, which would be expected from a smaller probe. Such uniform distribution is advantageous if we are interested in labelling all cells or treating all diseased cells within a specific region. The larger dextran molecule was delivered in a spot-like pattern, concentrating more around blood vessels. The different distribution is most likely due to the difference in size between the probes, but it could also be due to other characteristics of the compounds, such as surface properties and lipophilicity. If larger compounds, such as dextran, need to be delivered to the brain for diagnostic or therapeutic purposes, then a more uniform distribution of the probe can be obtained by emitting ultrasound in a different sequence, using our rapid short-pulse (RaSP) sequence [48] (as described in Chapter 2). We have shown that these short pulses improve the efficacy and safety of delivery, with a faster return to normal BBB permeability and reduced extravasation of endogenous proteins. With RaSP, dextran delivery was shown to elicit no glial cell uptake or activation, whereas when

emitting long pulses this did happen. These short pulses could therefore be the answer to many of the safety issues of focused ultrasound technology, which have been a recent topic of debate [69]–[72].

In this work, the distribution of the smaller Gd(rhodamine-pip-DO3A) was found to be homogeneous and not elicit any immediate glial cell uptake by emitting long pulses. However, by using these long pulses, the permeability of the BBB will be increased for longer periods of time, allowing endogenous proteins to continuously extravasate into the brain, and tissue damage will be caused, creating unnecessary risks. Therefore, in the future we will investigate the delivery of this probe with our RaSP sequence, to determine whether there are any disadvantages in using these shorter pulses, which have an improved safety profile, with this smaller Gd-based contrast agent.

4.5.3 MRI detection

Being able to detect the delivered probe by both MRI and fluorescence allows the advantages of both imaging modalities to be exploited to study neurons *in vivo*. In our study, an increase in signal was quantified in all MRI images from the three brains that were scanned *ex vivo*. A slight increase in the brightness of T_1-weighted images could be observed by eye in the left hippocampus of our MRI images, but the increase was not very high. Previous studies using Gd-rhodamine derived probes have reported a lack of MRI enhancement [29], [30]. In this study, the MRI enhancement was detected in *ex vivo* brains, rather than *in vivo*, due to logistical issues. In the future, brains with the delivered probe will be imaged using *in vivo* MRI, thereby avoiding some of the processing steps and time delays that were present when imaging *ex vivo*, which could result in an increased signal.

Although the fluorescence and MRI signals were detected in similar regions, the fluorescence images of the brains first scanned with MRI and then cut and imaged with fluorescence looked different from those imaged directly with fluorescence. The sensitivity of MRI contrast agents is inherently lower than that of optical agents [73], which could mean that not all the regions where the probe is delivered are visible in

the MRI images. However, the brains that were imaged via MRI *ex vivo* were perfused, put in a fixative and, instead of being cryoprotected, were embedded in a gel phantom so they could be imaged inside the MRI scanner. The MR signal could be low due to these processing steps. The fluorescence signal detected after cutting these brains could also be different and lower due to these additional processing steps, which will be avoided in future work by performing MRI *in vivo*. The concentration of the MRI agent injected *in vivo* might also need to be adjusted, as well as the timing of the injection. In these experiments, the ultrasound treatment and microbubbles were performed first to verify whether microbubble signal was present, and the probe was only injected after this confirmation, as we had limited amounts of the probe. In the future, the probe could be injected prior to the ultrasound treatment, which might increase the amount of probe delivered. In addition, when performing *in vivo* MRI scans, the highest achievable signal might be detected by waiting for the probe to diffuse within the brain, further accumulating within the targeted brain region.

4.5.4 Binding to albumin

We also investigated whether the probe interacted with albumin within the bloodstream by performing an *in vitro* assay. This was expected to occur *in vivo* as albumin is the most abundant protein in the blood [74]. A previous study with Gd(Rhoda-DOTA) had also shown interaction with albumin [29]. Our probe and albumin were found to interact in this assay and as a consequence we would expect the MRI signal to be increased due to a shorter relaxation time. Albumin binding to our probe within the bloodstream would also make the probe that needs to cross the BBB a lot larger. In the second chapter of this thesis, we have shown that using long pulse sequence, albumin does extravasate across the BBB into the brain [48]. However, given the uniform distribution of Gd(rhodamine-pip-DO3A) observed with fluorescence imaging, in these experiments we would expect there to be regions where the probe was delivered alone into the brain and other regions where it was attached to albumin (67 kDa in size). It is therefore possible that we are detecting both the probe

itself and the albumin-conjugated probe in our MRI and fluorescence images. As our probe binding to albumin increases the MRI signal, it is possible that in our MRI images we are only observing the probe that has bound to albumin and that has then been delivered into the left hemisphere. However, in the fluorescence images this cannot be the explanation for the different distribution observed after the MRI scans, since the fluorescence signal should be present whether the probe is bound to albumin or not, which is why the processing hypothesis seems more plausible.

4.5.5 Safety profile

Lastly, we looked at the tissue damage caused by delivering this probe into the brain with focused ultrasound and microbubbles. The long pulse sequence used to deliver this dual-modal probe was found to lead in all three stained brains to red blood cell extravasation, microvacuolations and dark neurons. To avoid such tissue damage, in the future we will use a rapid short-pulse sequence, which has been shown to deliver equivalent doses of a larger 3 kDa dextran into the brain with no tissue damage and an improved safety profile.

4.5.6 Limitations and future work

Although we were able to detect neurons using a dual-modal probe delivered with focused ultrasound, further improvements can be made. As mentioned previously, the cellular uptake and response to the probe were here investigated immediately after the ultrasound treatment. This allowed the probe less than ten minutes to enter the brain and interact with the environment. In the future, we want to look at these interactions at later time points, which would allow a more comprehensive understanding of how long the neurons are labelled and whether the probe would interact with microglia and astrocytes at later time points. Insight into how quickly the probe is cleared from the brain could also be provided. However, this last point is not as important for the purpose of this specific dual-modal probe, which is to facilitate the study of neuronal physiology in preclinical studies rather than for clinical

applications, where concerns regarding the presence of gadolinium deposits in the brain are high [75].

The mechanism by which this probe was specifically delivered into neurons and not into microglia and astrocytes is still unknown. We speculate that the probe is being taken up by neurons due to its positive charge and lipophilic properties and possibly due to facilitated receptor-mediated uptake. On the other hand, we believe that the probe may not be going into glia cells, such as microglia and astrocytes, because they have not yet recognised the probe as foreign and are therefore not in the process of phagocytosing unwanted molecules. However, we are unsure whether these are the reasons for the uptake being specific to neurons. Part of our future work will focus on elucidating the possible mechanism by which this probe is taken up by neurons alone, which will include investigating whether any increases in gene or protein expression levels in these cells could be related to specific intracellular transport mechanisms.

Lastly, our probe's location was detected via MRI in *ex vivo* brains, which allows for longer scanning times and therefore higher resolution. *In vivo*, the lower resolution could make the probe more difficult to detect. However, we predict that the lack of tissue processing and time delays between extracting the brain and the scanning could improve detection. As mentioned previously, techniques such as waiting longer after the ultrasound treatment might lead to increased probe diffusion within the brain, which could improve the MRI signal. In future work, we not only intend to detect the probe via *in vivo* MRI, but also explore the applications of this probe, such as studying changes in neuronal density during development and in specific disease states.

4.6 Conclusion

A method to image neurons with an optical-MRI imaging agent was introduced here, the agent being delivered non-invasively and locally to the brain using focused ultrasound and microbubbles. Unlike previous Gd-rhodamine probes designed for cellular uptake, here an 'always on' fluorescent rhodamine unit was combined with a

gadolinium complex. This is the first optical-MRI probe to be delivered with focused ultrasound and microbubbles into the brain to image neurons. The probe was found to spread uniformly within the left hemisphere of mice and its cellular uptake was confirmed in neurons, but not in microglia and astrocytes. Compared to a larger 3 kDa Texas-Red dextran molecule, our probe, which is substantially smaller in size, distributed more uniformly and elicited no glial cell uptake. An increase in signal following Gd(rhodamine-pip-DO3A) delivery was detected via both fluorescence and MRI *ex vivo*. The delivery of such dual-modal agents into neurons could facilitate the study of neuronal physiology using the advantages of both imaging modalities.

4.7 References

[1] A. Jasanoff, "Functional MRI using molecular imaging agents," *Trends Neurosci.*, vol. 28, no. 3, pp. 120–126, 2005.

[2] A. Jasanoff, "MRI contrast agents for functional molecular imaging of brain activity," *Curr. Opin. Neurobiol.*, vol. 17, no. 5, pp. 593–600, 2007.

[3] R. J. Duchatel, C. Shannon Weickert, and P. A. Tooney, "White matter neuron biology and neuropathology in schizophrenia," *npj Schizophrenia*, vol. 5, no. 1. 2019.

[4] E. Martínez-Pinilla, C. Ordóñez, E. del Valle, A. Navarro, and J. Tolivia, "Regional and gender study of neuronal density in brain during aging and in alzheimer's disease," *Front. Aging Neurosci.*, vol. 8, 2016.

[5] Y. H. Pan, N. Wu, and X. B. Yuan, "Toward a better understanding of neuronal migration deficits in autism spectrum disorders," *Front. Cell Dev. Biol.*, vol. 7, no. SEP, 2019.

[6] K. M. Broadhouse, "The Physics of MRI and How We Use It to Reveal the Mysteries of the Mind," *Front. Young Minds*, vol. 7, 2019.

[7] Y. D. Xiao, R. Paudel, J. Liu, C. Ma, Z. S. Zhang, and S. K. Zhou, "MRI contrast agents: Classification and application (Review)," *International Journal of Molecular Medicine*, vol. 38, no. 5. pp. 1319–1326, 2016.

[8] S. Aime, M. Botta, M. Fasano, and E. Terreno, "Prototropic and water-exchange processes in aqueous solutions of Gd(III) chelates," *Acc. Chem. Res.*, vol. 32, no. 11, pp. 941–949, 1999.

[9] P. Caravan, J. J. Ellison, T. J. McMurry, and R. B. Lauffer, "Gadolinium(III) chelates as MRI contrast agents: Structure, dynamics, and applications," *Chem. Rev.*, vol. 99, no. 9, pp. 2293–2352, 1999.

[10] A. D. Sherry, P. Caravan, and R. E. Lenkinski, "Primer on gadolinium chemistry," in *Journal of Magnetic Resonance Imaging*, 2009, vol. 30, no. 6, pp. 1240–1248.

[11] M. Le Fur and P. Caravan, "The biological fate of gadolinium-based MRI contrast agents: a call to action for bioinorganic chemists," *Metallomics*, vol. 11, no. 2, pp. 240–254, 2019.

[12] A. Elster, "Questions and Answers in MRI," *Elster Llc*, 2017. http://mriquestions.com.

[13] J. Lux and A. D. Sherry, "Advances in gadolinium-based MRI contrast agent designs for monitoring biological processes in vivo," *Curr. Opin. Chem. Biol.*, vol. 45, pp. 121–130, 2018.

[14] A. Y. Louie *et al.*, "In vivo visualization of gene expression using magnetic resonance imaging," *Nat. Biotechnol.*, vol. 18, no. 3, pp. 321–325, 2000.

[15] R. E. Jacobs, E. T. Ahrens, T. J. Mead, and S. E. Fraser, "Looking deeper into vertebrate development," *Trends Cell Biol.*, vol. 9, no. 2, pp. 73–76, 1999.

[16] P. J. Endres, K. W. MacRenaris, S. Vogt, M. J. Allen, and T. J. Meade, "Quantitative imaging of cell-permeable magnetic resonance contrast agents using X-ray fluorescence," *Mol. Imaging*, vol. 5, no. 4, pp. 485–497, 2006.

[17] M. Essig, J. Dinkel, and J. E. Gutierrez, "Use of contrast media in neuroimaging," *Magnetic Resonance Imaging Clinics of North America*, vol. 20, no. 4. pp. 633–648, 2012.

[18] J. Faiz Kayyem, R. M. Kumar, S. E. Fraser, and T. J. Meade, "Receptor-targeted co-transport of DNA and magnetic resonance contrast agents," *Chem. Biol.*, vol. 2, no. 9, pp. 615–620, 1995.

[19] S. Heckl *et al.*, "CNN-Gd3+ enables cell nucleus molecular imaging of prostate cancer cells: The last 600 nm," *Cancer Res.*, vol. 62, no. 23, pp. 7018–7024, 2002.

[20] R. Bhorade, R. Weissleder, T. Nakakoshi, A. Moore, and C. H. Tung, "Macrocyclic chelators with paramagnetic cations are internalized into mammalian cells via a HIV-tat derived membrane translocation peptide," *Bioconjug. Chem.*, vol. 11, no. 3, pp. 301–305, 2000.

[21] M. J. Allen and T. J. Meade, "Synthesis and visualization of a membrane-permeable MRI contrast agent," *J. Biol. Inorg. Chem.*, vol. 8, no. 7, pp. 746–750, 2003.

[22] M. Lewin *et al.*, "Tat peptide-derivatized magnetic nanoparticles allow in vivo tracking

and recovery of progenitor cells," *Nat. Biotechnol.*, vol. 18, no. 4, pp. 410–414, 2000.

[23] R. Mishra *et al.*, "Cell-penetrating peptides and peptide nucleic acid-coupled MRI contrast agents: Evaluation of cellular delivery and target binding," *Bioconjug. Chem.*, vol. 20, no. 10, pp. 1860–1868, 2009.

[24] M. J. Allen, K. W. MacRenaris, P. N. Venkatasubramanian, and T. J. Meade, "Cellular delivery of MRI contrast agents," *Chem. Biol.*, vol. 11, no. 3, pp. 301–307, 2004.

[25] W. P. R. Verdurmen and R. Brock, "Biological responses towards cationic peptides and drug carriers," *Trends Pharmacol. Sci.*, vol. 32, no. 2, pp. 116–124, 2011.

[26] N. Kamaly and A. D. Miller, "Paramagnetic liposome nanoparticles for cellular and tumour imaging," *International Journal of Molecular Sciences*, vol. 11, no. 4. pp. 1759–1776, 2010.

[27] T. Lee, X. an Zhang, S. Dhar, H. Faas, S. J. Lippard, and A. Jasanoff, "In Vivo Imaging with a Cell-Permeable Porphyrin-Based MRI Contrast Agent," *Chem. Biol.*, vol. 17, no. 6, pp. 665–673, 2010.

[28] A. Mishra *et al.*, "A new class of gel-based DO3A-ethylamine-derived targeted contrast agents for MR and optical imaging," *Bioconjug. Chem.*, vol. 17, no. 3, pp. 773–780, 2006.

[29] T. Yamane *et al.*, "Method for enhancing cell penetration of Gd 3+-based MRI contrast agents by conjugation with hydrophobic fluorescent dyes," *Bioconjug. Chem.*, vol. 22, no. 11, pp. 2227–2236, 2011.

[30] M. M. Hüber *et al.*, "Fluorescently detectable magnetic resonance imaging agents," *Bioconjug. Chem.*, vol. 9, no. 2, pp. 242–249, 1998.

[31] S. Thanos and F. Bonhoeffer, "Investigations on the development and topographic order of retinotectal axons: Anterograde and retrograde staining of axons and perikarya with rhodamine in vivo," *J. Comp. Neurol.*, vol. 219, no. 4, pp. 420–430, 1983.

[32] S. Thanos, M. Vidal-Sanz, and A. J. Aguayo, "The use of rhodamine-B-isothiocyanate (RITC) as an anterograde and retrograde tracer in the adult rat visual system," *Brain Res.*, vol. 406, no. 1–2, pp. 317–321, 1987.

[33] C. S. Ogilvy and L. F. Borges, "A quantitative analysis of the retrograde axonal transport of 4 different fluorescent dyes in peripheral sensory and motor neurons and lack of anterograde transport in the corticospinal system," *Brain Res.*, vol. 475, no. 2, pp. 244–253, 1988.

[34] C. Rivas, G. J. Stasiuk, J. Gallo, F. Minuzzi, G. A. Rutter, and N. J. Long, "Lanthanide(III)

complexes of rhodamine-DO3A conjugates as agents for dual-modal imaging," *Inorg. Chem.*, vol. 52, no. 24, pp. 14284–14293, 2013.

[35] X. Chen, T. Pradhan, F. Wang, J. S. Kim, and J. Yoon, "Fluorescent chemosensors based on spiroring-opening of xanthenes and related derivatives," *Chem. Rev.*, vol. 112, no. 3, pp. 1910–1956, 2012.

[36] H. N. Kim, M. H. Lee, H. J. Kim, J. S. Kim, and J. Yoon, "A new trend in rhodamine-based chemosensors: Application of spirolactam ring-opening to sensing ions," *Chem. Soc. Rev.*, vol. 37, no. 8, pp. 1465–1472, 2008.

[37] N. J. Abbott, A. A. K. Patabendige, D. E. M. Dolman, S. R. Yusof, and D. J. Begley, "Structure and function of the blood-brain barrier," *Neurobiol. Dis.*, vol. 37, no. 1, pp. 13–25, 2010.

[38] W. M. Pardridge, "The blood-brain barrier: Bottleneck in brain drug development," *NeuroRx*, vol. 2, no. 1, pp. 3–14, 2005.

[39] H. J. Weinmann, R. C. Brasch, W. R. Press, and G. E. Wesbey, "Characteristics of gadolinium-DTPA complex: A potential NMR contrast agent," *Am. J. Roentgenol.*, vol. 142, no. 3, pp. 619–624, 1984.

[40] R. A. Kroll and E. A. Neuwelt, "Outwitting the blood-brain barrier for therapeutic purposes: Osmotic opening and other means," *Neurosurgery*, vol. 42, no. 5, pp. 1083–1100, 1998.

[41] W. M. Scheld, "Drug delivery to the central nervous system: General principles and relevance to therapy for infections of the central nervous system," *Rev. Infect. Dis.*, vol. 11, no. 7, pp. S1669–S1690, 1989.

[42] K. Hynynen, N. McDannold, N. Vykhodtseva, and F. A. Jolesz, "Noninvasive MR imaging-guided focal opening of the blood-brain barrier in rabbits," *Radiology*, vol. 220, no. 3, pp. 640–646, 2001.

[43] L. Lamsam, E. Johnson, I. D. Connolly, M. Wintermark, and M. H. Gephart, "A review of potential applications of MR-guided focused ultrasound for targeting brain tumor therapy," *Neurosurg. Focus*, vol. 44, no. 2, p. E10, 2018.

[44] N. Sheikov, N. McDannold, N. Vykhodtseva, F. Jolesz, and K. Hynynen, "Cellular mechanisms of the blood-brain barrier opening induced by ultrasound in presence of microbubbles," *Ultrasound Med. Biol.*, vol. 30, no. 7, pp. 979–989, 2004.

[45] S. K. Wu *et al.*, "Characterization of different microbubbles in assisting focused

ultrasound-induced blood-brain barrier opening," *Sci. Rep.*, vol. 7, 2017.

[46] M. E. Downs *et al.*, "Long-term safety of repeated blood-brain barrier opening via focused ultrasound with microbubbles in non-human primates performing a cognitive task," *PLoS One*, vol. 10, no. 5, 2015.

[47] J. J. Choi, K. Selert, F. Vlachos, A. Wong, and E. E. Konofagou, "Noninvasive and localized neuronal delivery using short ultrasonic pulses and microbubbles," *Proc. Natl. Acad. Sci. U. S. A.*, vol. 108, no. 40, pp. 16539–16544, 2011.

[48] S. V. Morse *et al.*, "Rapid short-pulse ultrasound delivers drugs uniformly across the murine blood-brain barrier with negligible disruption," *Radiology*, vol. 291, no. 2, pp. 459–466, 2019.

[49] M. Aryal, I. Papademetriou, Y. Z. Zhang, C. Power, N. McDannold, and T. Porter, "MRI Monitoring and Quantification of Ultrasound-Mediated Delivery of Liposomes Dually Labeled with Gadolinium and Fluorophore through the Blood-Brain Barrier," *Ultrasound Med. Biol.*, vol. 45, no. 7, pp. 1733–1742, 2019.

[50] W. M. Pardridge, "Blood-brain barrier drug targeting: the future of brain drug development.," *Mol. Interv.*, vol. 3, no. 2, pp. 90–105, 51, 2003.

[51] F. A. Dunand, A. Borel, and A. E. Merbach, "How does internal motion influence the relaxation of the water protons in LnIIIDOTA-like complexes?," *J. Am. Chem. Soc.*, vol. 124, no. 4, pp. 710–716, 2002.

[52] J. J. Choi, S. Wang, Y. S. Tung, B. Morrison, and E. E. Konofagou, "Molecules of Various Pharmacologically-Relevant Sizes Can Cross the Ultrasound-Induced Blood-Brain Barrier Opening in vivo," *Ultrasound Med. Biol.*, vol. 36, no. 1, pp. 58–67, 2010.

[53] J. J. Choi, K. Selert, Z. Gao, G. Samiotaki, B. Baseri, and E. E. Konofagou, "Noninvasive and localized blood-brain barrier disruption using focused ultrasound can be achieved at short pulse lengths and low pulse repetition frequencies," *J. Cereb. Blood Flow Metab.*, vol. 31, no. 2, pp. 725–737, 2011.

[54] S. Wanga, B. Baserib, J. J. Choib, Y. S. Tungb, B. Morrisonb, and E. E. Konofagoua, "Delivery of Fluorescent Dextrans through the Ultrasound-Induced Blood-Brain Barrier Opening in Mice," in *Proceedings - IEEE Ultrasonics Symposium*, 2008, pp. 1702–1705.

[55] M. Aryal, J. Park, N. Vykhodtseva, Y.-Z. Zhang, and N. McDannold, "Enhancement in blood-tumor barrier permeability and delivery of liposomal doxorubicin using focused ultrasound and microbubbles: evaluation during tumor progression in a rat glioma

model," *Phys. Med. Biol.*, vol. 60, no. 6, pp. 2511–2527, 2015.

[56] M. Rogosnitzky and S. Branch, "Gadolinium-based contrast agent toxicity: a review of known and proposed mechanisms," *BioMetals*, vol. 29, no. 3, pp. 365–376, 2016.

[57] S. Davis, M. J. Weiss, J. R. Wong, T. J. Lampidis, and L. B. Chen, "Mitochondrial and plasma membrane potentials cause unusual accumulation and retention of rhodamine 123 by human breast adenocarcinoma-derived MCF-7 cells," *J. Biol. Chem.*, vol. 260, no. 25, pp. 13844–13850, 1985.

[58] M. F. Ross *et al.*, "Lipophilic triphenylphosphonium cations as tools in mitochondrial bioenergetics and free radical biology," *Biokhimiya*, vol. 70, no. 2, pp. 273–283, 2005.

[59] M. L. James and S. S. Gambhir, "A molecular imaging primer: Modalities, imaging agents, and applications," *Physiol. Rev.*, vol. 92, no. 2, pp. 897–965, 2012.

[60] M. Rudin and R. Weissleder, "Molecular imaging in drug discovery and development," *Nat. Rev. Drug Discov.*, vol. 2, no. 2, pp. 123–131, 2003.

[61] D. A. Galloway, A. E. M. Phillips, D. R. J. Owen, and C. S. Moore, "Phagocytosis in the brain: Homeostasis and disease," *Front. Immunol.*, vol. 10, no. MAR, pp. 1–15, 2019.

[62] G. W. Kreutzberg, "Microglia: A sensor for pathological events in the CNS," *Trends in Neurosciences*, vol. 19, no. 8. pp. 312–318, 1996.

[63] E. E. Benarroch, "Microglia: Multiple roles in surveillance, circuit shaping, and response to injury," *Neurology*, vol. 81, no. 12. pp. 1079–1088, 2013.

[64] K. M. Lenz and L. H. Nelson, "Microglia and beyond: Innate immune cells as regulators of brain development and behavioral function," *Front. Immunol.*, vol. 9, no. APR, p. 698, 2018.

[65] M. V. Sofroniew and H. V. Vinters, "Astrocytes: Biology and pathology," *Acta Neuropathol.*, vol. 119, no. 1, pp. 7–35, 2010.

[66] I. D. Vainchtein *et al.*, "Astrocyte-derived interleukin-33 promotes microglial synapse engulfment and neural circuit development," *Science (80-.).*, vol. 359, no. 6381, pp. 1269–1273, 2018.

[67] T. G. Chan, S. V. Morse, M. J. Copping, J. J. Choi, and R. Vilar, "Targeted Delivery of DNA-Au Nanoparticles across the Blood–Brain Barrier Using Focused Ultrasound," *ChemMedChem*, vol. 13, no. 13, pp. 1311–1314, 2018.

[68] M. A. Valdez, E. Fernandez, T. Matsunaga, R. P. Erickson, and T. P. Trouard, "Distribution and Diffusion of Macromolecule Delivery to the Brain via Focused Ultrasound using

Magnetic Resonance and Multispectral Fluorescence Imaging," *Ultrasound Med. Biol.*, vol. 46, no. 1, pp. 122–136, 2020.

[69] Z. I. Kovacs, S. R. Burks, and J. A. Frank, "Focused ultrasound with microbubbles induces sterile inflammatory response proportional to the blood brain barrier opening: Attention to experimental conditions," *Theranostics*, vol. 8, no. 8, pp. 2245–2248, 2018.

[70] Z. I. Kovacsa *et al.*, "Disrupting the blood-brain barrier by focused ultrasound induces sterile inflammation," *Proc. Natl. Acad. Sci. U. S. A.*, vol. 114, no. 1, pp. E75–E84, 2017.

[71] Z. I. Kovacs *et al.*, "MRI and histological evaluation of pulsed focused ultrasound and microbubbles treatment effects in the brain," *Theranostics*, vol. 8, no. 17, pp. 4837–4855, 2018.

[72] D. McMahon and K. Hynynen, "Reply to Kovacs et al.: Concerning acute inflammatory response following focused ultrasound and microbubbles in the brain," *Theranostics*, vol. 8, no. 8, pp. 2249–2250, 2018.

[73] L. Frullano and T. J. Meade, "Multimodal MRI contrast agents," *J. Biol. Inorg. Chem.*, vol. 12, no. 7, pp. 939–949, 2007.

[74] A. Nadal, E. Fuentes, and P. A. McNaughton, "Glial cell responses to lipids bound to albumin in serum and plasma," *Prog. Brain Res.*, vol. 132, pp. 367–374, 2001.

[75] V. Gulani, F. Calamante, F. G. Shellock, E. Kanal, and S. B. Reeder, "Gadolinium deposition in the brain: summary of evidence and recommendations," *Lancet Neurol.*, vol. 16, no. 7, pp. 564–570, 2017.

5 | Conclusions

The blood-brain barrier (BBB) represents a major hurdle for the diagnosis and treatment of brain diseases, as it prevents 98% of small molecule drugs and imaging agents from entering the brain. Focused ultrasound and microbubbles is a technology that allows drugs and imaging agents across the BBB in a non-invasive, local and transient way. To do this, ultrasound is currently emitted in long pulses, which can cause undesired effects, such as uneven distributions of the delivered drugs and the extravasation of unwanted compounds into the brain. To overcome these limitations, we have designed a rapid short-pulse (RaSP) ultrasound sequence to more uniformly distribute microbubble activity within the vasculature. In turn, this should improve the distribution of the BBB permeability enhancement and therefore the delivery of compounds into the brain. In this thesis, we investigated differences in performance and safety between emitting a RaSP sequence and a long pulse sequence to deliver a model drug into the brain. We then explored whether RaSP could also improve the delivery of much larger liposomal agents. Lastly, we investigated whether a fluorescently-labelled Gd-based MRI contrast agent could label neurons *in vivo* once delivered to the brain with focused ultrasound.

In Chapter 2, the efficacy and safety of delivering a model drug non-invasively with focused ultrasound was investigated by emitting a rapid short-pulse sequence and comparing it to the emission of a conventionally used long pulse sequence. RaSP was found to deliver the model drug more uniformly throughout the targeted brain region, without over or undertreating areas, with a comparable drug dose to that delivered with the long pulse sequence. These results were achieved by emitting the lowest acoustic energy reported so far to deliver drugs across the BBB. By designing this RaSP sequence to prolong the lifetime of microbubbles and spatially distribute their activity with the rapid emission of short pulses, an improved outcome was not only observed in the efficacy of delivery, but also in the safety. The permeability of the BBB was altered

for less than 10 minutes, minimising the amount of endogenous proteins (albumin and immunoglobulins) extravasating into the brain. In addition, no histological damage was observed. Higher cellular uptake was detected in neurons with RaSP, while less involvement of immune responsive glial cells was observed compared to long-pulse-treated brains. By monitoring the acoustic emissions during treatments, we were able to show a good correlation between the microbubble energy and the detected amount of drug delivered. Prolonged microbubble activity was also achieved when emitting RaSP. In future work, this sequence will be designed and optimised for different purposes, such as for various sized agents, different disease targets and organs, and for other ultrasound applications. New pulse sequence designs will also be explored as the technology moves towards more clinically relevant ultrasound frequencies and animal models.

In Chapter 3, the ability of the RaSP sequence to improve the delivery of large 100 nm liposomal compounds into the brain was investigated. The efficacy of delivery was found to be lower with RaSP compared to long pulses; however, an improved safety profile was observed. A higher acoustic pressure was required to deliver the liposomes with RaSP and a lower number of delivery regions and detected dose was found compared with long pulses. Only a single site of red blood cell extravasation was found in RaSP brains, while tissue damage was detected in all long-pulse-treated brains. In terms of cellular uptake, liposomes were detected in neurons, but to a lesser degree than in long-pulse-treated brains, possibly due to the lower delivery. Microglial uptake, on the other hand, was observed only at the higher pressure and after a two-hour recovery period, while no astrocyte uptake was observed within this time frame. These cellular uptake results indicate that drugs targeting neurons can be delivered with this technology to the required regions of the brain. The lower glial cell involvement with RaSP indicates a slower liposome removal from the brain. The reduced delivery and safer profile of RaSP in delivering liposomes into the brain indicates a gentler stimulation of the vasculature. However, future work will focus on optimising the RaSP

sequence to improve the efficacy of delivery of these larger liposomal compounds into the brain. The therapeutic effects of drugs released by liposomes delivered into the brain with focused ultrasound will also be explored in disease models.

In Chapter 4, we evaluated whether a fluorescently-labelled Gd-based MRI contrast agent (Gd(rhodamine-pip-DO3A)) could be delivered into the brain to image neurons. This is the first optical-MRI probe to be delivered *in vivo* with focused ultrasound and microbubbles to image neurons. The probe was delivered by emitting conventionally used long pulses and was found to spread uniformly within the brain, with uptake confirmed in neurons, but not in microglia and astrocytes. Compared to the fluorescently-labelled model drug tested in Chapter 2, its distribution was more uniform and no glial cell uptake was elicited. An increase in signal was detected via both fluorescence and MRI *ex vivo*. The delivery of such dual-modal agents into neurons can facilitate future studies of neuronal physiology, using the advantages of both imaging modalities. Future work will focus on performing MRI detection *in vivo* and on delivering the probe with a RaSP sequence for improved safety.

In conclusion, this thesis has contributed towards improving the way drugs and imaging agents are delivered into the brain with focused ultrasound and microbubbles. This work demonstrates that the way ultrasound sequences are designed can improve how agents are delivered across the BBB. Our aim is to provide a more efficient and safer method of performing treatments in future clinical trials with this promising non-invasive and targeted therapeutic technology.

6 | Appendix

Chapter 2

6.1 Mechanical index calculation incorporating pulse length

The following calculations were carried out to find the mechanical index taking into account the effect of pulse length [1]. The following formula was used:

$$MI = \frac{P_{neg}}{P_{t,n}\sqrt{f_c}}$$

Where $P_{t,n} = A + BL_p^{-m}$, with L_p being the pulse length (PL), $A = 0.536$, $B = 0.475$ and $m = 1.099$ in blood. For the RaSP sequence (PL = 5 μs), the MI was found to be 1.1, while for the long pulse sequence (PL = 10,000 μs) the MI was found to be 4636. These values indicate that when accounting for pulse length, the likelihood of ultrasound producing non-thermal bioeffects is much higher when emitting long pulse sequences.

6.2 Temperature increase calculation

The following calculations were carried out to find the temperature increase caused by our ultrasound sonications, to determine whether heating effects needed to be considered. The temperature increase can be calculated from the heat capacity C = ΔQ/ΔT. ΔQ is the total energy absorbed by the tissue, which we assume is equal to the acoustic energy (this will be the upper limit since not all sound will be completely absorbed), and ΔT is the temperature change. The heat capacity of the brain is 3,630 J/K for 1 kg [2]. The total energy ΔQ = E(J) = P(W) * t(s) = I(W/m^2) * A(m^2) * t(s), where E is energy, P is power, I is intensity, A is the tissue area, and t is the sonication time. The temperature increase will therefore be:

$$\Delta T(K) = I(W/m^2) * A(m^2) * t(s) / C(J/K)$$

The intensity (I_{SPTA} – spatial peak temporal average intensity) can be found as following: $I(W/m^2) = P^2/2Z$. The acoustic impedance ($Z = \rho c$) of brain tissue is $1.6*10^6$ kg/s*m^2 [3]. Therefore, $I(W/m^2) = P^2/2Z = (0.35*10^6)^2$ (Pa) / 2 * $(1.6*10^6)$ (kg/s*m^2) = 38281.25 W/m^2 given our inputted pressure of 0.35 MPa.

For the RaSP sequence:

$$\Delta T(K) = 38281.25\ (W/m^2) * 2*(10^{-6})\ (m^2) * 8.19*(10^{-3})\ (s) / 3630\ (J/K) = 1.72*10^{-7}\ K$$

For the long pulse sequence:

$$\Delta T(K) = 38281.25\ (W/m^2) * 2*(10^{-6})\ (m^2) * 1.26\ (s) / 3630\ (J/K) = 2.66*10^{-5}\ K$$

These calculations were made considering the total time that the ultrasound was on throughout the sonication. For RaSP, 13 pulses of 5 µs pulse length were emitted in each burst with a total of 126 bursts ($5*10^{-6}$(s)*13*126 = $8.19*10^{-3}$ s). For long pulses, 126 pulses of 10 ms pulse length were emitted ($10*10^{-3}$(s)*126 = 1.26 s).

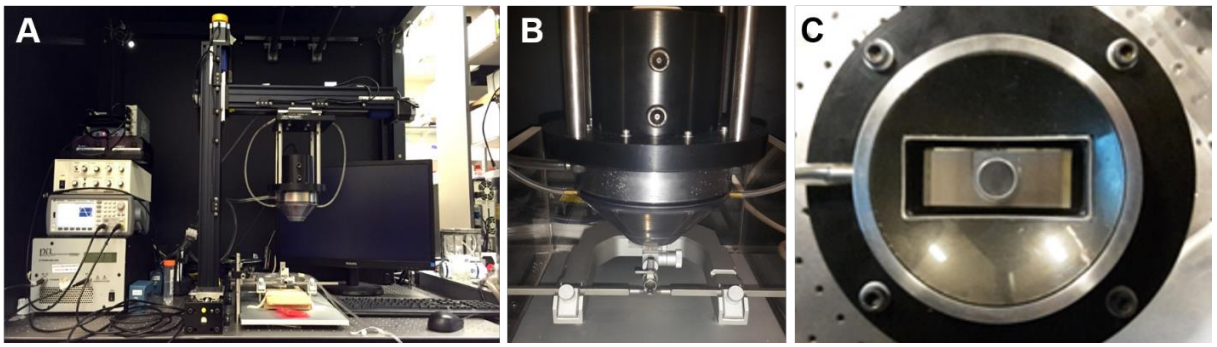

Figure 6.1. Experimental setup. (A) Photo of entire experimental setup. **(B)** Photo of transducer above the stereotaxic frame. **(C)** Therapeutic transducer without the plastic cone with the rectangular cut-out showing the 3D printed casing and PCD inside of it.

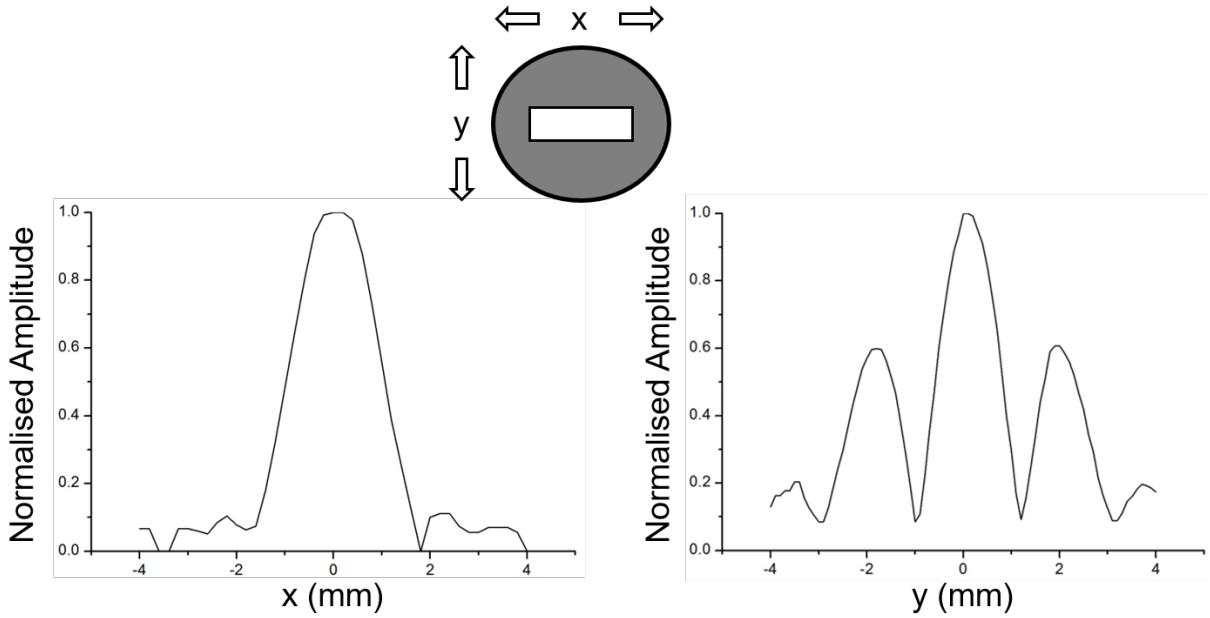

Figure 6.2. Beam profiles. These beam profiles along the lateral (x) and elevational (y) dimensions were obtained by calibrating the 1-MHz Sonic Concepts transducer. The FWHM was 2 mm and 1 mm, along the lateral and elevational dimensions respectively. These beam profiles show the side lobes in the elevational plane which lead to drug delivery approximately 2 mm from the main lobe in some brains treated with higher pressures (e.g. 0.6 MPa).

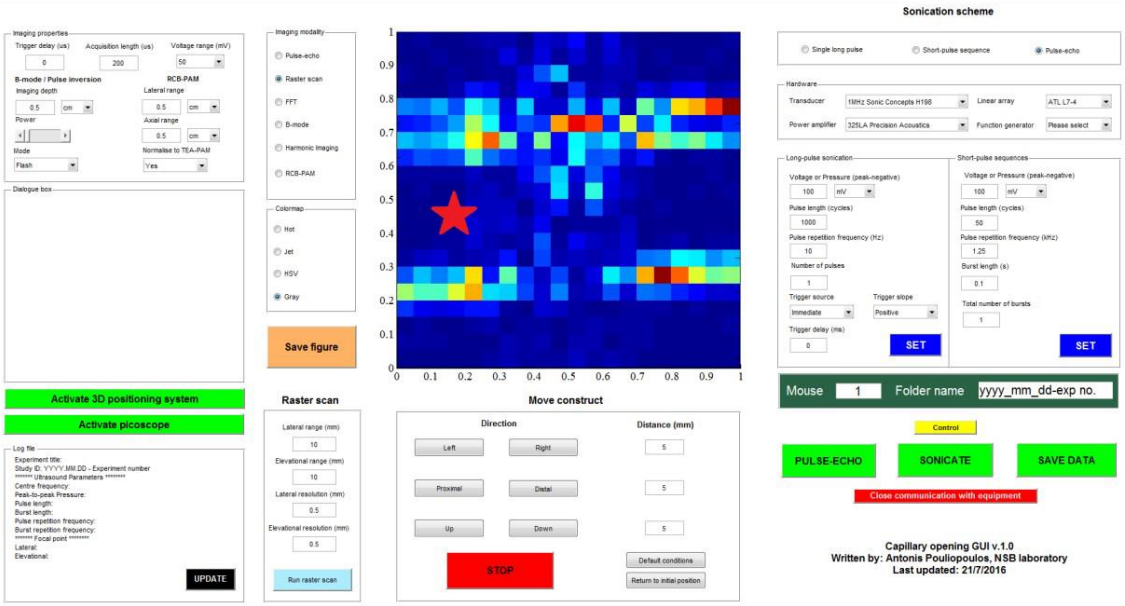

Figure 6.3. Graphical user interface (GUI). This user interface was used to communicate with the function generators, picoscope and 3D positioning system. This GUI was used to target the

left hippocampus by performing a raster scan to image the metal cross placed in alignment with the skull's sutures (image in the centre).

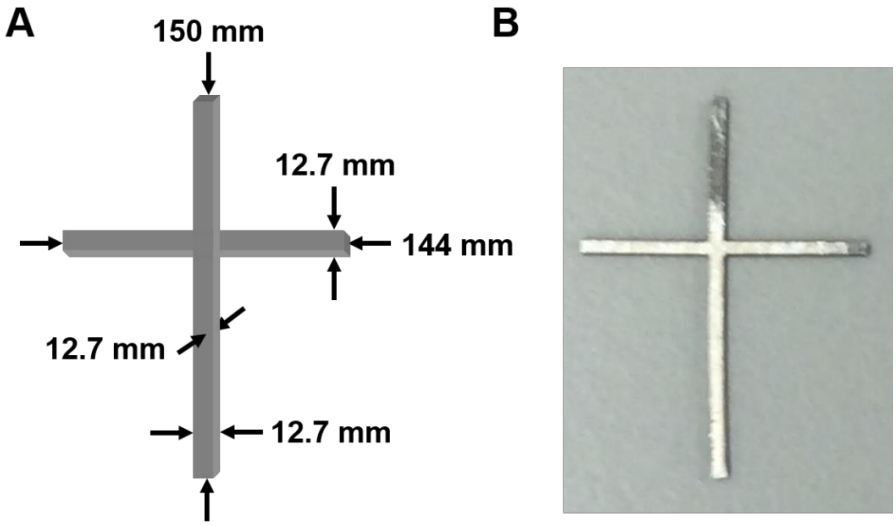

Figure 6.4. Exact dimensions of the stainless-steel cross. (A) Dimensions of the metal grid cross and **(B)** photograph of the actual metal cross.

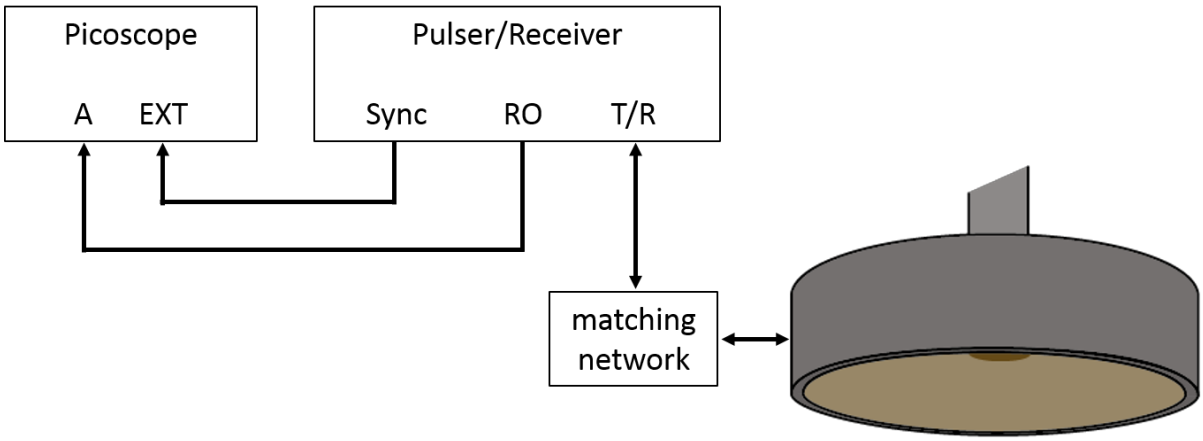

Figure 6.5. Pulse-echo mode connections. Communication between the picoscope, pulser/receiver and the therapeutic ultrasound transducer.

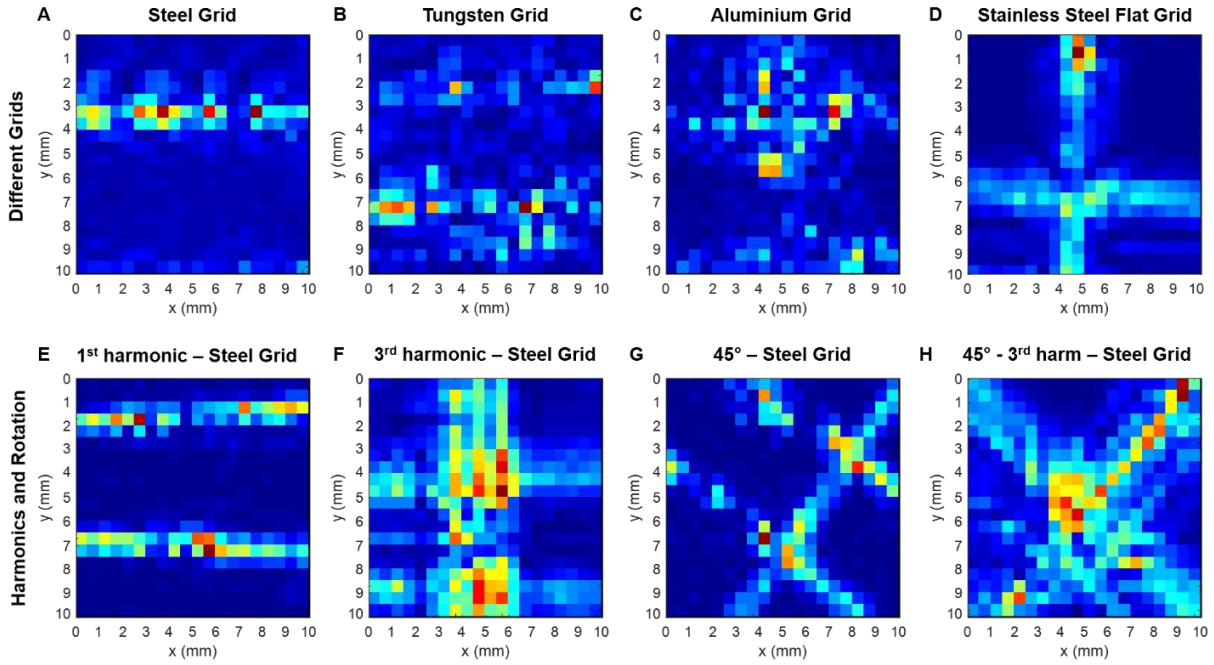

Figure 6.6. Example raster scans with different methods tested. Results obtained by testing **(A-D)** different types of material for the targeting grid, **(E-F,H)** by driving the transducer with the fundamental or third harmonic, or **(G-H)** by positioning the grid at 45 degrees.

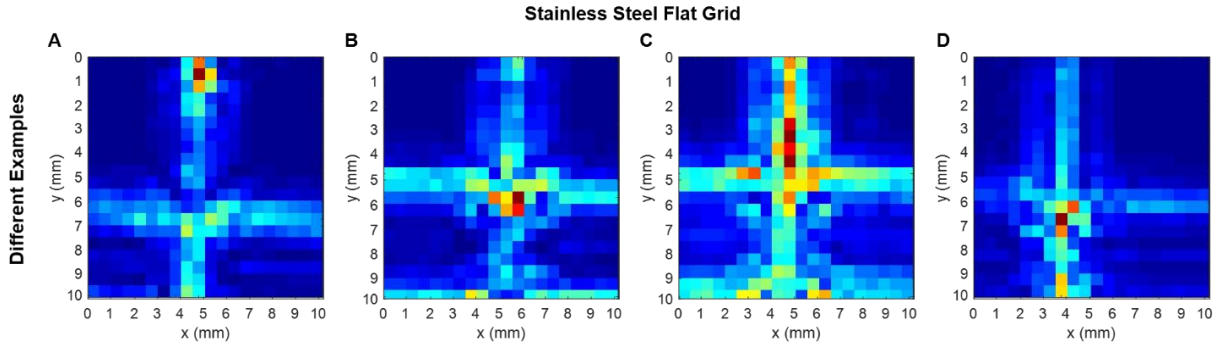

Figure 6.7. Example raster scans with the final grid chosen. The stainless steel flat grid gave the best results for targeting and here different examples of what the raster scans can look like are shown.

Table 6.1. Protocol for cryosectioning. Steps are highlighted with reagents or tools needed as well as the duration of the step (per brain). Relevant comments with details and suggestions are indicated on the right-hand column. Steps that come after a grey row indicate that they need to

be performed the next day. PBS = phosphate buffered saline, w/v = weight per volume, OCT = optimal cutting temperature.

Step	Reagent/Tool	Duration	Comments
Perfusion	20 mL PBS + heparin (10 units/mL) & 20 mL 10% formalin	15-20 min	Both reagents kept ice cold before use
Excision	Scissors + tweezers	1 min	Perform with care
Fixation	10% formalin	overnight	
Leave overnight in fridge			
Cryoprotection	15% sucrose (w/v) in PBS	6 h	Change to 30% when sample is not floating anymore
	30% sucrose (w/v) in PBS	overnight	
Leave overnight in fridge before cutting			
Freezing	OCT, isopentane, plastic mould	10 min	Place sample in mould filled with OCT and place inside isopentane brought to -60 °C by adding dry ice
Cutting	Cryostat	20-40 min	Use water droplets on slides (20 µL / slice) to avoid folds. Specimen temperature: -12 °C Chamber temperature: -14 °C
Leave overnight in fridge before imaging			
Imaging	Microscope	30-60 min	Make sure slides are dry

Table 6.2. Protocol for albumin staining. Steps are highlighted with reagents or tools needed as well as the duration of the step. Relevant comments with details and suggestions are indicated on the right-hand column. Steps that come after a grey row indicate that they need to be performed the next day. Primary antibody used: rabbit anti-mouse serum albumin antibody (ab19196); secondary antibody used: donkey anti-rabbit IgG H&L (Alexa Fluor® 488) (ab150073). TBS = tris buffered saline, PAP = peroxidase-antiperoxidase, Tx = Triton-X, BSA = bovine serum albumin, PBS = phosphate buffered saline, DAPI = 4',6-diamidino-2-phenylindole.

Step	Reagent/Tool	Duration	Comments
Wash	TBS	5 min 5 min 5 min	Place racks with slides inside plastic tub and place on shaker
Pen	PAP pen	-	-
Permeabilisation	TBS + 0.25% Tx	30 min	Place on shaker
Wash	TBS	5 min 5 min 5 min	Place racks with slides inside plastic tub and place on shaker
Pen	PAP pen	-	-
Blocking	TBS + 0.1% Tx + 1% BSA + 5% donkey serum	60 min	Match serum to secondary
Primary Antibody	Primary Antibody (1:100) in TBS + 0.01% Tx + 0.1% BSA	overnight	Put on shaker for 1 min before fridge (4 °C)
Wash	TBS	5 min 5 min 5 min	Place racks with slides inside plastic tub and place on shaker
Pen	PAP pen	-	-
Secondary Antibody	Secondary Antibody (1:200) in TBS + 0.01% Tx + 0.1% BSA	2 h	On shaker at room temperature
Wash	TBS	5 min 5 min 5 min 5 min	Place racks with slides inside plastic tub and place on shaker
Wash	PBS	20 min	-
Reduce Autofluorescence	0.1% Sudan Black in 70% Ethanol	20 min	Filter before use
Wash	Distilled running water	10 min	-
DAPI counterstain	Counterstain solution	5 min	Before coverslipping
Leave overnight in fridge before imaging			

Table 6.3. Protocol for immunoglobulin staining. Steps are highlighted with reagents or tools needed as well as the duration of the step. Relevant comments with details and suggestions are indicated on the right-hand column. Steps that come after a grey row indicate that they need to be performed the next day. Antibody used: donkey anti-mouse IgG H&L (Alexa Fluor® 488) (ab150105). TBS = tris buffered saline, PAP = peroxidase-antiperoxidase, Tx = Triton-X, BSA = bovine serum albumin, PBS = phosphate buffered saline, DAPI = 4',6-diamidino-2-phenylindole.

Step	Reagent/Tool	Duration	Comments
Wash	TBS	5 min 5 min 5 min	Place racks with slides inside plastic tub and place on shaker
Pen	PAP pen	-	Draw circle around each slide
Permeabilisation	TBS + 0.25% Tx	30 min	100 µL ontop of each slide and place on shaker
Wash	TBS	5 min 5 min 5 min	Place racks with slides inside plastic tub and place on shaker
Pen	Reapply PAP pen	-	Only if it has come off
Blocking	TBS + 0.1% Tx + 1% BSA + 5% donkey serum	60 min	Match serum to secondary
Secondary Antibody	Secondary Antibody (1:200) in TBS + 0.01% Tx + 0.1% BSA	2 h	On shaker at room temperature
Wash	TBS	5 min 5 min 5 min 5 min	Place racks with slides inside plastic tub and place on shaker
Wash	PBS	20 min	-
Reduce Autofluorescence	0.1% Sudan Black in 70% Ethanol	20 min	Filter before use
Wash	Distilled running water	10 min	-
DAPI counterstain	Counterstain solution	5 min	Before coverslipping
Leave overnight in fridge before imaging			

Table 6.4. Protocol for neuron staining. Steps are highlighted with reagents or tools needed as well as the duration of the step. Relevant comments with details and suggestions are indicated on the right-hand column. Steps that come after a grey row indicate that they need to be performed the next day. Primary antibody used: recombinant rabbit anti-NeuN antibody [EPR12763] (ab177487); secondary antibody used: goat anti-rabbit IgG H&L (Alexa Fluor® 488) (ab150077). PBS = phosphate buffered saline, PAP = peroxidase-antiperoxidase, Tx = Triton-X, BSA = bovine serum albumin, DAPI = 4',6-diamidino-2-phenylindole.

Step	Reagent/Tool	Duration	Comments
Antigen Retrieval	10% citrate buffer in deionised water	1 min	Heated to 80 °C
Cool down	-	20 min	-
Wash	PBS	5 min	Place racks with slides inside plastic tub and place on shaker
		5 min	
		5 min	
Pen	PAP pen	-	
Permeabilisation	PBS + 0.1% Tx	30 min	Place on shaker
Wash	PBS	5 min	Place racks with slides inside plastic tub and place on shaker
		5 min	
		5 min	
Pen	PAP pen	-	
Blocking	PBS + 0.1% Tx + 5% goat serum + 1% BSA	60 min	Match serum to secondary
Primary Antibody	Primary Antibody (1:500) in PBS + 0.01% Tx + 0.1% BSA	overnight	Put on shaker for 1 min before fridge (4 °C)
Wash	PBS	5 min	Place racks with slides inside plastic tub and place on shaker
		5 min	
		5 min	
Pen	PAP pen	-	
Secondary Antibody	Secondary Antibody (1:500) in PBS + 0.01% Tx + 0.1% BSA	2 h	On shaker at room temperature
Wash	PBS	5 min	Place racks with slides inside plastic tub and place on shaker
		5 min	
		5 min	
		5 min	
DAPI counterstain	Counterstain solution	5 min	Before coverslipping
Leave overnight in fridge before imaging			

Table 6.5. Protocol for microglia staining. Steps are highlighted with reagents or tools needed as well as the duration of the step. Relevant comments with details and suggestions are indicated on the right-hand column. Steps that come after a grey row indicate that they need to be performed the next day. Primary antibody used: goat anti-Iba1 antibody (ab5076); secondary antibody used: donkey anti-goat IgG H&L (Alexa Fluor® 488) (ab150129). TBS = tris buffered saline, PAP = peroxidase-antiperoxidase, Tx = Triton-X, BSA = bovine serum albumin, PBS = phosphate buffered saline, DAPI = 4',6-diamidino-2-phenylindole.

Step	Reagent/Tool	Duration	Comments
Wash	TBS	5 min 5 min 5 min	Place racks with slides inside plastic tub and place on shaker
Pen	PAP pen	-	-
Permeabilisation	TBS + 0.25% Tx	30 min	Place on shaker
Wash	TBS	5 min 5 min 5 min	Place racks with slides inside plastic tub and place on shaker
Pen	PAP pen	-	-
Blocking	TBS + 0.1% Tx + 5% donkey serum + 1% BSA	60 min	Match serum to secondary
Primary Antibody	Primary Antibody (1:500) in TBS + 0.01% Tx + 0.1% BSA	overnight	Put on shaker for 1 min before fridge (4 °C)
Wash	TBS	5 min 5 min 5 min	Place racks with slides inside plastic tub and place on shaker
Pen	PAP pen	-	-
Secondary Antibody	Secondary Antibody (1:500) in TBS + 0.01% Tx + 0.1% BSA	2 h	On shaker at room temperature
Wash	TBS	5 min 5 min 5 min 5 min	Place racks with slides inside plastic tub and place on shaker
Wash	PBS	5 min	-
Reduce Autofluorescence	Sudan Black (0.1% sudan in 70% ethanol)	20 min	Filter before using
Wash	Distilled running water	10 min	-
DAPI counterstain	Counterstain solution	5 min	Before coverslipping
Leave overnight in fridge before imaging			

Table 6.6. Protocol for astrocyte staining. Steps are highlighted with reagents or tools needed as well as the duration of the step. Relevant comments with details and suggestions are indicated on the right-hand column. Steps that come after a grey row indicate that they need to be performed the next day. Primary antibody used: rat GFAP monoclonal antibody [2.2B10] (13-0300); secondary antibody used: mouse anti-rat IgG2a (FITC) (11-4817-82). PBS = phosphate buffered saline, PAP = peroxidase-antiperoxidase, Tx = Triton-X, BSA = bovine serum albumin, DAPI = 4',6-diamidino-2-phenylindole.

Step	Reagent/Tool	Duration	Comments
Antigen Retrieval	10% citrate buffer in deionised water	10 min	Heated to 80 °C
Cool down	-	20 min	-
Wash	PBS	5 min	Place racks with slides inside plastic tub and place on shaker
		5 min	
		5 min	
Pen	PAP pen	-	
Permeabilisation	PBS + 0.3% Tx	60 min	Place on shaker
Wash	PBS	5 min	Place racks with slides inside plastic tub and place on shaker
		5 min	
		5 min	
Pen	PAP pen	-	
Blocking	PBS + 0.1% Tx + 1% BSA	60 min	Match serum to secondary
Primary Antibody	Primary Antibody (1:100) in PBS + 0.01% Tx + 0.1% BSA	overnight	Put on shaker for 1 min before fridge (4 °C)
Wash	PBS	5 min	Place racks with slides inside plastic tub and place on shaker
		5 min	
		5 min	
Pen	PAP pen	-	
Secondary Antibody	Secondary Antibody (1:500) in PBS + 0.01% Tx + 0.1% BSA	2 h	On shaker at room temperature
Wash	PBS	5 min	Place racks with slides inside plastic tub and place on shaker
		5 min	
		5 min	
		5 min	
DAPI counterstain	Counterstain solution	5 min	Before coverslipping
Leave overnight in fridge before imaging			

Table 6.7. Protocol for H&E staining. Steps are highlighted with reagents or tools needed as well as the duration of the step. Relevant comments with details and suggestions are indicated on the right-hand column. DPX = dibutylphthalate polystyrene xylene.

Step	Reagent/Tool	Duration	Comments
Clearing	Histo-Clear II	5 min 10 min	
Hydration	Water		Dripping with pipette careful not to wash off sections
Haematoxylin	Harris Haematoxylin	5 min	Filtered
Wash	Tap water		Running tap water
Remove excess background	1% Hydrochloric acid in 70% ethanol	3 dips	
Wash	Tap water		Running tap water
Eosin	Eosin Y solution	50 s	
Wash	Tap water		Running tap water
Dehydrate	90% ethanol	30 s	
	100% ethanol	30 s	
Clearing	Histo-Clear II		Leave slides until coverslipping
Mount	DPX mountant		Wipe excess xylene
Imaging	Microscope		Make sure slides are dry

Table 6.8. Protocol for paraffin-embedding. Protocol provided by IQPath laboratory at University College London.

Step	Reagent/Tool	Duration	Comments
Fixing	Formalin	1 h	At ambient temperature
Dehydration	Ethanol 70%	1 h	At ambient temperature
	Ethanol 90%	1 h	
	Ethanol 100%	1 h	
	Ethanol 100%	1 h	
	Ethanol 100%	1 h	
	Ethanol 100%	1 h	
Clearning	Xylene	1 h	At ambient temperature
	Xylene	1 h	
	Xylene	1 h	
Paraffin-embedding	Paraffin Wax	1 h	At 60 °C
	Paraffin Wax	1 h	
	Paraffin Wax	1 h	

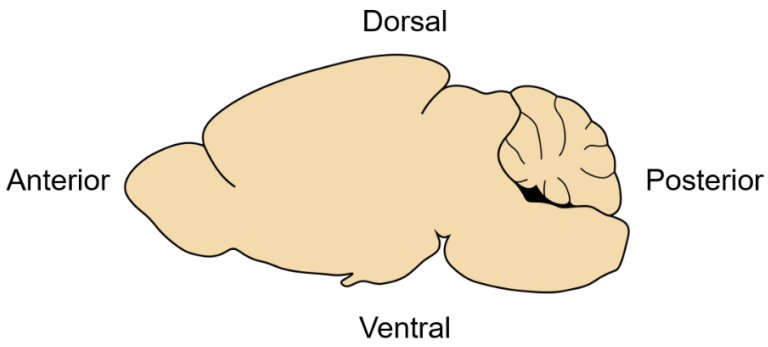

Figure 6.8. Anatomical orientations for the mouse brain. Anterior towards the front of the brain where the eyes are located; posterior towards the back of the brain where the cerebellum is located; dorsal is the top of the brain on the same side as the back; ventral is the bottom of the brain on the same side as the belly.

```
%% ---------------------- NOD and COV quantification ----------------- %%

Images_load = ls; start_index = 3;
NOD = zeros(1,1); COV_targeted = zeros(1,1);
Cropped_image_control_one_row = zeros(1,1);
Cropped_image_one_row = zeros(1,1);

for num_images = start_index:(length(Images_load(:,1)))

    Intensity_matrix = imread(Images_load(num_images,:));

    h = msgbox('Please crop out the targeted region');
    pause(0.1);
    Cropped_image = imcrop(Intensity_matrix); delete(h);

    BW_artefact = roipoly(Cropped_image);  %select the artefact ROI

    %%Set artefacts to NaN to eliminate them from quantification
    [row,col] = size(BW_artefact);

    for i = 1:col
       for j = 1:row
           if BW_artefact(j,i) == 1
                Cropped_image(j,i) = NaN;
           end
```

```
        end
    end

    BW_artefact = roipoly(Cropped_image);
    for i = 1:col
        for j = 1:row
            if BW_artefact(j,i) == 1
                Cropped_image(j,i) = NaN;
            end
        end
    end

    %%Find average intensity of the ROI on the right control side
    Intensity_matrix_control = imread(Images_load(num_images,:));
    Cropped_image_control = imcrop(Intensity_matrix_control);

    BW_artefact_control = roipoly(Cropped_image_control);

    %%Set artefacts in control to NaN to eliminate them from quantification
    [row_control,col_control] = size(BW_artefact_control);

    for i = 1:col_control
        for j = 1:row_control
            if BW_artefact_control(j,i) == 1
                Cropped_image_control(j,i) = NaN;
            end
        end
    end

    r = 1;
    for i = 1:col_control
        for j = 1:row_control
            Cropped_image_control_one_row(1,r) = Cropped_image_control(j,i);
            r = r + 1;
        end
    end

    r_2 = 1;
    for i = 1:col
        for j = 1:row
            Cropped_image_one_row(1,r_2) = Cropped_image(j,i);
            r_2 = r_2 + 1;
        end
    end

    %%Eliminate all the NaN values in the array in the control
    Cropped_image_control_one_row(find(isnan(Cropped_image_control_one_row))) = [];
    Cropped_image_one_row(find(isnan(Cropped_image_one_row))) = [];
```

```
    size_Control_array = size(Cropped_image_control_one_row,2);
    size_Targeted_array = size(Cropped_image_one_row,2);

    Average_intensity_control = mean2(Cropped_image_control_one_row);
    Stard_dev_control = std2(Cropped_image_control_one_row);

    Average_intensity_targeted = mean2(Cropped_image_one_row);
    Stard_dev_targeted = std2(Cropped_image_one_row);

    Threshold_value_twice_stard_dev = 2*Stard_dev_control + Average_intensity_control;

    %%Calculate sum of values in the control image above the threshold value
    New_matrix_control = zeros(1,1);

    k = 1;
    for i = 1:size_Control_array
           if Cropped_image_control_one_row(1,i) > Threshold_value_twice_stard_dev
                New_matrix_control(1,k) = Cropped_image_control_one_row(1,i);
                k = k + 1;
           end
    end

    Sum_control_matrix = sum(New_matrix_control);

    %%Calculate sum of value above threshold on targeted region
    k_1 = 1;
    New_matrix_fluoresc = zeros(1,1);

    for i = 1:size_Targeted_array
       if Cropped_image_one_row(1,i) > Threshold_value_twice_stard_dev
            New_matrix_fluoresc(1,k_1) = Cropped_image_one_row(1,i);
            k_1 = k_1 + 1;
       end
    end

    Sum_targeted_matrix = sum(New_matrix_fluoresc);

    NOD(num_images,1) = Sum_targeted_matrix - Sum_control_matrix;

    COV_targeted(num_images,1) = Stard_dev_targeted/Average_intensity_targeted;

end
```

Figure 6.9. Code to perform the NOD and COV quantification.

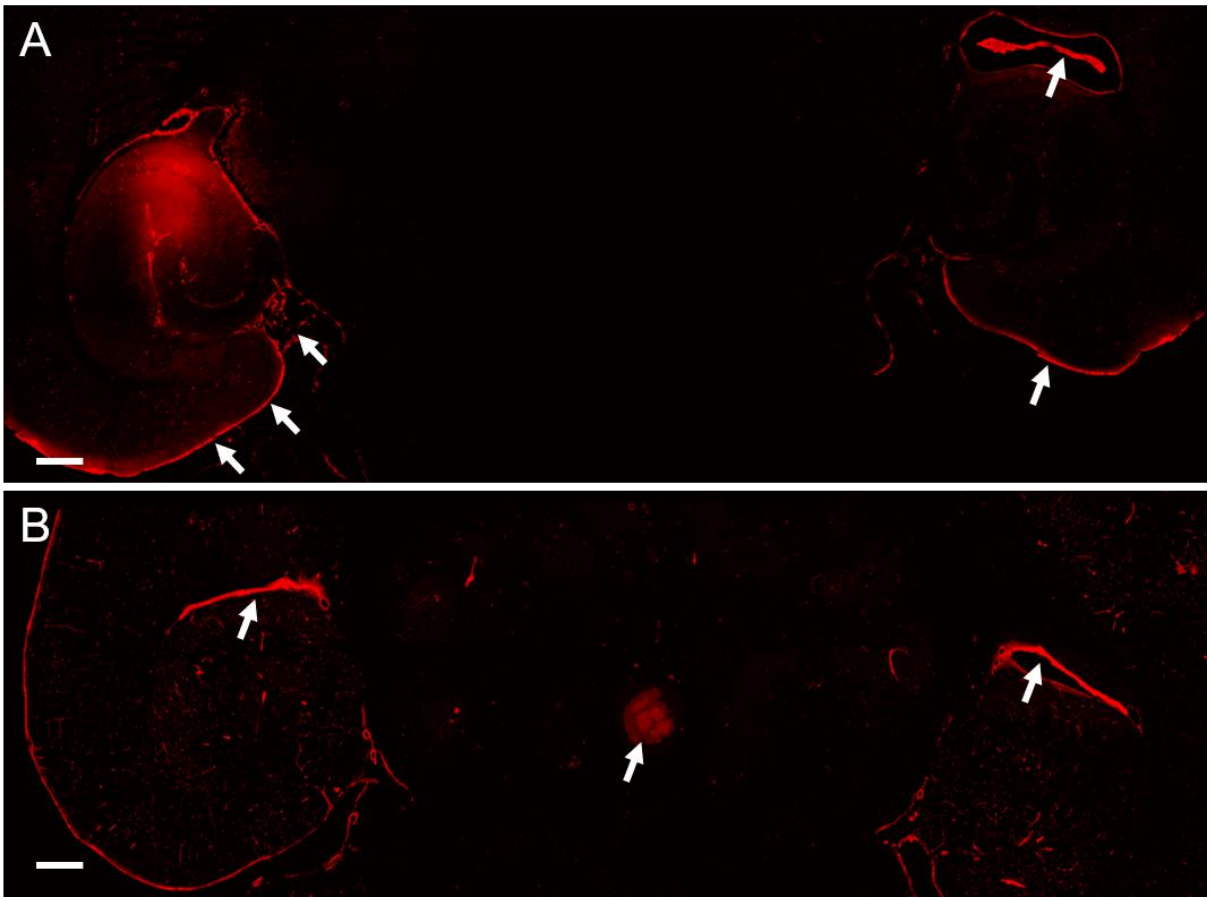

Figure 6.10. Examples of artefacts in fluorescence images. (A) Examples of artefacts around the edges of the brain and ventricles lighting up due to dextran flowing within the CSF (arrows). **(B)** Example of artefact from air bubbles (arrow in centre) and ventricles lighting up.

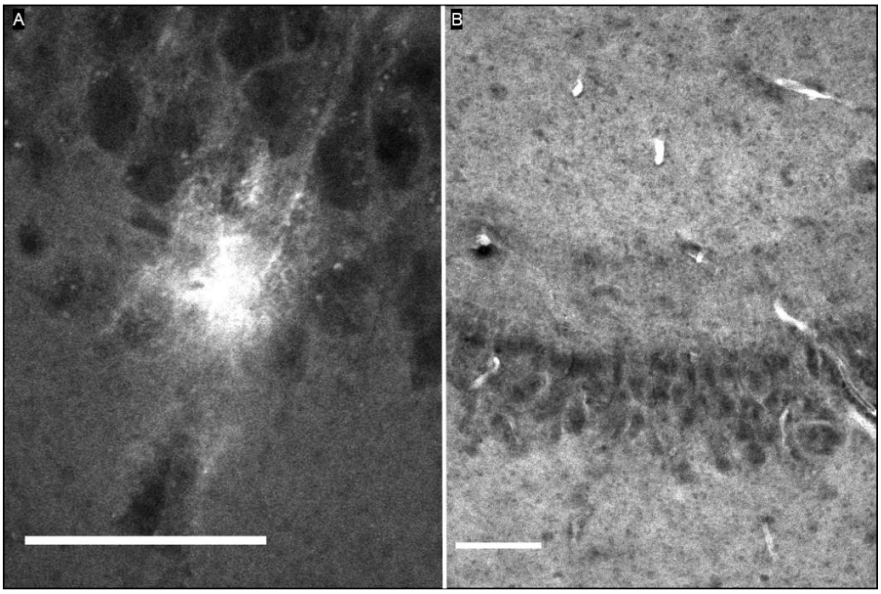

Figure 6.11. Dextran within glial cells and capillaries when delivered with a RaSP sequence. Confocal microscopy images (20x) of mouse brain regions exposed to ultrasound after intravenous injection of microbubbles and dextran reveal (**A**) glial cell uptake and (**B**) a homogeneous distribution of dextran throughout the parenchyma and in cerebral capillaries. Scale bars indicate 50 µm.

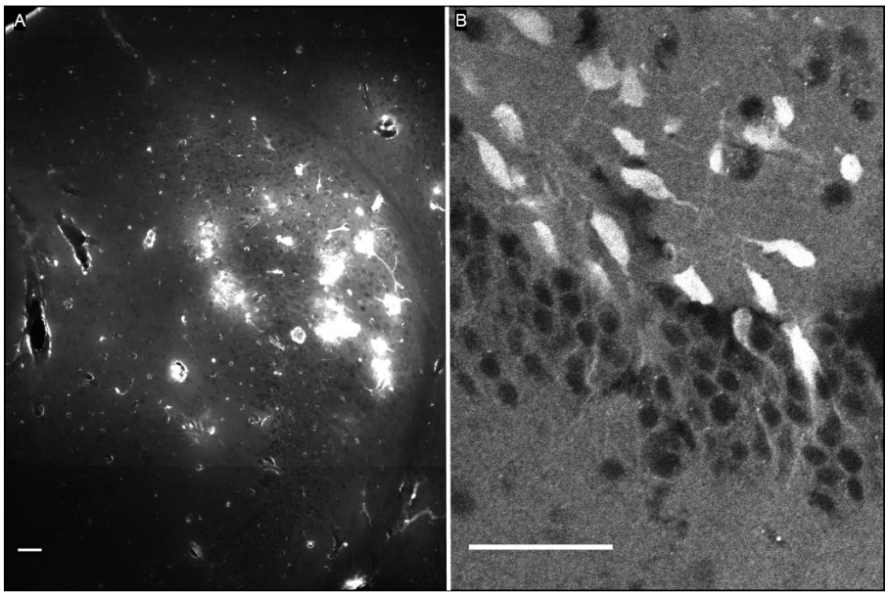

Figure 6.12. Dextran distribution and neuronal uptake when delivered with a long pulse sequence. Confocal microscopy images (20x) of mouse brain regions exposed to ultrasound after intravenous injection

of microbubbles and dextran reveal (**A**) an inhomogeneous distribution and (**B**) neuronal uptake. Scale bars indicate 50 µm.

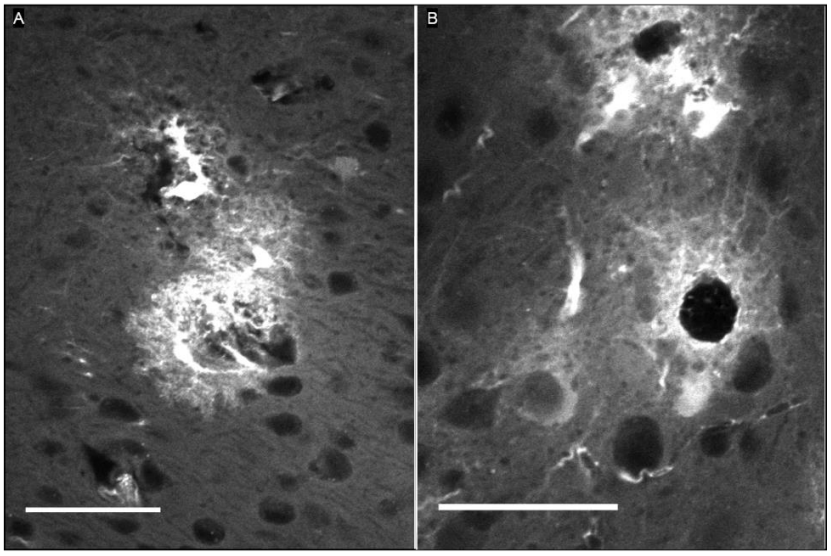

Fig. 6.13. Dextran delivery to glial cells and vessels when delivered with a long pulse sequence. Confocal microscopy images (20x) of mouse brain regions exposed to ultrasound after intravenous injection of microbubbles and dextran reveal (**A**) glial cell uptake and (**B**) high concentration of dextran in and around blood vessels. Scale bars indicate 50 µm.

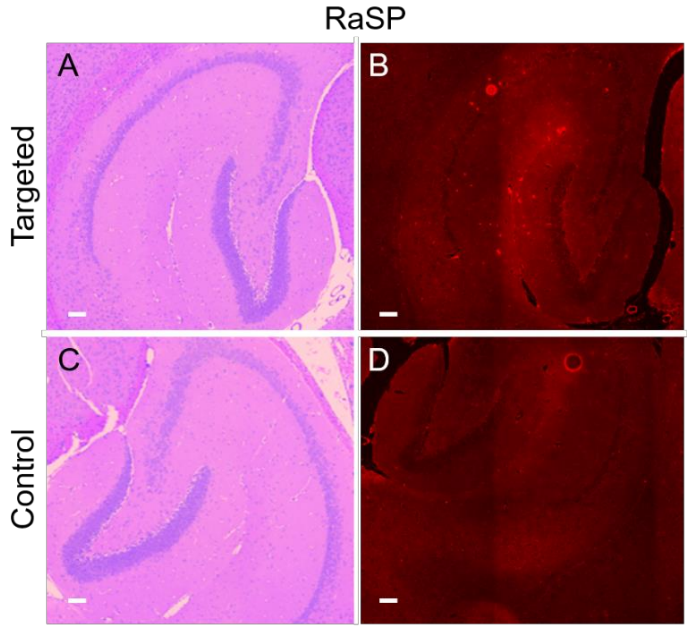

Figure 6.14. H&E and dextran images in RaSP-treated brains. Targeted and control sides of the H&E stained slices shown alongside the dextran image of the adjacent slice show where the opening is located. Scale bars indicate 50 μm.

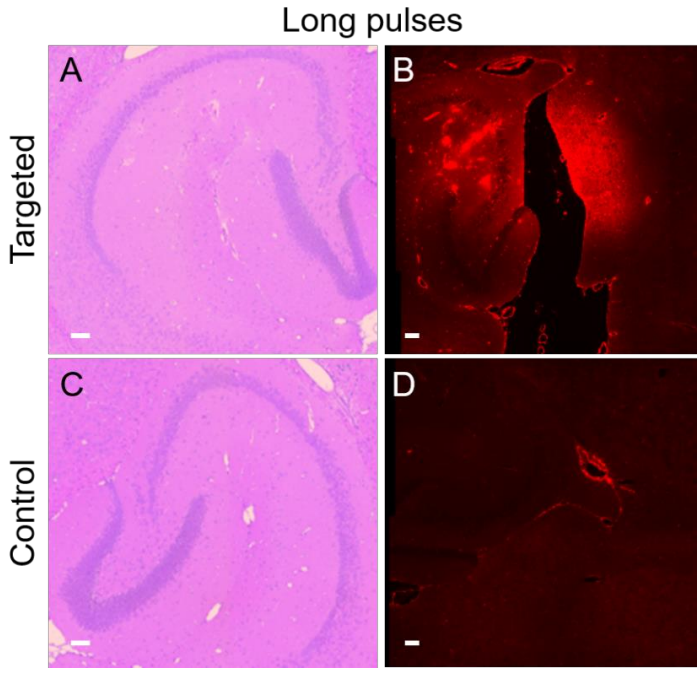

Figure 6.15. H&E and dextran images in long-pulse-treated brains. Targeted and control sides of the H&E stained slices shown alongside the dextran image of the adjacent slice show where the opening is located. Scale bars indicate 50 μm.

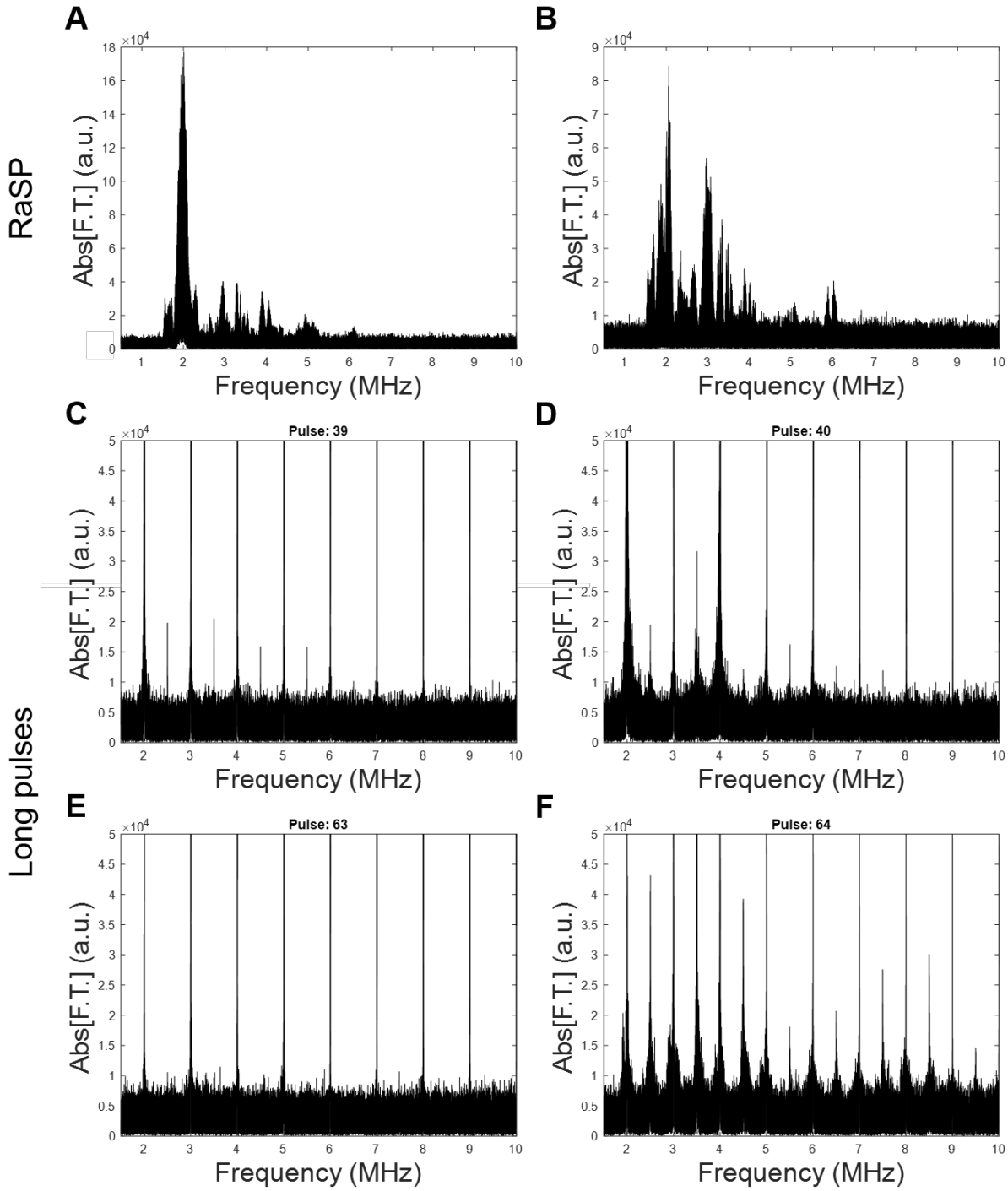

Figure 6.16. Spectral content of acoustic emissions from bursts of RaSP and long pulses. The spectral content from example bursts are shown for each sequence type. **(A-B)** With RaSP, lower magnitude harmonic emissions and very low magnitude ultraharmonic emissions were observed compared to long pulses. **(C-F)** With long pulses, strong harmonic emissions were observed and,

in some pulses **(D, F)**, broadening around the harmonics and the appearance of ultraharmonics was observed, while in other pulses this was not found **(E)**. The y axis was clipped to be able to show the broadening and ultraharmonics better.

Chapter 3

6.3 Experimental – Liposome Synthesis

6.3.1 Reagents and equipment

All solvents were of the highest purity grade available and used as received. Plain HSPC/Choline/mPEG2000-DSPE-liposomes (Doxebo) were obtained from FormuMax Scientific Inc., USA as a translucent whitish liquid in a clear glass vial. DiD' solid; DiIC18(5) solid (1,1'-Dioctadecyl-3,3,3',3'-Tetramethylindodicarbocyanine, 4-Chlorobenzenesulfonate Salt) dye was obtained from Invitrogen™.

Size exclusion chromatography (SEC) was performed on a Superose 10/30 column (GE Healthcare Life Sciences) run at 0.5 mL/min in PBS. Centrifugal filtration was performed using Merck Millipore Amicon™ Ultra 100 KDa Centrifugal Filter Units in a high speed Hettich MIKRO 20 centrifuge. UV detection was performed at 214 and 280 nm on a GE Purifier ÄKTA HPLC. The fluorescence was performed on Promega GLomax® discover system using red excitation source at wavelength 644 nm with emission detected at 660-720 nm.

6.3.2 Synthesis

DiD solid (2.5 mg, 2.3 µM) was dissolved in pure ethanol (1 ml) using sonication. The dye solution (3 µl) obtained was added to Doxebo dispersion (500 µl, 60 mM) yielding a final DiD concentration of 15 µg/ml in DiD/Doxebo dispersion. The DiD/Doxebo dispersion was incubated under constant rotation for 2 hrs at 37°C to give DiD-PEGylated liposomes (DPLs). Free DiD solid and ethanol was removed from formed DPLs using PD10 minitrap

G-25 size exclusion column (GE healthcare) following manufacturer's gravity protocol. DPLs were further purified using 100 kDa size exclusion centrifugal filter at maximum speed. Any leftover dye was pelleted out using centrifugation. Dynamic light scattering quantified the change in hydrodynamic size, zeta potential and PDIs of the DPLs pre and post DiD labelling. The incorporated dye concentration in the DPL sample was assessed by measuring fluorescence of samples at excitation wavelength of 644 nm and emission at 664 nm and comparison with standard curves for the DiD fluorescence measured in ethanol.

6.3.3 Serum stability of fluorescent liposomes

Serum stability was performed to assess the stability of labelled liposomes in serum and monitor leaking of the dye in vitro. The DPLs were incubated at 37°C in human serum albumin. Aliquots of the test sample were taken at different time points for this stability study and applied to SEC HPLC at 0, 24 h and 48 h. 1 ml fractions were eluted in PBS and the UV signal was recorded. The fluorescence of all collected fractions was measured to assess the leaked dye.

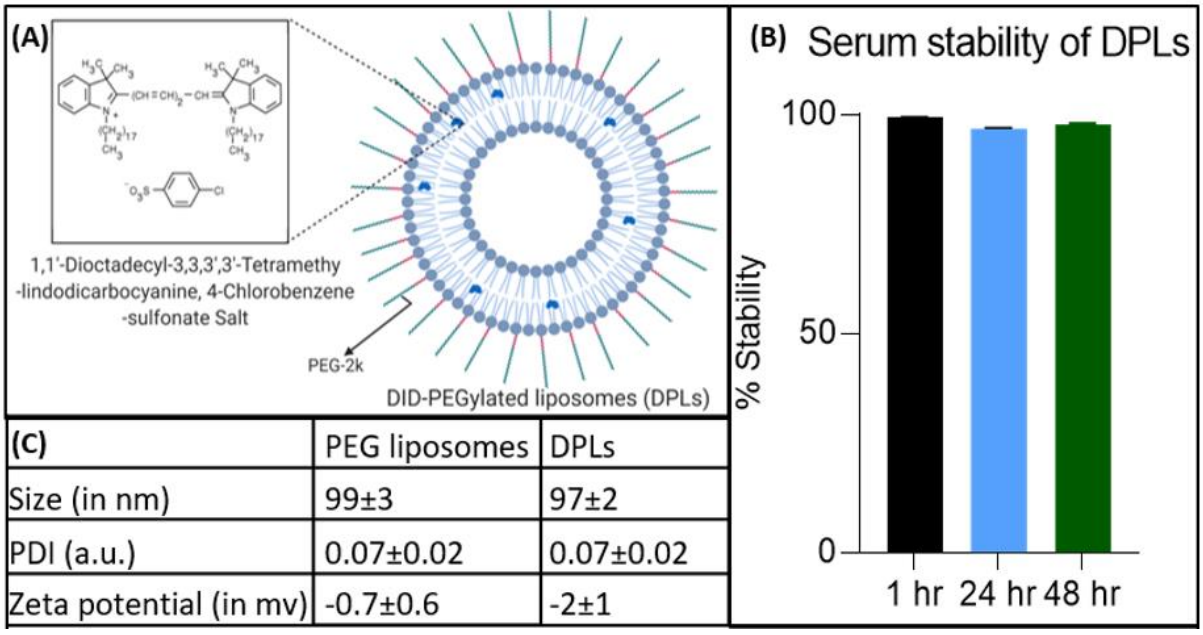

(C)	PEG liposomes	DPLs
Size (in nm)	99±3	97±2
PDI (a.u.)	0.07±0.02	0.07±0.02
Zeta potential (in mv)	-0.7±0.6	-2±1

Figure 6.17. Stability of liposomes in serum. (A) Structure of the DPLs; **(B)** serum stability of DPLs over 48 hours; **(C)** comparison of properties of synthesized DPLs with PEGylated liposomes. Figure made by Aishwarya Mishra (PhD student, Dr Rafael T. M. de Rosales).

Table 6.9. Studies showing delivery of liposomes into the brain using focused ultrasound and microbubbles. Abbreviations include DOX: doxorubicin; Lipo-DOX: doxorubicin liposomes; PTX: paclitaxel; Gd: gadolinium; FUS: focused ultrasound; MB: microbubbles.

							US Parameters					
Paper	**Purpose**	**Animal / Model**	**Delivered Agent / Size**	**Microbubbles / Dose**	**MRI-guided?**	**Tissue damage via H&E**	MHz	W/cm^2	MPa	PL (ms)	PRF (Hz)	Duration (min)
Treat et al. 2007 Int J Cancer	Investigate if FUS can deliver therapeutic concentrations of DOX	Rat	Lipo-DOX (5.67 mg/kg)	Optison 100 µl/kg	√	√ Vacuolations, RBC, dark neurons.	1.5 or 1.7	-	1.1 - 2.5	10	1	1
Treat et al. 2012 Ultrasound Med Biol	Investigate if FUS can reduce tumour growth delivering lipo-DOX	Rat Glioma	Lipo-DOX (5.67 mg/kg)	Definity 10-20 µl/kg	√	√ Vacuolations	1.7	-	1.2	10	1	1-2
Yang et al. 2012 PLoS ONE	Evalutate pharmacokinetics of 111In-labelled DOX liposomes	Mice Glioma	111In-labelled AP1-targeting DOX liposomes 101 nm	SonoVue 1-5x10^8 bubbles/mL	SPECT/CT	√	1	2.86	0.7	50	1	-
Aryal et al. 2013 J Control Release	Investigate if multiple FUS sessions can increase DOX delivered to glioma model	Rat Glioma	Lipo-DOX (5.67 mg/kg)	Definity 10 µl/kg	√	√ Small hemorrhagic regions Necrosis and apoptosis	0.69	-	0.55-0.81	10	1	1
Kovacs et al. 2015 J Therapeutic Ultrasound	Investigate delivery of fluorescent liposomes	Mice	BODIPY or IRDye labelled liposomes 80 nm	In-house microbubbles	X	X	0.612	-	0.4	10	1	4

Paper	Purpose	Animal / Model	Delivered Agent / Size	Microbubbles / Dose	MRI-guided?	Tissue damage via H&E	US Parameters					
							MHz	W/cm^2	MPa	PL (ms)	PRF (Hz)	Duration (min)
Guo et al. 2015 iUS IEEE UFFC proceedings	Investigate delivery of rhodamine-liposomes	Mice	Rhodamine-labelled liposomes 55 nm and 120 nm	0.1 µl/g	x	√ Small sites of microhaemorrhage	1.28	1.1	0.42	10	1	1
Aryal et al. 2015 J Control Release	Investigate if multiple sessions induce adverse effects in normal brain tissue	Rat	Lipo-DOX (5.67 mg/kg)	Definity 10 µl/kg	√	√ Scars and small cyst	0.69	-	0.55-0.81	10	1	1
Lin et al. 2015 J Control Release	Delivery of a gene liposome system via FUS	Mice	Liposomal-plasmid DNA complex 105 nm	SonoVue 2-5x10^8 bubbles/mL	Fluorescence IVIS system	√	0.5	-	0.3, 0.5, 0.8	10	1	1
Lin et al. 2016 Cancer Chemother Pharmacol	Investigate if cationic lipo-DOX suppress tumour growth	Rat Glioma	Cationic Lipo-DOX or quantum dot-loaded liposomes 175-187 nm	SonoVue 300 µl/kg	√	√	0.69	0.32		10	1	1
Shen et al. 2016 Ultras Med Biol	Explore size of deliverable liposomes	Mice	Rhodamine-tagged liposomes 55, 120, 200 nm	Home-made MBs 0.1 & 0.5 µL/g	X	√	1.282	-	0.53 0.64	7.8 (10,000 cycles)	1	1

Paper	Purpose	Animal / Model	Delivered Agent / Size	Microbubbles / Dose	MRI-guided?	Tissue damage via H&E	US Parameters					
							MHz	W/cm^2	MPa	PL (ms)	PRF (Hz)	Duration (min)
Shen et al. 2017 J Nanomedicine	Investigate the effect of PTX-Liposomes delivered in glioblastoma model	Mice Glioblastoma	Paclitaxel-loaded liposomes 98.3 nm	MBs 0.2 µL/g	√	X	1.1	-	0.64	10	1	1-2
Aryal et al. 2019 Ultrasound Med Biol	Track delivery of liposomes by adding Gd-agent and rhodamine fluorophore	Mice	Gadolinium and rhodamine labelled liposomes 77.5 and 140 nm	Optison 20 µl/kg	√	X	0.69	-	0.42	10	1	1
Lin et al. 2019 Brain Stimul	Delivery of DNA-loaded liposomes for Huntington's disease	Mice Wild-type & Huntington's disease model	GDNFp-Liposome complex 150 nm	SonoVue 0.1 mg/kg	√	√ No damage at 0.3 MPa	0.5	-	0.33	10	1	1
May et al. 2020 Theranostics	Invesitgate delivery of fluorescent liposomes of 10 nm and 100 nm in size	Nude mice	10 nm pHPMA polymer and 100 nm PEGylated liposomes	In-house microbubbles 0.05 MB/µl	X Fluorescence tomorgraphy	X	16	-	1.8	-	-	5
Papachristodoulou et al. 2019 J Control Release	Explore the delivery of liposomes loaded with an inactivator with FUS	Mice Gliomas	Liposomal inactivactor 72 nm	BG8235 microbubbles (Bracco) 7.2 mg/kg	√	X	0.65	-	0.28-0.55	10	1	3

Chapter 4

6.4 Experimental – Gd(rhodamine-pip-DO3A) synthesis

6.4.1 Reagents and equipment

Reagents were purchased and used without further purification from Sigma Aldrich, Fisher Scientific or Goss Scientific. To characterise the different steps of the probe's synthesis, NMR, MALDI and fluorescence spectra were acquired. Proton and carbon nuclear magnetic resonance (^{1}H-NMR; ^{13}C-NMR) spectra were recorded at room temperature on a Bruker AMX-400 spectrometer. Chemical shifts in the NMRs are reported in parts per million (ppm) with coupling constants quoted in hertz (Hz) to the nearest decimal point. Multiplicities are abbreviated as follows: s = singlet, d = doublet, t = triplet, q = quartet, m = multiplet, br = broad, sbr = broad singlet. Electrospray ionization (ES+) mass spectra were collected on a Waters LCT Premier spectrometer. MALDI spectra were collected on a low resolution Micromass MALDI-ToF machine. Fluorescence spectra were recorded on a Varian Cary Eclipse fluorescence spectrophotometer using quartz cuvettes. T_1 measurements were performed on a Bruker DRX-400 spectrometer. The complexes were dissolved in H_2O at five different concentrations and placed in 1.7 mm diameter capillary tubes, sealed with Parafilm. These were placed in 5 mm NMR tubes and filled with D_2O and 1/ T_1 measurements were performed. The concentration of Gd^{3+} in these samples was confirmed by measuring the chemical shift difference between HOD and H_2O signals induced by the paramagnetic Gd^{3+} at 25°C on a Bruker AV 500 [4]. Synthetic and spectral details are given in the supplementary information.

6.4.2 Synthesis

Tert-butyl-DO3A [5] and compound **1** [6] were prepared via literature methods from commercially available starting materials.

N-(9-(2-(4-(2-chloroacetyl)piperazine-1-carbonyl)phenyl)-6-(diethylamino)-3H-xanthen-3-ylidene)-N-ethylethanaminium (**2**)

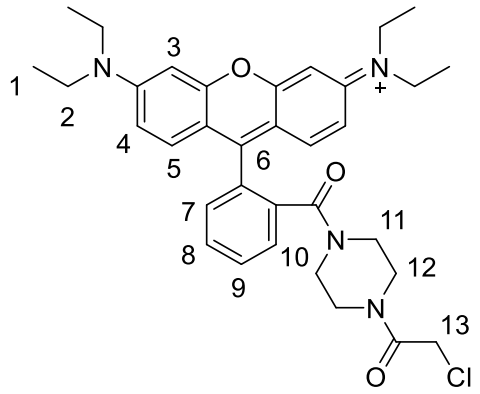

Compound **1** (1.53 g, 2.99 mmol) was dissolved in dichloromethane (50 mL) and cooled to 0°C. NEt_3 (1.67 mL, 11.96 mmol) was added, followed by chloroacetyl chloride (261.8 µL, 3.29 mmol) and the solution was stirred for 3 hours. Water (50 mL) was added to the reaction mixture and the organic layer was separated before extraction of water with dichloromethane (2 x 30 mL). The organic layers were combined, dried over $MgSO_4$, filtered and the solvent was removed under reduced pressure. The crude pink solid was purified by flash column chromatography (DCM/MeOH 100:0 v/v to 95:5 v/v), producing **2** (1.00 g, 62 % yield) as a pink powder.

^{1}H NMR (400 MHz, $CDCl_3$) δ(ppm): 1.26 (12 H, t, $^3J_{H\text{-}H}$ = 7.0, C^1H_2), 3.32-3.46 (8 H, m, $C^{11}H_2$ and $C^{12}H_2$), 3.50-3.65 (8 H, m, C^2H_2), 4.13 (2 H, s, $C^{13}H_2$), 6.67-6.72 (2 H, m, C^3H), 6.95-7.02 (2H, m, C^4H), 7.17 (2 H, d, $^3J_{H\text{-}H}$ = 9.6, C^5H), 7.26-7.31 (1 H, m, C^7H), 7.46-7.52 (1 H, m, $C^{10}H$), 7.60-7.66 (2 H, m, C^8H and C^9H).

^{13}C NMR (100 MHz, $CDCl_3$) δ(ppm): 12.5 (C^1H_3), 41.2 ($C^{13}H_2$), 41.6 ($C^{11}H_2$ or $C^{12}H_2$), 46.0 (C^2H_2), 47.6 ($C^{11}H_2$ or $C^{12}H_2$), 96.1 (C^3H), 113.7, 114.4 (C^4H), 127.5 ($C^{10}H$), 130.1 (br, C^8H, C^9H and C^7H), 130.2 (br, C^8H, C^9H and C^7H), 131.0, 132.0 (C^5H), 135.0 (C^7-C-C^6), 155.7, 155.8, 157.7, 165.8 (C13H2-*C*=O), 167.7 (C=O).

MS(ES+) calc. for C34H40ClN4O3 587.2789 $[M+H]^+$, found 587.2792.

N-(6-(diethylamino)-9-(2-(4-(2-(4,7,10-tris(2-(tert-butoxy)-2-oxoethyl)-1,4,7,10-tetraazacyclododecan-1-yl)acetyl)piperazine-1-carbonyl)phenyl)-3H-xanthen-3-ylidene)-N-ethylethanaminium (**3**)

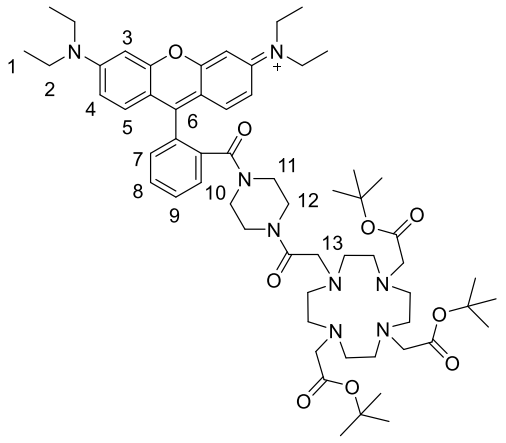

Tert-butyl-DO3A (0.14 g, 0.23 mmol) and compound **2** (0.20 g, 0.34 mmol) were dissolved in acetonitrile (40 mL) and K_2CO_3 (0.127 g, 0.92 mmol) was added. The solution was heated to reflux for 48 hours, cooled and filtered. The solvent was removed under reduced pressure and the crude pink solid was purified by flash column chromatography (DCM/ MeOH 100:0 v/v to 95:5 v/v) to yield **3** (0.16 g, 66 % yield) as a pink solid.

^{1}H NMR (400 MHz, $CDCl_3$) δ(ppm): 1.28 (12 H, t, $^3J_{H\text{-}H}$ = 7.0, C^1H_3), 1.40 (18 H, s, tBu), 1.42 (9 H, s, tBu), 1.70-2.68 (24 H, m), 3.23-3.40 (8 H, m, $C^{11}H_2$ and $C^{12}H_2$), 3.51-3.67 (8 H, m, C^2H_2), 6.73-6.77 (2 H, m, C^3H), 6.96-7.03 (2 H, m, C^4H), 7.15 (2 H, d, $^3J_{H\text{-}H}$ = 9.2, C^5H), 7.22-7.25 (1 H, m, C^7H), 7.42-7.46 (1 H, m, $C^{10}H$), 7.60-7.65 (2 H, m, C^8H and C^9H).

^{13}C NMR (100 MHz, $CDCl_3$) δ(ppm): 12.6 (C^1H_3), 27.9 (CH_3 tBu), 41.1, 41.7, 44.4 (br, $C^{11}H_2$ and $C^{12}H_2$), 46.1 (C^2H_2), 47.6, 48.4 (br), 52.7 (br), 54.9, 55.7, 81.4 (tBu), 81.8 (tBu), 96.2 (C^3H), 113.8, 114.6 (C^4H), 127.4 ($C^{10}H$), 130.1 (C^7H, C^8H or C^9H), 130.2 (C^7H, C^8H or C^9H), 130.9 (C^7H, C^8H or C^9H), 131.3, 132.0 (C^5H), 135.1 (C^7H-$\underline{C}$-C^6), 155.4, 155.8, 157.8, 168.1 (Rh-C=O), 170.6 (C=O), 172.6 (C=O) 172.7 (C=O).

MS(ES+) calc. for C48H65N8O9 897.4875 $[M+H]^+$, found 897.4906.

*N-(6-(diethylamino)-9-(2-(4-(2-(4,7,10-tris(carboxymethyl)-1,4,7,10-tetraazacyclododecan-1-yl)acetyl)piperazine-1-carbonyl)phenyl)-3H-xanthen-3-ylidene)-N-ethylethanaminium (**4**)*

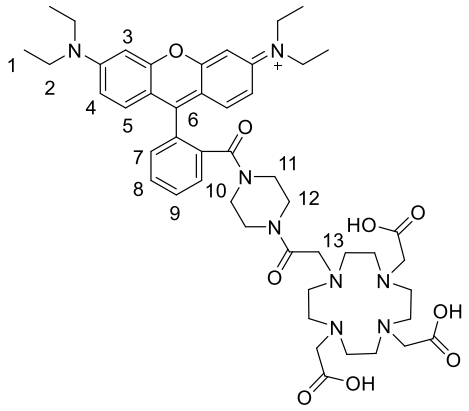

Compound **3** (101.6 mg, 95.3 µmol) was treated with trifluoroacetic acid/dichloromethane (1/1 *v/v,* 4 mL) and stirred for 16 hours at room temperature. The solvent was removed under reduced pressure and the residue purified by reverse phase flash column chromatography (H_2O/MeOH/ TFA 95:5:0 v/v to 0:99.9:0.1 v/v), yielding **4** (63.5 mg, 74 % yield) as a pink solid.

^{1}H NMR (400 MHz, CD_3OD) δ(ppm): 1.30 (12 H, t, $^3J_{H\text{-}H}$ = 7.2, C^1H_3), 3.04-3.14 (8 H, m, CH_2), 3.36-3.55 (10 H, m, CH_2), 3.64-3.73 (12 H, m, C^2H_2 and CH_2), 6.95 (2 H, d, $^3J_{H\text{-}H}$ = 2.4, C^3H), 7.05-7.11 (2 H, m, C^4H), 7.29 (2 H, d, $^3J_{H\text{-}H}$ = 9.6, C^5H), 7.48-7.49 (1 H, m, C^7H), 7.72-7.79 (3 H, m, C^8H, C^9H and $C^{10}H$).

^{13}C NMR (100 MHz, CD_3OD) δ(ppm): 12.9 (C^1H_3), 42.8 (br), 44.9, 45.4, 45.7, 46.9 (C^2H_2), 50.7 (br), 52.2 (br), 52.7 (br), 54.4 (br), 56.5, 57.1, 97.3 (C^3H), 114.8, 115.4 (C^4H), 129.0 ($C^{10}H$), 131.2 (C^8H or C^9H), 131.3(C^8H or C^9H), 131.7 (C^7H), 132.1, 133.2 (C^5H), 136.6 (C^7H-$\underline{C}$-C^6), 157.0, 157.2, 159.2, 169.5 (C=O), 170.0 (C=), 170.8 (C=O), 176.5 (C=O).

MS(ES+) calc. for C48H65N8O9 897.4875 $[M+H]^+$, found 897.4906.

*Compound **5***

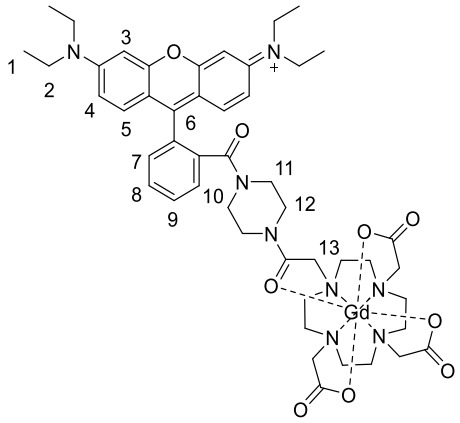

Compound **4** (33.8 mg, 38.0 µmol) and $GdCl_3.6H_2O$ (28.2 mg, 75.9 µmol) were dissolved in H_2O (10 mL) and the pH was adjusted to 5.5 using 1 M NaOH. The solution was stirred for 16 hours at room temperature, following which the solvent was removed under reduced pressure and the residue was purified by reverse phase flash column chromatography (H_2O/ MeOH/ TFA 95:5:0 v/v to 0:99.9:0.1 v/v), yielding **5** (29.4 mg, 74 % yield) as a pink solid.

MS(ES+) calc. for $C_{48}H_{62}N_8O_9Gd$ 1052.3881 $[M+H]^+$, found 1052.3900.

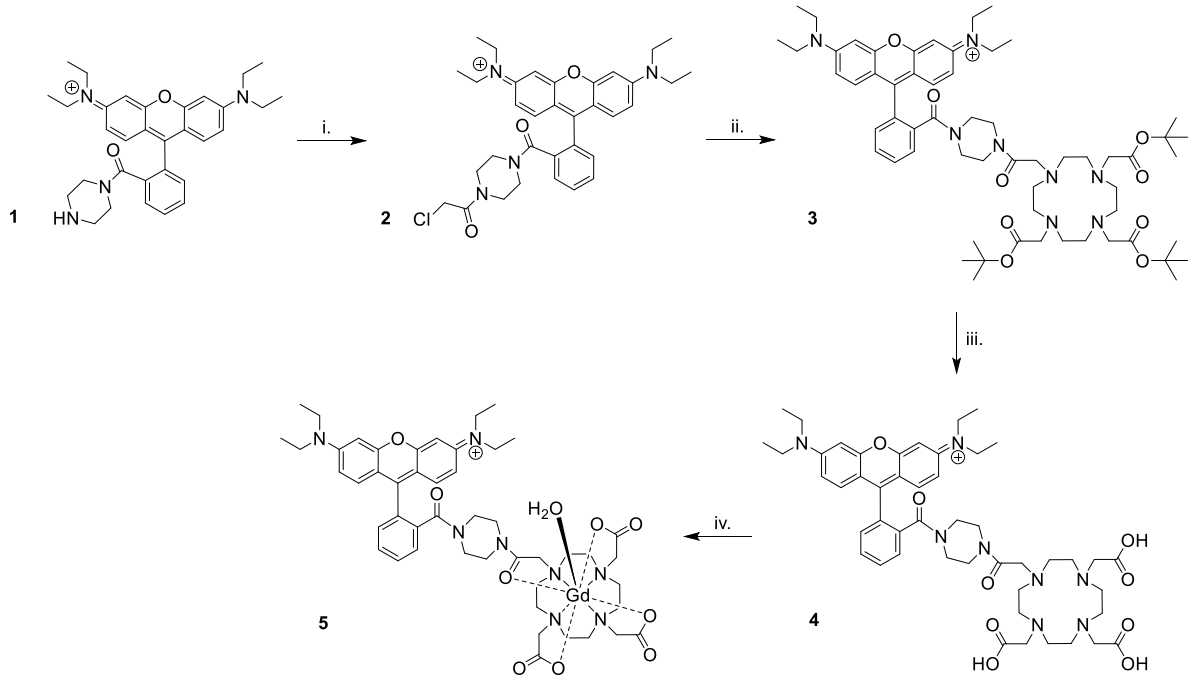

Figure 6.18. Synthesis of Gd(rhodamine-pip-DO3A). The following reaction conditions were used: i. Chloroacetyl chloride, NEt_3, DCM (dichloromethane), 3 h, 0 °C, 62% yield; ii. 1,4,7,10-

tetraazacyclododecane-1,4,7-tris(t-butyl acetate), K_2CO_3, CH_3CN, 48 h, 82 °C, 66% yield; iii. TFA (trifluoroacetic acid), DCM, 16 h, room temperature (RT), 74% yield; iv. $GdCl_3.6H_2O$, pH 5.5, 24 h, RT, 65-87% yield.

References

[1] C. C. Church, "Frequency, pulse length, and the mechanical index," *Acoust. Res. Lett. Online*, vol. 6, no. 3, pp. 162–168, 2005.

[2] IT'IS Foundation, "Tissue Properties - Heat Capacity," 2010. https://www.itis.ethz.ch/virtual-population/tissue-properties/database/heat-capacity/.

[3] H. Azhari, "Basics of Biomedical Ultrasound for Engineers," *Basics Biomed. Ultrasound Eng.*, 2010.

[4] D. M. Corsi, C. Platas-Iglesias, H. Van Bekkum, and J. A. Peters, "Determination of paramagnetic lanthanide(III) concentrations from bulk magnetic susceptibility shifts in NMR spectra," *Magn. Reson. Chem.*, vol. 39, no. 11, pp. 723–726, 2001.

[5] B. Jagadish, G. L. Brickert-Albrecht, G. S. Nichol, E. A. Mash, and N. Raghunand, "On the Synthesis of 1,4,7-Tris(tert-butoxycarbonylmethyl)-1,4,7,10-tetraazacyclododecane," *Tetrahedron Lett*, vol. 52, no. 17, pp. 2058–2061, 2011.

[6] L. Bi, "Novel probes and targeting compounds for mitochondria," 2014.

Permission documents for republication of copyrighted work

A summary table and copies of the emails providing permission to use published figures from my own work and others are appended below.

Page No.	Type of work:	Name of work	Source of work	Copyright holder and contact	permission requested on	I have permission yes /no	Permission note
82	figure	Figure 2.1. Morphology of resting and activated microglia.	C.T. Ekdahl, Microglial activation - tuning and pruning adult neurogenesis – Front. Pharmacol. (2012), doi: 10.3389/fphar.2012.00041	Authors retain copyright of work	08.04.20	yes	Written permission
82	figure	Figure 2.1. Morphology of resting and activated microglia.	Karperien et al, Quantitating the subtleties of microglial morphology with fractal analysis, Frontiers in Cellular Neuroscience (2013), doi: 10.3389/fncel.2013.00003	Authors retain copyright of work	08.04.20	yes	Written permission
83	figure	Figure 2.2. Morphology of resting and reactive astrocytes.	Wilhelmsson et al, Redefining the concept of reactive astrocytes as cells that remain within their unique domains upon reaction to injury, PNAS (2006), 103(46):17513-8	© 2006 National Academy of Sciences U.S.A.	08.04.20	yes	Written permission
85	figure	Figure 2.3. Excretion pathway of agents delivered to the brain via focused ultrasound.	Meng et al., Glymphatics visualization after focused ultrasound-induced blood-brain barrier opening in humans, Ann Neurol (2019), 86(6):975-980		08.04.20	waiting	Waiting – made a request via RightsLink
88	figure	Figure 2.4. Structure of rapid short-pulse (RaSP) and long-pulse sequences.	Morse et al., Rapid short-pulse ultrasound delivers drugs uniformly across the murine blood-brain barrier with negligible disruption, Radiology (2019), 291:459-466.	© Radiological Society of North America (RSNA®)	02.01.20	yes	Written permission
94	figure	Figure 2.5. Ultrasound experimental setup.	Morse et al., Rapid short-pulse ultrasound delivers drugs uniformly across the murine blood-brain barrier with	© Radiological Society of North America (RSNA®)	02.01.20	yes	Written permission

			negligible disruption, Radiology (2019), 291:459-466.				
99	figure	Figure 2.7. Ultrasound targeting.	Morse et al., Rapid short-pulse ultrasound delivers drugs uniformly across the murine blood-brain barrier with negligible disruption, Radiology (2019), 291:459-466.	© Radiological Society of North America (RSNA®)	02.01.20	yes	Written permission
120	figure	Figure 2.14. Detected dose and distribution of dextran delivered with rapid short-pulse (RaSP) and ms-long pulse sequences at 0.35 MPa.	Morse et al., Rapid short-pulse ultrasound delivers drugs uniformly across the murine blood-brain barrier with negligible disruption, Radiology (2019), 291:459-466.	© Radiological Society of North America (RSNA®)	02.01.20	yes	Written permission
121	figure	Figure 2.15. Dextran distribution throughout the parenchyma and in cells in RaSP treated brains.	Morse et al., Rapid short-pulse ultrasound delivers drugs uniformly across the murine blood-brain barrier with negligible disruption, Radiology (2019), 291:459-466.	© Radiological Society of North America (RSNA®)	02.01.20	yes	Written permission
123	figure	Figure 2.16. Dextran distribution throughout the parenchyma and in cells in ms-long pulse treated brains.	Morse et al., Rapid short-pulse ultrasound delivers drugs uniformly across the murine blood-brain barrier with negligible disruption, Radiology (2019), 291:459-466.	© Radiological Society of North America (RSNA®)	02.01.20	yes	Written permission
136	figure	Figure 2.27. Dextran delivery at 0, 10 and 20 min after ultrasound treatment with RaSP and ms-long pulse sequences.	Morse et al., Rapid short-pulse ultrasound delivers drugs uniformly across the murine blood-brain barrier with negligible disruption, Radiology (2019), 291:459-466.	© Radiological Society of North America (RSNA®)	02.01.20	yes	Written permission
138	figure	Figure 2.28. BBB closing timeline with RaSP and ms-long pulse sequences.	Morse et al., Rapid short-pulse ultrasound delivers drugs uniformly across the murine blood-brain barrier with negligible disruption, Radiology (2019), 291:459-466.	© Radiological Society of North America (RSNA®)	02.01.20	yes	Written permission

152	figure	Figure 2.40. Predicting the detected dextran dose based on the energy of the acoustic emissions.	Morse et al., Rapid short-pulse ultrasound delivers drugs uniformly across the murine blood-brain barrier with negligible disruption, Radiology (2019), 291:459-466.	© Radiological Society of North America (RSNA®)	02.01.20	yes	Written permission
153	figure	Figure 2.41. Energy from acoustic emissions during RaSP and long pulse sequence treatment.	Morse et al., Rapid short-pulse ultrasound delivers drugs uniformly across the murine blood-brain barrier with negligible disruption, Radiology (2019), 291:459-466.	© Radiological Society of North America (RSNA®)	02.01.20	yes	Written permission
155	figure	Figure 2.42. Lifetime of acoustic emissions from microbubbles.	Morse et al., Rapid short-pulse ultrasound delivers drugs uniformly across the murine blood-brain barrier with negligible disruption, Radiology (2019), 291:459-466.	© Radiological Society of North America (RSNA®)	02.01.20	yes	Written permission
158	figure	Figure 2.45. Spectral content of the acoustic emissions produced by RaSP and long pulse sequence.	Morse et al., Rapid short-pulse ultrasound delivers drugs uniformly across the murine blood-brain barrier with negligible disruption, Radiology (2019), 291:459-466.	© Radiological Society of North America (RSNA®)	02.01.20	yes	Written permission
257	figure	Figure 4.5. Ultrasound experimental setup.	Morse et al., Neuron labelling with rhodamine-conjugated Gd-based MRI contrast agents delivered to the brain via focused ultrasound, Theranostics (2020), 10(6):2659-2674.	© Ivyspring International Publisher	08.04.20	yes	Written permission
262	figure	Figure 4.6. 3D reconstruction of the mouse brain from the MRI images and sagittal, axial and coronal brain slices.	Morse et al., Neuron labelling with rhodamine-conjugated Gd-based MRI contrast agents delivered to the brain via focused ultrasound, Theranostics (2020), 10(6):2659-2674.	© Ivyspring International Publisher	08.04.20	yes	Written permission

265	figure	Figure 4.8. Delivery of Gd(rhodamine-pip-Do3A) to the left hemisphere of the mouse brain.	Morse et al., Neuron labelling with rhodamine-conjugated Gd-based MRI contrast agents delivered to the brain via focused ultrasound, Theranostics (2020), 10(6):2659-2674.	© Ivyspring International Publisher	08.04.20	yes	Written permission
266	figure	Figure 4.9. Neuronal staining of brain slices with Gd(rhodamine-pip-DO3A) delivery.	Morse et al., Neuron labelling with rhodamine-conjugated Gd-based MRI contrast agents delivered to the brain via focused ultrasound, Theranostics (2020), 10(6):2659-2674.	© Ivyspring International Publisher	08.04.20	yes	Written permission
271	figure	Figure 4.13. Distribution of Gd(rhodamine-pip-DO3A) within the brain.	Morse et al., Neuron labelling with rhodamine-conjugated Gd-based MRI contrast agents delivered to the brain via focused ultrasound, Theranostics (2020), 10(6):2659-2674.	© Ivyspring International Publisher	08.04.20	yes	Written permission
272	figure	Figure 4.14. Subcellular localisation of Gd(rhodamine-pip-DO3A) within neuronal-like cells.	Morse et al., Neuron labelling with rhodamine-conjugated Gd-based MRI contrast agents delivered to the brain via focused ultrasound, Theranostics (2020), 10(6):2659-2674.	© Ivyspring International Publisher	08.04.20	yes	Written permission
273	figure	Figure 4.15. Distribution of dextran within the brain.	Morse et al., Neuron labelling with rhodamine-conjugated Gd-based MRI contrast agents delivered to the brain via focused ultrasound, Theranostics (2020), 10(6):2659-2674.	© Ivyspring International Publisher	08.04.20	yes	Written permission
274	figure	Figure 4.16. Neuronal, microglial and astrocyte	Morse et al., Neuron labelling with rhodamine-conjugated Gd-based MRI contrast agents	© Ivyspring International Publisher	08.04.20	yes	Written permission

		staining of brain slices with dextran delivery.	delivered to the brain via focused ultrasound, Theranostics (2020), 10(6):2659-2674.				
274	figure	Figure 4.17. Quantified distribution of Gd(rhodamine-pip-DO3A) and dextran within the brain.	Morse et al., Neuron labelling with rhodamine-conjugated Gd-based MRI contrast agents delivered to the brain via focused ultrasound, Theranostics (2020), 10(6):2659-2674.	© Ivyspring International Publisher	08.04.20	yes	Written permission
276	figure	Figure 4.18. Ex vivo MRI images of brain with Gd(rhodamine-pip-DO3A) delivery to the left hemisphere.	Morse et al., Neuron labelling with rhodamine-conjugated Gd-based MRI contrast agents delivered to the brain via focused ultrasound, Theranostics (2020), 10(6):2659-2674.	© Ivyspring International Publisher	08.04.20	yes	Written permission
277	figure	Figure 4.20. Fluorescence detection of Gd(rhodamine-pip-DO3A) in brain scanned with MRI.	Morse et al., Neuron labelling with rhodamine-conjugated Gd-based MRI contrast agents delivered to the brain via focused ultrasound, Theranostics (2020), 10(6):2659-2674.	© Ivyspring International Publisher	08.04.20	yes	Written permission
278	figure	Figure 4.21. Binding of Gd(rhodamine-pip-DO3A) to albumin.	Morse et al., Neuron labelling with rhodamine-conjugated Gd-based MRI contrast agents delivered to the brain via focused ultrasound, Theranostics (2020), 10(6):2659-2674.	© Ivyspring International Publisher	08.04.20	yes	Written permission

- Permission from *Radiology*.

RADIOLOGICAL SOCIETY OF NORTH AMERICA
820 JORIE BLVD, OAK BROOK, IL 60523
TEL 1-630-571-2670 FAX 1-630-571-7837
RSNA.ORG

RSNA® Radiological Society of North America

January 9, 2020

Dear Sophie Morse:

The Radiological Society of North America (RSNA®) is pleased to grant you permission to reproduce the following figures in print and electronic formats for educational use in your PhD thesis, provided you give full credit to the authors of the original publication.

> Figures 1, 2, 3, 4, 5
> Morse S V, Pouliopoulos A N, Chan T G, et al. Rapid short-pulse ultrasound delivers drugs uniformly across the murine blood-brain barrier with negligible disruption. *Radiology* 2019;291:459-466.

This permission is a one-time, non-exclusive grant for English-language use and is exclusively limited to the usage stated and underlined above. The requestor guarantees to reproduce the material as originally published. Permission is granted under the condition that a full credit line is prominently placed (i.e. author name(s), journal name, copyright year, volume #, inclusive pages and copyright holder).

This permission becomes effective upon receipt of this signed contract. Please sign a copy of this agreement, return a signed copy to me and retain a copy for your files. Thank you for your interest in our publication.

[Print Name]: SOPHIE MORSE

SIGNATURE: Sophie Morse Date: 13/01/20

Sincerely,

Ashley E. Daly

Ashley E. Daly
Senior Manager, Journal Rights & Communications
Publications

Phone: 630-590-7771
Fax: 630-590-7724
E-mail: *permissions@rsna.org*

- Permission from *Theranostics*.

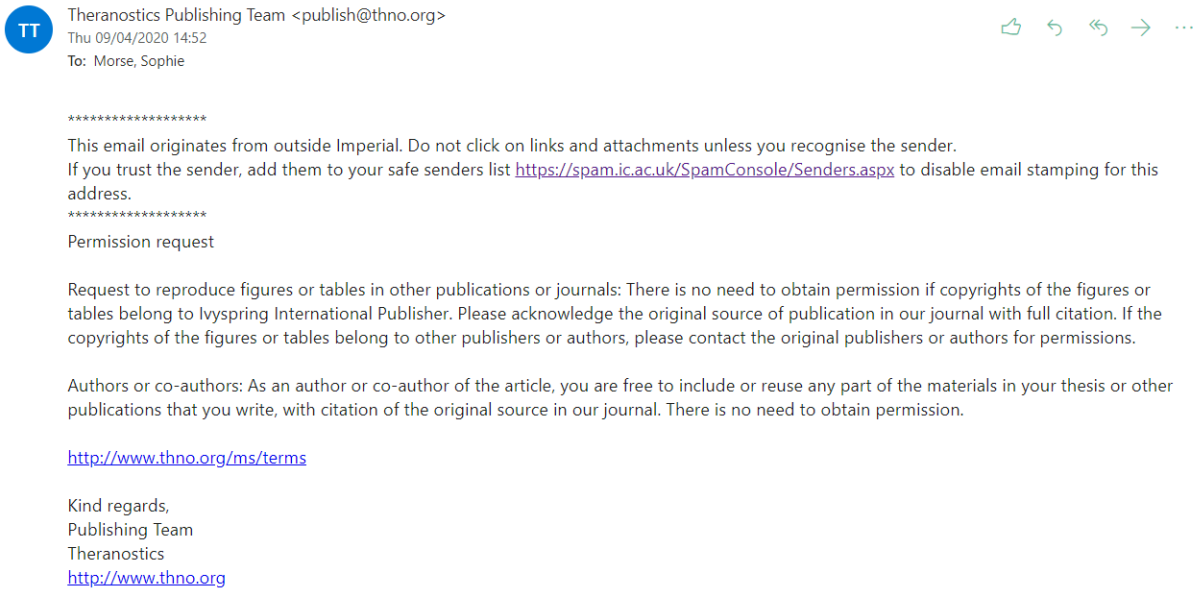

Theranostics Publishing Team <publish@thno.org>
Thu 09/04/2020 14:52
To: Morse, Sophie

****
This email originates from outside Imperial. Do not click on links and attachments unless you recognise the sender.
If you trust the sender, add them to your safe senders list https://spam.ic.ac.uk/SpamConsole/Senders.aspx to disable email stamping for this address.
****
Permission request

Request to reproduce figures or tables in other publications or journals: There is no need to obtain permission if copyrights of the figures or tables belong to Ivyspring International Publisher. Please acknowledge the original source of publication in our journal with full citation. If the copyrights of the figures or tables belong to other publishers or authors, please contact the original publishers or authors for permissions.

Authors or co-authors: As an author or co-author of the article, you are free to include or reuse any part of the materials in your thesis or other publications that you write, with citation of the original source in our journal. There is no need to obtain permission.

http://www.thno.org/ms/terms

Kind regards,
Publishing Team
Theranostics
http://www.thno.org

- Permission from *PNAS*.

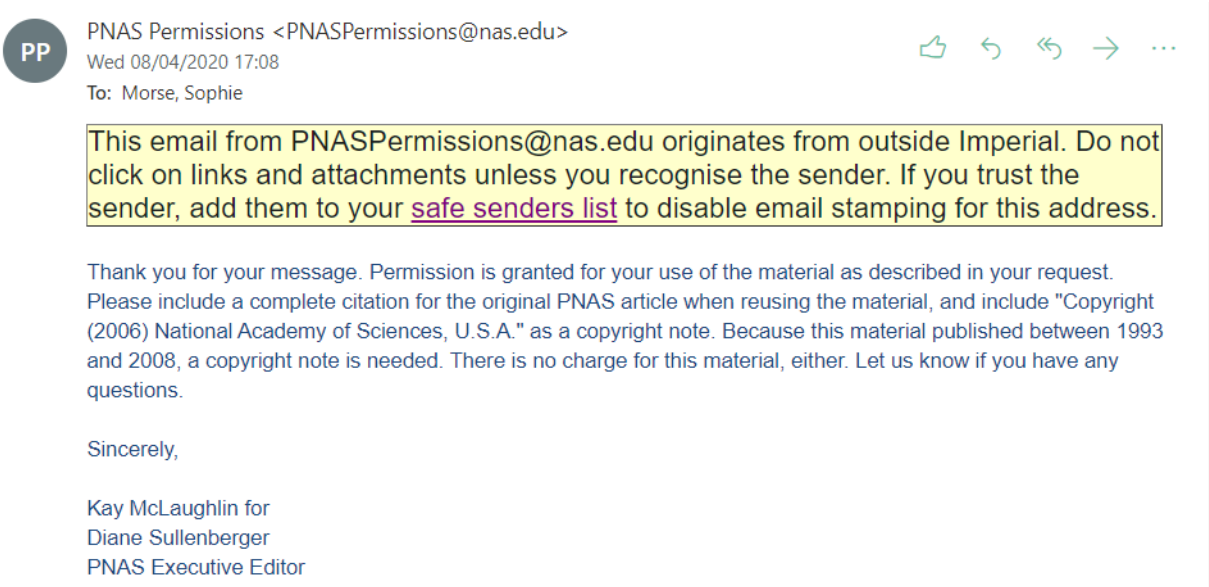

PNAS Permissions <PNASPermissions@nas.edu>
Wed 08/04/2020 17:08
To: Morse, Sophie

This email from PNASPermissions@nas.edu originates from outside Imperial. Do not click on links and attachments unless you recognise the sender. If you trust the sender, add them to your safe senders list to disable email stamping for this address.

Thank you for your message. Permission is granted for your use of the material as described in your request. Please include a complete citation for the original PNAS article when reusing the material, and include "Copyright (2006) National Academy of Sciences, U.S.A." as a copyright note. Because this material published between 1993 and 2008, a copyright note is needed. There is no charge for this material, either. Let us know if you have any questions.

Sincerely,

Kay McLaughlin for
Diane Sullenberger
PNAS Executive Editor

- Permission from the *Frontiers*.

Dear Sophie,

Thank you for your email. I am happy to clarify for you the reuse policies of published work at Frontiers.

All Frontiers articles are fully Gold Open Access which allows authors to retain copyright of their work. Articles are currently distributed under the terms of the Creative Commons Attribution License (CC-BY 4.0), which permits the use, distribution, and reproduction of material from published articles, provided the original authors and source are properly credited, and subject to any copyright notices concerning any third-party content. The latest version of the Frontiers Copyright Statement can be found here (https://www.frontiersin.org/Copyright.aspx).

You are therefore free to include this figure in your thesis, provided that correct attribution of the original source is given.

Please do not hesitate to contact me if you have any further questions.

Kind regards,

Maura

Maura Ferrer Ferrer, PhD
Journal Development Specialist

Frontiers | Editorial Office - Journal Development Team
Neuroscience Portfolio Manager: Stéphanie Maret, PhD

Frontiers
www.frontiersin.org
Avenue du Tribunal-Fédéral 34
1005 Lausanne, Switzerland
Office T +41 215 10 17 75
Connect with us

- Permission requested from *Annals of Neurology*.

Request for permission to reproduce figure from Annals of Neurology

MS

Morse, Sophie
Wed 08/04/2020 18:00
To: cs-journals@wiley.com

Hello,

I would like to request permission to reproduce Figure 3 form this paper in Annals of Neurology, however, I cannot find a contact to ask for this. Would you be able to direct me to the right email address please?

https://onlinelibrary.wiley.com/doi/abs/10.1002/ana.25604

Thank you,
Sophie